Probing the cosmic-ray pressure in the Virgo Cluster and the origin of the very-high-energy gamma rays of M87 with H.E.S.S. and CTA

D i s s e r t a t i o n

zur Erlangung des akademischen Grades

d o c t o r r e r u m n a t u r a l i u m

(Dr. rer. nat.)

im Fach Physik

eingereicht an der
Mathematisch-Naturwissenschaftlichen Fakultät
der Humboldt-Universität zu Berlin

von
M.Sc. **Victor Barbosa Martins**

Acting Präsident der Humboldt-Universität zu Berlin:
Prof. Dr. Peter Frensch

Dekan der Mathematisch-Naturwissenschaftlichen Fakultät:
Prof. Dr. Elmar Kulke

Gutachter/innen: 1. Prof. Dr. David Berge
2. Prof. Dr. Marek Kowalski
3. Prof. Dr. Christoph Pfrommer

Tag der mündlichen Prüfung: 24.05.2022

Selbständigkeitserklärung

Ich erkläre, dass ich die Dissertation selbständig und nur unter Verwendung der von mir gemäß § 7 Abs. 3 der Promotionsordnung der Mathematisch-Naturwissenschaftlichen Fakultät, veröffentlicht im Amtlichen Mitteilungsblatt der Humboldt-Universität zu Berlin Nr. 42/2018 am 11.07.2018 angegebenen Hilfsmittel angefertigt habe.

Berlin, July 1, 2022.	Victor Barbosa Martins

To my father Elias.

Abstract

The High Energy Stereoscopic System (H.E.S.S.) is an array of five Imaging Atmospheric Cherenkov Telescopes (IACTs) located in Namibia. The H.E.S.S. telescopes are sensitive to Very-High-Energy (VHE) gamma rays between $\sim$ 30 TeV and $\sim$ 100 TeV. At a distance of 16.5 Mpc Messier 87 (M87) is one of the closest radio-galaxies, hosting one of the most massive Super-Massive Black Hole, which accretes matter and launches an inclined jet of relativistic particles. The jet is detected and studied by radiation emitted through the entire electromagnetic spectrum. M87 is located at the very center of the Virgo galaxy cluster, a Cool Core (CC) cluster, characterized by an Intra-cluster Medium (ICM) that is colder close to the center and hotter towards the outskirts of the galaxy cluster. According to the Cooling Flow (CF) theory, the plasma in CC clusters cools in the outskirts of the cluster and falls inwards, increasing the star formation ratio in the region. However, optical measurements of the Virgo Cluster seem to contradict this model. The Active Galactic Nucleus (AGN) feedback mechanism is proposed as a heating mechanism, which counterbalances the cooling of the ICM and avoids its CF. The cosmic rays from the jet interact with the ICM producing neutral pions, which decay to gamma rays, forming a non-variable and extended gamma-ray signal. However, no gamma-ray observations could be associated with pion decay in galaxy clusters. In this work, deep H.E.S.S. observations of M87's low state are analyzed, and the results have shown no significant gamma-ray extension leading to a $3\,\sigma$ upper limit of $0.016^\circ \approx 4.6$ kpc. The ratio of cosmic-ray pressure to thermal pressure X_{CR} is constrained to < 0.36 at its maximum position, assuming a steady-state between the heating and the cooling processes. The new generation of IACTs, the Cherenkov Telescope Array Observatory (CTAO) will offer unprecedented sensitivity and angular resolution. To assure the long-term availability of the telescopes, a structure monitoring system based on vibration measurements was developed and successfully tested at the Medium-sized Telescope (MST) prototype between 2019 and 2020 in Berlin. CTAO should be able to probe the gamma-ray emission from the Virgo Cluster, and, according to simulations and to the steady-state model, significantly detect it after ≈ 210 h.

Kurzzusammenfassung

Das High Energy Stereoscopic System (H.E.S.S.) ist ein System von fünf atmosphärischen Cherenkov-Teleskopen (IACT) in Namibia. Die H.E.S.S. Teleskope sind empfindlich für sehr energiereiche (VHE) Gammastrahlen zwischen $\sim 30\,\mathrm{TeV}$ und $\sim 100\,\mathrm{TeV}$. Mit einer Entfernung von 16,5 Mpc ist Messier 87 (M87) eine der nächsten Radiogalaxien und beherbergt eines der massereichsten supermassiven Schwarzen Löcher, das Materie in einen Plasmastrahl relativistischer Teilchen emittiert. Der Strahl wird im Bereich des gesamten elektromagnetischen Spektrums beobachtet und untersucht. M87 befindet sich im Zentrum des Virgo-Galaxienhaufens, eines kühlen Galaxienhaufens, der von Gas gefüllt ist, das in der Nähe des Zentrums kälter und in den Außenbereichen des Galaxienhaufens heißer ist. Gemäß der Cooling Flow (CF) Theorie kühlt das Plasma in Cool Core (CC) Haufen am Rand des Haufens ab und sinkt nach innen, wodurch die Sternentstehungsrate im Zentrum erhöht wird. Optische Messungen des Virgo Galaxienhaufens scheinen diesem Modell jedoch zu widersprechen. Als Heizmechanismus wird der aktive galaktische Kern Rückkopplungsmechanismus vorgeschlagen, der die Abkühlung des ICM ausgleicht und dessen CF vermeidet. Die kosmische Strahlung des Jets interagiert mit der ICM und erzeugt neutrale Pionen, die in Gammastrahlen zerfallen und ein nicht variables und ausgedehntes Gammastrahlensignal erzeugen. Allerdings konnten keine Gammastrahlen-Beobachtungen mit dem Pionenzerfall in dem Galaxienhaufen in Verbindung gebracht werden. In dieser Studie der H.E.S.S. Beobachtungen des niedrigen Strahl-Aktivitätszustands von M87 haben keine signifikante Ausdehnung der Emissionsregion gezeigt, woraus eine 3σ Obergrenze von $0.016^\circ \approx 4.6\,\mathrm{kpc}$ abgeleitet wurde. Das Verhältnis des Drucks in kosmischer Strahlung zur thermischen Strahlung ist auf <0.36 im Zentralregion beschränkt. Diese abgeleitete Obergrenze nimmt einen Gleichgewichtszustand zwischen den Erwärmungs und den Kühlprozessen an. Die neue Generation von IACTs, das Cherenkov Telescope Array Observatory (CTAO), wird eine unvergleichbare Empfindlichkeit und Winkelauflösung bieten. Um die langfristige Verfügbarkeit der Teleskope sicherzustellen, wurde ein auf Schwingungsmessungen basierendes Strukturüberwachungssystem entwickelt und zwischen 2019 und 2020 in Berlin am Prototyp des mittelgrossen Teleskopes erfolgreich getestet. CTAO wird in der Lage sein die Gammastrahlung des Virgo Haufens zu untersuchen und sie laut Simulationen und dem Steady-State-Modell innerhalb von $\approx 210\,\mathrm{h}$ zu detektieren.

Acronyms

a.u. arbitrary unit
ACCEPT Archive of Chandra Cluster Entropy Profile Tables
AD Analog-to-Digital
ADAF Advection Dominated Accretion Flow
ADC Analog Digital Converter
AGN Active Galactic Nucleus (Nuclei)
App. Appendix

BDT boosted decision tree

c.l. confidence level
c.r. containment radius
CAD Computer Aided Design
CAT Cherenkov Array Telescope
CC Cool Core
CCD Charge-Coupled Device
CF Cooling Flow
Ch. Chapter
CMB Cosmic Microwave Background
CR Cosmic Ray
CSD Cross Spectral Density
CSS Camera Support Structure
CT Cherenkov Telescope
CTA Cherenkov Telescope Array
CTAO Cherenkov Telescope Array Observatory

d.o.f. degrees of freedom
DEC Declination
DFFT Discrete Fourier Transform

EAS Extensive Air Shower
EBL Extra-galactic Background Light
EHT Event Horizon Telescope

FDD Frequency Domain Decomposition
FEM Finite Element Method
FF Flat Fielding
FITS Flexible Image Transport System
FoV Field of View
FR-1 Fanaroff-Riley-I
FTP File Transfer Protocol
FWHM Full Width at Half Maximum

GRB Gamma-Ray Burst

H.E.S.S. High Energy Stereoscopic System
HDBSCAN Hierarchical Density-Based Spatial Clustering of Applications with Noise
HE High Energy
HEGRA High Energy Gamma Ray Astronomy
HST Hubble Space Telescope

i.e. *id est*
IACT Imaging Cherenkov Telescope
IC Inverse Compton
ICM Intra-Cluster Medium
IFFT Inverse Fourier Transform

ImPACT Monte Carlo Template-based analysis for the Air-Cherenkov Arrays
IR Infra-red
IRF Instrument Response Function

KN Klein-Nishima

LED Light-emitting diode
LHAASO Large High Altitude Air Shower Observatory
LHC Large Hadron Collider
LMXB Low-Mass X-ray Binaries
LOFAR Low Frequency Array
LST Large-Sized Telescope

M87 Messier 87
MAC Modal Assurance Criteria
MAGIC Major Atmospheric Gamma-Ray Imaging Cherenkov Telescope
MC Monte Carlo
Mrk Markarian Galaxies Catalog
MRS Mean Reduced Scaled
MST Medium-Sized Telescope
MWL Multi-wavelength

NoSQL Not only Structured Query Language
NSB Night Sky Background
NuSTAR Nuclear Spectroscopic Telescope Array

OMA Operational Modal Analysis
OSO-3 Third Orbiting Solar Observatory

p-p proton-proton
PKS Parkes Catalogue of Radio Sources
PL Power-law
PLC Programmable Logic Controller
PMT Photo Multiplier Tubes
PSF Point Spread Function
PWN Pulsar Wind Nebulae

RA Right Ascension
RIAF Radiatively Inefficient Accretion Flow
ROI Region Of Interest
ROSAT Röntgensatellit
RS Reduced Scale

SDSSg Sloan Digital Sky Survey g-band
Sec. Section
SED Spectra Energy Distribution
SMBH Super-massive Black Hole
SSC Synchrotron Self-Compton
SST Small-Sized Telescope
SVD Singular Value Decomposition

Tab. Table
ToO Target-of-Opportunity
TS Test Statistic

UHECR Ultra-high energy cosmic rays
UL Upper Limit
UV Ultra-violet

VERITAS Very Energetic Radiation Imaging Telescope Array System
VHE Very High Energy
VLA Very Long Array
VLBA Very Long Baseline Array

List of Figures

List of Tables

Contents

1. Introduction

Space has been fascinating us since the birth of civilization. Without the technology to measure and the knowledge to explain natural phenomena such as supernova explosions, the passage of comets and eclipses, the imagination of the ancient people was the protagonist and gave origin to many beliefs. With the emergence of the scientific revolution in the 16^{th} century marked by Nicolaus Copernicus' publication *De revolutionibus orbium coelestium* (On the Revolutions of the Heavenly Spheres)[1], a new view of the universe started to be painted. The traditional Aristotelian deduction method was slowly substituted by an inductive and experimental approach, which defines the scientific method of modern science.

The telescope was invented in 1608 in the Netherlands[2] and was first adapted to astronomy by Galileo Galilei in 1609 with his observations of Jupiter's moons and lunar craters[3]. In the 19^{th} century, non-visible light started being observed by scientists, as ultra-violet (UV) light, radio, and X rays. In the first half of the 20^{th} century, radio and X-ray emissions were first detected from celestial objects outside of our solar system. Only in the 1960s did experimental gamma-ray astronomy start. It has led up to now to the discovery of more than 5000 gamma-ray emitters[4].

Gamma rays are the highest energy photons (>100 kiloelectronvolt (keV)) in the electromagnetic spectrum, and celestial objects were predicted to produce these high-energy photons as by-products of interactions of cosmic rays[5]. Cosmic rays are relativistic particles produced with such high energies that they can not be described by a black-body spectrum but by non-thermal processes. The existence of cosmic rays was confirmed in 1912 by Victor Franz Hess[6]. While cosmic rays are deflected in ubiquitous magnetic fields, gamma rays are not influenced by them and point directly to their origin[5]. The search for gamma-ray emission from astrophysical objects motivated in 1965 the launch of the first gamma-ray satellite, the Explorer 11[7]. Nevertheless, only in 1967, the Third Orbiting Solar Observatory (OSO-3 satellite)[8] reached sufficient sensitivity to significantly detect astrophysical gamma rays[9].

The more energetic the gamma rays, the rarer they are, which makes Very High Energy (VHE) gamma rays (100 GeV<E<100 TeV) difficult to detect from space with satellites and their limited detection area. Furthermore, since the atmosphere is opaque to gamma rays, a direct measurement is also impossible. Nevertheless, the atmosphere works as a calorimeter, as in

particle detectors such as the Large Hadron Collider (LHC)[10], which makes indirect detection possible. The initial gamma ray interacts with air molecules in the upper atmosphere, producing a cascade of secondary particles, which emit Cherenkov radiation when moving faster than the speed of light in the air. Cherenkov radiation can be detected from the ground as flashes of very short (10s of ns) UV and optical light over large areas ($\sim$ 100s of m^2) by Imaging Atmospheric Cherenkov Telescopes (IACTs). The first IACTs were built in the 1980s and were sensitive in the energy range between a few hundreds of Gigaelectronvolt (GeV) up to 100 Teraelectronvolt (TeV). The use of multiple telescopes and their operation in stereoscopic mode since the late 1990s has proven to deliver the highest quality data of a gamma-ray instrument. The current operational IACT experiments are the High Energy Stereoscopic System (H.E.S.S.)[11], the Major Atmospheric Gamma-Ray Imaging Cherenkov Telescopes (MAGIC)[12], the Very Energetic Radiation Imaging Telescope Array System (VERITAS)[13], and the Large High Altitude Air Shower Observatory LHAASO[14]. The current IACTs offer an angular resolution of $\approx 0.05^\circ$ in the core energy range between 300 GeV and 100 TeV, better than the typical resolution offered by gamma-ray satellites.

Although VHE gamma rays can be used to localize the origin of the parent VHE cosmic rays, a unique association with them is not straight-forward due to the various interaction processes responsible for producing gamma rays. For instance, one of the closest[15,16] Active Galactic Nuclei (AGN) and host of one of the most massive[17] Super-Massive Black Holes (SMBHs) in its center, the radio-galaxy Messier 87 (M87) emits radiation over the entire electromagnetic spectrum. However, the origin of the VHE gamma-ray emission is not yet well established.

M87 is located at the very center of the Virgo Cluster[18], a massive cluster of galaxies extending up to 8° on the night sky. Galaxy clusters and superclusters are the largest gravitationally bound structures in the universe. The Virgo Cluster is a Cool Core (CC) cluster, i.e., its central region is filled with a plasma that is colder and denser than the gas in its outskirts[19]. While the Intra-Cluster Material (ICM) at the cluster center cools down, it is compressed by the weight of the overlying gas. The hotter gas from the outer region flows inwards to replace the compressed gas in the model known as the Cooling Flow (CF)[20]. As a consequence of the CF, a high star formation rate is expected at the center of CC clusters, though optical observations point to the contrary. In the absence of a high star formation rate, a heating mechanism must stabilize the system. Such a mechanism can be provided by the energy feedback of the central AGN, which accretes cooled gas and launches relativistic jets, transferring energy to the surrounding gas and delaying the radiative cooling[21]. There has been so far no observational proof of AGN feedback in CC clusters[22–24], hence, the question remains open for the CF problem. VHE gamma-ray observations of M87 might provide an estimate of the total energy of the cosmic rays propagating towards the ICM and; therefore, test the AGN feedback model as a solution for the CF problem.

Cosmic rays accelerated in the relativistic jet diffuse into the ICM and interact inelastically with the gas. Neutral pions are produced among other mesons and almost immediately decay to gamma rays. The detection of gamma rays is, hence, an indirect measurement of the cosmic-ray pressure exerted into the ICM, which depends only on the ICM density and the energy density of cosmic rays. Given sufficient energy in cosmic rays, the CF of the ICM towards the cluster center can be halted and, therefore, the CF problem and the low star formation rate of CC clusters better understood. The gamma-ray emission due to π^0 decay at the inner-most part of the Virgo Cluster is expected to be non-variable and to extend up to several kilo-parsecs (kpc)[21]. Detection of an extended VHE gamma-ray emission from M87 would not only establish a new class of gamma-ray emitters but also provide estimates on the total energy of cosmic rays accelerated in AGNs and its efficiency. Furthermore, it would support the hypothesis that cosmic rays play a crucial role in heating the ICM, counterbalancing the cooling processes, and it could shed light on the origin of ultra-high energy cosmic rays (UHECRs)[25].

In this work, I present the search for an extended gamma-ray emission from M87 with H.E.S.S. and its implications for the AGN feedback model. I put a special emphasis on the stability of the H.E.S.S. results against systematic uncertainties, in particular regarding the angular resolution. Chapter 2 introduces the H.E.S.S. experiment, where the IACT detection technique, the H.E.S.S. telescopes, and the data analysis are presented. In Ch. 3 I introduce the radio-galaxy M87 and the Virgo Cluster and discuss the current interpretation for the gamma-ray emission from M87. I show my analysis results of the M87's morphology in Ch. 4, including the gamma-ray spectral measurement and flux throughout time. In the same chapter, I also discuss the contribution of relativistic protons to the total gamma-ray emission of M87 and its implications for the AGN feedback mechanism in the Virgo Cluster. The next generation of gamma-ray instruments, the Cherenkov Telescope Array (CTA), is introduced in Ch. 5. Motivated by the challenges, which accompany maintaining a high number of telescopes available for observations, I propose and develop a solution for the monitoring system of the Medium-sized Telescope (MST) structure based on vibration measurements. The system will assure the high availability of the telescopes, the fulfillment of their technical requirements, thereby allowing to exploit its key science projects[26]. The CTA Observatory (CTAO) will also observe M87 and the prospects of these observations and implications for the AGN feedback in the Virgo Cluster are discussed in Ch. 5.

During the preparation of the plots for the thesis, I followed the guidelines for color-blind friendly publications from CTA[27], with the exception of the color maps. The structure monitoring system led to two conference proceedings, namely Barbosa Martins et al. (2019)[28] and Barbosa Martins & Garczarczyk (2020)[29]. The publication of the M87's morphology results is currently under preparation.

2. The H.E.S.S. experiment

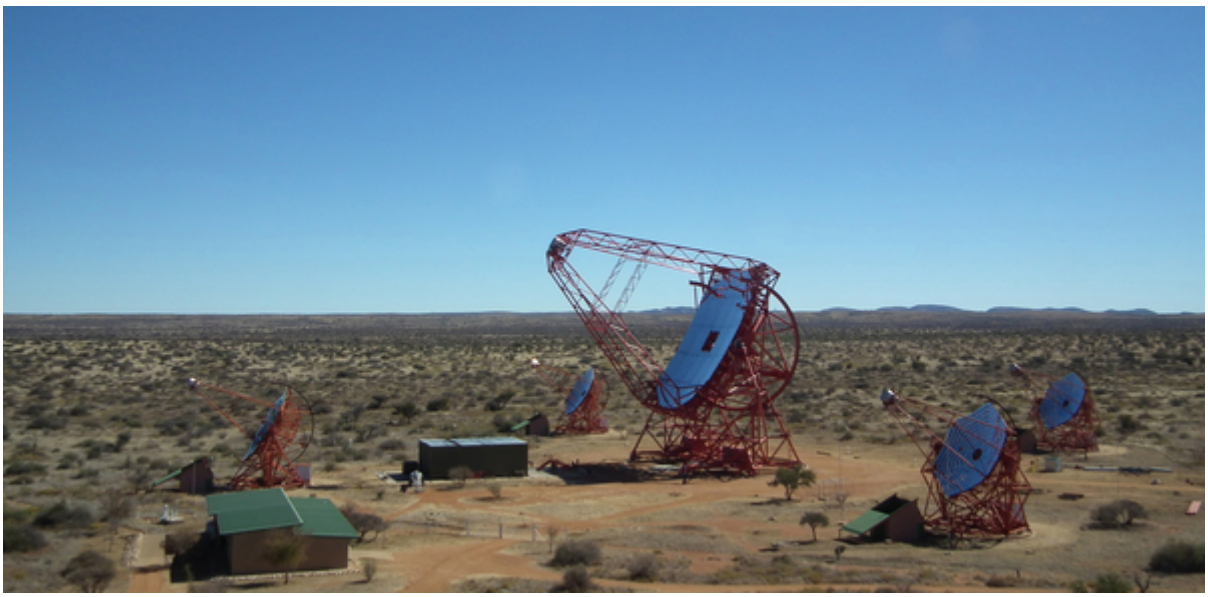

Figure 2.1.: The four small and the large H.E.S.S. telescope at the center of the array. Extracted from MPI(2021)[30].

H.E.S.S.[31] is an array of five IACTs located in the Khomas Highland in Namibia (23°16′18″ South, 16°30′0″ East) at an altitude of 1800 m above the sea level. The high altitude and the dry local weather help keep the night sky clear throughout the year, essential for astronomical observations. The acronym is a tribute to Victor Hess[6], who conducted balloon flights in early 1912 to unravel the extraterrestrial nature of the atmospheric ionizing radiation, later coined cosmic rays. Victor Hess was awarded a Nobel Prize for his discovery in 1936. An aerial view of the telescopes is shown in Fig. 2.1[30].

The H.E.S.S. experiment has been in operation since December 2003. It was composed in its first phase (H.E.S.S. I era) by four identical 12 m Cherenkov Telescopes (CT1-4) with 5° field of view placed 120 m away from each another. The total reflector area of each of the four telescopes comprises 107 m^2, and their cameras are composed of 960 Photo-Multiplier Tubes (PMT) each[11]. In July 2012, a fifth, large telescope, CT5, was added at the center of the

array, marking the beginning of the second phase of the experiment (H.E.S.S. II era). CT5 provides, with a dish diameter of 28 m, 614 m^2 of reflector area though with a smaller field of view of around 3.2 °, especially suitable for low-energy gamma rays[32,33]. A third phase of the experiment started in April 2017, when the cameras of the CT1-4 telescopes were upgraded, improving its read-out system and the stability of the system[11]. In 2020 the camera of CT5 was also upgraded.

The H.E.S.S. telescopes detect gamma rays only indirectly, through the Cherenkov radiation as it is explained in Sec. 2.1. The calibration of the acquired data is explained in Sec. 2.3, and the data quality criteria are described in Sec. 2.4. Finally, in Sec. 2.5 the analysis pipeline is described with the results accounting for the source map, spectrum, and flux.

2.1. Detection technique

The Earth's atmosphere is opaque to gamma rays; however, photons with sufficient energy, i.e., a few tens of GeV, initiate cascades of relativistic particles, which are detectable on Earth. Once gamma rays hit the atmosphere, they form a cascade of secondary particles, the Extensive Air Shower (EAS). First, the gamma ray interacts via Coulomb field with the nucleus of an air molecule and produces a pair of electron-positron, which then emit HE photons via *bremsstrahlung*. This process repeats until the ionization losses take over as the dominant energy loss process, around the electron critical energy of $E_C \approx 85$ MeV in the air. On the other hand, incident cosmic rays, primarily protons, interact hadronically, i.e., via the strong force, with the nucleus of air molecules and give origin to a hadronic cascade. The product of the interaction is π^+, π^- and π^0, produced in similar amounts. While the charged pions decay to muons and neutrinos, the neutral pions quickly decay to gamma rays, which initiate further an electromagnetic cascade. Figure 2.2 shows a toy model (Heitler's model) of the electromagnetic and hadronic showers. At each interaction n, the particle energy is split between the secondary particles, shown in the figure by the different line styles[34].

The hadronic and electromagnetic showers can be distinguished by their lateral and longitudinal distribution. Since the hadronic shower contains other electromagnetic showers that originated from the pion decays, the spread of the secondary particles is larger than in the pure electromagnetic shower. For better visualization, a simulation of a 1 TeV photon-initiated shower is shown in Fig. 2.3 (a), and (b) and a 1 TeV proton-initiated shower in Fig. 2.3 (c), and (d). The red lines are electrons, the black line represents hadrons, and the green lines stand for the muons[35].

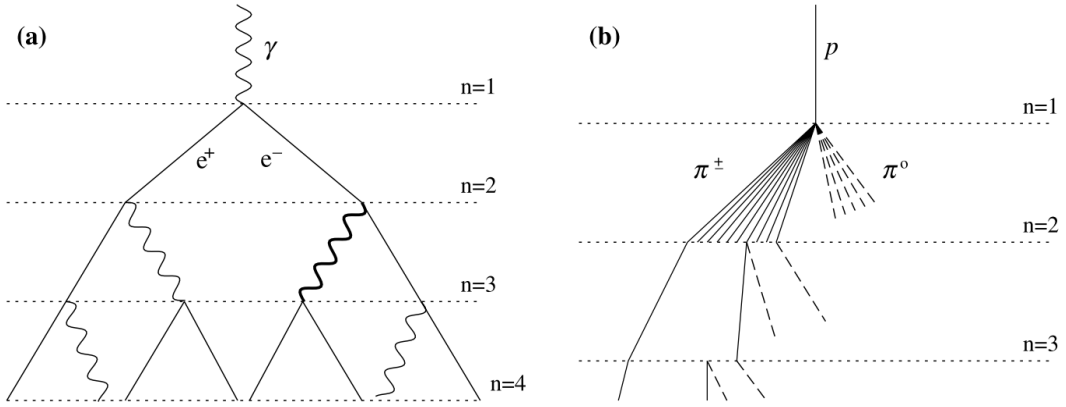

Figure 2.2.: Schematic of the development of (left) an electromagnetic cascade and a (b) hadronic cascade. None of the schematics are on scale. Extracted from Matthews (2005)[34].

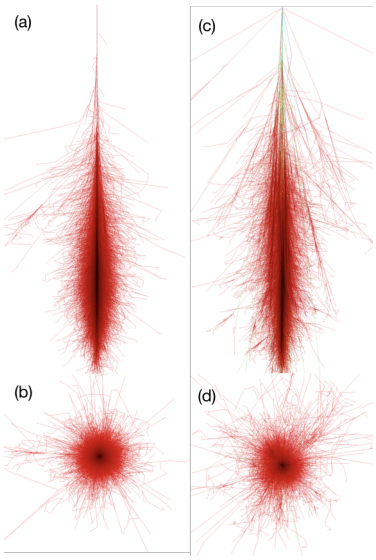

Figure 2.3.: Simulation of an EAS initiated by a 1 TeV photon in a (a) longitudinal and (b) projected views in comparison to an EAS initiated by a 1 TeV proton in a (c) longitudinal and (d) projected views. While the longitudinal direction follows the direction of the incoming particle, the projected view is the perpendicular view from the ground. Extracted from Schmidt & Knapp (2005)[35].

2.1.1. Cherenkov radiation

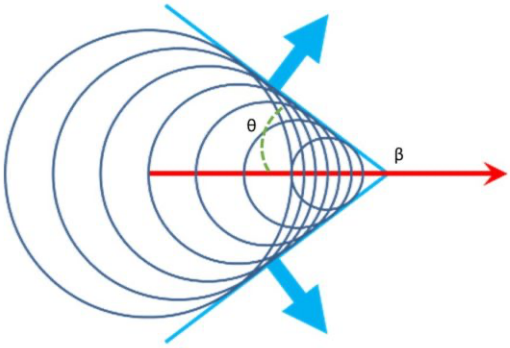

Figure 2.4.: The charged particle moves along the direction of the red line with velocity $\beta = v/c_n > 1$, where $c_n = c/n$ is the speed of light in the medium with refractive index n. The circles show the wavefront of the Cherenkov radiation emitted when the particle was at their centers. The light blue lines and arrows show the Cherenkov cone's propagation direction. Credit: The University of Sheffield.

The secondary charged particles from EAS induced by gamma rays and by cosmic rays have enough energy to produce Cherenkov radiation, emitted when the particles move faster than the speed of light in the medium. The effect was discovered in 1934 by Pavel Cherenkov, who was awarded the Nobel prize for his discovery in 1958[36]. The radiation is emitted as a shock wave in the form of a cone, as seen in Fig. 2.4. The opening angle θ of the cone is given by:

$$cos(\theta) = 1/(\beta n_{\text{air}}), \tag{2.1}$$

where $\beta = v/c$ is the particle speed in comparison to the speed of light, and n_{air} is the refraction index of the air. Due to the variable air density with altitude h, the refractive index n_{air} also changes described as the barometric formula:

$$n_{\text{air}}(h) = 1 + n_0 e^{-h/h_0}, \tag{2.2}$$

where n_0 is defined as $n_0 = n(h_0) = 2.9 \cdot 10^{-4}$ and $h_0 = 7.1\,\text{km}$. The typical shower maximum, i.e. the altitude at which the number of particles in the EAS is the largest, is at around 10 km, which results in a refractive index of $n_{\text{air}}(10\,\text{km}) \approx 1.0007$, and, consequently, an aperture angle of $\theta \approx 0.7°$. The projection of the cone on the ground reaches ≈ 122 meters for a vertical shower and up to several hundreds of meters for inclined showers.

The spectrum of the emitted Cherenkov light peaks at the ultraviolet and the energy loss per

unit length dx and unit of emitted frequency $d\omega$, provided $\beta > 1/n(\omega)$, is given by[37]:

$$\frac{dE}{dxd\omega} = \frac{q^2}{4\pi}\omega\mu(\omega)\left(1 - \frac{1}{n^2(\omega)\beta^2}\right), \tag{2.3}$$

where ω is the emitted frequency, q is the particle's charge, and μ is the medium's permeability. Due to absorption in the atmosphere, the Cherenkov spectrum on the ground peaks at the optical blue band. For instance, the Cherenkov radiation is also responsible for the famous blue light seen in nuclear reactors in power plants.

The duration of the Cherenkov signal from a gamma-ray event detected on the ground is of the order of $\sim 10\,\mathrm{ns}$ for a typical telescope mirror area ($\approx 100\,\mathrm{m}^2$) and depends on the geometrical orientation of the Cherenkov cone to the pointing direction of the telescopes. IACTs detect the gamma-rays indirectly, through the Cherenkov radiation originating by EAS. Although an IACT operates in the optical range, the high-speed pulse of radiation and the stochastic behavior of EAS pose technical difficulties for the detection and reconstruction of the gamma-ray proprieties, as is explained in the next section.

2.1.2. IACTs

The flux of VHE gamma rays is very low ($\sim 10^{-11}\,\mathrm{cm}^{-2}\,\mathrm{s}^{-1}$ for TeV-strong sources), which translates into a few photons per m^2 in a year. Therefore, direct detection by satellites is inconvenient. On the other hand, IACTs take advantage of the atmosphere, which works as a calorimeter, to detect part of the light within the Cherenkov light cone and, consequently, provides enough information for the reconstruction of the gamma-ray proprieties.

The Whipple experiment was the first to successfully measure the Crab Nebula in VHE gamma rays in 1989[38], and the first extra-galactic object Mrk 421[39]. The Cherenkov Array Telescope (CAT)[40] also started operations in 1996. However, only with the High Energy Gamma-Ray Astronomy (HEGRA) stereoscopic system[41], and the CANGAROO telescope system[42], the revolutionary technique of stereoscopic observation started being applied to improve the sensitivity and uncertainties in the reconstructed parameters.

Since 2003, the new generation of experiments, composed by H.E.S.S.[11], MAGIC[12], and VERITAS[13] has rapidly increased the number of VHE sources in the gamma-ray sky, revealing, for instance, a large population of Pulsar Wind Nebulae (PWN), blazars, radiogalaxies, star-forming galaxies and unidentified sources[43].

2.2. The H.E.S.S. array

An IACT consists of three essential elements: a mechanical tracking system, a collecting surface, and a receiver element[43]. While the mechanical tracking system is responsible for compensating Earth's rotation and pointing to the target, the collecting surface gathers and concentrates the photons from the EAS into the receiver element, which records the collected light of the Field of View (FoV).

Each of the CT1-4 telescopes were built according to the Davis-Cotton[44] design to reduce wide FoV spherical aberrations. The mechanical tracking precision is $\approx 60''$ and can reach down to $3''$ with offline corrections[45]. The maximum speed that the drive system can achieve is $\sim 100°$/min. Each telescope is equipped with 383 mirror facets, yielding a total mirror surface of $107\,\mathrm{m}^2$. The mirror's initial reflectivity of $\approx 80\%$ degrades with time due to aging effects. The camera is composed of 960 light amplifying PMTs, and light collecting Winston cones to reduce the dead space between the PMTs. The PMTs are arranged in a plane and packed in electronic modules (drawers), which consist of 16 PMTs each. Since each PMT has an opening angle of 0.16°, the whole camera has a FoV of $\sqrt{960} \times 0.16° \approx 5°$. The quantum efficiency, i.e. the fraction of incoming photons that contribute to the signal, is $\approx 25\%$ in the Cherenkov light wavelength from 320 nm to 420 nm, though the PMT sensitivity extends from 300 nm to 600 nm[46]. A procedure for mirror alignment assures the focussing of the reflected Cherenkov light into the camera[47].

The CT5 consists of 875 mirror facets and has a total mirror area of $614\,\mathrm{m}^2$. Its focal length is 36 m, and the camera is composed of 2048 PMTs with Winston cones. The FoV is 3.2°, smaller than CT1-4, though in favor of a larger sensitivity towards low energies. The CT5 is optimized for the energy range from 30 GeV to 10 TeV.

The Night Sky Background (NSB) is the residual light from stars and undesired sources at night, composed mainly of starlight, moonlight (in case of observations during moonlight), light pollution, and artificial satellites. The NSB is also detected by the cameras, though the trigger system[48] is responsible for minimizing its signal. Two trigger levels are defined. First, a camera trigger occurs when a certain number of neighbor pixels, typically 3 pixels, exceed, in a time window of 1.3 ns, a threshold level of 5.5 photoelectrons (pe) for dark nights (no moonlight) and 6.6 pe in nights under partial moonlight. Both the threshold and the number of neighboring pixels can be adjusted according to the local NSB. For a very bright region, i.e., close to bright stars or a nebulae region, the PMTs high voltage has to be decreased to avoid damage, and, hence, the trigger criteria have to be increased. The second trigger level provides the condition for stereoscopic observations. It requires that at least two telescope cameras are triggered within a time window of 80 ns in the central trigger system. After the second trigger level, the signal

is integrated within an interval of 16 ns, sampling resolution of 1 ns, and recorded on the disk. To make use of the full array capabilities, CT5 can also operate in monoscopic mode, i.e., it can trigger and record events even if no other telescope passed the first trigger level. As a consequence of it and due to the different mirror areas, the typical CT1-4 trigger rate close to zenith is smaller ($\sim$ 100s of Hz) than the CT5 trigger rate (1.5-3 KHz)[49].

The system read-out time process consists of the inquiry for coincident events between telescopes, the PMT signal integration, the conversion of the PMT data to digital, and their transfer to a database. The telescopes are busy during the read-out period, and no other events can trigger the system. Therefore, the read-out time effectively leads to a dead-time of the event detection. The dead-time of CT1-4 was improved from $\approx 460\,\mu$s in the H.E.S.S. I era to $7\,\mu$s[50] after the upgrade of the cameras in the H.E.S.S. IU era. The upgraded CT5 camera is fully digitized and has effectively no dead-time up to 30 kHz, which increases the sensitivity of the telescope and improves the estimates on the gamma-ray flux of the observed sources[49].

The observation plan of the H.E.S.S. telescopes follows strict criteria to optimize the use of the dark time and maximize the quality of the science results. In this regard, the H.E.S.S. experiment has recently started taking data under partial moon-light and twilight conditions to extend the available time of observations. Apart from the usually planned observations, The Targets of Opportunities (ToO) observations, which follow up on alerts by other instruments, have been lately an essential aspect of the H.E.S.S. observation strategy. The selection of astrophysical sources for the ToOs observations occur according to an internal process of proposal evaluation.

2.3. Calibration

After the observations, an automatic procedure calibrates the data by considering the influence of the various parameters from the mirrors' optics to the camera's response.

2.3.1. Pedestal

An analog-digital converter (ADC) converts the electric current produced in the PMTs to digital counts per pixel. The converted signal contains information about the Cherenkov and the NSB photons. The calibration is the process of filtering out the NSB and estimating the actual emitted Cherenkov radiation.

The first step is the determination of the pedestal P, i.e., the irreducible current. It is composed of electronic noise and the NSB photons. The electronic noise is calculated based on a dedicated data acquisition run when the camera shelter shields the camera from external light sources. A series of images are acquired, and the mean and width of the distribution of ADC

counts per pixel give the final electronic noise. On the other hand, the NSB estimation must be estimated for each observation. Typical Cherenkov showers in a H.E.S.S. camera trigger only from 10 to 100 out of 960 PMTs. The rest of PMTs are used for the NSB estimation as long as their signal is smaller than 6 pe, and they do not have neighbor pixels above 3 pe. The NSB is estimated either by the pedestal width or by the PMT current.

2.3.2. Gain factor

The gain factor is the conversion factor from single photoelectron to ADC counts. Dedicated data are taken with the camera shielded from external light, and it is only illuminated by an LED flasher mounted inside the camera hut. The LED pulses at a frequency of 70 Hz and illuminates every PMT with ~ 1 pe. The histogram of the ADC count is fitted to a model[51], which considers the combination of two effects: the pedestal as a Gaussian distribution and the Poisson distribution from the photoelectron distribution. Both signals are convolved with a Gaussian distribution to account for the resolution of the PMT.

Two channels are available in each PMT: the low-gain, suited for high photon counts, and the high-gain channel suited for low photon counts. The gain γ_e is estimated for the high gain channel, whereas the low gain is derived based on the high gain γ_e and the pre-established amplification between the channels HG/LG. Usual values are defined since an upgrade in June 2020 to be $\gamma_e \approx 60$ ADC/pe and HG/LG ≈ 14 for both dark nights and nights with partial moonlight.

2.3.3. Flat fielding

Inhomogeneities in the PMT responses can arise due to variations in the quantum efficiency. Flat fielding is a process to calibrate the relative response of the individual PMTs to a homogeneous illumination by LEDs. Dedicated data acquisition is conducted twice at each observation period (≈ 28 days). The LED intensity is adjusted to bring the PMT ADC counts to the range between 10 and 200 pe per image. The previous knowledge about the gain factor and the pedestal is used to analyze the flat fielding data and derive a Flat Fielding (FF) coefficient for each pixel. The FF coefficient corresponds to the mean of the PMT signal over the mean of all PMTs in the camera.

The final conversion from ADC counts to photoelectrons can be derived according for the calibration procedure and the number of photoelectrons A can be estimated by:

$$
\begin{aligned}
A_{\mathrm{HG}} &= \frac{ADC_{\mathrm{HG}} - P_{\mathrm{HG}}}{\gamma_e} \times FF_{\mathrm{HG}} \\
A_{\mathrm{LG}} &= \frac{ADC_{\mathrm{LG}} - P_{\mathrm{LG}}}{\gamma_e} \times \frac{FF_{\mathrm{HG}}}{LG} \times FF_{\mathrm{LG}}
\end{aligned}
\tag{2.4}
$$

2.3.4. Image cleaning

Before analyzing the data, the cleaning procedure must be applied to the shower images to filter out pixels, which do not correspond to Cherenkov light. The signal from Cherenkov photons is spatially and temporally correlated, while the noise tends to be uncorrelated. The cleaning procedure comprises a two-level filter: first, two neighboring pixels with a high threshold of $\epsilon_2 = 10\,\mathrm{pe}$, and secondly, an additional neighbor pixel with a lower threshold of $\epsilon_1 = 5$ pe is required to define a cluster. Alternatively, for less intense NSB regions, $\epsilon_1 = 4$ and $\epsilon_2 = 7\,\mathrm{pe}$ can also be applied[52]. The two-level filter might affect the array's sensitivity towards reconstructed low-energy gamma rays; however, once the cluster is identified in the image, the neighbor pixels can be reactivated, which includes additional information of fainter components of the shower.

2.3.5. Pointing model

Mechanical effects such as the sagging of the telescope structure and unavoidable differences between the telescope structure and its designed model lead to pointing uncertainties[53]. A calibration procedure is responsible for generating a pointing model of each telescope and correcting for mismatches in the pointing direction. It relies on two CCD cameras in the center of each telescope dish are taking pictures during dedicated observations: the SkyCCD acquires images of the sky around the Cherenkov camera, and the LidCCD acquires images of the camera lid, which remains closed. At the camera, LEDs shine in the outer edges of the lid, and their intersection indicates the center of the camera. The telescope mirrors reflect the starlight onto the camera lid. The relative position between the center of the camera derived through the LEDs and the position of the star reflected image on the camera lid gives the deviation of the azimuth and elevation angles to the target position. A mechanical model can be derived from the LidCCD images based on the observation of stars in a set of different angles. The model is not time-independent and is recalculated periodically[54].

The derived mechanical model is applied at the software level to correct the pointing mismatch. Telescope mechanical structures can change their behavior with time, and the systematic uncertainty of the pointing depends on how long the mechanical model has been used. According to Ch. 4 of Braun (2007)[54], the pointing uncertainty gets as low as $11''$ right after the application

of the model and reach up to $>17''$ one year after that. Without the corrections offered by the model, a default systematic uncertainty on the pointing of $20''$ is estimated[45], which also includes other sources of uncertainties such as the tracking precision.

Precision Pointing is a dedicated method to improve the pointing precision of the H.E.S.S. telescopes. It uses the images of the SkyCCD camera, eliminating some of the sources of uncertainties and, therefore, improving the systematic uncertainty of the pointing down to $6''$, as described in Ch. 5 of Braun (2007)[54]. The method is only applied to specific studies where the SkyCCD images are available, and the science case requires the best pointing precision, for instance, the identification of the central galactic source in Acero et al. (2010)[55].

2.4. Data quality and selection

Evaluating the data taken is an important step towards a reliable analysis result. Various uncertainties can influence the final result and even invalidate a data set. The H.E.S.S. analysis chain uses two sets of quality criteria: one for the detection of the source and the other for the reconstruction of the spectrum. While the analysis focuses on maximizing the number of photons detected for the first set, the second set expands the first set. It focuses, instead, on yielding reliable information about the source spectrum. The quality criteria for detection include the parameters explained in Sec 2.4.1 to 2.4.3 and the quality criteria for spectrum expands the detection criteria with the considerations introduced in Sec 2.4.4 and 2.4.5.

2.4.1. Data acquisition time

Each H.E.S.S. observation occur in a time slot of 28 minutes, which defines an *observation run*. The period maximizes the number of photons acquired and, at the same time, avoids a large range of different zenith angles and atmospheric conditions during the observation run. An interruption of the data acquisition can occur for several reasons, for instance, the end of the dark time, a malfunctioning of the hardware, an abrupt change in the weather conditions, or a ToO triggered by other instruments. Since interrupted runs might indicate faulty observations, a quality criterion discards the less than 10 minutes long runs due to their low event statistics.

2.4.2. Participation fraction

The participation fraction represents the number of triggered events by one telescope from the complete set of triggered events during the observation. The same event triggers more than one telescope if the time difference between their detection is smaller than 80 ns. The participation fraction of the telescopes CT1-4 must be larger than 0.4 to pass the quality criteria, i.e., each

telescope has to detect at least 40% of the total events; otherwise, the analysis excludes the telescope data. Suppose CT5 is included in the analysis. In that case, the minimum participation fraction of CT1-5 is 0.04, since CT5 has a much higher trigger rate and participates alone in most of the events. The criterion improves the event reconstruction by assuring the presence of more telescopes in the stereoscopic analysis.

2.4.3. Deactivated pixels

The number of deactivated camera pixels (PMTs) is a criterion to monitor the status of the camera. The more deactivated pixels, the less sensitive the camera is to the Cherenkov light and the more systematic uncertainties it introduces in the analysis. Hardware problems or the camera safety system might deactivate the pixels. The camera system automatically turns off pixels when they are over-saturated to avoid serious damage to the PMTs. Stars in the FoV, a bright NSB, or lightning could over-saturate camera pixels, which could decrease the PMT lifetime. While the fraction of deactivated pixels due to hardware problems must be kept below 12.5% for CT1-4 and 7% for CT5, the fraction of deactivated pixels due to over-saturation must be kept below 5% for CT1-4 and 4% for CT5[56].

2.4.4. Trigger rate

The trigger rate is monitored constantly for each telescope. During observations under good weather conditions, the trigger rate is $\approx 250\,\mathrm{Hz}$ for CT1-4 and $\approx 5\,\mathrm{KHz}$ for CT5. The NSB, weather conditions, and zenith angle of observation strongly influence the trigger rate. Whenever clouds pass through the telescope FoV, the trigger rate drops by several percent; lightning provokes spikes in the trigger rate and might even turn off some PMTs. Slow decreasing trigger rates point towards a worsening in the dust attenuation, usually linked to observation under high zenith angle or high cloud layers. Variations in the trigger rate affect the quality of the acquired data; more specifically, it directly influences the estimated gamma-ray flux, the energy threshold, and, consequently, the estimated spectrum. The trigger rate fluctuation is allowed by the quality criteria to vary within $\pm 30\%$ of the mean value throughout the *observation run* and $\pm 10\%$ of the mean value in the time scale of minutes.

2.4.5. Atmospheric transparency

The trigger rate variations reflect some weather effects; however, some atmospheric proprieties are not accessible through these means. For instance, the aerosol distribution affects the absorption of Cherenkov light in the atmosphere[57], while nearby fires pollute the atmosphere and decrease its transparency. Therefore, a transparency coefficient is defined based on the trigger

rates, the muon efficiency, and the camera gains and used to filter the data at good weather conditions[58].

2.5. Analysis methods

After the data acquisition, the calibration of the data, and a careful data selection through the quality criteria, the remaining Cherenkov images from gamma-ray and hadronic showers are finally ready for analysis.

2.5.1. Hillas reconstruction

The image in the Cherenkov camera of a gamma-ray-initiated air shower has an ellipsoidal shape, while it can vary in shape for a cosmic-ray-initiated shower. Figure 2.5 shows a schematic view of the travel path and detection of gamma-ray and proton-initiated showers[59]. While the gamma-ray shower develops along the initial particle's propagation direction, the hadronic shower has more lateral momentum due to the composition of hadrons, strong interactions, and sub-showers, which is directly recognizable in the image shape at the camera. Michael Hillas[60] proposed in 1985 the pioneering method of gamma-ray reconstruction from Cherenkov images through the Hillas parameters, which characterize the geometry of the images as shown in Fig. 2.5. The parameters are the following: the length L, the width w, the size (total image amplitude), the nominal distance d (angular distance between the center of the camera and the image center of gravity), the azimuth angle of the main image axis ϕ, and the orientation angle α.

The reconstruction of the initial gamma ray based on stereoscopic observations increases the arrival direction's precision and energy resolution. It improves the rejection of cosmic rays in comparison to a single telescope reconstruction[62]. Geometrical considerations of the telescopes are the base of stereoscopic reconstruction. The camera images of the triggered telescopes are projected into a common plane, and the intersection of the main shower axis yields the direction of the air shower.

Monte Carlo (MC) simulations reproduce the development of gamma-ray-initiated showers over an extensive range of the parameter space, for instance, the zenith angle of observation, the impact distance, and primary energy. The Cherenkov images resulting from the MC simulation provide a set of reconstructed Hillas parameters in tables (*look-up tables*). The Cherenkov images from observations are compared to the *look-up tables*, and information of the initial gamma-ray is derived. The energy resolution achieved from this method reaches the level of $\approx 20\%$ and the angular resolution of $\approx 0.1^{\circ}$[52].

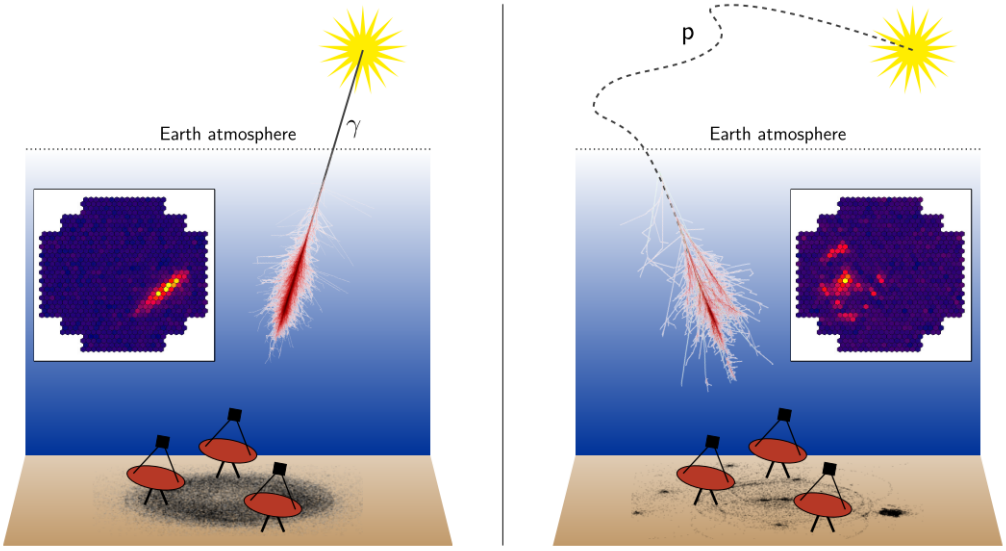

Figure 2.5.: Schematic view of the development and detection of (left) a gamma-ray initiated air shower and (right) a proton-initiated air shower. Extracted from Holch (2020)[59].

2.5.2. Template reconstruction

Additional information can be obtained from the detailed shape of the shower images rather than the Hillas parameters. A template method was introduced in the 1990s by Le Bohec et al. (1998)[63], and further developed in de Naurois & Rolland (2009)[64]. The MC Template-based analysis for the Air-Cherenkov Arrays (ImPACT) approach was developed for H.E.S.S. in Parsons & Hinton (2014)[65], in which the shower images are fitted directly to template images generated from MC simulations. The template images are the results of MC simulations[46] based on the air-shower development and the proprieties of the telescopes. Finely binned histograms are generated for 100,000 images, covering 8 zenith angles (0 - 65°), 2 azimuth angles, 17 energies (0.08 - 100 TeV/$cos(\phi)$), where ϕ is the zenith angle, and 25 impact distances (0 - 1000 m)[65].

The ImPACT template reconstruction improves the angular resolution up to 50% at 500 GeV and 15% at 100 TeV and the energy resolution in ≈ 50%. The Point Spread Function (PSF), which is the response of the telescope to a point-like light source, can improve down to a 68% containment radius of ≈ 0.05° for energies above 1 TeV. The PSF also depends on the zenith angle of observation. The larger the zenith angle, the worse the PSF due to the larger uncertainties in the shower reconstruction for inclined showers. Figure 2.7 shows the PSF as function of the zenith angle of M87 observations after 2017 for three different gamma-ray energies.

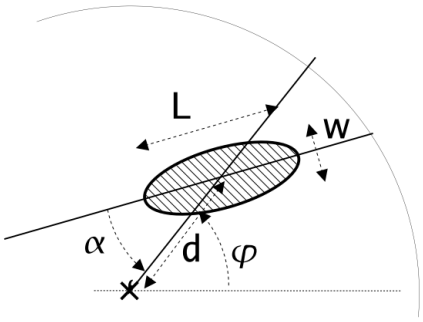

Figure 2.6.: Geometrical definitions of the Hillas Parameters. Extracted from de Naurois (2006)[61].

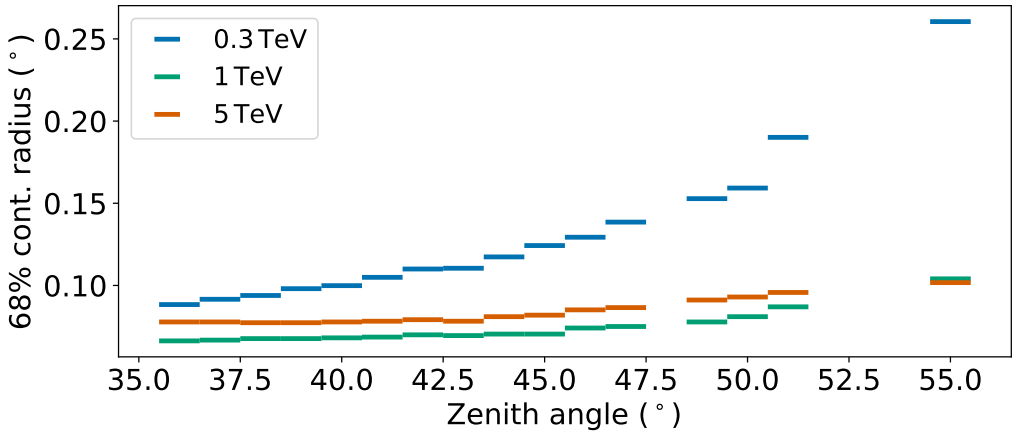

Figure 2.7.: 68% containment radius (c.r.) of the H.E.S.S. PSF of M87 observations after 2017 for three different energies.

2.5.3. Gamma-hadron separation

Air showers initiated by cosmic rays are the main contributors to the background in ground-based gamma-ray astronomy. Due to the different shapes of the Cherenkov images in the telescope camera, a gamma-hadron separation method based on the Hillas length L and width d is used to suppress the background. Therefore, the Reduced Scaled (RS) width and length are the following[52]:

$$W_{\mathrm{RS}} = \frac{W - \langle W \rangle}{\sigma_{\mathrm{W}}}, \qquad L_{\mathrm{RS}} = \frac{L - \langle L \rangle}{\sigma_{\mathrm{L}}}, \tag{2.5}$$

where $\langle W \rangle$ and $\langle L \rangle$ are the mean width and length, and σ_W and σ_L are their standard deviation obtained from the *look-up tables*. The closer the RS parameters are to zero, the better the image represents the expected shape for the specific shower proprieties. The background suppression is improved by combining the RS length and width from the telescopes to yield the Mean Reduced Scaled (MRS) parameters:

$$W_{\mathrm{MRS}} = \frac{1}{N} \sum_{i=1}^{N} W_{\mathrm{RS,i}}, \qquad L_{\mathrm{MRS}} = \frac{1}{N} \sum_{i=1}^{N} L_{\mathrm{RS,i}}, \tag{2.6}$$

where N is the number of telescopes, which recorded images of the shower. Selection cuts optimized for different purposes include the W_{MRS}, L_{MRS}, the distance θ from the reconstructed shower position to the source, and the amplitude of the image[52]. The background rejection based on the shape parameters reaches the level of 90%.

A second and more modern gamma-hadron separation technique is a multivariate analysis, which applies a boosted decision tree (BDT) algorithm to separate the background from the gamma-ray events[66]. A decision tree is a binary split criterion (signal or background) representing an image parameter at each branch. A *forest* of decision consists of various trees with different proprieties, for instance, the training set and the orders of the branches. A weighted mean of the trees robustly yields an event's final signal-to-background-likeliness ξ. Figure 2.8 shows the ξ for an independent set of an equal number of simulated gamma-ray and cosmic-ray showers between 0.5 and 1 TeV and the zenith angles from 15° to 25°.

At each zenith angle and energy band, a cut in the signal-likelihood ξ_{cut} defines the limit between the two types of events. Since the distribution in Fig. 2.8 is different for each zenith angle and energy band, a definition of a cut valid for all observations would yield different rates of signal to background within the selected events. Therefore, a new variable, the gamma-ray efficiency $\epsilon_\gamma(\xi_{\mathrm{cut}})$ is defined as the rate of gamma rays in the events after applying the ξ_{cut}. A gamma-ray efficiency of $\approx 83\%$ is chosen for ImPACT to remain equal for every zenith angle and energy band.

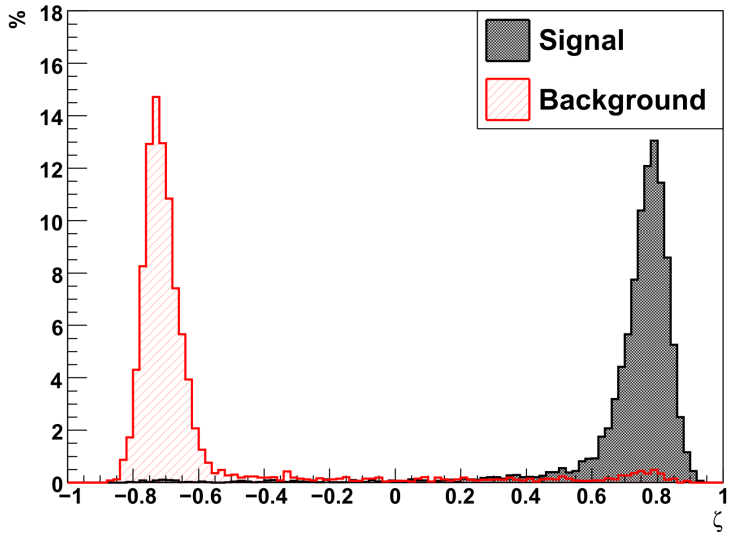

Figure 2.8.: Histogram of the signal(background)-likeliness ξ for a set of an equal number of simulated gamma-ray and cosmic-ray showers simulated in the energy range of $0.5-1$ TeV and the zenith angle range of $15°-25°$. Extracted from Ohm et al. (2009)[66].

2.5.4. Instrument acceptance and effective area

The estimation of the instrument acceptance to incoming gamma rays relies on MC simulation. The acceptance describes the probability of the incoming particle of a given type to be detected after the selection cuts. It depends on the shower position in the FoV, type and energy of the primary particle, the zenith angle of observation, the NSB level, and the state of the instruments.

The acceptance is maximum for events at the camera center and decreases down to 40% of the peak value at an offset of 2° from the camera center[52], due to the decreasing triggering probability. The air shower at high zenith angle observations ($> 50°$) traverses more atmosphere than observations close to the zenith angle. Consequently, a significant fraction of the low-energy particles are absorbed by ionizing air molecules before reaching the telescope, and the air shower image appears smaller in the camera. Furthermore, variations in the NSB lead to inhomogeneities in the camera image, which ultimately lead to the event's exclusion by the selection criteria. Finally, the observation date indicates the state of the instruments and must be considered within the instrument response. Hardware updates, for instance, the replacement of mirrors, which naturally degrade with time, directly influences the telescope's sensitivity.

The estimation of the detector acceptance towards gamma-ray events is obtained based on a large set of MC simulations. Due to the efficient background rejection, many incident background events would have to be simulated to accurately determine the acceptance of the detector towards

it, which makes simulations too time demanding and, therefore, impractical. Instead, dedicated observations of signal-free regions in the sky provide the acceptance towards the background.

Instead of generating the acceptance profile from observations of signal-free regions, an alternative method is based on the source observation itself. It uses signal-free regions in the FoV to produce the acceptance profile. This method is more faithful to the current instrument conditions and does not depend on observations from other periods. However, it is not reliable for sources with little observation time.

The effective area is the area covered by the telescopes in which they are sensitive to gamma rays. The area is much larger than the size of the telescopes themselves since they can detect incoming gamma rays with an impact distance up to hundreds of meters away from the array. The effective area is obtained from MC simulations for a large set of zenith angles, primary energy, impact distances within an area of $\sim 1\,\mathrm{km}^2$ around the array. The ratio of the detected and simulated events $\epsilon = \dfrac{N_{\mathrm{det}}(E)}{N_{\mathrm{sim}}(E)}$ yields the effective area $A_{\mathrm{eff.}} = \epsilon(E) A_{\mathrm{sim}}$.

The true energy E_{true} refers to the simulated primary energy, while the reconstructed energy E_{reco} results from the analysis. An energy bias of $\Delta E = \dfrac{E_{\mathrm{reco}} - E_{\mathrm{true}}}{E_{\mathrm{true}}}$ is introduced by the uncertainties in the reconstruction method. Therefore, a safe energy range is defined as the region where $\Delta E < 10\%$, which usually excludes the very-low-energy part of the spectrum and the high energy end due to low event statistics[52].

2.5.5. Background estimation

The background in ground-based gamma-ray astronomy originates from cosmic rays, i.e., air showers initiated by protons, electrons, and heavy nuclei. The largest part of the background is rejected by the selection cuts as described in Sec. 2.5.3, although some of them produce very similar images as a typical gamma ray and, therefore, pass the selection cut. For a strong source, for instance, the Crab Nebula, the signal-to-background ratio after the selection cut is about 1:1[52].

The most widely adopted methods for determining the background are currently the *Ring Background* and the *Reflected-region Background*[67]. The *Ring Background* consists of a ring around a trial source position, in celestial coordinates, in which the background events are sampled (N_{off}). The trial position is the expected position of the source, and the source region is a circle of squared angular radius of $\theta^2 = 0.005^{\circ^2}$ from the source position for the template analysis method[65]. The number of events within the source position is defined as *On counts* and represented by N_{on}. The *Ring Background* is illustrated in Fig. 2.9 (left). The parameter α gives the ratio of the solid angle between the source region and the ring (radius 0.5°), considering corrections for the effective area and exposure time. It is usually set to be $\alpha \approx 1/7$, which yields a

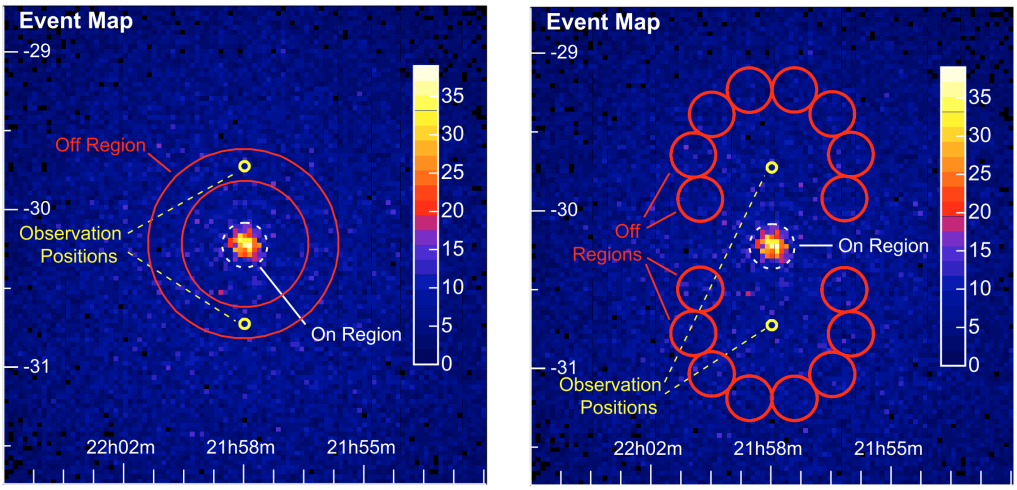

Figure 2.9.: Schematic of the Ring (left) and Reflected-region (right) background methods applied to 5h of H.E.S.S. data of the AGN PKS 2155-304. The maps show the counts of gamma-ray-like events from the source. Extracted from Berge et al. (2007)[67].

sufficient homogeneous background estimation, defined as $N_{\mathrm{bkg}} = \alpha N_{\mathrm{off}}$. The *Ring Background* can be applied directly to stacked observations, and it is the preferred method for morphology studies. Its disadvantage is the radial and energy dependence of the acceptance within the ring, which makes a reliable spectrum estimation very difficult.

The *Reflected-region Background* was developed for *wobble observations*, i.e. the telescopes pointing position is slightly shifted from the source ($\approx 0.5°$)[52]. A number n_{off} of regions is defined in a ring around the pointing position, reflecting the source position. The ring of n_{off} excludes the source itself and its surroundings to avoid contamination as shown in Fig. 2.9 (right). Both the source position and the n_{off} regions are at the same distance from the pointing position; therefore, they have the same radial acceptance. The α parameter is simply $1/n_{\mathrm{off}}$, and the background is estimated as $N_{\mathrm{bkg}} = \alpha N_{\mathrm{off}}$. The method is very appropriate for spectral studies. The disadvantage is that it cannot deal with observations, in which the telescopes were pointed directly to the source position, and cannot yield reliable sky maps. For extended sources, where the integration radius of the source region is not sufficient to comprise all the emissions, other background methods such as the FoV background or the template background method are necessary[67].

2.5.6. Source detection

After the background estimation the excess events N_{excess} from the source can be simply estimated as:

$$N_{\text{excess}} = N_{on} - N_{\text{bkg}} = N_{\text{on}} - \alpha N_{\text{off}}. \tag{2.7}$$

The correct evaluation of the significance S of the result has to consider the uncertainties in the N_{on} and N_{off} counts. Based on the maximum likelihood principle, the significance is given by Eq. 17 of Li & Ma (1983)[68]:

$$S = \sqrt{2}\left\{N_{\text{on}} ln\left[\frac{1+\alpha}{\alpha}\left(\frac{N_{\text{on}}}{N_{\text{on}}+N_{\text{off}}}\right)\right] + N_{\text{off}} ln\left[(1+\alpha)\left(\frac{N_{\text{off}}}{N_{\text{on}}+N_{\text{off}}}\right)\right]\right\}^{1/2}. \tag{2.8}$$

A source is detected whenever $S > 5\,\sigma$, i.e., the significance of the excess counts is larger than five standard deviations from the expected background level.

2.5.7. Flux and spectrum

The excess counts detected by H.E.S.S. is the integrated gamma-ray flux over the time of observation, considering the effective area Φ, as a function of the reconstructed energy E. Since it is not possible to directly know the true energy of the incoming gamma ray, a convolution function considers the probability $E_{\text{disp}}(E|E_{\text{true}})$ of an event with energy E_{true} being detected with an energy E. The energy bias and energy resolution directly influence the convolution function. The energy range is kept within the safe region, as discussed in Sec 2.5.4. A similar argument applies to the true position of the event. It is also not possible to certainly know the position of the incoming gamma ray; hence, the probability $PSF(p|p_{\text{true}})$ of detecting the gamma ray at the position p given the real position p_{true} is considered. The combination of the energy and position probability distribution function with the detector acceptance and effective area gives the Instrument Response Function (IRF), defined as $R(p, E|p_{\text{true}}, E_{\text{true}})$. Therefore, the expected number of detected events $N(p, E)$ can be calculated as[69]:

$$N(p,E)dpdE = t_{\text{obs}} \int_{E_{\text{true}}} dE_{\text{true}} \int_{p_{\text{true}}} dp_{\text{true}} R(p, E|p_{\text{true}}, E_{true}) \times \Phi(p_{\text{true}}, E_{\text{true}}), \tag{2.9}$$

where t_{obs} is the time of observation in seconds, $R(p, E|p_{\text{true}}, E_{\text{true}})$ is the IRF given in $\text{m}^2\,\text{TeV}^{-1}$ and $\Phi(p_{\text{true}}, E_{\text{true}})$ is the sky flux model given in units of $\text{m}^{-2}\,\text{s}^{-1}\,\text{TeV}^{-1}\,\text{sr}^{-1}$. The IRF can be approximated by separating it into its three independent functions:

$$R(p, E|p_{\text{true}}, E_{\text{true}}) = A_{\text{eff}}(p_{\text{true}}, E_{\text{true}}) \times PSF(p|p_{\text{true}}, E_{\text{true}}) \times E_{\text{disp}}(E|p_{\text{true}}, E_{\text{true}}), \tag{2.10}$$

where A_{eff} is the effective area given in m^2.

The spectrum of the source is defined as the gamma-ray flux as function of the energy and is given by the integration of the sky flux model over the source region (see Sec. 2.5.5) in units of $\text{sr}^{-1}\,\text{s}^{-1}$, or using the distance to the source, $\text{cm}^{-2}\,\text{s}^{-1}$:

$$\frac{d\Phi(E_{\text{true}})}{dtdE_{\text{true}}} = \int_{p_{\text{true}}} dp_{\text{true}} \Phi(p_{\text{true}}, E_{\text{true}}). \tag{2.11}$$

The integration of Eq. 2.11 over the energy yields the total gamma-ray flux of the source. The total flux is usually compared to the Crab Nebula gamma-ray flux, due to its high flux[52], and expressed in terms of percentage of the Crab emission.

Another useful representation is the energy flux per energy band given in s^{-1} by:

$$\frac{d\Phi_E(E_{\text{true}})}{dtdE_{\text{true}}} = E_{\text{true}} \times \frac{d\Phi(E_{\text{true}})}{dtdE_{\text{true}}}. \tag{2.12}$$

The integration of $d\Phi_E(E_{\text{true}})/dtdE_{\text{true}}$ over the gamma-ray energy yields the total energy flux detected in gamma rays. The gamma-ray luminosity L_γ, most commonly expressed in ergs, is given by the energy flux integrated over the solid angle defined by the distance from Earth to the source.

To derive the flux, energy flux, and luminosity from an observed source, Eq. 2.9 has to be solved for the sky flux model Φ. Since the equation cannot be solved analytically, a numerical method is necessary to derive the gamma-ray flux of the source. Therefore, different approaches have been developed to estimate the spectrum, for instance, χ^2-fitting, unfolding, and the default in H.E.S.S. analysis, the forward folding method. The last method assumes a specific spectral distribution for the source; usually, a power-law or a power law with an exponential cut-off convolves it with the instrument response functions and compares it with the detected energy distribution. Considering the Poisson statistics, the spectral parameters are adjusted until the expected distribution matches the detected distribution. This procedure is repeated for each observation and then combined in the stacked analysis to provide the source spectrum.

2.6. Status of the H.E.S.S. experiment

The H.E.S.S. experiment has been operational since 2003 and will operate at least until 2023. It has detected more than 100 VHE sources and has made a large contribution to Galactic and extra-galactic high-energy astrophysics[70].

The array went through several upgrades throughout the time, which were indispensable for the latest discoveries. The construction of a fifth telescope (CT5) at the center of the array with the focus in the 50 GeV-10 TeV energy range increased its sensitivity and turned it into

the first IACT hybrid array worldwide[32,70]. A major upgrade of the CT1-4 cameras in 2016 also increased the array sensitivity by decreasing the dead-time of the read-out system and the trigger criteria[11]. Lately, a new and modern camera[49] was installed in CT5. The continuous hardware and software upgrades drove the experiment towards new and ambitious strategies, which led to unprecedented results.

In the last years, the focus of the experiment has moved to ToO observations. It led, for instance, to the discovery of the first GRB at VHE gamma rays[71]. The optimum angular resolution achieved with a reliable template analysis[65] and the dedicated simulations for the individual *observation runs*[72] lead to many discoveries. For instance, the extended gamma-ray emission from the Crab Nebula[73], and ultimately, the first extra-galactic extended emission in gamma rays from the closest radio galaxy Centaurus A[74].

The extended gamma-ray emission from Centaurus A indicated an origin for the emission further away from the central black hole, where the magnetic fields are usually highest, and the emission is expected. The most accepted explanation is the emission originating from the same region in the relativistic jet of Centaurus A, since its radio and gamma-ray emissions have similar shapes. While Centaurus A is located at 3.8 Mpc from the Earth[74], the second closest and most prominent radio galaxy is the M87 at $\approx 16.5\,\mathrm{Mpc}$[15,16]. Differently from Centaurus A, its jet axis is closer to the line of sight (30°)[75], yet a prominent jet is observed from radio to X-ray bands. Furthermore, M87 is at the very heart of the Virgo galaxy cluster, and its complex structure with knots and extended jet poses a challenge in pinpointing the origin of the emission. The next chapter introduces the radio-galaxy M87, explains the emission mechanisms of gamma rays, and the motivation for searching an extended gamma-ray emission from M87 arises.

3. The radiogalaxy Messier 87 (M87)

M87 is a giant elliptical galaxy discovered by the astronomer Charles Messier in 1781 in its famous Nebula catalog[76]. The galaxy is located 16.5 Mpc ($1\,\mathrm{Mpc} = 10^6\,\mathrm{pc} \approx 3.086.10^{24}\,\mathrm{cm}$) away, at the Virgo Cluster[15,16]. It hosts at its center a SMBH of ~ 6.5 billion solar masses[17,77–80], one of the closest AGN. The accretion of matter into SMBHs can release an enormous amount of energy in the form of a jet extending up to hundreds of kiloparsecs (kpc). The first hint of the existence of jets dated back from 1912[81], yet the processes behind their formation and propagation are not fully comprehended[82,83].

M87 is a Fanaroff-Riley Class I (FR-1) radio-galaxy[84], due to its brighter radio center in comparison to the darker lobes. The jet is $\approx 30°$ inclined in respect to the line of sight[75] and contains several prominent knots. Due to Doppler boosting and the inclination of the jet, only one side of it is visible, though hints for a counter-feature have been identified[85]. The knots are dense regions along with the jet, where shocks might accelerate particles to the highest energies. The Hubble Space Telescope knot 1 (HST -1), the most peculiar knot, is located $0.86''$ (70 pc) from the core and has violent flares in X-rays, surpassing even the emission from the core[86].

Before the following chapter details the study of M87, it is essential to introduce some concepts from astrophysics and to identify the problem to be approached. First, Sec. 3.1 introduces the concept of AGN and the process behind particle acceleration. Afterward, Sec. 3.2 explains the physical processes behind the gamma-ray emission. Sec. 3.3 presents the Virgo Cluster, home of the M87 galaxy, and the problem of the CC cluster with a possible solution for it. Finally, an updated multi-wavelength picture of M87 is drawn in Sec. 3.4, spanning from the radio to the gamma-ray energies. The current interpretation of the VHE gamma-ray observations cannot identify the origin of M87's emission in the VHE regime as explained in Sec. 3.5. Therefore, it motivates the search of an extended gamma-ray emission in M87 and the investigation of the possible emission regions conducted in the subsequent chapter.

3.1. Active Galaxy Nuclei (AGN) and particle acceleration

AGN represent the class of extra-galactic objects characterized by extremely intense electromagnetic radiation powered by accretion onto supermassive black holes (SMBHs)[87,88]. The current

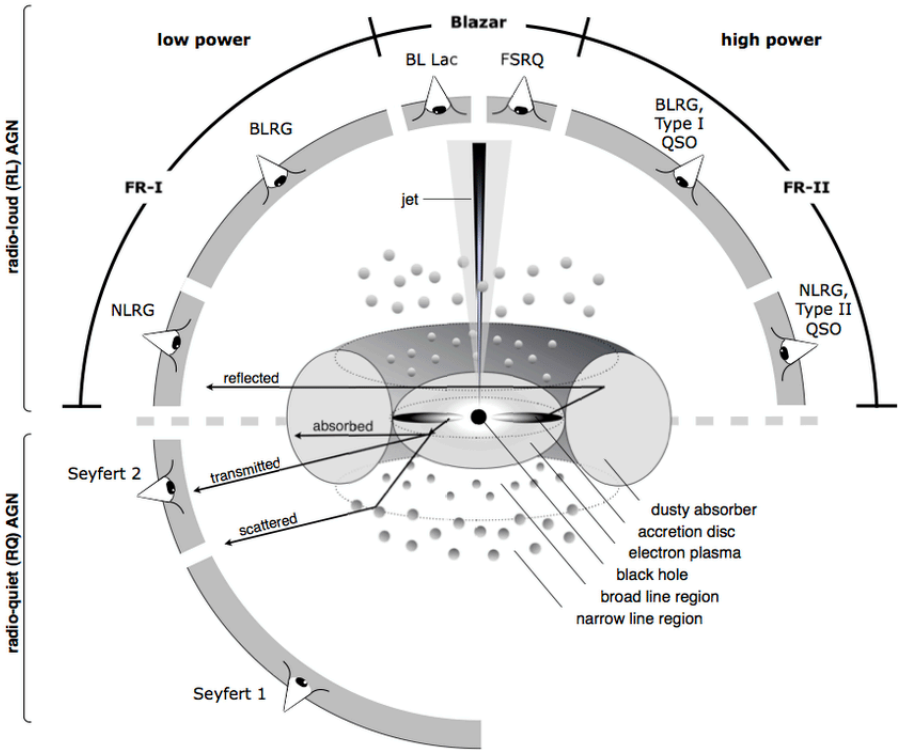

Figure 3.1.: The unified model of AGN explains the different features of the observations as the same type of object detected through different orientation angles. Extracted from Beckmann & Shrader (2012)[89].

classification of AGNs is based on the direction of the relativistic jet to the line of sight as shown in Fig. 3.1. The most prominent emission is from blazers when the jet points towards the Earth, and the emission is Doppler-boosted.

The observation of VHE gamma rays from AGNs traces the most energetic particle accelerated in relativistic outflows. Fermi first proposed a mechanism to explain the particle acceleration in 1949[90] as a stochastic mean by which particles collide with clouds in the interstellar-medium and are accelerated to VHE energies. In his model, 'magnetic mirrors' associated with irregularities in the magnetic field of the galaxy reflect charged particles[91]. The mirrors move randomly with velocity U, and the particles gain energy in these reflections. Fermi estimated the average energy gain per collision to be:

$$\left\langle \frac{\Delta E}{E} \right\rangle = \frac{8}{3} \left(\frac{U}{c} \right)^2 , \tag{3.1}$$

where E is the particle's energy, ΔE is the energy gain per collision, U is the velocity of the clouds, and c is the speed of light. Considering that a particle remains in the acceleration region for a characteristic time of $\tau_{\rm esc}$, a Power-Law (PL) distribution of particle energies is obtained: $N(E) = K \times E^{-\Gamma}$, where K is a constant and Γ>0 is the spectral index. The spectral index is given as a function of the characteristic time $\Gamma = 1 + (\alpha\tau_{\rm esc})^{-1}$. The acceleration mechanism is denominated Fermi acceleration of second-order because the mean energy gain per collision grows with the square of the cloud velocity. Some problems with Fermi's assumptions were later identified. First, the cloud velocities in the interstellar medium and the mean free path for the scattering of cosmic rays are very low for the particles to accelerate. The ionization losses were not included in the process, but they hamper the acceleration of the particles, especially the low-energy particles. Either the acceleration of particles would have to be very fast, or they shall be injected in the acceleration site with energy sufficient large to survive the ionization. Furthermore, nothing in Fermi's theory explains the reason why the energy spectrum index of accelerated particles should be between 2 and 3, which is obtained from observations. In the modern view of the second-order Fermi acceleration, the gain in energy of the initially mono-energetic particles is considered in shocks with plasma waves. The process results in a spread of the energy distribution of the particles. However, the problem with the spectral index not converging to the observed ≈ 2 persists.

Since the 1970s, particle acceleration has been related to strong shock waves. The key feature of this process is that the acceleration is first order in the shock velocity, which yields the spectral index of the resulting accelerated electrons $\Gamma \approx 2$. Therefore, the process is denominated first-order Fermi Acceleration (diffuse shock acceleration)[91]. In this case, a flow of relativistic charged particles reaches a cloud of material at rest and produces a shock front with speed U ($\sim 10^4\,{\rm km\,s^{-1}}$). Due to turbulence in the magnetic field before the shock and irregularities after it, particles cross the shock region in both directions. The velocity distribution on each side becomes isotropic. Figure 3.2 shows a schematic view of the region of the shock. At the reference frame of the shock, the particles which come from both sides are thermalized by the flow speed and gain energy ($\frac{\Delta E}{E} = \frac{2U}{3c}$ at each shock, for an ideal gas). Given a mono-energetic particle injection, the resulted distribution of the accelerated particles is a PL in energy with index 2.

The first-order Fermi acceleration improves the second-order, but it is still not rapid. Further studies revealed that the effects of the magnetic field and the differences between weak, strong, and relativistic shocks are crucial to understanding the differences in the resulting electron spectral indexes. The diffuse particle acceleration can be very effective ($\approx 50\%$) in converting the kinetic energy of the shocks, for instance, supernova remnants, into high energy particles[91].

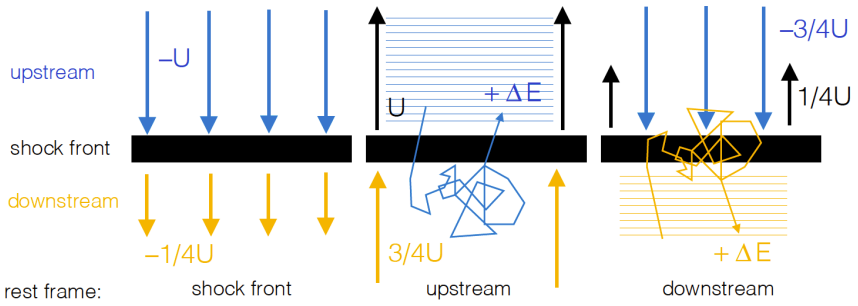

Figure 3.2.: Schematic of Fermi first order acceleration: shock wave propagating with velocity U into an upstream medium. Left: shock front at rest frame, the gas flows from the upstream region with velocity $-U$ to the shock region, and the downstream moves away from the shock with velocity $1/4U$ in respect to the rest frame, in case of an ideal gas. Middle: upstream region at rest frame, the particles from the downstream region reaches the shock region with velocity $3/4U$, scatter the upstream particles initially at rest, which then get isotropic distributed due to the turbulence in the downstream and gain energy ΔE. Right: downstream at rest frame, the particles in the downstream region cross to the upstream region, gain energy ΔE, encounter the upstream particles, and get isotropic distributed. This process repeats until the particle escapes the shock region. Extracted from Funk (2005)[92].

3.2. Radiative processes

The gamma-ray production in astrophysical objects implies non-thermal interactions of accelerated particles. Electrons, protons, and nucleons are accelerated at diffuse shocks. In the presence of a magnetic field, the charged particles lose energy through synchrotron radiation. Different photon fields might be present in the region through which the relativistic particles propagate, for instance, the photons emitted by dust and stars. The Cosmic Microwave Background (CMB) light, the isotropic radiation emitted during the Big Bang, and the Extra-galactic Background Light (EBL), the sum of the contribution of all radiations between galaxies, are important photon fields to be considered in the interaction processes. The relativistic particles up-scatter the photons from the local field, which reach energies up to VHE gamma rays through the Inverse Compton (IC) scattering. If they up-scatter on the generated synchrotron photons, the process is denominated Synchrotron Self-Compton (SSC). In the presence of a dense medium, the particles lose energy through bremsstrahlung. For relativistic protons and nucleons, hadronic collisions with particles from the local medium might produce mesons, mainly charged and neutral pions, which decay, respectively, to electron/positrons and gamma rays. The gamma rays might also be absorbed on the way to Earth, for instance, by the thick torus around an AGN (Fig. 3.1) or

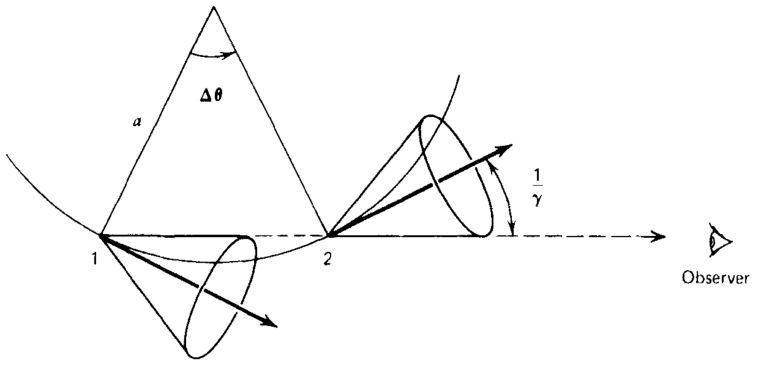

Figure 3.3.: Emission of synchrotron radiation at two points during the trajectory of the accelerated particle. Extracted from Rybicki & Lightman (1979)[94].

by the photon fields through γ-γ interaction, which produces pairs of electron-positron.

The interpretation of the astronomical observations requires unambiguous identification of the relevant radiative processes[87]. Therefore, the main interaction processes are briefly discussed in the following subsections according to the character of the emission.

3.2.1. Leptonic emission

The leptonic emission refers to the gamma rays emitted by leptons, mainly electrons and positrons. The main radiation losses are the synchrotron emission and IC scattering, which dominate the less intense bremsstrahlung and adiabatic losses[93].

Synchrotron radiation is the radiation emitted by relativistic particles under the influence of a magnetic field. Synchrotron radiation dominates much of high-energy astrophysics. It is the process responsible for the radio emission of our galaxy, supernova remnants, and extragalactic radio sources such as M87[91]. The relativistic particles, under the presence of a constant magnetic field, move in a helical shape along the magnetic field lines and emit synchrotron radiation perpendicular to them, as shown in Fig. 3.3.

For an isotropic distribution of velocities v of relativistic electrons, the total power emitted radiation is given by[91]:

$$\left(\frac{dE}{dt}\right)_{\text{sync}} = \frac{4}{3}\sigma_{\text{T}} c \omega_{\text{B}} \left(\frac{v^2}{c^2}\right) \gamma^2 \tag{3.2}$$

where $\sigma_T = 8\pi r_0^2/3$ is the Thomson cross-section with r_0 being the classical electron radius, $\gamma = 1/\sqrt{1-\beta^2}$ is the Lorentz factor, $\beta = v/c$ and $\omega_{\text{B}} = B^2/(8\pi)$ is the magnetic energy density in CGS units.

The shape of the synchrotron spectrum is strongly peaked and for mono energetic electrons with energy E_e photons at energy $E_{\rm sync}$ are emitted[95]:

$$E_{\rm sync.} = 0.2 \left(\frac{B}{10\,\mu G}\right) \left(\frac{E_{\rm e}}{1\,{\rm TeV}}\right)^2 eV, \tag{3.3}$$

where B is the magnetic field in the region. The typical magnetic field of $10\,\mu$G, as in the radio lobes of M87[96], TeV electrons produce photons at $\approx 0.2\,$eV, which is in the visible wavelength band. For a PL distribution of electrons with index $\alpha = 2$, typical for diffuse shock acceleration, the index of the synchrotron PL spectrum is $\Gamma_{\rm sync.} = (\alpha_e + 1)/2$. The energy loss rate due to synchrotron process is proportional to the inverse of the electron energy ($dE_{\rm e,sync.}/dt \propto 1/E_{\rm e}$), which alters the initial spectral shape of electrons, introducing a break from $\alpha_{\rm e}$ to $\alpha_{\rm e} + 1$ in the spectral index. Consequently, a break of $\Delta\Gamma = 0.5$ appears in the gamma-ray spectral index. Assuming a constant injection of electrons with spectral index α_e and that the synchrotron and IC dominate over other radiative processes, the position of the break energy $E_{\rm e,br}$ depends on the magnetic field B and the age of the system $\tau_{\rm age}$[93,95]:

$$E_{\rm e,br} = 1.2 \times 10^4 \left(\frac{B}{10\,\mu{\rm G}}\right)^{-2} \left(\frac{\tau_{\rm age}}{10^4\,{\rm year}}\right)^{-1} {\rm GeV}. \tag{3.4}$$

Given Eq. 3.4, the older the system, the lower the break energy. For instance, as shown in De Gasperin et al. (2012)[96], the break energy in the spectrum of the M87's halo at 1.3 GHz yields an age of the halo of $\approx 40\,$Myr.

IC scattering is a process through which ultra-relativistic electrons scatter low-energy photons to high energies at the expense of part of their kinetic energy[91]. The IC cross-section, and consequently the energy loss rate, depends on the energy regime of the system. In the Thomson regime the product of the incoming photon energy $E_{\rm ph}$ and the electron energy $E_{\rm e}$ should be much smaller than the product of their rest energies: $\kappa = \dfrac{E_{\rm ph} E_{\rm e}}{(mc^2)^2} \ll 1$. In this case, the IC cross-section can be approximated to $\sigma_\gamma \approx \sigma_T(1 - 2\kappa)$, where σ_T is the Thomson cross-section. The peak of the scattered photon is at E_γ[95]:

$$E_\gamma = 5 \left(\frac{E_{\rm ph}}{10^{-3}\,{\rm eV}}\right) \left(\frac{E_{\rm e}}{1\,{\rm TeV}}\right)^2 {\rm TeV}. \tag{3.5}$$

Energy losses in the IC Thomson regime are also proportional to $1/E_{\rm e}$ and modify the parent electron spectral shape in the same way as the synchrotron losses. Equation 3.6 can be applied, for instance, to the CMB energy of $h\nu = 2.7kT \approx 6 \times 10^{-4}\,$eV to yield for an electron of 20 TeV the gamma-ray spectrum peaked at 1 TeV. The expression for the total loss rate of the photon field in the Thomson regime is very similar to the total loss due to synchrotron radiation (Eq.

3.3) and is given by[91]:

$$\left(\frac{dE}{dt}\right)_{\mathrm{IC}} = \frac{4}{3}\sigma_T c\omega_{\mathrm{ph.}}\left(\frac{v^2}{c^2}\right)\gamma^2, \tag{3.6}$$

where $\omega_{\mathrm{ph.}}$ is the energy density of the photon field.

With Eq. 3.3 and Eq. 3.6 the connection of the synchrotron and IC emission can be established for the same electron population. The energy fluxes f_i of both emission mechanisms for the same electron energy E_e are related through[93]:

$$\frac{f_\gamma(E_\gamma)}{f_S(E_{ph.})} = \frac{\omega_{ph.}}{\omega_B}. \tag{3.7}$$

When $\kappa \gg 1$, the Klein-Nishima (KN) cross-section has to be considered, where most of the electron energy is transferred to the photon in a single collision. The exact cross-section can be found in the literature, for instance, in Eq. 2.27 from Blumenthal et al. (1970)[97]. In this regime, the scattered photon spectrum in an isotropic photon field is proportional to $1/ln(\kappa)$, which produces a break in the spectrum of the gamma rays by a single electron. The break is interpreted as the maximum possible energy that the scattered photon can have, i.e., approximately the initial energy of the electron.

For a population of electrons and a given distribution of the photon field (usually Black Body distribution), the final gamma-ray spectrum is given by the convolution of those with the IC cross-section. In a more complex model, the relativistic electrons not only scatter the photons from the CMB but can also scatter photons from starlight, IR fields, and the produced synchrotron photons themselves.

Figure 3.4 shows the semi-analytical evolution of the particle and radiation spectra. A constant injection of electrons from 0.1 TeV to 100 TeV distributed as a PL with index $\alpha_e = 2$, total energy of $E = 10^{42}\,\mathrm{erg/s}$, $B = 10\,\mu\mathrm{G}$, and the distance to the source $d = 16.5\,\mathrm{Mpc}$ were used in the estimation. The thermal CMB and synchrotron emission were also included as the photon fields for the IC emission. The figure shows also the spectral energy distribution (SED). The break in the particles SED moves towards lower energies for later times. In the radiation SED, there is a flattening of the two peaks towards lower energies with time. The photon flux does not increase further in a steady state, and the system becomes stable. I used the C++/Python open-source GAMERA[98] package to simulate the spectra shown in Fig. 3.4.

3.2.2. Hadronic emission

Relativistic protons and nuclei may also produce HE gamma rays in inelastic collisions (p-p interaction) with the ambient gas (Intercluster Medium - ICM) due to the production and

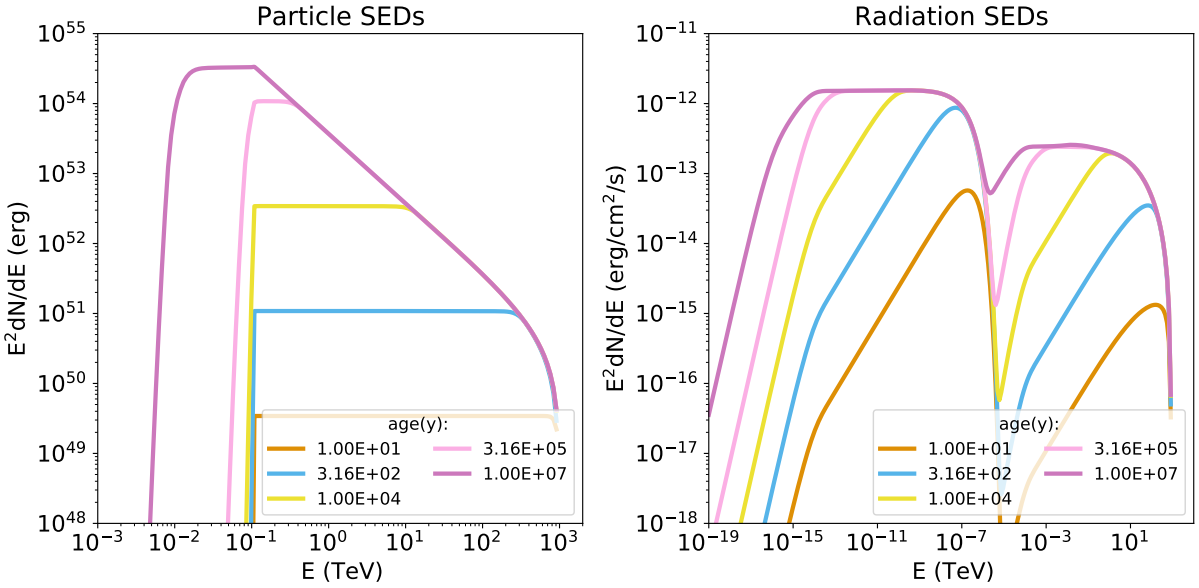

Figure 3.4.: Particle (left) and radiation (right) SED for a population of electron injected with spectral index $\alpha = 2$ and total particle energy of $E = 10^{42}$ erg evolved up to 10 Myr. The longer the time the more the particles cool down and the further the break in the curves move towards lower energies. The cooled electrons accumulate in the lower energy part of the spectrum.

decay of secondary mesons (mainly pions), where π^0s provide the main channel for HE gamma rays[87]:

$$\begin{aligned} pp &\rightarrow pp\pi^0, \\ \pi^0 &\rightarrow \gamma\gamma. \end{aligned} \tag{3.8}$$

Charged pions are also produced in p-p interaction, though their lifetime is much larger (2.6×10^{-8} s) in comparison to the neutral pion (8.4×10^{-17} s)[87]. They decay instead to muon and muon-neutrinos, and the low-energy charged muons further decay to electron, electron-neutrinos and muon-neutrinos:

$$\begin{aligned} \pi^+ &\rightarrow \mu^+ + \nu_\mu, \\ \mu^+ &\rightarrow e^+ + \nu_e + \overline{\nu_\mu}. \\ \pi^- &\rightarrow \mu^- + \overline{\nu_\mu}, \\ \mu^- &\rightarrow e^- + \overline{\nu_e} + \nu_\mu. \end{aligned} \tag{3.9}$$

While the gamma rays produced in π^0 decay reproduce its spectral shape faithfully, the gamma rays from $\pi^{\pm}$ might have enough time to interact in the local medium before the decay, therefore, possibly yielding fewer electrons and neutrinos than expected[87].

For kinematic reasons, the π^0 decay gives each of the two gamma rays the energy $E_\gamma = m_{\pi^0}c \approx 67.5\,\mathrm{MeV}$ in the rest frame of the neutral pion.[95] The gamma-ray distribution is then symmetric around $\approx 67.5\,\mathrm{MeV}$ in a log-log representation. This distinct feature denominated pion-decay bump is independent of the spectral distribution of the pions and even the protons. It is a unique signature of the π^0 decay and relativistic protons in astrophysical environments. In the GeV-TeV range the total p-p cross-section can be approximated to[87]:

$$\sigma_{\mathrm{pp}}(E_{\mathrm{kin}}) \approx 30[0.95 + 0.06ln(E_{\mathrm{kin}}/1\,\mathrm{GeV})]\,\mathrm{mb}, \tag{3.10}$$

valid for E_{kin}>1 GeV and with the assumption of $\sigma_{\mathrm{pp}} = 0$ at lower energies. The cooling time of relativistic protons due to p-p interaction is given then by:

$$\tau_{\mathrm{pp}} = (n_0\sigma_{\mathrm{pp}}fc)^{-1} \approx 5.3 \times 10^7 (n_0/(1\,\mathrm{cm}^{-3}))^{-1}\,\mathrm{yr}, \tag{3.11}$$

where n_0 is the number density of the hydrogen medium, $f_{\mathrm{c}} \approx 0.5$ is the fraction of the proton energy it losses at each p-p interaction and $\sigma_{\mathrm{pp}} \approx 40\,\mathrm{mb}$. As t_{pp} is almost independent of the proton kinetic energy and other processes such as ionization are subdominant, the gamma-ray spectrum has the same shape as the proton spectrum. In the total photon SED, the p-p interaction adds a second component to the HE region, which poses a challenge to the identification of the nature of the injected relativistic particles.

3.2.3. Propagation

The importance of the study of gamma rays relies on the fact that it does not get deflected by magnetic fields and can directly point to the source, tracing the acceleration of cosmic rays. However, gamma rays can be absorbed due to the various photon fields on their way to the observer. The pair production due to γ-γ absorption is the relevant process. Its cross-section depends only on the product of the incoming gamma-ray energy and the energy of the photon field $\kappa = \dfrac{E_\gamma E_{ph}}{(mc^2)^2}$. For large energies ($\kappa \gg 1$) it behaves similarly to the IC of electrons in the KN regime, as $\sigma_{\gamma\gamma} \approx (2/3)\sigma_T\kappa^{-1}ln(\kappa)$ with a maximum at $\sigma_{\gamma\gamma} \approx 0.2\sigma_T$ achieved at $\kappa \approx 3.5-4$, while for low energies ($\kappa \ll 1$), the cross-section approaches zero. An exact formula for the cross-section can be found, for instance, in Eq. 3.23 of Aharonian (2010)[87].

The gamma-ray absorption is mainly characterized through the optical depth parameter, defined as[87]:

$$\tau(E_\gamma) = \int_0^R \int_{\omega_1}^{\omega_2} \sigma(E_\gamma, \omega) n_{\mathrm{ph.}}(\omega, r) d\omega dr, \tag{3.12}$$

where R is the source size, $n_{\mathrm{ph.}}(\omega, r)$ is the photon density as a function of energy and distance to the source. The γ-γ absorption is important in two different cases: for extra-galactic sources and TeV emission near intense sources of radiation[99]. For extra-galactic observations, the relevant photon field is the EBL, composed mostly by the integrated, red-shifted emission from all epochs of the evolution of the universe. In this case, R in Eq. 3.12 becomes the distance from the source to the observer. Several models consider the EBL[100], through its influence on the photon SED of M87 is expected only above energies around 10 TeV[101], where the flux is very low even in flare states[102].

As discussed in Sec. 3.2, the main processes which may be behind the VHE gamma-ray emission in M87 are the SSC (in a leptonic scenario) and the gamma rays from π^0 decay (in a hadronic scenario). The knowledge of the environment, such as the magnetic field, the local photon field, and the ICM density, is key to understanding the possible contribution of each of these processes to the total emission. In the next section, I put M87 into perspective regarding its location in the galaxy cluster. Its proprieties, such as temperature and number density, are derived from X-ray data. I also introduce the problem of the CC cluster and a possible solution based on cosmic-ray heating.

3.3. The Virgo Cluster

The Virgo Cluster is the nearest big cluster of galaxies, comprising about 2000 galaxies and spanning 8 degrees on the sky centered at M87[18]. The Milky Way is located at the Local Group cluster. Both clusters are part of the Virgo supercluster as shown in Fig. 3.5.

Clusters and superclusters are the largest bound structures known in the universe. They play an essential role in the evolution of the universe and in understanding the nature of dark matter[104]. The clusters are permeated by a hot ionized gas, which due to thermal bremsstrahlung emit X rays[105,106]. Figure 3.6 (left) shows the Virgo Cluster as seen by the X-ray satellite *Röntgensatellit* (ROSAT)[107]. M87 at its center is the most intense emission region. A hot spot is observed from M86 and other galaxies, and a diffuse emission permeates the cluster.

The X-ray data provides valuable information about the gas density and temperature. The electron density distribution in the gas, although driven by cosmological and mass models[108], it is empirically well described by a β-model[109,110]:

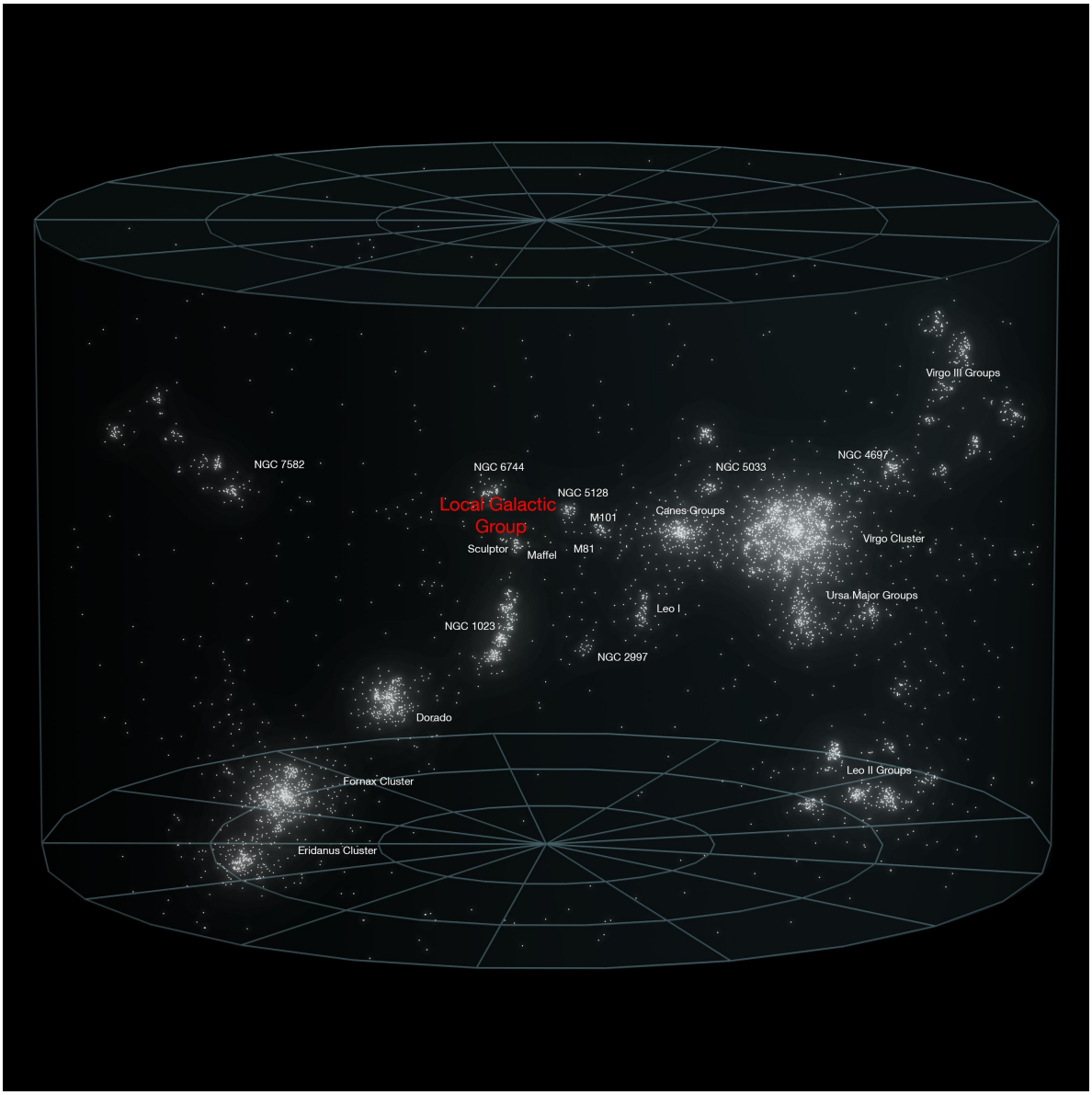

Figure 3.5.: Virgo supercluster of galaxies. Extracted from ESO (2021)[103].

$$n_e = n_0 \left[1 + \left(\frac{r}{r_c}\right)^2\right]^{3\beta/2}, \tag{3.13}$$

where $n_0[\mathrm{cm}^{-3}]$, β and r_c [kpc] are free parameters. The fit applied in Jacob & Pfrommer (2017)[110] used a gas composition of 70% hydrogen, 28% helium and data from the Archive of Chandra Cluster Entropy Profile Tables (ACCEPT)[111] until 44 kpc to derive the best fit

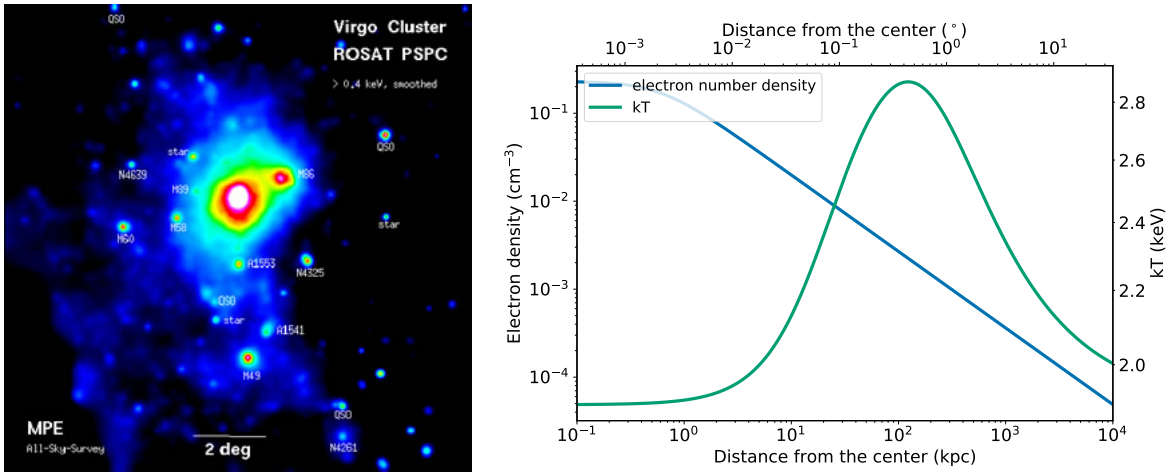

Figure 3.6.: (Left) ROSAT X-ray image of the center of Virgo Cluster, extracted from MPI (2021)[107] and (right) the electron number density and temperature (kT) as function of the distance from the center of the cluster for the Virgo Cluster. The curves are the best fit according to the analysis in Jacob & Pfrommer (2017)[21].

parameters for the Virgo Cluster: $n_0 = 0.230\,\mathrm{cm}^{-3}$, $\beta = 0.29$ and $r_c = 0.6\,\mathrm{kpc}$. Similarly, the temperature profile also follows a simple function across the cluster[21]:

$$T = T_0 + (T_1 - T_0)\left[1 + \left(\frac{r}{r_T}\right)^{-\eta}\right]^{-1}\left[1 + \left(\frac{r}{ar_{200}}\right)^{2}\right]^{-0.32}, \tag{3.14}$$

where T_0, T_1, r_T and η are free parameters and $a = 0.2$. r_{200} is the virial radius, in which the mean density inside it is 200 times the critical density for closure $\rho = 3H(z)^2/(8\pi\,\mathrm{G})$, where $H(z)$ is the Hubble function at the redshift z and G the gravitational constant. The best fit parameters for the Virgo Cluster are found to be[21]: $T_0 = 1.9$, $T_1 = 3.1$, $r_T = 28$ and $\eta = 1.4$. Based on Eq. 3.13 and 3.14, the electron density and temperature profiles are estimated and shown in Fig. 3.6 (right).

X-ray observations of high gas densities in the center of many clusters led in the 1970s to the development of the CF model[19]. It suggests that the cooling at the cluster center is so fast (faster than the Hubble time) that the material is compressed by the ICM pressure. As a result, the hotter gas from the outer regions flows inwards to replace the compressed gas, resulting in a CF. Mass deposition rates of the order of $1000\,\mathrm{M}_\odot/\mathrm{yr}$, where $\mathrm{M}_\odot$ is the solar mass, should then be expected but are not observed in such clusters, giving rise to the problem of the CC cluster[19,20]. CC clusters are characterized by low entropy and short cooling time at the center[21]. A classification was proposed in Peterson & Fabian (2006)[19] based on the central cooling time: strong cool-core ($\tau_{cool}<1h_{71}^{-1/2}\,\mathrm{Gyr}$), weak cool-core ($1h_{71}^{-1/2}<\tau_{cool}<7.7h_{71}^{-1/2}\,\mathrm{Gyr}$)

and non-cool-core clusters (τ_{cool}>$7.7h_{71}^{-1/2}$ Gyr), where $h_{71} = H_0/71$ is the reduced Hubble constant and H_0 is the present-day Hubble constant. A low central entropy characterizes strong cool-core clusters and a systematic central temperature drop, as seen in Fig. 3.6 (right) for the Virgo Cluster.

Several heating mechanisms have been proposed to solve the issue with the cool core clusters or contribute to the solution[19]: conduction, central AGN heating, sound waves, and turbulence. Since most of these mechanisms can only contribute with a small fraction of the heating, the AGN feedback and the thermal conduction are considered the main heating channels[21]. If the relativistic CRs escape the inner hot bubble, they hadronically interact with the ICM. The product of the interaction is, among other mesons, neutral pions, which almost immediately decay into gamma rays. This model is described in more detail in Sec. 4.5.1 as it is used later in the gamma-ray analysis of M87.

3.4. Multi-wavelength picture of M87

While the first radio detection of M87 dates back to the 1940s, only after the 1980s the large-scale radio lobes have been studied (see Bolton & Slee (1949)[112] and references therein). Later in 2000, VLA observations at 90 cm[113] showed details in the large-scale halo structure, connecting them to activities at the core region. More recently, simultaneous observations across various observatories coordinated by the Event Horizon Telescope (EHT) allowed a better understanding of the M87's broad-band emission.

The two aspects of multi-wavelength observations carry information about the variability and the morphology. The variability is related to the size of the emission regions. Since the relativistic particles cannot travel faster than light, a flare duration imposes a limit on the size of the emission region through:

$$R \leq c \times \Delta t \times \delta, \tag{3.15}$$

where R is the size of the emission region, c the speed of light, Δt the flare duration, and δ the relativistic Doppler factor. Suppose the instrument, which detects a flare, has sufficient angular resolution to resolve different emission regions. In that case, it might distinguish a flare by identifying which region had an increase in intensity in the image. For instance, the Chandra satellite can distinguish the emission from the core and the HST −1 knot[114,115]. On the other hand, due to its indirect detection method (Sec. 2.2), the IACTs have poorer spatial resolution and face difficulties resolving features smaller than $\approx 0.05°$. In this case, one profits from a correlation analysis with an instrument with a better spatial resolution, as I will show in Sec.

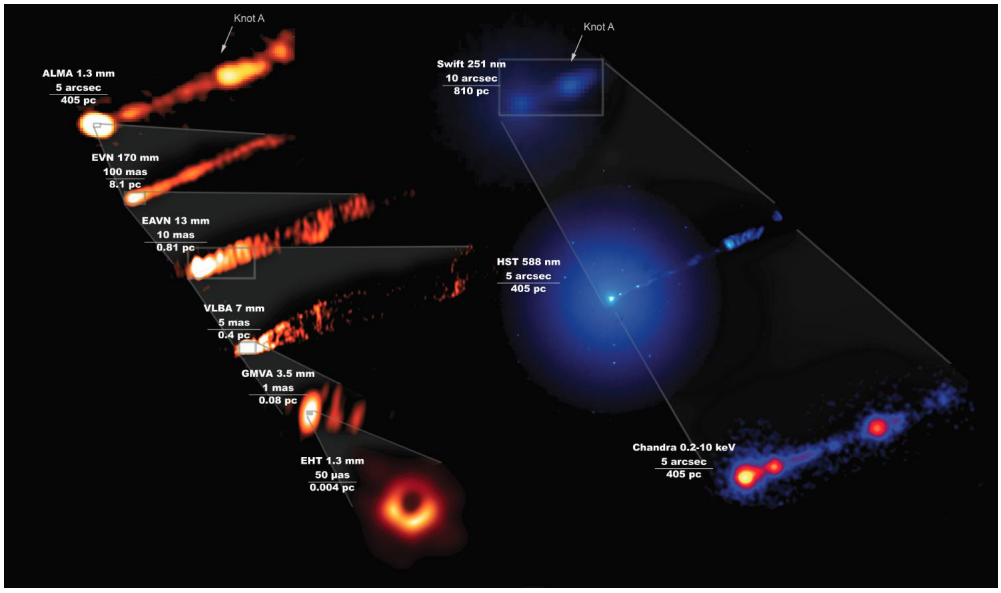

Figure 3.7.: Compilation of images obtained during the EHT 2017 campaign from the various instruments. Extracted from Algaba et al. (2021)[114].

4.1. Despite the limitation in the spatial resolution, IACTs were able to detect time variability of M87's gamma-ray emission of the order of 2 days[102], which translates, for estimated Doppler factor ($1<\delta<50$), to $R \approx 5 \times 10^{15}$ cm, only a few Schwarzschild radii from the SMBH.

The spatial resolution is given in general by the diffraction limit. For an array of telescopes it takes the form of:

$$r = \frac{\lambda(f)}{B} = \frac{1}{fB}, \tag{3.16}$$

where r is the resolution achieved by the observations, $\lambda(f)$ is the measured wavelength (frequency), and B is the baseline (maximum physical distance between the telescopes in the array). Figure 3.7 extracted from Algaba et al. (2021)[114] shows the radio images of M87's core at the different EHT baselines. The jet and the knots are well identified, as well as the EHT first picture of the SMBH 'shadow'.

Due to the limitation in the angular resolution and rate of events, the gamma-ray signal must be interpreted in conjunction with other wavelengths to unravel the nature and location of the emission. In the next section, the current state of the interpretation of M87's data is presented as a motivation for this work.

3.5. The current interpretation of the M87's gamma-ray emission

Evidence for VHE emission in M87 was first reported by HEGRA Collaboration[116] in 2002 and then confirmed by H.E.S.S. in 2006[102]. M87 has a low to moderate jet beaming and a low bolometric luminosity ($10^{41} - 10^{42}\,\mathrm{erg\,s^{-1}}$), which hampers the gamma-ray absorption by the local photon field. Therefore, the environment is considered transparent to gamma rays up to 10 TeV in the modeling of the source emission[93]. The low bolometric luminosity can be explained by a Radiatively Inefficient Accretion Flow (RIAF) or Advection Dominated Accretion Flow (ADAF), characteristic of BL Lac objects[117]. Three major gamma-ray flares occurred in 2005, 2008, and 2010. The gamma-ray flare from 2005 was accompanied by a strong X-ray flare detected by Chandra in the most prominent knot (HST -1)[102,115], ≈ 78 pc away from the galaxy core. On the other hand, the flare from 2008 was correlated with a later enhancement in the 43 GHz flux of the core region in the VLBA radio measurements[118]. In the 2010 flare, an enhancement in the Chandra X-ray data suggests a correlation of the VHE flare with the core of M87[119]. The three flares have similar timescales (1 - 2 days) and peak flux levels, though the overall variability varies. This fast variability interval suggests that the emission region from the gamma-ray flares is constrained to the inner 10^{16} cm≈ 0.003 pc from the core[120]. The duty cycle of VHE flares is estimated to be $\approx 28\%$[119]. However, due to observation strategies, M87 was more observed by the IACT instruments during high states than low states, therefore, overestimating the duty cycle.

In the VHE range, M87 was investigated by the MAGIC Collaboration in 2020[120] with quasi-simultaneous VHE data from 2012 to 2015, when the source was in a relatively low state. Two models to describe the SED were tested: first, a single-zone leptonic model, which took into account the time evolution of the electron and photon energy. Secondly, a single zone hybrid model, in which protons and electrons are accelerated in the jet and suffer energy losses under the presence of a magnetic field. The leptonic model describes well the data, apart from underestimating the SED flux in the mm-wavelength, a problem likely originated in the non-simultaneity of the data-sets[114]. The hybrid model described well the VHE data, with the largest contribution coming from the synchrotron emitted by relativistic protons. In the hybrid model, the radio and X-ray emission is found to come from a different and larger region than the VHE emission. The main conclusion derived from Acciari et al. (2020)[120] is the high particle energy of the jet in comparison to the magnetic energy (about 5 orders of magnitude), indicating that the system is not in equipartition. It suggests a VHE emission outside the immediate vicinity of the SMBH, where the magnetic energy density is the highest. The argument is supported by the EHT observations in Algaba et al. (2021)[114], which concluded based on simultaneous VHE observations from 2017 that an additional emission region outside the EHT

-core ($R \gtrsim 10 r_g \approx 10^{16}\,\mathrm{cm} \approx 0.003\,\mathrm{pc}$)[1] is necessary to explain the VHE emission of the M87's low state. Recalling the size of the emission region of the VHE flares, based on their variability ($R \lesssim 10^{16}\,\mathrm{cm}$), the origin of the VHE emission of (most of) the M87's low state is likely not the same as the region emitting during flare states. Algaba et al. (2021)[114] suggest that the base of the jet is moderately magnetized, it reaches around equipartition within the EHT region and particle dominance in the region probed by MAGIC ($R \sim 10^{20}\,\mathrm{cm}$).

Other physical scenarios might also originate from the gamma-ray emission detected by the IACTs. For instance, theoretical models[121] describe the dark-matter particles' annihilation and production of an extended gamma-ray emission. Bednarek (2020)[122] considers the shock of the relativistic particles from the jet with a denser blob of matter in the outer jet and the consequent gamma-ray emission. Furthermore, as described in Sec. 3.3, relativistic protons might interact with the ICM , produce among other mesons, π^0, which decay to gamma rays[21]. An effective way to test and exclude the gamma-ray emission models is to probe the size of the gamma-ray emission region and put constraints on its maximum allowed size.

The extension of M87's gamma-ray emission has been probed by different publications from the H.E.S.S. , MAGIC and VERITAS collaborations[102,120,123]. While in Aharonian et al. (2006)[102] and Acciari et al. (2008)[123] the entire H.E.S.S. observations, without distinction of source state were fitted, in Acciari et al. (2021)[120] only the morphology of the M87's low state of the MAGIC observations is fitted, where the low state was defined as the flux up to 10% of the Crab Unit (CU), and $1\,CU = 5.6 \times 10^{-11}\,\mathrm{cm^{-2}s^{-1}}$ in the energy range 400 GeV-1 TeV[124]. An extended gamma-ray emission is expected to be constant due to the causality argument (Eq. 3.15), hence, the necessity of separating the source states and concentrating on the low state emission. The best published limit on the extension of the low state gamma-ray emission is from the MAGIC collaboration[120], where it was constrained with a 99.7% confidence level (c.l.) to a radius smaller than 0.042 mdeg ($\approx 11.5\,\mathrm{kpc}$), which is much larger than the sub-structures of the jet seen in Fig. 3.7.

The same relativistic electrons that emit X rays through the synchrotron process could also produce VHE gamma rays, through IC scattering (Sec. 3.2). Therefore, the search for a correlation between the X-ray and gamma-ray emissions in the low state could suggest a common emission region. The Nuclear Spectroscopic Telescope Array (NuSTAR)[125] is the first focusing high-energy X-ray telescope in orbit since 2012. It can access the $20 - 40\,\mathrm{keV}$ X-ray spectrum of M87, which is dominated by non-thermal processes, though its angular resolution ($18''$) is larger than the substructures of the inner jet[82]. On the other hand, Chandra[126] can resolve the sub-structures of the jet, though the energy range corresponds to the soft X rays (E<10 keV), where the emission is dominated by thermal bremsstrahlung. The main components of the NuSTAR

[1] r_g: the gyroradius of the magnetic field in the vicinity of the SMBH.

Name	**Γ**	**K**	$f_{20-40\,\mathbf{keV}}$
Core+HST −1+Jet	$2.12^{+0.12}_{-0.13}$	102^{+38}_{-29}	$7.7^{+1.1}_{-1.0}$
Core	$2.11^{+0.15}_{-0.11}$	63^{+28}_{-15}	$4.8^{+0.9}_{-1.0}$
HST −1	[1.94]	$5.5^{+1}_{-0.9}$	$0.7^{+0.1}_{-0.1}$
Jet	$2.36^{+0.16}_{-0.17}$	52^{+10}_{-10}	$1.8^{+0.9}_{-0.6}$

Table 3.1.: Best fit of the combined Chandra-NuSTAR data for the individual components in M87. The normalization is given in 10^{-5} photons $\mathrm{keV}^{-1}\,\mathrm{cm}^{-2}\,\mathrm{s}^{-1}$ at 1 keV and the flux is given in 10^{-13} $\mathrm{erg}^{-1}\,\mathrm{cm}^{-2}\,\mathrm{s}^{-1}$. The brackets in HST1 spectral index indicates, only Chandra data were used. Extracted from Wong et al. (2017)[82].

soft X-ray emission are the X-ray core, the jet, and the knots along with the jet, the diffuse ICM, and the unresolved low-mass X-ray binaries (LMXBs)[82]. Wong et al. (2017)[82] show that the center position of the hard X-ray emission (E>10 keV) is marginally consistent with the soft X rays in NuSTAR data. It can be interpreted as both soft and hard X ray having the same emission region. If the X-ray core, jet, and knots are also the origin of the hard X rays, hence, non-thermal processes take place in these locations and could also lead to gamma-ray emission through IC scattering. A joint observation and analysis of Chandra and NuSTAR provide a better understanding of the X-ray contribution of the individual components and their spectral shape as shown in Tab. 3.1[82]. The core is expected to dominate the emission in the range 20 keV - 40 keV and have a hard index (Γ=2.11), remarkably similar to the spectral index of the H.E.S.S. observations during flaring states[119]. Such a similarity is expected if the same relativistic electrons are responsible for both X-ray and gamma-ray emissions. According to the fit results shown in Tab. 3.1, the jet is the second largest contributor to the non-thermal X-ray emission with a spectral index $\Gamma = 2.36$. The jet spectral index in X rays is similar to the spectral index in VHE of M87's low state reported by MAGIC[120], which could suggest a strong jet emission in gamma-rays.

Despite extensive investigations since the early 2000s, the nature and location of the gamma-ray emission of M87 is still a mystery. While for the VHE flares, evidences for correlations between instruments rely on variability studies and indicate very compact regions as the origin of the gamma-ray flares, the study of the low state emission has to rely on spectral and morphological information. The question of whether the flares and the low state emission have the same origin is also unanswered.

Due to the improvements within the last years in the H.E.S.S. sensitivity and angular resolution both from the software and hardware side, observations with H.E.S.S. are the most promising among the IACTs to localize better the origin of VHE sources. In the next chapter, I use the three aspects of analysis (temporal, morphological, and spectral) to investigate the

M87's gamma-ray low state based on the deep H.E.S.S. observations. First, I approached the temporal aspect, i.e. the correlation of the gamma-ray emission with the X-ray emission and the definition of gamma-ray source states throughout time. Secondly, I conducted a detailed study of the morphology to constrain the location of the gamma-ray emission of M87's low state. Based on the morphology results, I investigated in detail the hadronic model for the gamma-ray emission, in which the interaction of the relativistic protons from the jet with the ICM is responsible for production and decay of π^0, and derive conclusions about the cosmic-ray pressure in the inner Virgo Cluster. Finally, I explored the spectral information of a single-zone emission model to explain M87's low state emission in gamma rays.

4. The gamma-ray morphology of M87 as seen with H.E.S.S.

M87 has been observed with H.E.S.S. since 2004. Data spanning from 2004 to 2021 were used for this analysis. I selected observations in which at least three telescopes participated. This criterion assures a better direction reconstruction. Furthermore, data from CT5 were not included in the analysis since events, which are only detected with CT5, would have a larger uncertainty in the reconstructed direction and would worsen the overall PSF. A cut on the zenith angle of observation was defined at 50° (recall Fig. 2.7) to improve the angular resolution, which excluded less than 5% of the observations. The smaller the zenith angle, the less light absorption by the atmosphere. A lower energy cut-off at 300 GeV was considered to avoid the region with a worse effective area due to the stronger absorption by the atmosphere. I obtained a total of 194 hours of observation after the selection by the application of the quality criteria for spectrum, according to Sec. 2.4. It is the most extensive data set yet analyzed with H.E.S.S. data for this source.

The default H.E.S.S. analysis software HAP[52,127] was used to analyze the data with its template analysis *std_imPACT*[65] as described in Sec. 2.5.2. The test position, i.e., the position where the source is expected, was set to the position of the SMBH, at RA=187.7059° and DEC=12.3911°. The Reflected Region Background method was used for deriving spectral and flux information, while the Ring Background method for generating the source gamma-ray sky maps (Sec. 2.5.5).

Python[128] scripts were developed for the morphology fit[1]. The objective of a morphology analysis is to probe the extension of the M87 gamma-ray low state emission, motivated by the propagation and interaction of cosmic rays with the ICM, as described in Sec. 3.3, and unravel the origin of the emission from the different source states.

As described in Sec. 3.1, VHE gamma rays probe particle acceleration in relativistic outflows. Relativistic electrons are mainly expected to lose energy through synchrotron and IC scattering (Sec. 3.2). The synchrotron radiation can be detected from radio to X rays, while the IC photons are detected between hard X ray and gamma rays. By detecting the synchrotron

[1] NumPy[129] 1.17.2, SciPy[130] 1.3.1, Astropy[131,132] 3.2.2, Gammapy[133,134] 0.17, and Sherpa[135,136] 4.12.0.

radiation, one can trace the position and distribution of the relativistic electrons in the source and, consequently, the magnetic field. Since the acceleration process is independent of the particle mass, protons should also be accelerated in the outflow[83]. However, the protons lose $m_{\rm p}/m_{\rm e}$ slower energy than the electrons through synchrotron radiation, and, hence, they are more difficult to be detected. Nevertheless, protons might also interact inelastically with the local plasma since the inner regions of galaxy clusters are permeated with a considerable amount of plasma. The product of the inelastic (hadronic) interactions between the relativistic protons and the local plasma is mainly charged and neutral pions. While the charged pions decay to electrons and positrons, the neutral pions decay almost immediately (8.4×10^{-17} s)[87] to gamma rays. Since the protons keep their energy through longer distances than the electrons during its propagation, with a sufficient cosmic-ray pressure, they might reach kpc distances and still leave a trace in gamma rays. The detection of gamma rays further away from the jet would probe the injection and diffusion of particles in the system and allow a comparison between the injected protons and electrons.

The gamma rays produced by π^0 decay in the cluster core are expected to produce a stable and extended gamma-ray emission (Sec. 3.3 and App. A.1). Variable emission (flares) as seen from M87 in different wavelength bands, including gamma rays, and over different timescales (hours - days/months) can be associated with localized emission regions in the vicinities of the core[119]. They are, hence, not associated with gamma-ray emission from π^0 decay. To probe the gamma rays from π^0 decay, one shall first select the observations, excluding the variable emission (flares) and keeping the stable (low state) emission. Part of the variable VHE emission from M87's core is expected to be still present in the low state. An extended diffuse gamma-ray emission signal may be detectable if enough protons are accelerated and interact with the ICM. This emission has a larger spatial morphology, and, therefore, it can be distinguished from the contribution by the jet, presumably of leptonic origin.

Therefore, the search for an extension in the M87's gamma-ray flux is motivated by the question of how much energy can be accelerated in relativistic protons and how far they can travel before losing their energy. It is also possible that the gamma-ray emission from M87's low state comes either from further down the jet or from the knots along with the jet (see Sec. 3.4). Figure 3.7 shows the Chandra soft X-ray image with M87's jet and knots. However, given the size of the inner jet (≈ 1 kpc up to the Knot A), the current generation of IACTs is not able to resolve the inner jet.

The first step to probe the propagation of relativistic protons is to study M87's gamma-ray flux throughout time. To find the state where the jet contribution is lowest, one needs to construct the gamma-ray flux throughout time (light curve) and compare it to the jet activity in other wavelength bands, for instance, X rays. X rays trace jet activity, partly non-thermal electrons,

and the X-ray instruments have better temporal sampling rates and angular resolution. However, this approach can only be considered if the X-ray and gamma-ray light curves are significantly correlated. If the light curves are not correlated, the source states will be classified based on the gamma-ray flux. Since the flux measurements of IACTs have relatively large statistical uncertainties, an appropriate time window (bin) shall be defined, within which the nightly flux is averaged and the statistical uncertainties minimized. The larger the time bin, the better the statistical uncertainties. However, for large-time bins, the flux of enhanced states will get smoothed out and contaminate the selection of the low state. After the appropriate selection of the time bin, a Bayesian Block analysis is conducted to finally derive the source states based on their flux levels. Point-like and Symmetrical Gaussian models fit the morphology of the source states. The difference in the Test Statistic (TS) indicates which model is preferred. The best-fit position of the source states will also indicate if they are compatible with the same emission region.

Assuming that the dominant emission originates from M87's core, I proposed a one-zone leptonic model to explain the synchrotron X-rays and the SSC emission. I used data from the X-ray instruments Chandra and Nustar and the gamma-ray instrument Fermi-LAT from Algaba et al. (2021)[114] when the source was in a low state and fitted to the model alongside the H.E.S.S. low state spectrum. For a hadronic scenario, in which the decay of neutral pions produces the gamma rays, I applied the model from Jacob & Pfrommer (2017)[21,110] to explain the propagation of relativistic protons into the ICM, and used it to predict the extension and the total flux of the gamma-ray emission. Afterward, I fitted the predicted model to the H.E.S.S. low state morphology and derived constraints to the cosmic-ray pressure. After testing both leptonic and hadronic scenarios for the gamma-ray low state emission of M87, I investigated the potential of deeper observations.

This chapter is organized as following: In Sec. 4.1 I investigated the correlation between the X-ray Chandra[137] and the H.E.S.S. light curve. Sec. 4.2 shows the derivation of the Bayesian Blocks, and the search for an extended gamma-ray emission follows in Sec. 4.3. In Sec. 4.4 and 4.5, I fitted the one-zone leptonic model and the hadronic model, respectively, to the low state data. Finally, in Sec. 4.6 I derived the potential of deeper observations with H.E.S.S. through simulations of sky maps.

4.1. X-ray - gamma-ray correlation studies

The same electron population that produces X rays through synchrotron radiation might also produce gamma rays through the IC scattering of the electrons in the synchrotron radiation field. X-ray instruments and IACTs have very different characteristics, for instance the angular

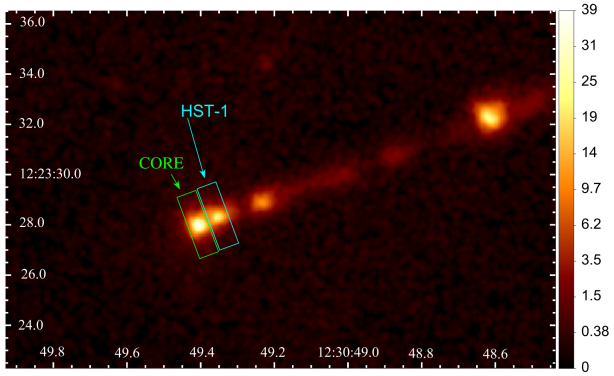

Figure 4.1.: Chandra X-ray image of M87's jet. The green and cyan rectangle of length 2.6″ transverse to the jet and 0.8″ along the jet are the selected source regions for the CORE and HST −1. Extracted from Yang et al. (2019)[115].

resolution of Chandra is in the sub-arc-second region[115], while the H.E.S.S. PSF is $\approx 3'$ (see Sec. 2.5.2). A significant correlation between the light curve of both instruments would indicate a common origin for the non-thermal emission. In 2005 Chandra detected a flare from the knot HST −1, while H.E.S.S. detected a gamma-ray flare, hence, their origin are likely correlated[102]. Despite hints for a correlation in flares, no study has tested so far for a correlation of the X-ray and gamma-ray long-term light curves in M87. In this section, I investigated a correlation between the Chandra X-ray light curve of M87's core and the knot HST −1 with the H.E.S.S. VHE emission. If the correlation is significant, the M87's low state in gamma rays could be defined by excluding data when the core and the HST −1 are flaring in X rays.

Figure 4.1 reproduces Fig. 1 from Yang et al. (2019)[115] and highlights the core and HST −1 knot regions. The H.E.S.S. PSF is $\approx 3'$ and is much larger than the entire figure. The bin size used in the H.E.S.S. analysis is 0.01°, which is also larger than the jet emission shown in the figure, demonstrating the limitation of the angular resolution of IACTs. Figure 4.2 shows the long-term X-ray light curves of HST −1 knot and the core as obtained with the Chandra satellite[115]. I extracted the monthly-binned flux points from the H.E.S.S. data set and plotted them alongside the Chandra light curve for comparison. The strong gamma-ray flare from 2005[102] was seen both in X ray and gamma rays. Both the core and the HST −1 had shown increased activities in X rays, though the HST −1 was at a higher level. Another prominent gamma-ray flare occurred in 2008[118], which was accompanied by a flare from the X-ray core. The flare from 2010[119] showed similar behavior. Indications of an elevated gamma-ray state in 2012 and 2018 were not accompanied by a significantly increased flux in the X-ray light curve of neither HST −1 nor the core.

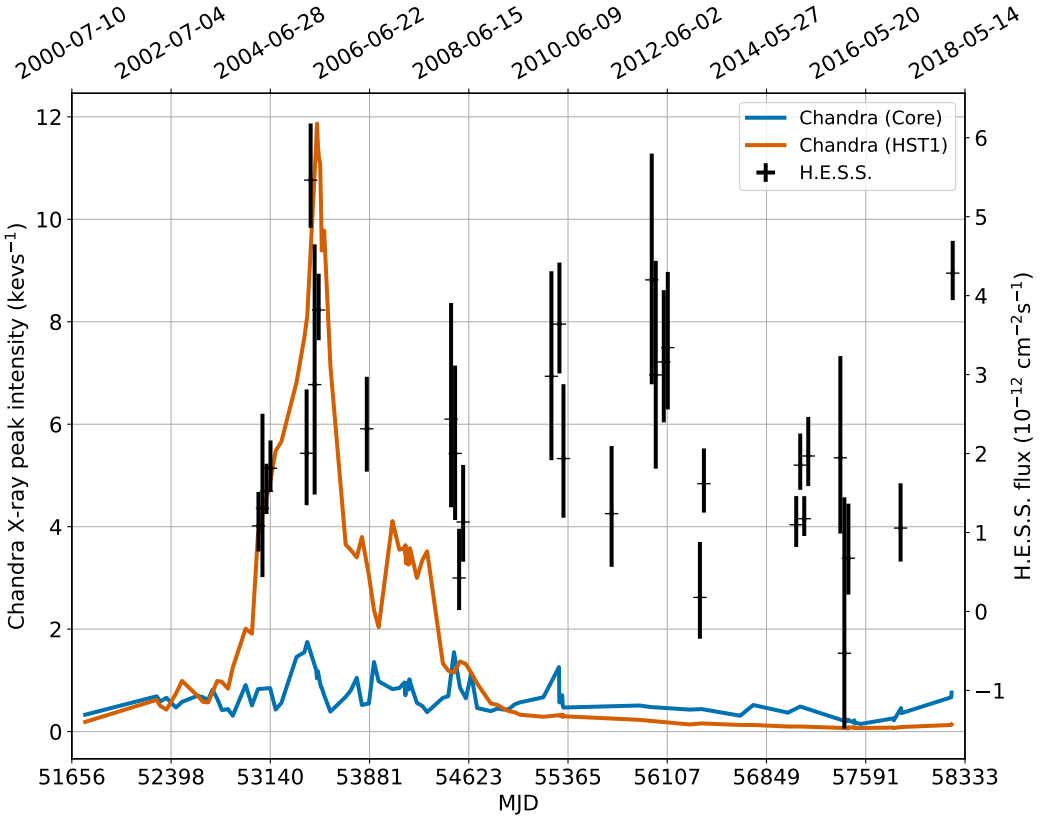

Figure 4.2.: Chandra light curve extracted from Yang et al. (2019)[115] (blue for core and orange for HST −1) plotted alongside H.E.S.S. data points (black), which was binned according to a period of 30 days (month calendar).

If the X-ray and the gamma-ray emission originate from the same emission region, they could simultaneously show an enhanced flux. In this case, their light curves would be statistically correlated, and the correlation can be tested according to different methods. For instance, the Spearman statistical[138] test quantifies the level of correlation between the H.E.S.S. and Chandra data. The Spearman statistic is a generalized version of the Pearson statistic. While the Pearson coefficient measures the linear correlation between two variables (light curves), the Spearman coefficient measures how monotonic the correlation is between their ranks, i.e., the correlation between the sorted data points. The coefficient ranges between -1 and 1, where -1 indicates anti-correlation, 1 indicates a correlation, and 0 stands for no correlation.

Yang et al. (2019)[115] present the long-term light curve of HST −1 and the core emission using Chandra observations from 2000 to 2018 and with a 0.4 s to 3.2 s frame time. The data acquisition is more homogeneous in time as the H.E.S.S. observations, which either follow external triggers

or the sporadic schedule from the H.E.S.S. monitoring campaigns.

The challenge behind the estimation of the cross-correlation of different instruments is that the temporal coverage, temporal sampling, and flux sensitivity are different. A solution is to use time bins to convolve the flux points of both instruments to the same time window. The choice for the time bin size is a trade-off between more data points available and fewer statistical uncertainties. Furthermore, for larger bin sizes, it is expected that the high states get averaged out with the low states, which results in a loss of information and reliability in the method.

The 194 hours of H.E.S.S. data were used to derive a gamma-ray light curve, as explained at the beginning of this chapter. The correlation between the light curves was estimated for a set of bin sizes with periods 1, 7, 15, 30, 60, and 90 days. The results for the Spearman coefficient are shown in Fig. 4.3 as a function of the bin size for the three correlation channels: Chandra core with Chandra HST −1, Chandra core with the H.E.S.S. flux, and Chandra HST −1 with the H.E.S.S. flux. The p-value gives the chance coincidence for estimating the specific coefficient. The lower the p-value, the lower the probability that the estimated coefficient is due to chance, as Fig. 4.3 shows. For all three correlation channels, the same time window was used, defined by the H.E.S.S. time bins. Whenever the time bins are not coincident, the bin is dropped from the analysis.

While a very strong correlation (>0.80) is observed between the Chandra core and Chandra HST −1 throughout all the bin sizes, a moderate correlation (0.4 - 0.6) is found between H.E.S.S. data and Chandra core and between H.E.S.S. data and the HST −1 X-ray flux.

The p-value is shown for a null hypothesis, in which there is no correlation between the variables. The correlation coefficient for Chandra Core and Chandra HST −1 is always more significant than by comparing them with the H.E.S.S. flux points. Table 4.1 shows the Spearman coefficient, p-value, and significance for all the three channels and the bin size of 30 days. None of the Spearman coefficients, which includes H.E.S.S. data, are significant ($>3\,\sigma$). More coincident observations between both instruments would increase the binned flux points and help search for a significant correlation. On the other hand, the Spearman coefficient between Chandra core and Chandra HST −1 is significant for every bin size.

Even if the X-ray and gamma-ray light curves originated from the same region, it would not be easy to detect their correlation significantly. The reasons are the large uncertainties in IACTs flux in comparison to X-ray instruments, the small number of gamma-ray flares, and the small number of coincident observations. Since no significant correlation is detected between the long-term light curves of the X-ray and gamma-ray emissions, one can not assume that the emissions are originated from the same regions. Therefore, the classification of the source states should rely on the gamma-ray data itself, as described in the next section.

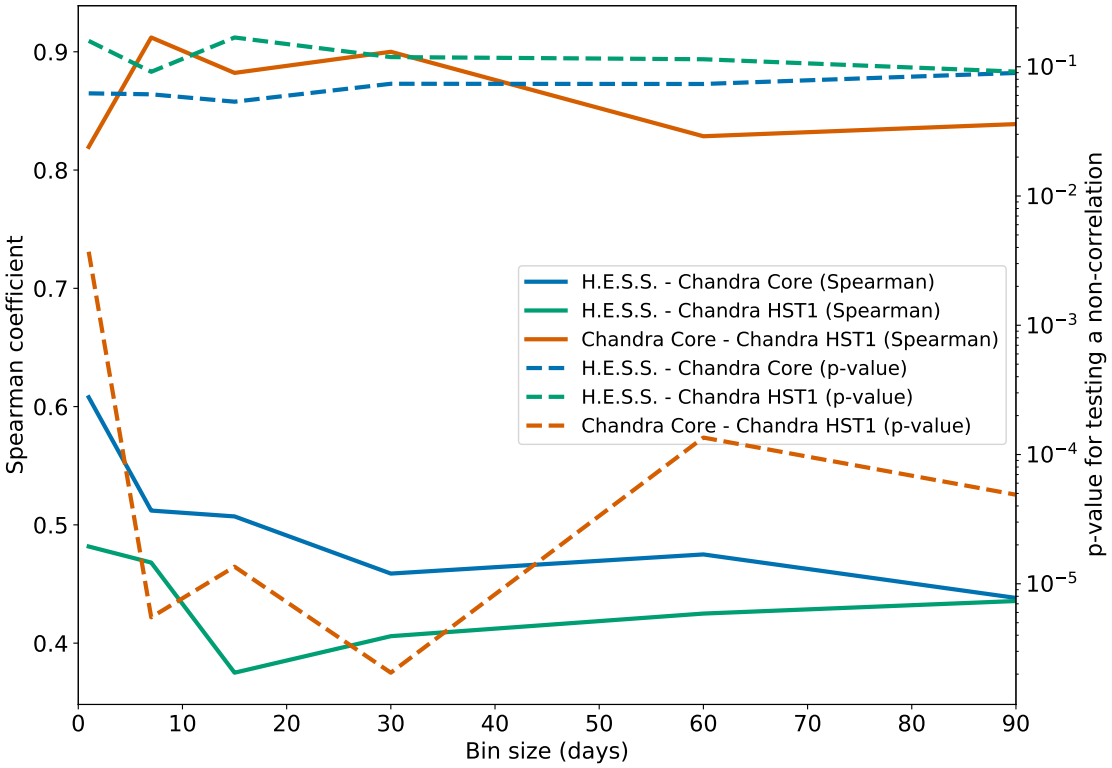

Figure 4.3.: The Spearman coefficient for the Chandra X-ray flux from the core (Chandra core), from the HST −1 and the H.E.S.S. gamma-ray flux according to time bin sizes. The closer to 1 the larger the correlation between the variables.

	30-day period		
	Chandra core - Chandra HST −1	**H.E.S.S. - Chandra core**	**H.E.S.S. - Chandra HST −1**
Spearman coeff.	0.90	0.46	0.40
p-value	2.05×10^{-5}	7.38×10^{-2}	1.19×10^{-1}
Sign.(σ)	4.75	1.79	1.56

Table 4.1.: The results of the correlation between Chandra X-ray core, Chandra X-ray HST −1 and H.E.S.S. flux points. The Spearman coefficient, their p-values and significance values are shown for the bin size of 30 days.

4.2. M87's source states

The VHE gamma-ray emission from M87 has shown variability from days to months[102,119]. The time the light takes to travel from one place to the other within the source region must not exceed the variability timescales; otherwise, causality is broken. Due to the very small periods, flares in VHE gamma rays are thought to come from the inner regions of the galaxy center, a few Schwarzschild radii from the central supermassive black hole. As motivated at the beginning of the chapter, the gamma-ray emission due to π^0 decay is expected to be extended and without any sign of variability (see Sec. 3.3)[139,140]. The first step to test for an extended gamma-ray emission from M87 is to define the source states and exclude the emission from the high states (flares), which are known to be constrained to very compact regions. A Bayesian approach[141] is used in Sec. 4.2.1 to extract the flux levels of the source, and, consequently, the source states as described in Sec. 4.2.2.

4.2.1. Bayesian Block analysis

The Bayesian Block analysis is designed to extract localized signals from counting data, where statistical fluctuations dominate over systematic uncertainties. The method generates a block-wise constant representation of sequential data based on statistically significant flux variations. It requires a prior function, which considers the object's prior knowledge regarding its variability. In practice, the larger the prior function value, the fewer blocks are generated from the data points. The prior function that minimizes false positives for a given normal distribution is given by[141]:

$$P(N) = 1.32 + 0.577\, log10(N) \tag{4.1}$$

where P is the prior function and N is the number of data points.

Since M87 is a rather faint gamma-ray emitter (7.5% of the Crab VHE gamma-ray flux), its low state can be significantly detected after $\approx 5\,\mathrm{h}$ of observation, which comprises from two to seven nights. Therefore, short integration periods of (1 - 7 days) might not result in a significant detection. On the other hand, due to its fast variability, a large integration period (60 - 90 days) would smooth out the flares, and information would be lost in the final Bayesian blocks. Therefore, the bin size of 30 days was found to represent the optimum between reaching sufficient statistical uncertainties in the flux points and keeping information about the flares. Figure 4.4 shows the monthly binned flux points with their derived Bayesian blocks. The H.E.S.S. flux points are shown in black, the Bayesian blocks are color-coded according to the classification of state (Sec. 4.2.2), and the best fit of constant flux is shown in dark orange.

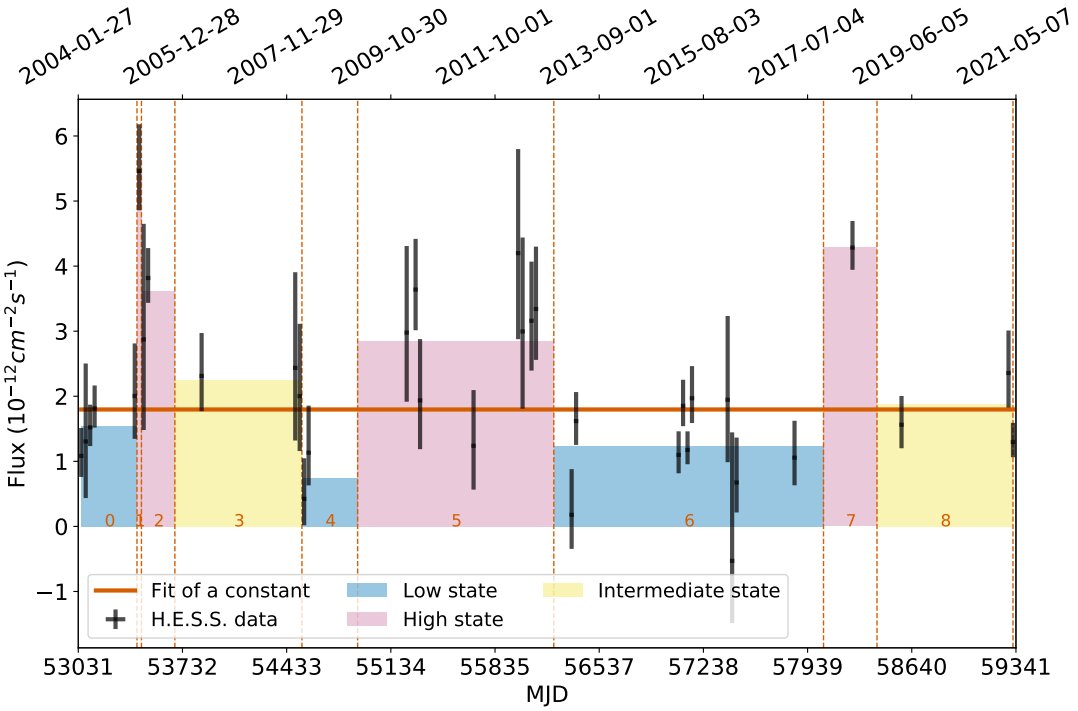

Figure 4.4.: Monthly binned H.E.S.S. light curve with the Bayesian blocks.

4.2.2. M87's flux states

The definition of high and low states is relatively sparse and spans a lot of different definitions according to the authors: Yang et al. (2019)[115] and Ahnen et al. (2016)[142] define a high state whenever the flux doubled, while Resconi et al. (2019)[143] classified the states into the characteristic level and flaring state, and finally, Wolk et al. (2005)[144] classify the states into characteristic, elevated and very elevated levels. However, it is a consent that the term "quiescent" is misleading when used to characterize the low state. "Quiescent" means "marked by inactivity"[144], therefore is not an appropriate definition to use in a highly variable source as M87 .

Instead of using one of the definitions above, which are mainly focused on analyzing high states, I have developed another concept. The Bayesian blocks (Fig. 4.4), which lie below the mean (best fit of a constant function), are defined as the low state. The intermediate state is defined as the blocks reaching the flux level up to 30% above the mean, which includes the flare from 2008 and the data after 2019. Therefore, the four highest states are the flares from 2005,

Block	State	Start date	End date
0	Low	2004-02-16	2005-02-25
1	High	2005-02-25	2005-03-27
2	High	2005-03-27	2005-11-07
3	Intermediate	2005-11-07	2008-03-11
4	Low	2008-03-11	2009-03-21
5	High	2009-03-21	2012-10-31
6	Low	2012-10-31	2017-10-20
7	High	2017-10-20	2018-10-15
8	Intermediate	2018-10-15	2021-04-17

Table 4.2.: The Bayesian blocks of the monthly-binned H.E.S.S. light curve with its classification into low, intermediate and high states. The blocks are enumerated from the left to right (from 0 to 8) in Fig. 4.4.

2010 and the high fluxes found in 2012 and 2018. Table 4.2 shows the Bayesian blocks with their classification, start and end date according to the H.E.S.S. observations.

Data from the individual observations were stacked according to the defined source states. The stacked data provide better event statistics than individual observations, which is key to constraining the spectral and morphological parameters. I conducted a separate H.E.S.S. analysis for each source state according to the procedure described in Sec. 2.5. The background was estimated using the Ring Background method to extract the source morphology and according to the Reflected Region Background to extract the spectral information (see Sec. 2.5.5). Table 4.3 shows the statistics of the H.E.S.S. analysis: Excess, Significance[68], live-time, flux, and spectral index. The spectral index Γ gives the flux ϕ dependence on the gamma-ray energy E and ϕ_0 gives the normalisation at 1 TeV: $d\phi/dE = \phi_0(E/\mathrm{TeV})^{-\Gamma}$. The integrated flux above 300 GeV is also given in the table. Although not significantly, the reconstructed gamma-ray spectral index is different in the different flux states. The high state shows a harder spectral index, while the intermediate state transitions to the low state with a steeper spectral index. Harder indexes are linked to more efficient particle acceleration since more energy is stored in the higher energy electrons. On the other hand, steeper indexes are linked to either a less efficient acceleration mechanism or an older cooled electron population. While the spectrum of M87's low state is further discussed in Sec. 4.4, the next section discusses the morphology of M87 according to its source states.

	Low state	**Intermediate state**	**High state**
Excess (counts)	593.6	198.8	397.1
Signal-to-noise ratio	0.49	0.68	1.34
Significance (σ)	15.6	10.5	19.4
Livetime (h)	120.4	28.5	29.0
Flux at 1 TeV (10^{-13}cm^{-2} s^{-1})	3.4 ±0.2	4.1±0.9	10.4±0.5
Spectral index	2.63±0.09	2.40±0.10	2.25±0.05
Integrated flux (10^{-12}cm^{-2} s^{-1})	1.48±0.14	1.58±0.22	3.75±0.43

Table 4.3.: Results of the H.E.S.S. analysis for the low, intermediate and high states. The integrated flux is given above 300 GeV.

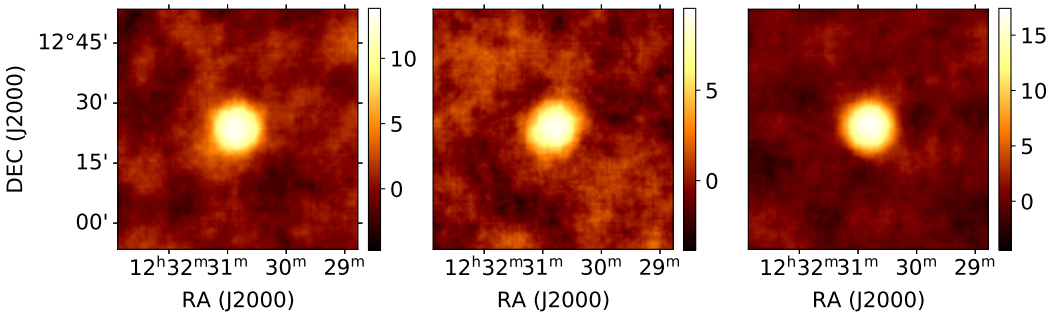

Figure 4.5.: The significance maps of M87's flux states: (left) low, (middle) intermediate, and (right) high states.

4.3. Morphology of M87

The gamma-ray emission from M87's low state could either be originated from the leptonic emission from the core, knots, and jet or the diffuse emission resulting from the relativistic protons interactions with the ICM, through π^0 decay. On the other hand, due to their variability, the intermediate and high states are expected to be dominated by emission from compact regions (for instance, M87's core or the knot HST -1). With the variability timescales observed and the limited angular resolution of H.E.S.S. , no extended emission region is expected to be detected with the H.E.S.S. telescopes in the intermediate and high states. Nevertheless, suppose the emission region from different Bayesian Blocks within the same source state does not come from the same region. In that case, the morphology fit of the stacked analysis might indicate a hint for extended emission. Therefore, all three states are included in the morphology studies. Finally, I explain the morphology fit algorithm in Sec. 4.3.1 and apply it to the source states in Sec. 4.3.2. Afterward, I show the results of the morphology fit, discuss and compare them to previous results in Sec. 4.3.3.

4.3.1. Morphology fit algorithm

The algorithm applied to study M87's morphology was inspired by recent publications from the H.E.S.S. collaboration: the morphology of the Crab-pulsar[73] and the Centaurus A galaxy[74]. As in these publications, Sherpa[135], the modeling and fitting package from the Chandra X-ray Observatory, was used. The stability of the morphology fit against sources of systematic uncertainties; for instance, an analysis without taking the pointing uncertainties into account and an analysis where the center of the emission model is fixed to M87's core have been conducted in App. B. The study of the sources of systematic uncertainties in App. B showed a very good agreement with the morphology fit results of the main analysis, presented in the next section.

The morphology fit algorithm is applied to pre-defined morphological models of the gamma-ray emission. Afterward, the model that best describes data is found through a TS. Since counts are sampled from Poisson distributions, the Cash-statistic[145], defined based on the same distribution, was used in the fit algorithm:

$$C = 2\Sigma_i[M(i) - D(i)logM(i)], \tag{4.2}$$

where $M(i) = S(i) + B(i)$ is the sum of the source and background model amplitudes and $D(i)$ is the number of counts in the bin i.

The Cash-statistic can be compared to the more widely used χ^2-statistic. While the last works well for a large number of counts but biases the results when the counts are low ($\lesssim 3$ counts per

bin), the Cash-statistic overcomes this limitation. For a larger number of counts, both methods should provide the same results[146]. For instance, the widely used Nelder-Mead simplex[147], conveniently implemented in the Sherpa library, is chosen as the optimization method for the morphology fit.

Despite the most important aspect of the morphology fit being the shape of the gamma-ray emission (the best morphological model), one has to consider how the background influences it, the exposure time of the observations, and the angular resolution (PSF) of the H.E.S.S. telescopes. The background, exposure time, and the detected signal are obtained directly from the H.E.S.S. analysis. On the other hand, the PSF is derived from MC simulations, given the observational conditions, i.e. according to the zenith angle, effective area, and the reconstruction methods as described in Sec. 2.3. Three concentric 2D Symmetrical Gaussian functions (G_i) with a scaling factor(C_0) are used to describe the PSF distribution from the simulations and define the PSF function P:

$$P = C_0 \times (G_1 + G_2 + G_3), \tag{4.3}$$

where G_i are the Sherpa functions for a 2D Gaussian. The generalised form of G_i could also describe a non-symmetrical 2D Gaussian. The Sherpa function is defined according to:

$$\begin{aligned} G(x,y) &= C_0 \exp[-4\ln(2) r(x,y)^2], \\ r(x,y)^2 &= \frac{r_x(x,y)^2(1-e)^2 + r_y(x,y)^2}{\mathrm{FWHM}^2(1-e)^2}, \\ r_x(x,y) &= (x-x_0)\cos\theta + (y-y_0)\sin\theta, \\ r_y(x,y) &= (y-y_0)\cos\theta - (x-x_0)\sin\theta, \end{aligned} \tag{4.4}$$

where A is the amplitude (maximum peak of the model), e is the ellipticity of the Gaussian, FWHM is the Full-Width Half Maximum of the Gaussian along the major axis, θ is the angle of the major axis measured in radians counterclockwise from the X-axis, x_0 and y_0 are the centers of the Gaussian.

A convenient way to treat the data is through the standardized Flexible Image Transport System (FITS)[134] files, which are input to the morphological models. The first and simplest morphological model is a point-like function. It is defined as the PSF function, i.e., the three concentric 2D Symmetrical Gaussian functions. As part of the investigation of the systematic effects, I tested alternative functions for the point-like model and discuss their results in App. B.6. Despite describing its shape correctly, the alternative functions for the point-like source did not allow the optimization method to scan the parameter space of the Gaussian's center. The

function that best describes the PSF and allows the scan of the parameter space for its optimal center position is the analytical formula of the three concentric Symmetrical Gaussians, which I used in the analysis. The model for the detected gamma-ray signal M_{D}, given the intrinsic emission is point-like, is defined according to:

$$M_{\mathrm{D}} = B + P \odot E, \tag{4.5}$$

where P is the PSF function (Eq. 4.3), B is the estimated background, and E is the effective area (exposure time times the acceptance). The symbol '$\odot$' indicates an element-wise product of matrices.

Since the PSF shape is defined by the results of the MC simulations (Sec. 2.5.4), the only free parameters in the point-like model are the PSF center position x, y and its amplitude C_0.

The second morphological model in the sequence of degrees of freedom (d.o.f.) is the 2D symmetrical Gaussian function G. It adds one free parameter in comparison to the point-like model, the width (FWHM). The model for the detected signal M_D is constructed slightly differently as in the case of the point-like model. For this case, the PSF is treated as a Sherpa PSF model, which allows a convolution with the emission model M_E during the fit procedure:

$$M_{\mathrm{D}} = B + P \circledast M_{\mathrm{E}} \odot E, \tag{4.6}$$

where M_{E} is the emission model, in this case G given by Eq. 4.4. The symbol '$\circledast$' indicates a convolution of the PSF with the emission model. For the Gaussian model, the free parameters are its center and amplitude (x, y, and C_0 as for the point-like model), and its extension, given by the FWHM. As the 2D Gaussian function is symmetric, the ellipticity e and the angle of the main axis θ are fixed to 0 according to Eq. 4.4. The PSF shape obtained from the MC simulations is given by a slightly different definition as the definition from Eq. 4.5:

$$PSF(\theta) = A \times [e^{-\theta^2/\sigma_1^2} + A_2 \times e^{-\theta^2/\sigma_2^2} + A_3 \times e^{-\theta^2/\sigma_3^2}], \tag{4.7}$$

where θ is the angle from the center of a point source, A is the scale parameter, σ_n, and A_n are the width and amplitude from the n^{th} Gaussian function. The best PSF parameters, according to the H.E.S.S. MC simulation results, the 68.7% c.r. and the 99.7% c.r. are given in Tab. 4.4 for the three source states. Equation 4.7 with its best fit parameters are easily rearranged to Eq. 4.5 to allow the use of the Sherpa PSF function in the model. The PSF is normalized by its maximum value and the parameters are fixed throughout the entire analysis.

The PSF function in the point-like and Gaussian models is convolved with a Gaussian kernel with width $\sigma = 20''$ to account for the systematic uncertainties from the telescope pointing, as

State	**68% c.r.** (°)	**99% c.r.** (°)	**A (counts)**	σ_1 (°)	$\mathbf{A_2}$ **(counts)**	σ_2 (°)	$\mathbf{A_3}$ **(counts)**	σ_3 (°)
Low	0.071	0.361	3.6	0.132	85.7	0.026	20.8	0.055
Intermediate	0.070	0.356	4.2	0.128	76.3	0.025	20.1	0.052
High	0.070	0.361	4.3	0.129	82.0	0.024	19.4	0.052

Table 4.4.: PSF parameters resulted from the H.E.S.S. analysis for the source states. Eq. 4.7 defines the model used by H.E.S.S. analysis to fit the simulated PSF and Tab. 4.2 defines the source states.

described in Sec. 2.3.5[73]. As part of the systematic uncertainties studies, I also analyzed the data without the convolution in App. B.2 and obtained similar results.

The same initial conditions for the fit algorithm are set for the point-like and Gaussian models. The background amplitude B in Eq. 4.5 and Eq. 4.6 shall be fixed, such that the background does not vary from one model to the other, but it is fixed to the level derived from the H.E.S.S. background estimation. The effective area amplitude E is also fixed since it only depends on the observational time and acceptance and not on the morphological model. The center position of the point-like and the Gaussian models and the amplitude of the morphological model C_0 are free to vary. The Region Of Interest (ROI) is defined as the region within a circle of radius 0.5° from the source position. This size is large enough to encompass a potential intrinsically extended emission convolved with the PSF (see the same region in Fig. 4.5). The ROI consists of a total of 7845 pixels since the resolution of the H.E.S.S. sky maps is set to 0.01° per pixel. The fit d.o.f. is given by the difference between the number of the pixels (7845) and free parameters. While the point-like model has three free parameters, the Gaussian model has four. Finally, with the initial conditions set up, the optimization method searches for the best parameters to fit the H.E.S.S. data according to the defined morphological model. The best fit is given by the lowest TS.

The Cash Statistic cannot directly assign the goodness of fit as the χ^2_{ndf} would do in the χ^2 statistic. To quantify how much better one model is in comparison to the other, Wilks' theorem[148] is invoked. The theorem says, if a given variable is distributed in a large sample according to a probability function, under the assumption of a hypothesis H_0, C (Eq. 4.2) is distributed as a χ^2 with $h - m$ d.o.f., where h and m are the number of free parameters of H_1 and H_0, respectively. The difference between the TS between both morphological models is calculated according to:

$$\Delta TS = C_{H_0} - C_{H_1}, \tag{4.8}$$

where C_{H_0} is the TS from the null hypothesis and C_{H_1} is the TS from the alternative hypothesis. Given that the conditions for the Wilks' theorem are satisfied,[148] the p-value is calculated according to:

$$p = 1 - \frac{\gamma(\Delta TS/2, \lambda/2)}{\Gamma(\Delta TS/2)}, \tag{4.9}$$

where γ is the lower incomplete gamma function, $\lambda = |h - m|$ is the difference of the number of free parameters, and Γ is the gamma function.

The p-value p, which represents the chance probability that ΔTS is due to a random fluctuation, can still be numerically calculated in terms of significance by using the inverse of the complementary error function $\mathrm{erf_c^{-1}}$, defined according to:

$$\begin{aligned} S &= \mathrm{erf_c^{-1}}(p), \\ p &= \mathrm{erf_c}(S) \end{aligned} \tag{4.10}$$

where $\mathrm{erf_c}(S)$ is the complementary of the error function $\mathrm{erf}(S)$, which is given by:

$$\mathrm{erf_c}(S) = 1 - \mathrm{erf}(S) = \frac{2}{\sqrt{\pi}} \int_S^\infty e^{-t^2} dt. \tag{4.11}$$

Equations 4.8 to 4.11 are only valid when the alternative model has more free parameters than the null hypothesis, i.e. fewer d.o.f., and it improves the fit ($C_{H_1} \leq C_{H_0}$). This condition is obvious for alternative models that can asymptotically approximate the null hypothesis model through one of its parameters. For example, a 2D symmetrical Gaussian approximates a point-like model when its width asymptotically approximates zero.

The significance S from Eq. 4.10 is the final statement of whether one morphology model is preferred in comparison to the null hypothesis. If S>5, the alternative model is significantly preferred over the null hypothesis.

I tested the morphology fit algorithm on H.E.S.S. observations of the Crab Nebula and compare the fit results with the published gamma-ray extension from Abdalla et al. (2020)[73]. The results of the Crab extension are compatible with the published results as shown in App. B.4.

4.3.2. Results of the gamma-ray extension studies

I applied the morphology fit algorithm from Sec. 4.3.1 to the gamma-ray emission of M87 in the different source states. In App. B I conducted extensive systematic tests to validate the stability of the extension fit results. The tests show the stability of the morphology results regarding

State	Point-like model		
	RA (°)	**DEC (°)**	**Ampl. (a.u.)**
Low	187.711±0.003	12.398±0.003	3.6±0.2
Intermediate	187.707±0.005	12.395±0.005	4.0 ±0.4
High	187.705±0.002	12.397±0.002	9.8±0.6

Table 4.5.: The best-fit parameters for the source states for point-like model. $1\,\sigma$ statistical errors are given in brackets and the states are defined in Tab. 4.2. The amplitude is given in arbitrary units (a.u.), since the PSF is normalized to 1.

State	Symmetrical Gaussian model			
	RA(°)	**DEC (°)**	**Ampl. (a.u.)**	**FWHM (°)**
Low	187.711±0.002	$12.397^{+0.003}_{-0.002}$	9^{+59}_{-8}	$0.008^{+0.010}_{-0.001}$
Intermediate	187.706±0.005	12.395±0.005	$0.2^{+0.4}_{-0.1}$	$0.04^{+0.01}_{-0.02}$
High	187.705±0.003	12.397±0.003	3^{+68}_{-2}	0.02±0.01

Table 4.6.: The best-fit parameters for the source states for the symmetrical Gaussian model. $1\,\sigma$ statistical errors are given in brackets and the states are defined in Tab. 4.2. For comparison, the SMBH is located at RA = 187.7059, DEC = 12.3911[149].

changes in the maximum zenith angle of observation, the energy threshold, and the systematic uncertainties in the pointing precision of the H.E.S.S. telescopes.

The best-fit parameters for both source states and morphological models are shown in Tab. 4.5 and 4.6. The statistics of the fit and the significance of the symmetrical Gaussian in comparison to the point-like model are given in Tab. 4.7. Detailed information on the residuals is given in App. B.1.

The results of the morphology fit show that the Gaussian model is not preferred over the point-like model in any of the source state morphology; therefore, no indication of an extension was found. The best-fit position of the point-like model from the gamma-ray emission of the different source states is consistent with each other and with M87 's core within the statistical uncertainties.

The best FWHM extension (0.008°) of the Gaussian model in the low state might indicate at a first glimpse a significant extension. However, since the bin size of the H.E.S.S. sky maps is 0.01°, the optimization method is not able to scan the width for values lower than the resolution of the maps; therefore, the FWHM width lower boundary is not to be taken into account. On the other hand, the upper statistical error on the FWHM width is at the level of the H.E.S.S. sky map resolution, hence, describes correctly the $1\,\sigma$ standard deviation from the best FWHM. The amplitude of the Gaussian models indicates how sharp the intrinsic distribution is. After the

	Point-like		Symmetrical Gaussian		Comparison	
	Final stat.		**Final stat.**	**d.o.f.**	**ΔTS**	**Signif.(σ)**
Low	-130038.1	7842	-130037.5	7841	-0.6	-
Intermediate	10774.2	7842	10771.5	7841	2.7	1.6
High	10147.1	7842	10146.7	7841	0.4	0.6

Table 4.7.: Fit statistics for the source states for the two emission models: point-like and symmetrical Gaussian model. The Final Cash statistic and the d.o.f. of each model are given. The lower the Final statistic, the better the fit is, which explains the negative value in the low state, where a larger data-set is available (Tab. 4.3). The ΔTS must be positive such that Eq. 4.9 can be used. The states are defined in Tab. 4.2.

convolution of a Gaussian distribution with the PSF, the distribution width broadens, although the integrated counts remain the same. Therefore, for Gaussian distributions with small FWHM width, the Gaussian amplitude is higher to maintain the integrated intensity at the same level of the H.E.S.S. sky map. The amplitude of the Gaussian models for the low and high states have very large statistical uncertainties due to the effect of the convolution of a sharp Gaussian distribution with the PSF.

The slightly worse TS found in the Gaussian model in comparison to the point-like model (Tab. 4.7) is an effect of the mathematical nature of the functions used in the morphological model. While the point-like model (PSF function) only varies its position and amplitude, the Gaussian model is also described by its extension, which is limited to the resolution of the H.E.S.S. sky maps. This limitation prevents the fit algorithm from exploring the region where the extension is smaller than 0.01°.

As part of the systematic studies, I conducted in App. B.3 a morphology fit of the M87's gamma-ray emission when the position of the models are fixed to the SMBH position. The results showed an agreement of the point-like with the Gaussian best-fit parameters ($\Delta TS = 0$), indicating no sign for extended emission.

The more excess counts available (see Tab. 4.3), the smaller are the uncertainties in the FWHM estimation. However, none of the source states showed a width significantly larger than zero. Interestingly, the significance of the Gaussian model in comparison to the point-like model in the intermediate state is $1.6\,\sigma$, which could be an indication of statistic fluctuations or a hint for different emission regions, which comprises the intermediate source state from different periods of observation. Therefore, I conducted a separate analysis in App. C looking at the best-fit position of individual flares. The results showed it was not possible to distinguish different emission regions due to the low event statistics, and consequently, higher statistical uncertainties in the source position fit.

Although no extension has been found in the gamma-ray emission of M87's low state, an extension UL can be derived and constrain the cosmic-ray pressure, based on assumed cosmic rays and target gas distributions. With 99.7% c.l., the UL on the extension is estimated through:

$$\sigma_{\mathrm{G,UL}} = \sigma_{\mathrm{G}} + 3\Delta\sigma_{G}^{+}, \tag{4.12}$$

where $\sigma_{\mathrm{G,UL}}$ is the UL on the best Gaussian σ_{G} extension with 99.7% c.l. and $\Delta\sigma_{\mathrm{G}^+}$ is the $1\,\sigma$ upper boundary of the statistical uncertainty on the Gaussian σ_{G} extension. The Gaussian FWHM extension can be converted to the more commonly used σ_{G} following:

$$\sigma_{\mathrm{G}} = \frac{FWHM}{2\sqrt{2ln2}}. \tag{4.13}$$

Therefore, I estimated the extension UL from the H.E.S.S. measurements using the results from Tab. 4.6, Eq. 4.12 and 4.13. The UL can be expressed in degree (or conveniently mdeg) as well as in kpc by considering the distance from Earth to M87 ($d_{\mathrm{M87}} = 16.5\,\mathrm{Mpc}$)[15,16]:

$$\sigma_{\mathrm{G,UL}}[\mathrm{kpc}] = \arctan(\sigma_{\mathrm{G,UL}}[^{\circ}]) \times d_{\mathrm{M87}}[\mathrm{kpc}]. \tag{4.14}$$

The results for the UL are shown in Tab. 4.8 for the different source states and in Fig. 4.6 with the 90 cm radio contours from VLA[113]. Previous results were: 50 mdeg from H.E.S.S.[102] in 2006, 75 mdeg from VERITAS[123] in 2008, and 42 mdeg from MAGIC[120] in 2020. While the H.E.S.S. results from 2006 and the VERITAS results from 2008 considered the entire dataset with no separation of source state, MAGIC[120] analyzed only observations during the low state. The low state is defined in Acciari et al. (2020)[120] as the flux up to 10% of the Crab Unit (CU), where $1\,\mathrm{CU} = 5.6 \times 10^{-11}\,\mathrm{cm^{-2}\,s^{-1}}$ in the energy range 400 GeV-1 TeV[124]. The MAGIC low state corresponds, for a light curve with a bin size of 20 days[120], to flux states below $\approx 5.6 \times 10^{-12}\,\mathrm{cm^{-2}\,s^{-1}}$ within the same energy range, while my definition of M87's low state corresponds to flux states below $\approx 1.8 \times 10^{-12}\,\mathrm{cm^{-2}\,s^{-1}}$ for energies above 300 GeV in a 30 days binned light curve (Fig. 4.4). Since the H.E.S.S. low state corresponds to lower fluxes than the MAGIC definition, the H.E.S.S. extension limit derived in this work is stricter than the MAGIC result. I improved the best limit on the Gaussian extension of the M87's gamma-ray low state emission in this study from 42 mdeg to 16 mdeg. The ULs for the intermediate and high states are directly influenced by the amount of data available. The comparison of the UL results shown in Tab. 4.2 with the excess counts in Tab. 4.7 indicates an inverse correlation, i.e. the more excess events are detected from one source state, the smaller (better) is the upper limit on the emission extension.

Figure 4.6 also shows the best-fit position of the point-like model with the error bars accounting

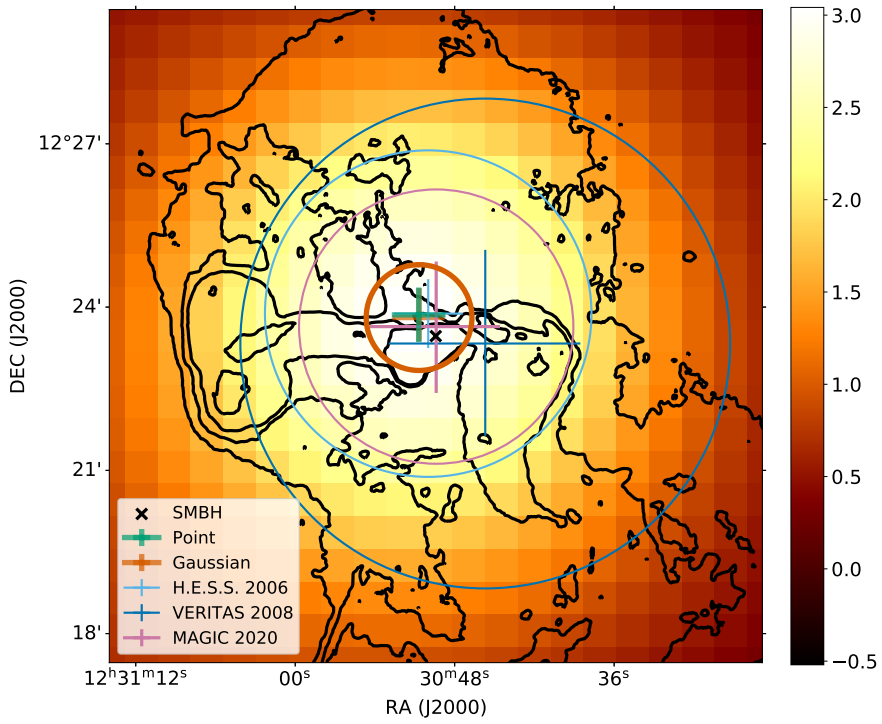

Figure 4.6.: H.E.S.S. low state excess counts with the derived UL plotted alongside previous results for the UL and the radio contour from VLA 90cm[113]. The H.E.S.S. map is smoothed with a Gaussian FWHM with width 0.05°. The best-fit position is shown for the point-like model and the Symmetrical Gaussian with its 99.7% c.l. UL. Error bars in the position include the $1\,\sigma$ statistical uncertainty from the fit and $20''$ systematic uncertainty. The best-fit position of the point-like model and the Gaussian model are consistent with each other and with M87's core, and they are in agreement with previous results.

for the 99.7% c.l. statistical uncertainties and the $20''$ from the systematic uncertainties. Based on the extension UL and the uncertainties in the best-fit position, the large-scale ($\approx 80\,\mathrm{kpc}$) radio lobes[96], seen on the east (left) and north of the SMBH, can be for the first time significantly excluded as the main sources of the gamma-ray emission in M87's low state.

Figure 4.7 summarizes the results of the current analysis on M87 , the sanity check on H.E.S.S. observations of the Crab nebula (App. B.4), and the latest morphology results. The 99.7% c.l.

State	$3\,\sigma$ UL (mdeg)	$3\,\sigma$ UL (kpc)
Low	16.2	4.6
Intermediate	36.0	10.3
High	22.3	6.4

Table 4.8.: Results of the estimated UL with 99.7% c.l. of the σ extension for the source states. The UL is given both in units of mdeg and in kpc by considering the distance from Earth to M87.

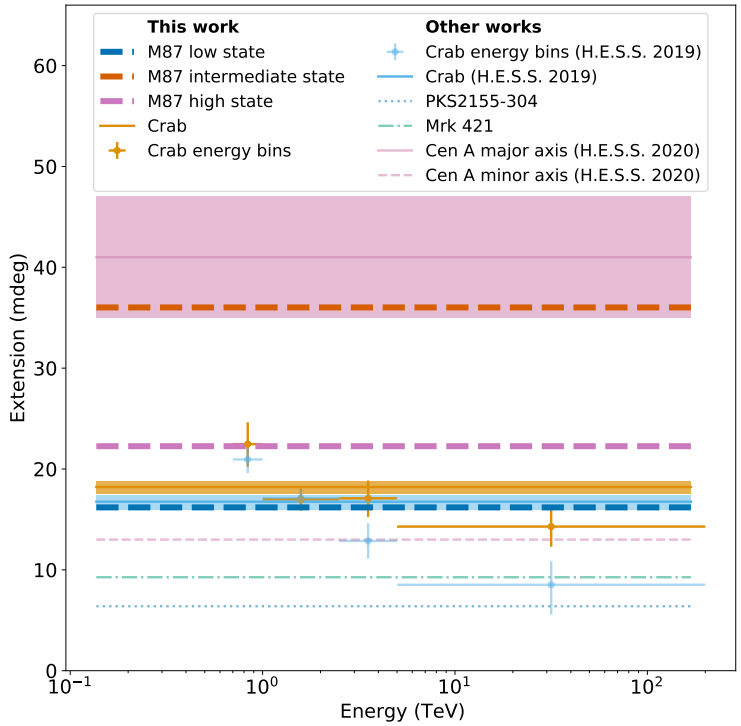

Figure 4.7.: Gaussian σ extension is shown for Centaurus A[74], Crab[73], and Crab (this work). ULs are shown for M87's low, intermediate and high state(this work), PKS2155 and Mkr421 as a sanity check conducted for the Crab publication[73]. Dashed, dashed-dotted and dotted lines represent 99.7% c.l. ULs, while solid lines are significant Gaussian $1\,\sigma$ extensions.

ULs resulting from this work are shown in dashed lines. The results of the H.E.S.S. observations of the Crab nebula are in good agreement with the results from Abdalla et al. (2020)[73].

The energy-dependent gamma-ray morphology of the Crab nebula was obtained from private communication with the corresponding authors from Abdalla et al. (2020)[73], since they were not published in the article with the integrated gamma-ray extension. As a sanity check, Fig. 4.7 also shows the ULs on the gamma-ray extension from PKS 2155−304 and Mrk421, extracted from Abdalla et al.(2020)[73], since distant AGNs are used as calibration tools as no extension is expected from them[150]. The extension UL given by distant AGNs, which are well covered by H.E.S.S. observations throughout time, indicate how small the extension UL can be probed by the H.E.S.S. telescopes for a substantial amount of data ($\gtrsim 500\,\mathrm{h}$). The results for the recently discovered Centaurus A gamma-ray extension[74] (major and minor axes) are also shown for comparison. $1\,\sigma$ statistical errors are presented for the energy bins as error bars and the energy-integrated extension as a filled region.

The good agreement between the Crab results from the publication and the analysis in this work increases the reliability of the M87's gamma-ray morphology results, which were derived based on the same procedure. The gamma-ray extension UL from the AGN PKS −2155 shown in Fig. 4.7 reaches $\approx 8\,\mathrm{mdeg}$ for a data-set of $\sim 1000\,\mathrm{h}$ of observation, which indicates that with more data, the UL of the M87's gamma-ray low state could still be improved by a factor of 2.

4.3.3. The origin of the VHE gamma-ray emission from M87's low state

In order to understand better the origin of the gamma-ray emission from M87, I compared the results to the radio morphology at 21.4 cm measured by VLA[151]. The radio emission traces non-thermal electrons and is, hence, indicative of the presence and distribution of accelerated particles outside the jet. The radio emission can be interpreted as the synchrotron emission from old cooled electrons (with an age of $\sim 10\,\mathrm{Myr}$)[140].

I used the same strategy adopted in Abdalla et al. (2020)[74] for comparing the radio and the gamma-ray emission. The VLA 21.4 cm radio emission[151] traces the electrons in the inner radio cocoon (see the central $1''$ in Fig. 4.6) and is convolved to the H.E.S.S. PSF to yield Fig. 4.8, where the radio emission is put into perspective with the H.E.S.S. extension UL. The extension UL contains the entire radio cocoon, which indicates that this region is still a candidate for the origin of the M87's low state gamma-ray emission. Since the maximum allowed size for the VHE low state emission is only slightly larger than the radio cocoon, further H.E.S.S. observations could probe the inner radio cocoon as the origin of the VHE gamma-ray emission.

Given the slight difference of $31''$ ($\approx 2.4\,\mathrm{kpc}$) between the best-fit position of the gamma-ray emission and the SMBH, I investigated its origin by exploring the parameter surface of the best-fit position. The conclusion is that this deviation is not significant, as Fig 4.9 shows. The best-fit position of the point-like model for all three states is within $3\,\sigma$ coincident with the radio

center, where the central SMBH is located. The intermediate state best-fit position is the closest to the radio center but also the result with the largest uncertainty due to limited statistics (Tab. 4.7). The low state best-fit position is located about $3\,\sigma$ from the radio center, which could hint at a different emission region or simply an effect of the systematic and statistical uncertainties.

Regarding the optical emission of M87, there is no definition for the boundaries of a galaxy. However, the size of a galaxy is normally given by the optical half-light radius of the stars $R_{1/2}$, i.e., the radius which contains half of the star optical luminosity. For M87 it is estimated to be $R_{1/2} \approx 7.2\,\mathrm{kpc}$[152]. According to the uncertainties of the best fit position (Tab. 4.6) and the

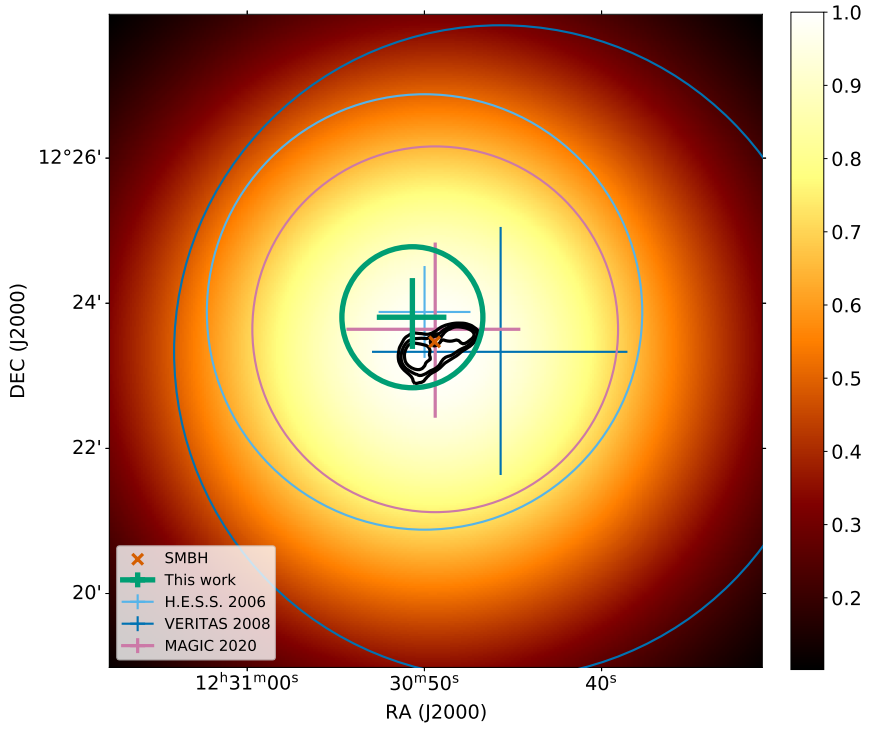

Figure 4.8.: H.E.S.S. extension UL of M87's low state compared with radio VLA 21.4 cm contours. The color map is the linear intensity of the radio emission at 21.4 cm convolved with the H.E.S.S. PSF 68% c.r. given in arbitrary units (normalized) and the contours in black show the original radio VLA 21.4 cm image highlighting the central radio cocoon. The improved UL on the gamma-ray extension of M87's low state resulted from this work and other works are also shown.

derived 99.7% c.l. extension UL from this work of 4.6 kpc (Tab. 4.8), the H.E.S.S. observations are probing already the inner-most part of the Virgo Cluster on the edges of the elliptical galaxy as shown in Fig. 4.10.

To summarize, the origin of M87's gamma-ray emission of the different source states is compatible with each other and with the SMBH. The intrinsic emission can not be resolved in TeV gamma rays, though the inner radio cocoon is not excluded as a possible origin of the emission from M87's low state. On the other hand, the large-scale radio lobes (≈ 80 kpc) are excluded as the main source of the gamma-ray emission from M87's low state. The inner jet ($\lesssim 1$ kpc) and the X-ray knots could also be the origin of the M87's gamma-ray low state emission. However, due to the limited angular resolution, IACTs are not sensitive to probe the morphology at the sub-kpc scale at the distance of 16.5 Mpc. From previous results, the VHE emission of the low state can not be originated from within the EHT region ($10\ r_g \approx 0.003$ pc)[114]. A second exclusion comes from this thesis, where the extension is constrained to be smaller than 4.6 kpc (Tab. 4.8). Figure 4.11 summarizes the scales of some known structures in M87 and the extension UL. In the next section, the origin of the low state emission is investigated based on the spectral information of the source.

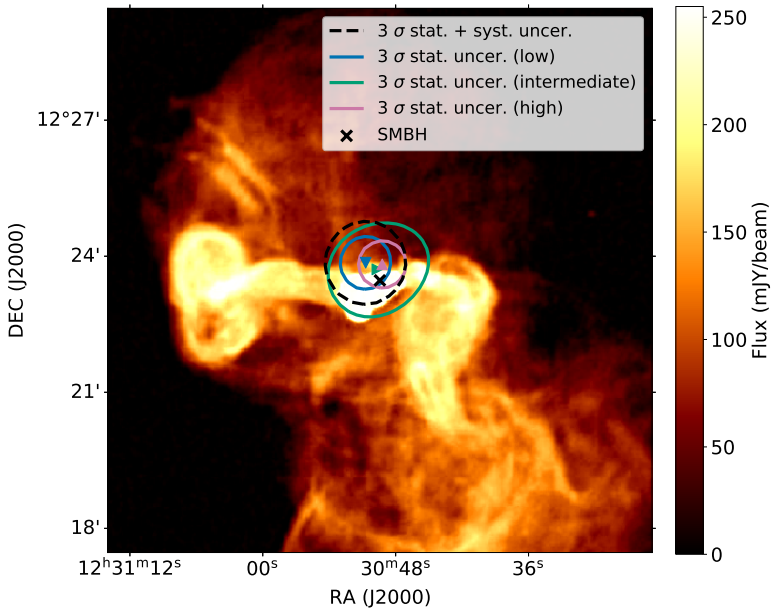

Figure 4.9.: The best position for the point-like model both for low, intermediate and high states compared to the shape of the radio map from VLA 90 cm[113]. The contours are $3\,\sigma$ statistical uncertainties. A black dashed-dotted line adds the systematic uncertainty to the best fit position of the low state. The SMBH (M87's radio center) is given by the black cross[149].

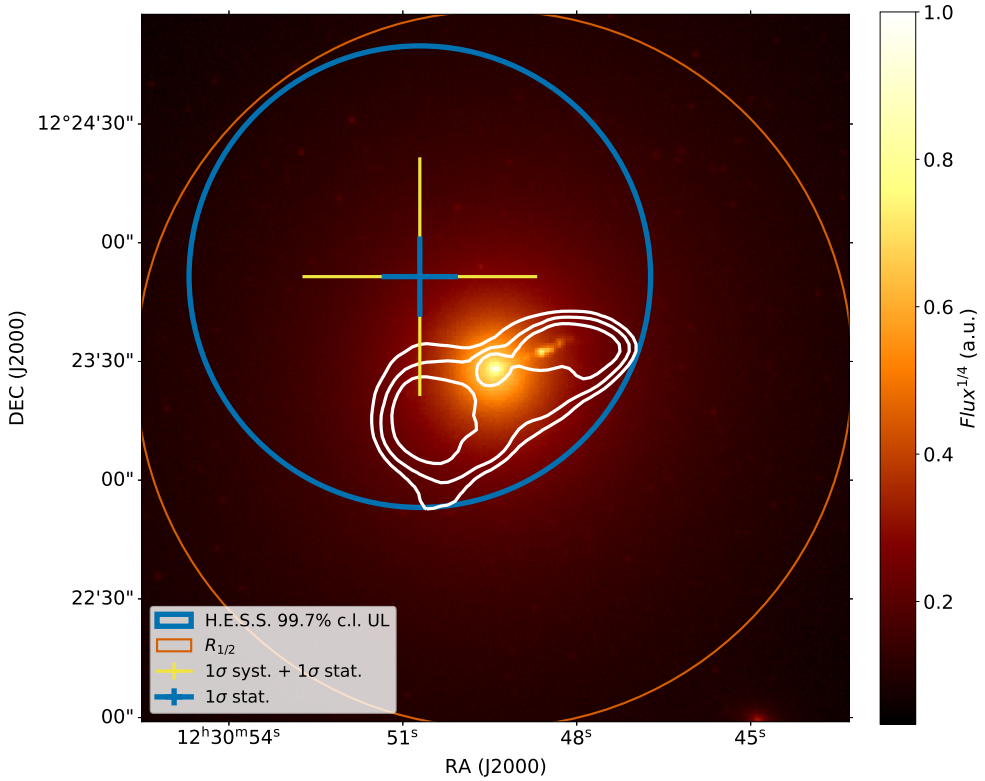

Figure 4.10.: The 99.7% c.l. extension UL of the M87's low-state gamma-ray emission is shown in blue with the $1\,\sigma$ uncertainties in the best fit position and in yellow considering, in addition, the systematic uncertainties. The results are put into perspective with optical emission of M87 from SDSSg (646 THz) displayed, for better vizualization, as the intensity to the power of 1/4, in arbitrary units. The half-light radius of stars ($R_{1/2} = 7.2\,\mathrm{kpc}$) and the VLA 21.4 cm radio contours overlaid in white are also shown.

4.4. Spectral energy distribution (SED)

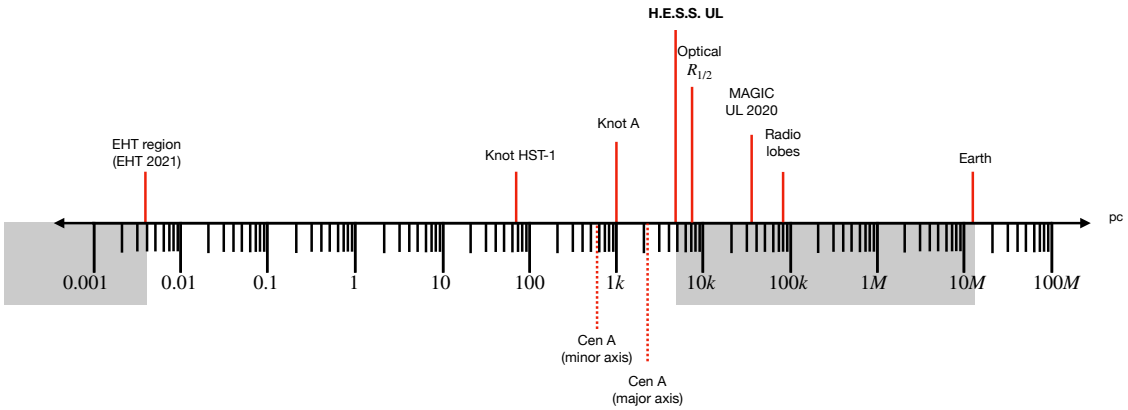

Figure 4.11.: Physical scales and prominent (jet) components in M87 in a logarithm scale with the exclusion region shaded in gray. The measured extension from Centaurus A is also shown for comparison[74]. The half-light radius of the stars $R_{1/2} \approx 7.2\,\mathrm{kpc}$[152] and the dimension scale of the radio lobes are also shown.

The morphology studies of M87's gamma-ray low state emission constrained the size of the emission, although it could not pinpoint the origin of the VHE emission. Therefore, investigating the spectral shape of the emitted radiation is an alternative to constrain the origin of the gamma-ray emission.

Recently, MWL observations have confirmed that a single emission region in the inner core region is not able to describe the entire SED of the M87's emission since the gamma-ray component is significantly underestimated in this model[114]. Therefore, Algaba et al.(2021)[114] interprets the gamma-ray emission as originating from outside the EHT core region, where the core region is defined as $R{<}10r_g \approx 10^{16}\,\mathrm{cm} \approx 3.2 \times 10^{-3}\,\mathrm{pc}$, where r_g is the gyro-radius of the magnetic field in the vicinities of the SMBH. Several models have been proposed earlier to explain the gamma-ray emission within a leptonic scenario. For instance, Acciari et al. (2008)[123] explains the TeV emission from electrons at the large-scale jet or the HST-1 knot with a large particle dominance in the emission region.

As discussed in Sec. 3.5 and shown in Tab. 3.1, M87's core, the jet and the HST-1 are expected to contribute to the hard X-ray emission from M87 with an overall predicted flux of $7.7 \times 10^{-13}\,\mathrm{erg\,cm^{-2}\,s^{-1}}$ and the spectral index of $2.12^{+0.12}_{-0.13}$[82]. Approximately 60% of the hard X-ray flux is expected to come from the core with a spectral index of $2.11^{+0.15}_{-0.11}$. At the same time, the jet contributes with 23% of the emission and a spectral index of $2.36^{+0.16}_{-0.17}$ and the HST-1 knot with 9% and a spectral index of 1.94, fixed to Chandra's measurements only[82].

Within a leptonic scenario, the relativistic electrons that emit the synchrotron X rays will also produce VHE gamma rays through IC scattering. Therefore, a one-zone model is applied to perform a joint-fit to the H.E.S.S. low state gamma-ray emission with the hard X-ray data of the core from NuSTAR and the Fermi-LAT gamma rays[114]. The objective of the fit is not to find a unique solution to explain the high energy spectrum of M87 but to probe if one single zone model can describe it and what are the implications of the model. The C++/Python open-source GAMERA[98] package was used for the modeling and the SciPy package to fit the data[130]. A PL gives the electron distribution function:

$$\frac{dN}{dE} = N_0 \left(\frac{E}{E_0}\right)^{-\alpha}, \tag{4.15}$$

where α is the spectral index. The total energy E_{T} is given by the integration of EdN/dE and is a free parameter:

$$E_T = \int_{E_{\min}}^{E_{\max}} dE E N_0 \left(\frac{E}{E_0}\right)^{-\alpha}. \tag{4.16}$$

The Chandra, NuSTAR and Fermi-LAT data were extracted from Tab. A8 of Algaba et al. (2021)[114]. The data correspond to the EHT observations of M87 in April 2017, when the source was in a very low state throughout the entire wavelength range. The Chandra data were not included in the fit but used as an UL for the model since the model does not consider the thermal emission from the electrons, expected to dominate in soft X ray. The entire H.E.S.S. low state data (Bayesian Blocks 0, 4, 6, see Sec. 4.2) is used and is not limited to the simultaneous data taken in 2017 as in Algaba et al. (2021)[114]. The advantage of using a larger data set is to obtain better statistical uncertainties of the flux estimation and, consequently, the spectral fit parameters. Nevertheless, it comes at the expense of including some of the variable emissions into the low state data-set, which might influence the spectral fit slightly, though at an acceptable level. The spectral index of the relativistic electron distribution is fixed to $\Gamma = 3.03$, as found in Algaba et al. (2021)[114] for the model focused on the high energy part of the SED. The assumed electron spectral index of $\Gamma = 3.03$ assures that the model perfectly matches the spectral index of the detected NuSTAR synchrotron flux. The total energy store in the relativistic electrons E, the electrons threshold energy $E_{\min}$, and the electron maximum energy $E_{\max}$ are free parameters. The size of the emission region is fixed to $626 r_g \approx 0.2\,\mathrm{pc}$, which is the size encountered by the best fit in Algaba et al. (2021)[114].

Considering the case of SSC model, where the relativistic electrons up-scatter the synchrotron photons, the best fit for the X-ray and gamma-ray range (Nustar, Fermi, and H.E.S.S. data) is shown in Fig. 4.12 with the parameters in Tab. 4.9. The fit describes the data very well,

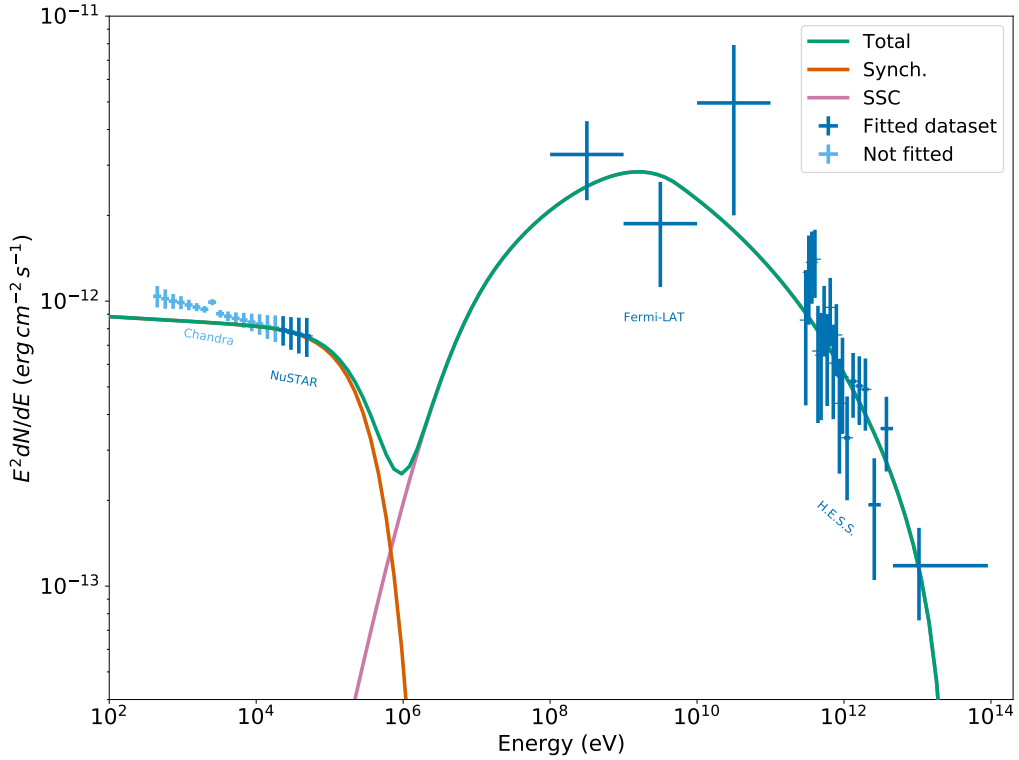

Figure 4.12.: SED for the SSC model of a population of relativistic electrons fitted to the M87's low state X-ray and gamma-ray data (Chandra, NuSTAR, Fermi-LAT and H.E.S.S.)[114].

although it shows some level of degeneracy. The size of the emission region can be increased while the energy stored in particles and the magnetic field decrease for the same fit statistic. The magnetic field of $B \approx 5\,\mathrm{mG}$ is of the same order of magnitude of the estimate from Algaba et al. (2021)[114] and from Acciari et al. (2020)[120]. The magnetic potential energy of $E_B = B^2/8\pi \approx 2.3 \times 10^{47}\,\mathrm{erg}$ yields a ratio of the particle to the magnetic energy of $\sim 10^5$, which indicates a particle dominance in the emission region, in agreement with the previous estimate from MAGIC[120].

The contributions of the IC emission based on the interactions of the relativistic electrons with the IR photon field from the stars and CMB radiation were also estimated and found to be three orders of magnitude smaller than the SSC component. Therefore, those contributions were not included in the final results.

The single-zone SSC model describes very well the observed hard X-ray and gamma-ray emission. Therefore, a single zone region can describe the observations at these wavelengths. It is possible that the inner and outer jet and the HST -1 knot also contribute up to a certain

Parameter	Value
$E_{\rm p}$(erg)	$(1.1^{+14}_{-0.6}) \times 10^{53}$
$E_{\rm min}$(GeV)	$5.2^{+4.8}_{-2.5}$
$E_{\rm max}$(TeV)	31.7^{+30}_{-15}
B (mG)	$5.0^{+1.0}_{-1.0}$

Table 4.9.: Best fit parameters of the SSC model fitted with the M87's low state X-ray and gamma-ray data, as shown in Fig. 4.12.

level to the VHE emission, as in soft X rays. However, a large number of free parameters in multi-zone models and, consequently, their degeneracies complicate the search for a solid and unique solution for the origin of the gamma-ray emission in M87.

Two regions are already probed as the main source of the M87's VHE low state emission: the core region where $R<10r_g \approx 0.003\,$pc, probed by EHT observations from 2017[114], is likely not the main component of the emission; and the region $R>4.6\,$kpc is excluded by the H.E.S.S. extension UL (Tab. 4.8). The region between these limits includes the inner jet ($R \sim 1\,$pc), HST -1 knot ($R \approx 67\,$pc), other X-ray knots ($R<1\,$kpc), the outer jet ($R \lesssim 1\,$kpc) and the radio cocoon seen with VLA 21.4 cm ($R \approx 4\,$kpc, see contours in Fig. 4.9). Furthermore, the gamma-ray emission can arise from the interactions of the relativistic protons with the ICM at kpc-scale as it is investigated in the next section.

4.5. Hadronic model for the M87's low state emission

As discussed in the introduction of the chapter and Sec. 3.3, the streaming of relativistic protons from the M87's core region towards the ICM and the thermal emission by the hot cluster plasma transfer energy to the ICM and might be responsible for their heating. The heating of the ICM prevents the matter from falling towards the cluster center and could explain the low star formation rate seen in the center of the Virgo Cluster[21]. The relativistic protons accelerated in the vicinity of the SMBH may escape the influence of the galaxy magnetic field with sufficient energy to interact through proton-proton collision with the gas in the ICM. Charged and neutral pions are produced, which decay to electrons/positrons and gamma rays, respectively. The gamma rays can be detected at Earth, given that the relativistic protons carry sufficient energy. The protons accelerated in the jet exert a pressure ($P_{\rm CR}$) into the ICM, which is used to estimate the number of relativistic protons in the system. The cosmic-ray pressure can be expressed as function of the thermal pressure ($P_{\rm th.}$) exerted by the local hot plasma as $X_{\rm CR} = P_{\rm CR}/P_{\rm th.}$. Jacob & Pfrommer (2017)[21,110] propose a steady-state solution, in which the cosmic-rays heat the ambient matter at the same level as the matter cools down due to radiative losses. The

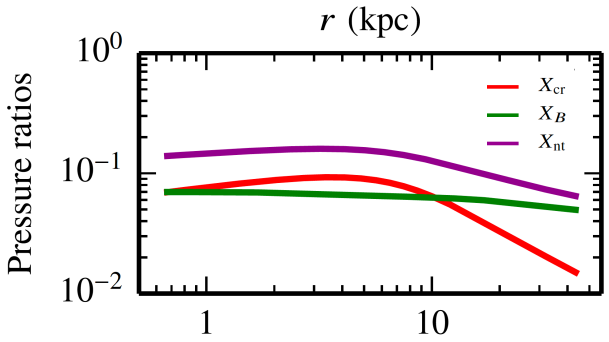

Figure 4.13.: Ratios of CR-to-thermal pressure $X_{\rm CR}$, magnetic-to-thermal pressure $X_{\rm B}$, and the total non-thermal-to-thermal pressure $X_{\rm NT}$ as a function of distance from the cluster center. Extracted from Jacob & Pfrommer (2017)[21].

equilibrium between cooling and heating rates is assumed regardless of the distance from the cluster core. The model assumes a relativistic population of protons that follows a power-law in energy with proton spectral index[2] $\Gamma_p = 2.26$, and energy threshold of $0.5 m_{\rm p} c^2$, where $m_{\rm p}$ is the proton mass and c is the speed of light. Energy equipartition between particles and the magnetic field is also assumed in the model. The energy equipartition is a valuable argument, expected to be true at sites further away from the injection region, although the argument is not a necessary condition for the balance between the heating and cooling processes.

Thermal X-ray observations from the ACCEPT[111] provide a good estimate on the free electron and their temperature distributions in the Virgo Cluster[21] (Sec. 3.3). The ICM is assumed to be composed of 70% hydrogen, 28% helium, and 2% of heavier elements. Since the matter is neutral and in a plasma state, the mean molecular weight per free electron is $\mu_e = 1.19$ for the assumed composition. Therefore, based on the free electron distribution and the mean molecular weight per free electron, the ICM radial distribution is derived. Moreover, the temperature of the cluster plasma follows the distribution of the temperature of the free electrons.

Jacob & Pfrommer (2017)[21,110] considers the estimated ICM and temperature distributions, the cross-section of the p−p interaction and the assumed relativistic proton distribution to estimate the cosmic-ray pressure ratio $X_{\rm CR}$. The parameters of the proton distribution are adjusted until the equilibrium between the steady state is reached. The cooling rate is also estimated based on the ICM thermal emission, given by the X-ray emission from ACCEPT[111]. The result, from Jacob & Pfrommer (2017)[21], is the $X_{\rm CR}$ distribution as function of the distance from the cluster core as seen in Fig. 4.13.

[2]Jacob & Pfrommer (2017) [21] consider $\alpha_p = 2.4$ and in a following publication, Pfrommer (2018) [140] uses α=2.26, which is derived from the joint-fit of Fermi-LAT and H.E.S.S. spectra.

Based on the cosmic-ray pressure ratio $X_{\rm CR}$, the radial profile of the expected π^0 decay, and, consequently, the radial gamma-ray distribution can be derived. I used the equations from App. B.2 of Jacob & Pfrommer (2017)[110] to, first derive the gamma-ray radial distribution and integrate it in the energy range between 300 GeV and 200 TeV, where the H.E.S.S. telescopes are most sensitive. I described the procedure more details in App. A.1. I then used the radial distribution of gamma rays to produce a 3D profile of the gamma-ray emission, assuming an isotropic distribution. Afterward, I integrated the 3D distribution along the line of sight to derive the 2D template of the gamma-ray emission, as described in detail in App. A.2. Figure 4.14 shows the resulted 2D template for the gamma-ray emission from π^0 decay and the contours of radio emission from the VLA 21.4 cm[151] for comparison. The radio emission traces the distribution of the relativistic electrons. Meanwhile, the hadronic model assumes an isotropically distributed relativistic proton distribution. This assumption is an approximation since we do not have any direct information about the proton distribution in the cluster core. A more sophisticated alternative approach, not pursued in this work, would be to assume that the relativistic protons are distributed in the same way as the relativistic electrons, and the radio contours would give the shape of the distribution.

The spherical integration of the radial gamma-ray distribution up to 30 kpc from the core yields the total gamma rays produced in the source per unit time. Considering the distance from M87 to Earth, I calculated the total total gamma-ray flux at Earth due to this hadronic model to be $1.76 \times 10^{-13}\,{\rm cm}^{-2}\,{\rm s}^{-1}$, which represents $\approx 10\%$ of the H.E.S.S. low state gamma-ray flux (Tab. 4.3). Details of the integration are given in App. A.2.

Based on the emission template derived in App. A.1 for the hadronic emission, I defined a set of three models with increasing levels of complexity. The first model is the template for the extended (diffuse) emission to the low state, representing the case in which the entire emission is described by the gamma rays from the π^0 decay. The only free parameter is the amplitude of the template emission. The second model is a hybrid model composed of the diffuse and a point-like component centered at the M87's core (RA = 187.7059°, DEC = 12.3911°). The point-like component is motivated by the emission from the core, inner jet, or any source of gamma rays below the resolution of the H.E.S.S. telescopes, centered at M87. Since the center is fixed for the point-like component, the template amplitude and the point-like model amplitude are the only free parameters. Finally, a second hybrid model, in which the point-like model is free to vary, is motivated by the emission originating from a region further down the jet. In this case, there are four free parameters: template amplitude, RA and DEC position of the point-like model and its amplitude. I applied the same fit algorithm from Sec. 4.3.1 to fit the morphology of the set of three models. The results are shown in Sec. 4.5.1, Sec. 4.5.2 and Sec. 4.5.3 for the template (diffuse emission) and the hybrid models.

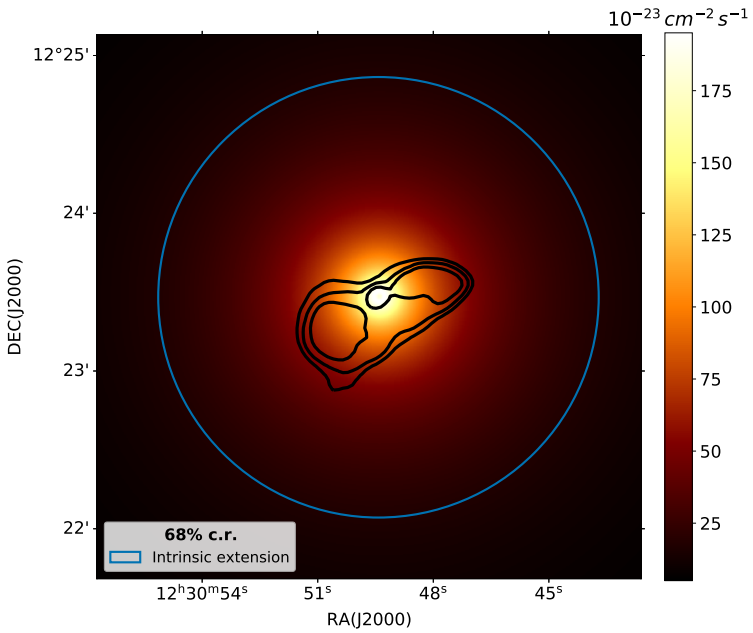

Figure 4.14.: 2D template for the gamma-ray emission resulted from π^0 decay in the Virgo Cluster according to the steady state model[21,110] and the 68% c.r. showing the predicted intrinsic extension of $0.024° \approx 6.7\,\mathrm{kpc}$. The bin size of the sky map is $\approx 0.13\,\mathrm{mdeg}$ and the values in the color bar indicates the photons produced in the source per unit area and time. The contours of the radio emission from the VLA 21.4 cm is shown in black[151]

4.5.1. Morphology fit with the hadronic model

The diffuse gamma-ray emission shown in the 2D template of Fig. 4.14 is finely binned, while the H.E.S.S. sky maps have a bin size of 0.01°. Therefore, I converted the 2D template into the shape of the typical H.E.S.S. sky map. The results are shown in Fig. 4.15 (a) for diffuse emission and Fig. 4.15 (b) for the diffuse emission convolved with the H.E.S.S. PSF.

Following the algorithm described in Sec. 4.3.1, the 2D matrix of the diffuse emission convolved with the PSF (Fig. 4.15 (b)) is inserted into Eq. 4.6 as $PSF \circledast M_{\mathrm{E}}$.

The point-like and the Gaussian models are the same as used in Sec. 4.3, defined by Eq. 4.3 and Eq. 4.5, respectively. The diffuse model is centered at the cluster core because it is supposedly the location of particle acceleration. Since the diffuse model has fewer free parameters (one) than the point-like model (three), and the symmetrical Gaussian (four), it is chosen as the

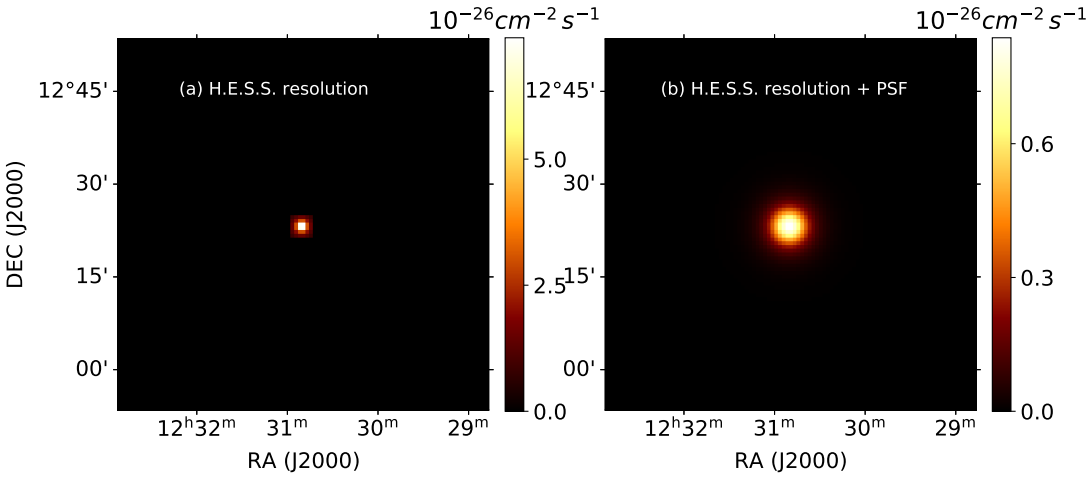

Figure 4.15.: 2D templates for the gamma-ray emitted in the source due to π^0 decay given in the typical shape of a H.E.S.S. sky map: (a) the model as derived in Fig. 4.14, though with bin size of 0.01° and (b) the template as in (a) but convolved with the H.E.S.S. PSF. The values in the color bar indicate the photons produced in the source per unit area and time.

null hypothesis. Table 4.10 shows the results of the fit of the diffuse emission and the significance of the point-like model in comparison to the diffuse model. The point-like model is preferred by more than $5\,\sigma$; therefore, the low state emission of M87 cannot be considered to originate entirely from the steady-state model. This result is already expected since the integrated gamma-ray flux from the 2D template yielded only 10% of the low state gamma-ray flux as seen with H.E.S.S.

	M87's low state		
Null hypothesis Model	**Ampl. (a.u.)**	**Final stat.**	**Signif. of the point-like model(σ)**
Steady state	4.0±0.2	-130002.6	5.6

Table 4.10.: The best fit statistics for the parameters of the steady state model fitted to the M87's low state. The null hypothesis is the template emission (1 free parameter) and the alternative model is the point-like model (3 free parameters).

4.5.2. Hybrid model: hadronic and core emission

Since the pure diffuse emission from the 2D template does not account for the entire emission of M87's gamma-ray low state, a second component is added to the model to account for the core emission. The hybrid model with a fixed center is represented by M_H and described by:

$$M_H = B + (P + PSF \circledast M_{\mathrm{E}}) \times E, \tag{4.17}$$

where B is the background, P is the point-like emission model (Eq. 4.5), and $PSF \circledast M_E$ is the emission model convolved with the PSF and E is the exposure.

The center of the point-like component is kept fixed at the position of the SMBH (RA = 187.7059°, DEC = 12.3911°) since this emission is expected to come from the core region. While the only free parameters for the hybrid model are the intensities of the point-like and the diffuse component, the point-like model with its three free parameters (RA, DEC positions, and amplitude) is treated as the alternative hypothesis. Table 4.11 shows the fit results of the hybrid model for the low state. More informative than the diffuse amplitude is the total emission from the diffuse component compared to the total emission from the best fit model. Therefore, the percentage of the total emission, which belongs to the diffuse component, is shown in the table, and it is effectively zero. Analogously to the fit of the pure diffuse emission (Sec. 4.5.1), the point-like model is preferred by $3\,\sigma$ in comparison to the hybrid model. This is possible since the position of the point-like component is free to vary in the point-like model while it is fixed in this hybrid model. This could be an indication that the core is not one of the main contributors to the low state gamma-ray emission of M87 or the shift in the best-fit position is merely a systematic effect, for instance, due to the pointing uncertainty. The diffuse component has 0% of the total emission according to the best fit. It indicates a preference of the fit algorithm for a point-like source, even though the center of the point-like component is fixed at the cluster core. The reason for that is that the tails of the diffuse emission distribution (with 68% c.r. of 0.024°) are larger than the shift in the best-fit position of the point-like model (0.008°). A hybrid model with the center of the point-like component free to vary compensates for possible deviations due to systematic effects is presented in the following subsection.

4.5.3. Free hybrid emission

The same template for the hadronic emission is used as in Sec. 4.5.1 and Sec. 4.5.2 for the hybrid model with the point-like component free to vary. The number of free parameters is now four: RA and DEC of the point-like component, the intensity of the point-like component, and the intensity of the diffuse component. The hybrid model has more free parameters than

Hybrid Model	M87's low state				
	Ampl. point	**Ampl. diffuse**	**Diffuse (%)**	**Final stat.**	**Signif. of the point-like model (σ)**
Center fixed at the core	$3.5^{+0.2}_{-0.4}$	$0^{+0.4}_{-}$	0	-130028.9	3.0

Table 4.11.: The fit statistics for the best fit from the low state of the hybrid models.[21,110]. The center of the point-like component was fixed during the fit. The amplitude of the diffuse component is compatible with zero, therefore, does not have a lower limit above zero.

Hybrid Model	M87's low state					
	RA (°)	**DEC (°)**	**Ampl. point**	**Ampl. diffuse**	**Diffuse (%)**	**Final stat.**
Center free	187.711±0.003	12.398±0.003	$3.6^{+0.2}_{-0.4}$	$0^{+0.4}_{-}$	0	-130038.1

Table 4.12.: The fit statistics for the best fit from the low state of the hybrid model with an unconstrained point-like component and the steady state[21,110]. The center of the point-like component was free during the fit. The final statistic is exactly the same as for the point-like model from Tab. 4.7. The amplitude of the diffuse component is compatible with zero, therefore, does not have a lower limit above zero.

the point-like model and is used as the alternative model. Table 4.12 shows the results for this more complex hybrid model. As no hint for an extension was detected in the Gaussian model (Tab. 4.6), it is expected that the hybrid models converge to the point-like component. The fit algorithm yields the point-like component as dominant, and the best-fit position and final TS are the same as the values yielded by the pure point-like model (Tab. 4.7) as shown in Tab. 4.12.

Although the hybrid model in Tab. 4.12 cannot be ruled out, an upper limit on the amplitude of the diffuse component can be derived. According to the previous results, I developed a procedure to estimate the maximum allowed percentage of the diffuse component. It consists of defining a set of hybrid models with the center fixed at the best position ($187.711°, 12.398°$ - Tab. 4.5) and with increasing fixed amplitude. The TS of the model (TS_m) is compared to the TS of the best point-like model ($\Delta TS = TS_m - TS_P$). Figure 4.16 shows the significance of the point-like model in comparison to the hybrid models with increasing fixed amplitude. Once ΔTS reaches $3\,\sigma$, the UL on the diffuse amplitude, and, hence, the integrated diffuse emission is derived. It corresponds to a total of 55% of the H.E.S.S. low state emission, i.e. a flux of $\approx 8.1 \times 10^{-13}\,\mathrm{cm}^{-2}\,\mathrm{s}^{-1}$.

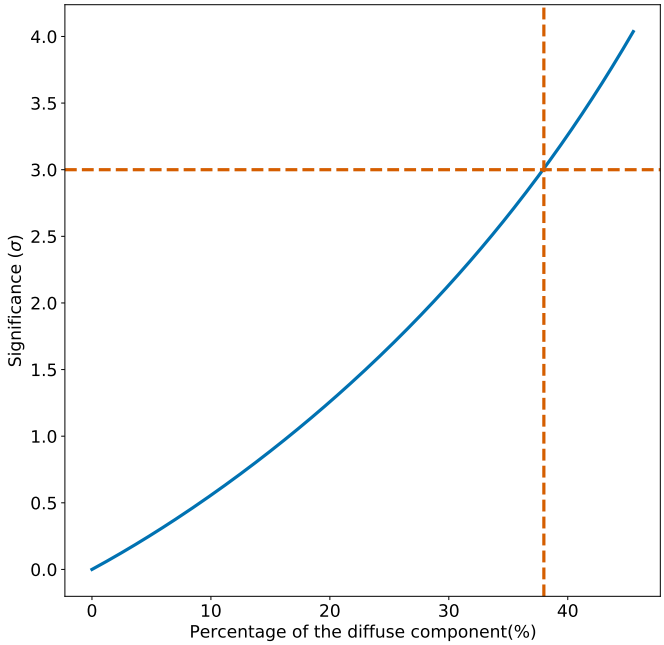

Figure 4.16.: The significance of the point-like model in comparison to the hybrid model with the center fixed at the best-fit position of the point-like model according to Tab. 4.5. The point-like model is significantly preferred when the fraction of the diffuse emission is higher than 55% of the total emission.

4.5.4. Constraints on the cosmic-ray pressure and the ICM

The steady-state emission model[21] considers not only the equilibrium between the heating and the cooling of the ICM but also the energy equally shared between the magnetic field and the kinetic energy in cosmic rays ($X_{\rm B}/X_{\rm NT} = X_{\rm CR}/X_{\rm NT} = 0.5$). Although the energy equipartition minimizes the total potential energy of the system, it might not represent the true state. The cosmic-ray pressure ratio ($X_{\rm CR} = P_{\rm CR}/P_{\rm th.}$) and the magnetic pressure ratio ($X_{\rm B}$) could vary, as long as their combined contribution $X_{\rm NT}$ remains the same, the steady-state is respected. Estimates on the magnetic field could help narrow down this relation, though estimates of a magnetic field in astrophysical sources usually have large associated uncertainties. Therefore, in this section, I derived the maximum cosmic-ray pressure ($X_{\rm CR}$) allowed using the H.E.S.S. extension limit, and the steady-state model developed from Jacob & Pfrommer (2017)[21].

According to the results from the previous section, the diffuse component contribute at most with 55% of the M87's low state gamma-ray flux, while the steady-state model predicts it $\approx$ 10%

(App. A.1). Figure 4.17 shows the dependence of the gamma-ray emission with the distance to the core and with the CR pressure. The CR pressure at steady-state is limited by the total non-thermal pressure ($X_{\rm NT}$) from Jacob & Pfrommer (2017)[21], delimited by the shaded region in the map. The H.E.S.S. UL lies within the shaded area; therefore, it cannot constrain the CR pressure of a steady-state model. Table 4.13 summarizes the main $X_{\rm CR}$ values from Fig. 4.17 for the cases shown.

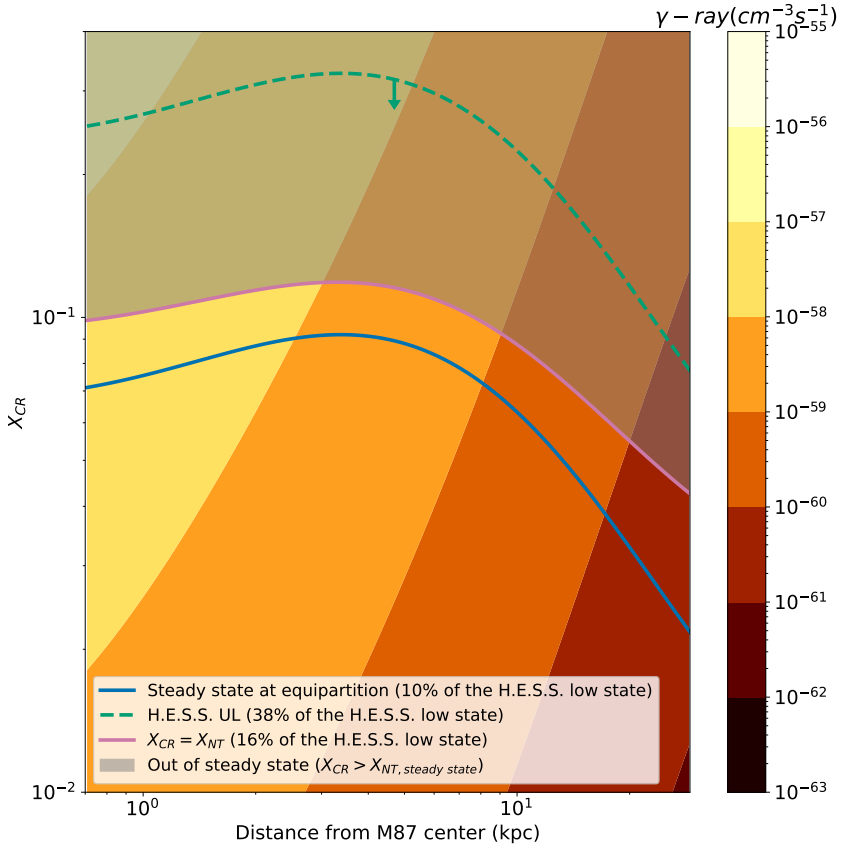

Figure 4.17.: The gamma-ray emission as function of the distance from the cluster core and the CR pressure rate ($X_{\rm CR} = P_{\rm CR}/P_{\rm th.}$). The $X_{\rm CR}$ profiles are shown for the steady state at equipartition (10% of the H.E.S.S. low state emission) in blue, for the extreme case of particle dominance (16% of the H.E.S.S. low state emission) in pink and for the case derived from the H.E.S.S. extension UL (55% of the H.E.S.S. low state emission) in dashed green.

According to Tab. 4.13, the maximum ratio of cosmic-ray to thermal pressure allowed by the H.E.S.S. extension UL is $X_{\rm CR,max} \leq 0.52$ at the maximum position ($\approx 3.3\,$kpc). Ackermann et al. (2015)[24] used a different approach and estimated the mean ratio of cosmic-ray to thermal

	Distance from the core (kpc)	$\mathbf{X_{CR}/X_{NT} = 0.5}$ **(equipartition)**	$\mathbf{X_{CR}/X_{NT} = 1}$ **(particle dominance)**	**H.E.S.S. UL**
$\mathbf{X_{CR}}$ **at the core**	<1	0.07	0.11	0.40
$\mathbf{X_{CR}}$ **at the maximum**	3.3	0.09	0.14	0.52
$\mathbf{X_{CR}}$ **at the outskirts**	20.0	0.03	0.05	0.19

Table 4.13.: The cosmic-ray pressure ratio ($X_{\rm CR}$), calculated according to the model in Jacob & Pfrommer (2017)[21,110] at the core position, at its maximum and at the cluster outskirts for the steady state at equipartition, a pure cosmic-ray steady state ($X_{\rm NT} = X_{\rm CR}$) and the derived H.E.S.S. upper limit on the diffuse component.

pressure within the virial radius of the Virgo Cluster ($r_{200} = 1.7\,\mathrm{Mpc}$[24]), and, therefore, cannot be directly compared to the limit obtained in this thesis. Further H.E.S.S. studies, not in the scope of this work, could consider estimating the UL of the gamma-ray flux at larger distances from the cluster core extending up to the virial radius. In this case, no AGN-related leptonic emission is expected to contribute to the measurement. Hence, for a given proton distribution, the average cosmic-ray pressure could be determined and compared to the Fermi results[24].

4.6. Potential of deeper observations with H.E.S.S.

To summarize the previous results, first, I studied the gamma-ray flux and derived the Bayesian blocks and the source states. I fitted the H.E.S.S. observations of M87's low state with geometrical models. Since no extension has been detected, I derived an UL on the emission size of 16 mdeg (4.6 kpc). The diffuse model was significantly disfavored (5.6 σ in Tab. 4.7) in comparison to the point-like model. As a result, I defined a set of hybrid models in which I included the template and a point-like component. The hybrid model cannot explain the gamma-ray low state emission detected by H.E.S.S. when the point-like component is fixed to the radio center. When the center of the point-like component is set free in the hybrid model, the fit converges to an emission composed only by the point-like component. However, some contributions from the diffuse component can not be discarded. I estimated the maximum contribution from the diffuse component to the total gamma-ray emission to be 55% of the total low state emission. As a consequence of this upper limit, I constrained the cosmic ray pressure ratio at its maximum position to $X_{\rm CR,max}$<0.52.

In this section, I investigate the potential of the H.E.S.S. telescopes to further test the hadronic scenario for the gamma-ray emission based on the π^0 decay by detecting or constraining an

extension in gamma rays, considering the next years of operation.

Based on the M87's gamma-ray low state observations, the background profile, the detected signal, and the PSF were used to simulate 2D sky maps. I created three sets of simulations to explore the influence of the live-time and the percentage of the diffuse component on the reconstructed extension and the preferred model. The first simulated set considers a completely point-like source. The second set adds a 10% contribution from the diffuse component, a steady-state at equipartition, according to the derived 2D gamma-ray template in Sec. 4.5.1. The third set adds, instead of it, a contribution of 16% from the diffuse component to account for the steady-state in an extreme particle dominance scenario ($X_{\rm NT} = X_{\rm CR}$).

For the first set of simulations, I simulated a pure point-like model at the M87's center (RA = 187.7059°, DEC = 12.3911°). The live-time ranges from 10 to 810 h in intervals of 100 h. For comparison, the current low state live-time of the H.E.S.S. M87's low state data is 120 h (Tab. 4.3), which shows that the simulation can predict the results of up to an additional 690 h of observations. For every step in live-time, 200 maps were simulated based on the known distributions of the background and the template and fitted according to four different models: the point-like, a 2D symmetrical Gaussian, the steady-state template, and a hybrid model with the point-like component centered at the M87's center. The models are the same from the last sections, defined by Eq. 4.3, Eq. 4.5 and Eq. 4.17 and the fit was conducted based on the same algorithm, defined in Sec. 4.3.1. Since the sky maps were simulated centered at M87's core, the position of the point-like component in the hybrid model was fixed but was kept free in the pure point-like model as in the analysis of Sec. 4.5.2. Figure 4.18 shows the significance histogram of the 200 simulated maps, in which the alternative model is compared to the null hypothesis for each bin in live-time, according to the models shown in the legend. The alternative model always has more free parameters (fewer d.o.f.). The results of the simulation show that the hybrid model cannot be distinguished from the pure point-like model (orange markers) since most of the fits (>100) have significance equal to 0. This is indeed expected for a point-like source, since the hybrid model converges to the point-like component when the diffuse component is zero. Similarly, the Gaussian model cannot be distinguished from a point-like source because it asymptotically approximates a point for a minimal σ extension. On the other hand, the diffuse model is disfavored at any live-time but only significantly after ≈ 110 h of observations, when the significance average is above $5\,\sigma$. For comparison, the actual H.E.S.S. significance of the point-like model in comparison to the steady-state model is $5.6\,\sigma$ (Tab. 4.10). The significance distribution of the simulated point-like source with 110 h live-time has an average of $4.9\,\sigma$ and a standard deviation of $0.4\,\sigma$. Therefore, H.E.S.S. result is consistent with a point-like source.

The 99.7% c.l. extension UL of the Gaussian model is shown in Fig. 4.19 with the best fit σ extension for the simulated sky maps. The improvement of the UL estimation is clear with

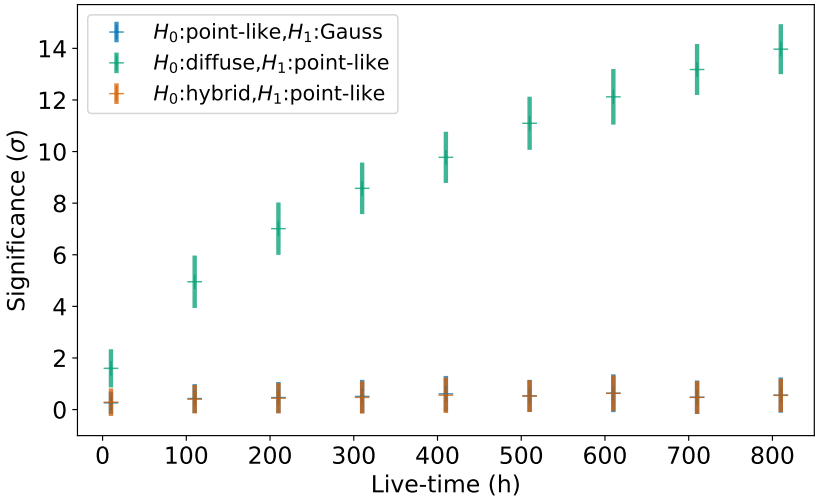

Figure 4.18.: Morphology fit results for the simulated maps with 0% of diffuse emission. Each time bin contains 200 simulated maps, fitted according to four models: point-like, Gaussian, diffuse and hybrid. The error bars give the 1 σ standard deviation of the 200 simulated sky maps.

the increase of the live-time, though it becomes very small after 200 h and reaches a limit of 11 mdeg at $\approx$ 700 h. For comparison, the H.E.S.S. UL is 16.2 mdeg (Tab. 4.8), while the mean of the simulated map of a point-like source with 110 h live-time is 19 ± 5 mdeg. Therefore, the H.E.S.S. morphology of M87's low state is consistent with the expected signal of a point-like source, though the extension UL can slightly improve with more observations.

I investigated the fit performance of the simulated sky maps by accessing the reconstructed number of events in each source component in the hybrid model. Figure 4.20 shows the 2D histograms of the reconstructed number of events for the different live-times. The blue arrow indicates the simulated percentage of the components, which should pinpoint the location of perfect reconstruction. The algorithm reconstructs correctly, with a slight spread, the events as originating from a point-like origin, especially for larger live-times. In the simulations of 10 h live-time, there is a larger spread of the reconstructed events, indicating a limitation of the algorithm when dealing with small event statistics. For larger live times, a small tail in the distribution is seen towards a pure diffuse reconstruction, though most of the events are correctly attributed to a point-like source. The more statistics available, the better the fit algorithm attributes the origin of the events. The spread in the reconstructed number of events in each component

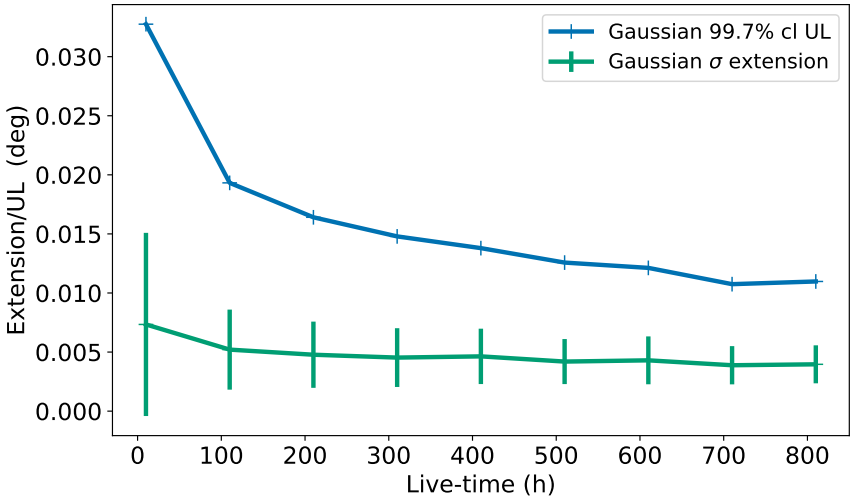

Figure 4.19.: 99.7% UL of the extension of the point-like simulated maps shown with the best σ Gaussian extension for the various simulated live-times. Error bars are the $1\,\sigma$ standard deviations of the distribution at each live-time.

demonstrates the limitation of the H.E.S.S. PSF to distinguish a small percentage of a diffuse component from a pure core emission.

I used the same procedure to simulate a hybrid model, in which the steady-state emission contributes with 10% of the H.E.S.S. low state emission. Similar to the simulation of maps with 0% of diffuse, the Gaussian model can very poorly be distinguished from the hybrid model. The estimation of the extension UL showed similar results as before. The 99.7% UL at 110 h live-time is 23 ± 5 mdeg, which places the H.E.S.S. UL at -1.4 standard deviations away from the mean, therefore, still consistent with the steady-state solution.

The simulation results for the third case, with 16% of the emission originated from the diffuse component, are shown in Tab. 4.14 , which summarizes the simulation results. The significance of the Gaussian model in comparison to the point-like model and the 99.7% extension UL are shown for the live-time of 110 h. The larger the percentage of the diffuse component, the larger is the significance of the Gaussian and the extension UL. For comparison, the H.E.S.S. UL is 16.2 mdeg (Tab. 4.8) and it is consistent within $3\,\sigma$ with the scenarios 0%, 10% and 16% of a diffuse component. Most important is the prediction at which live-time the fit can significantly detect the extension. Unfortunately, the detection of an extended emission in the H.E.S.S. low state emission from M87 is not feasible for the considered hadronic model, even considering more

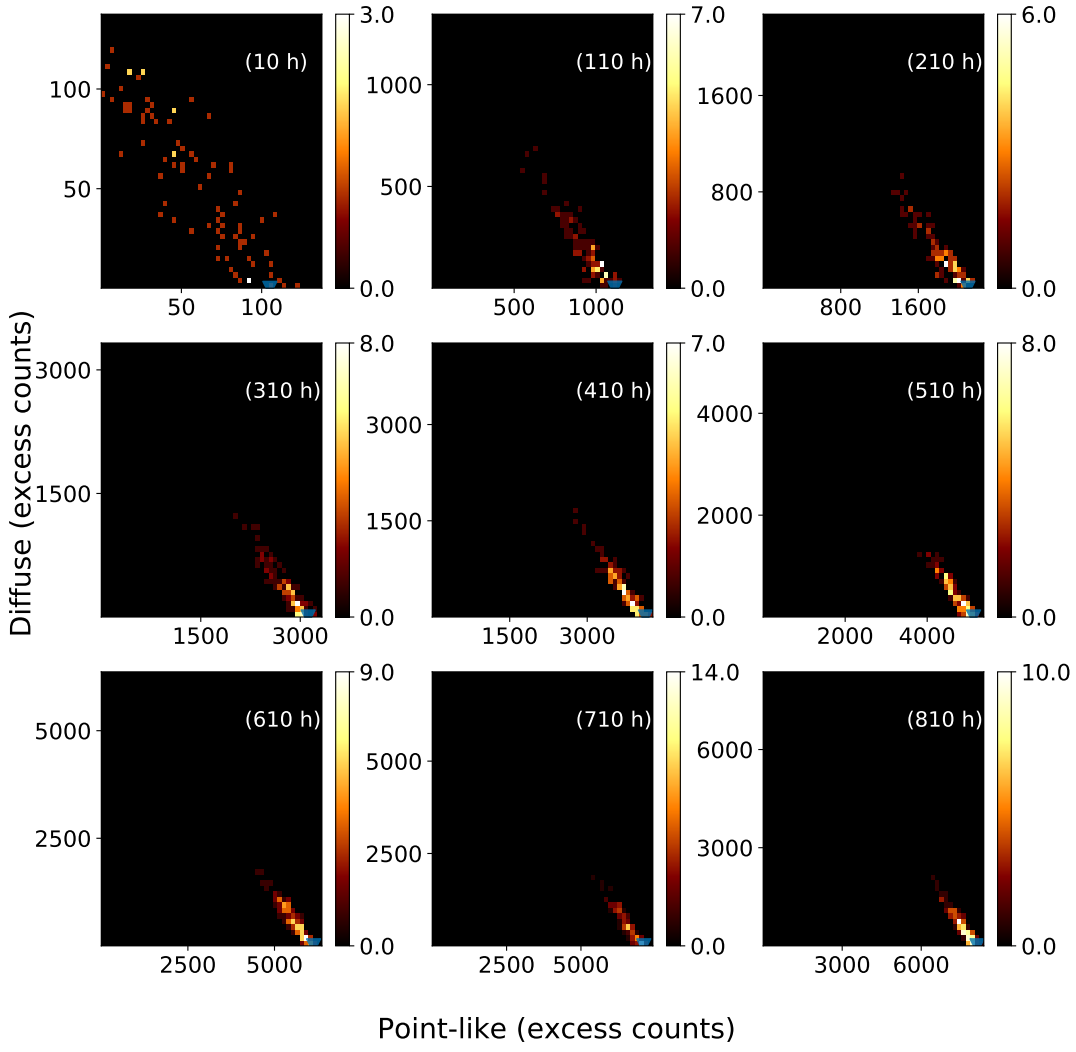

Figure 4.20.: Reconstructed number of events from the point-like and diffuse component from a pure point-like set of simulated sky maps for the different live-times. 200 maps were generated at each step in live-time and fitted with the hybrid model. The blue arrows show the original simulated percentages applied to the mean number of events.

Simulation set (percentage diffuse) at 110 h (current H.E.S.S. = 120 h)	**Sign. of Gaussian model to a point-like (σ)**	**Extension UL (mdeg)**
0%	0.4 ± 0.6	19 ± 5
10%	0.7 ± 0.6	23 ± 5
16%	0.8 ± 0.7	23 ± 5

Table 4.14.: Summary of the three sets of simulation results for 110 h live-time, to be compared with the current H.E.S.S. live-time of the gamma-ray low state (120 h). The uncertainties show the $1\,\sigma$ standard deviation from the spread of the 200 simulated maps.

Simulation set (percentage diffuse) at 410 h (current H.E.S.S. = 120 h)	**Sign. of Gaussian model to a point-like (σ)**	**Extension UL (mdeg)**
0%	0.6 ± 0.7	14 ± 3
10%	0.9 ± 0.9	16 ± 3
16%	1.2 ± 0.9	17 ± 2

Table 4.15.: Summary of the three sets of simulation results for 410 h live-time, to be compared with the future H.E.S.S. live-time of the gamma-ray low state, considering more 290 h of observations (total of 410 h). The uncertainties show the $1\,\sigma$ standard deviation from the spread of the 200 simulated maps.

300 h of H.E.S.S. observations (total live-time of 410 h) as shown in Tab. 4.14. The steady-state model at equipartition (10% diffuse) in the 410 h live-time would result in a $0.9\,\sigma$ preference for a Gaussian model compared to the point-like model. The average of the significance of the Gaussian model is relatively stable for increasing live-time, which points toward a limit in which the systematic uncertainties dominate over the statistical uncertainties, and no further improvement is expected. A better PSF could be achieved through a higher energy threshold, but it would at the same time reduce the event statistics. In this case, enough observations would not be possible within the probably next three years of H.E.S.S. operations.

Within the considered scenarios for the hybrid emission from M87's low state, the simulations have shown no expectation of the detection of the extended gamma-ray emission in a reasonable amount of time. Nevertheless, the extension UL can still be improved with further observations. The reasons why the H.E.S.S. telescopes do not detect the simulated extended emission are mostly due to the limitations imposed by the H.E.S.S. angular resolution. For instance, a large PSF is unable to distinguish a slightly extended diffuse component from a point-like emission. Furthermore, M87's jet is inclined towards Earth, and it is not seen in profile as the Centaurus

A jet. The smaller the viewing angle of the jet and the further away the source is, the harder it is for an extension to be detected. That is also the reason why distant AGNs are used as calibration tools and sanity checks in extension studies.

An angular resolution of at least several times better than the H.E.S.S. PSF will finally be achieved by CTA, the next generation gamma-ray observatory. The M87 extension will be probed at a new level with the potential to be detected. In the next chapter, I introduce CTA with its telescope composition, performance, and the status of construction. I put a focus on the systematic uncertainties and on the observatory potential of resolving VHE gamma-ray sources. Very stable telescopes are key to morphology studies; hence, I developed a monitoring system of the Medium-sized Telescope (MST) structure and present it in Sec. 5.3. Lastly, I investigated the sensitivity of CTA towards the detection of M87 extended gamma-ray emission in Sec. 5.7.

5. CTA and the structure monitoring of the MST prototype

CTA is the next generation of IACTs, which will extend our knowledge in VHE astrophysics to new frontiers. While the current instruments (H.E.S.S., VERITAS[13], and MAGIC[12]) still have been producing relevant results within the last years[71,73,74,153–155], the limitations in the performance of those experiments prevent many other science topics to be addressed[26,156]. With a ten times better sensitivity and 2-3 times better angular resolution, CTA will be able to investigate the morphology of galactic and extra-galactic gamma-ray emission at unprecedented details, improve spectral studies and discover new sources. The emission variability will be probed at the scale of hours, even for faint sources (few percentages of Crab). Consequently, the emission region will be constrained to even smaller sizes in the case of extra-galactic flares. Furthermore, the sensitivity of the observatory to gamma rays up to 300 TeV will probe the galactic PeVatrons[26,157], while the lower energy threshold of 30 GeV will improve the sensitivity towards the detection of GRBs due to the weaker absorption of lower energy gamma rays through the EBL[26].

Observations of M87 with CTA will probe the extension of the gamma-ray emission down to a few kpcs (eventually sub-kpc) from the SMBH. The puzzle of the origin of the VHE emission might unveil itself into the different source components, and the broadband SED would be complete. EBL studies would also benefit from such observations, and the theoretical models could be further constrained at low red-shifts (z<0.01).

The excellent performance and the long-term operations will depend on the data quality and the availability of the telescope. For instance, a better angular resolution must be accompanied by a better pointing precision. In addition, the structure of the telescopes must be stable and withstand both time and environmental conditions.

This chapter describes the condition monitoring system for the MST of CTA, which I developed to assure that the status of the telescopes structure is known at any time. The system aims to avoid major failures from the structure by reacting to the monitoring status and, ultimately, guaranteeing the high availability of the telescopes and the impact of the science results. I start by introducing the CTA observatory and its performance, composition, and layout in Sec. 5.1.

Afterward, I describe in Sec. 5.2 the MST design and the prototype, which was built in Berlin and used for tests between 2012 and 2020. I introduce and develop the structure monitoring system of the MST prototype in Sec. 5.3 and Sec. 5.4. In Sec. 5.5 the proof-of-concept for the monitoring system is established and in Sec. 5.6 I show the results of the long-term monitoring of the MST prototype structure throughout the end of 2019. Finally, in Sec. 5.7 I discuss the prospects of CTA observations of M87 and the potential detection of an extended emission in gamma rays.

5.1. CTA design and performance

CTAO consists of two arrays of IACTs, the first one is located in the northern hemisphere in La Palma (Spain), and the second one will be located in the southern hemisphere in Cerro Paranal (Chile). Three different types of telescopes will assure the coverage of the energy range from 20 GeV up to 300 TeV: the Small-sized Telescope (SST), the MST, and the Large-sized Telescope (LST).

The current official funded layout of the CTAO is the Alpha configuration[156], which consists of 4 LSTs and 9 MSTs in the CTAO Northern Array (0.25 km^2) and 14 MSTs with 37 SSTs in the CTAO Southern Array (3 km^2)[156]. Future expansion of the arrays will depend on further funds. Figure 5.1 shows the sensitivity curve of the CTAO arrays in comparison to current instruments. The improvement in sensitivity in comparison to H.E.S.S., MAGIC, and VERITAS is up to 10-fold for the region around 1 TeV. A small overlap with Fermi-LAT in the low energy range and the three particle detector experiments (HAWC[158], LHAASO[14] and the future SWGO[159]) with a focus on energies above 10 TeV are also shown. Most important for morphology studies, the angular resolution of CTAO improves with relation to the current instruments by almost a factor of 2 at 1 TeV as shown in Fig. 5.2 for the Northern and Southern arrays. The H.E.S.S. angular resolution is shown for a Hillas based (Hillas) and a template-based reconstruction (ImPACT)[65], while the other IACTs lean only on the Hillas reconstruction. Although the apparent comparable resolution of H.E.S.S. (ImPACT) and CTAO, the latter will also benefit from a template analysis and the resolution will further improve.

Apart from the improved sensitivity and angular resolution, the energy range of CTAO will be broadened in comparison to the current instruments. The low-energy end (20 GeV - 100 GeV) will be covered by the LSTs. With its 23 m mirror diameter and fast positioning of 30 s[156], able to follow-up transient alerts and detect low energy gamma-ray events, for instance low-luminosity GRBs[160]. The core energy range (150 GeV-5 TeV) will be covered by the MSTs with its modified Davis-Cotton design, and the highest energies (5-300 TeV) are covered by a large number of SSTs spread over a large area[26,156]. Figure 5.3 shows an artistic view of the three

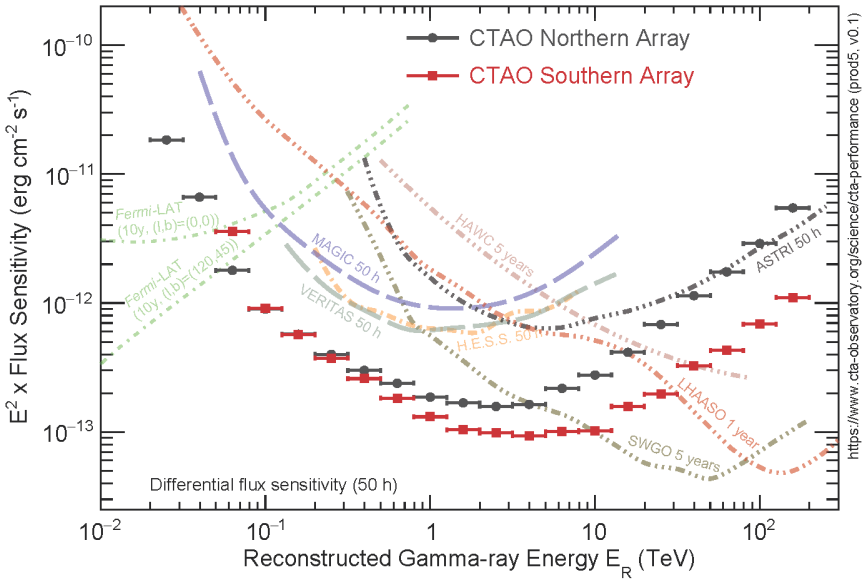

Figure 5.1.: Differential sensitivity curves for currently operating and planned instruments are shown for comparison. The sensitivity is defined by the minimum flux needed for the CTAO to obtain a $5\,\sigma$ detection of a point-like source calculated at non-overlapping logarithmic bins (five per decade). Extracted from CTA (2021)[156].

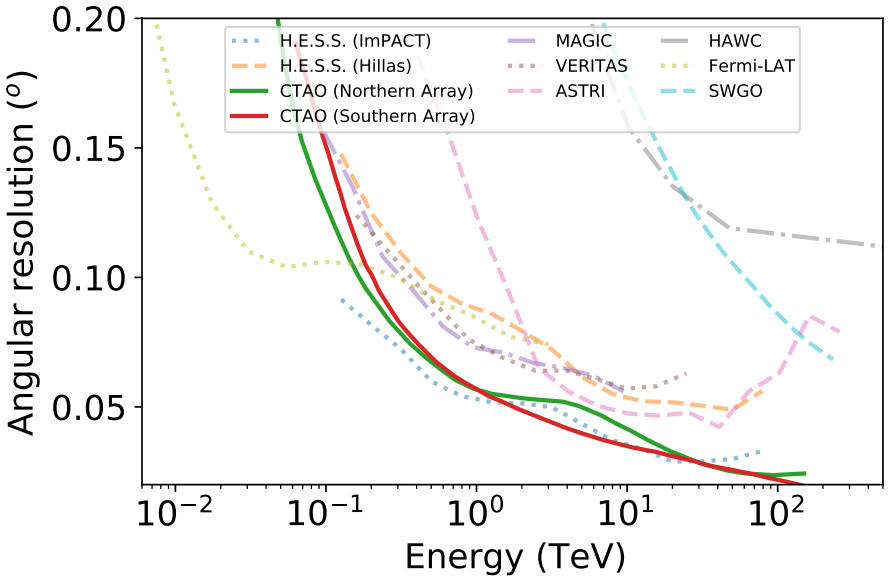

Figure 5.2.: Angular resolution as function of the reconstructed energy (containment radius of 68%). Adapted from from CTA (2021)[156] with H.E.S.S. resolution from Parsons & Hinton (2014)[65].

Figure 5.3.: Image rendering of the CTAO Northern Array with LSTs, MSTs, and the two MAGIC telescopes on the right side. Extracted from CTA (2021)[156].

kinds of telescopes side by side.

5.2. The MST design

The MST is subdivided into the following main assemblies: the positioner, the optical support structure, and the Cherenkov camera. The positioner is made of a 10 m height and 1.8 m diameter tower, which hosts on the top the drive assembly. The alt-azimuth drive uses two motors for the azimuth movement and four for the elevation movement. The optical support structure is made of a dish structure, counter-weight structure, and camera support structure (CSS). The Cherenkov camera is made out of ≈ 2000 very sensitive PMTs. The camera housing hosted the respective electronics inside. A model of the telescope is depicted in Fig. 5.4.

The MST optical system is based on a modified Davies-Cotton design. The reflector has a diameter of 12 m and a radius of curvature of 19.2 m. The focal length, i.e., the distance between the Cherenkov camera focal plane and the center of the reflector, is 16 m[161]. In the Davies-Cotton telescope design, the camera's focal plane is positioned precisely at the center of the reflector radius of curvature. The Davies-Cotton optics is characteristic for good optical PSF, but it generates a time dispersion of the photon arrival times at the focal plane. For a parallel light beam, photons reflected at the edge of the reflector arrive earlier than photons reflected in the central part of the reflector. A typical Cherenkov shower event generated by a photon in the GeV energy range lasts about 6 ns. In contrast, a time dispersion of a MST size Davies-Cotton reflector would be ~ 3 ns, which would degrade the performance of the telescope trigger. The solution implemented in some of the current largest IACTs (MAGIC, the H.E.S.S. CT5, and the LST from CTA) is the parabolic reflector, which is known to be synchronous in respect to the arrival times of photons. In this case, the radius of curvature of the dish becomes larger further away from the dish center, which increases the light path from the mirror to the

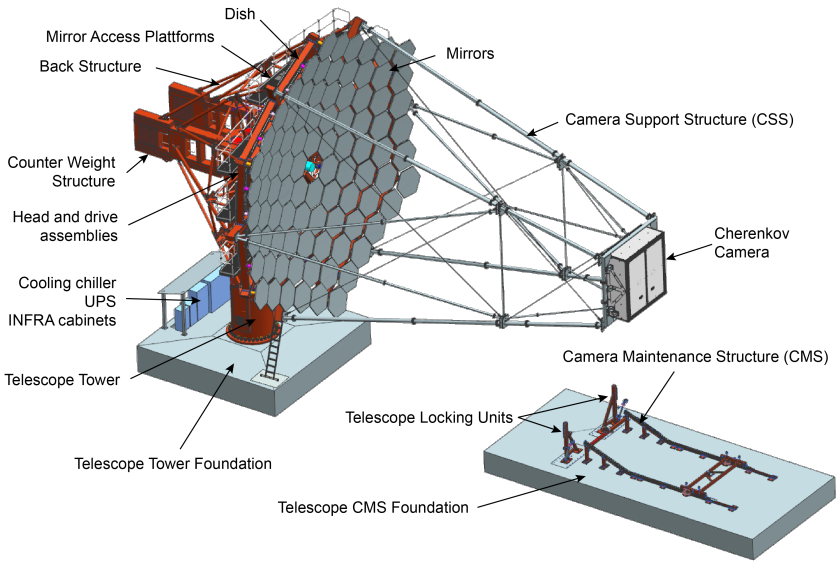

Figure 5.4.: The MST design and its components.

camera center (up to 60 cm for a mirror 6 m away from the dish axis when the focal distance is 16 m). The problem of time dispersion is solved; nevertheless, if all the segmented mirrors have the same focal distance (16 m), the image projected by the outer mirrors will be focused slightly before the focal plane of the telescope producing a degraded PSF. Outer mirrors with a larger radius would correct for this effect; however, it would not be a cost-effective solution for a large number of telescopes as it is planned for the MSTs. In order to optimize the time dispersion, optical performance as well as to reduce the costs in mass production, a modified Davies-Cotton design was proposed for the MST. An optimization process based on ray-tracing simulations resulted in a modified Davies-Cotton design with a radius of curvature of the reflector of 19.2 m, by keeping the distance between the center of the reflector and the focal plane at 16.0 m, and an individual mirror focal length of 16.07 m. The first modification decreases the time dispersion, while the second one improves the overall PSF. While images projected by outer mirrors are focused slightly before the telescope's focal point, the projection of the inner mirrors is slightly after the focal point. In the modified Davies-Cotton design, the normal vector of the mirrors must be aligned to the $2D$ position alongside the telescope axis, where D is the vertical distance of the mirror to the telescope axis.

The tower of the MST has a cylindrical shape of 1.8 m diameter. There are three floors inside it and access is possible through a door on its base. The tower's purpose is to transfer the load of the telescope structure to the foundations and provide shelter for a large fraction of electrical cabinets. The drive assembly, responsible for moving the telescope, is divided into

azimuth and elevation assemblies. Positioning encoders are used to read the telescope orientation continuously. Since many contact surfaces require lubrication, a system controlled by the safety PLC was developed to manage its flow automatically. A counterweight mounted on the back of the dish balances the elevation axis and reduces the momenta for the motors. A prototype of the MST was built and mounted in 2012 in Berlin, Germany, to test its design and developed systems[161]. Different designs for the CSS were developed and tested at the prototype during its eight years of operations. The challenge for the CSS design is to make a stiff structure that maintains the camera still at the focus of the reflector, does not cast large shadows on the mirrors, and resists environmental conditions. The final CSS design is made of steel beams and ropes, which maintain the stiffness of the structure when correctly tensioned and reduce the shadow by the elements. Two camera designs (the FlashCam[162] and NectarCAM[163]) and three kinds of mirrors were also developed for the MST and tested at the prototype.

The design of the telescope and the conducted tests are driven by CTAO requirements, which are proposed to assure the fulfillment of the observatory science cases and achievement of the promised performance. Table 5.1 summarizes the main requirements for the MST[164]. A good angular resolution for morphology studies is achieved through requirements $R6$, $R8$, $R12$ and $R13$. $R6$ depends mostly on the mirrors and their alignment, while $R8$ is determined by the dimensions of the PMTs. $R12$ is influenced by the structural stiffness and drive components parameters, and $R13$ is given by the combination of a stiff structure, a very good alignment, a pointing model, and a dedicated pointing CCD camera.

To assure steady performance and the fulfillment of the requirements by all MSTs of the array during the planned 30 years of the project lifetime, it is vital to monitor safety variables and behavior of the mechanical and electrical components. These parameters allow for planning and coordinating the maintenance efforts and keeping the telescopes' availability and data quality at the highest levels. In this context, a condition monitoring concept[28] was developed and tested at the prototype to keep track of the health of the instrument, raise awareness of structural changes, and emit early alerts in case of failures. The concept can be sub-divided into three branches: the structure health monitoring, which tracks its modal parameters throughout the time; the drive monitoring system, only interested in the state of the drive motors and lastly, the monitoring of multiple parameters, for instance, the motor torque, the local temperature, the status of the PLC, the lubrication level and the position of the telescope. Therefore, I introduce in the next section the development of the structure monitoring system for the MST with its hardware, software, analysis pipeline, proof of concept, and results from the long-term monitoring conducted in 2019.

	Parameter	Requirement
R1	Effective mirror area (corrected for shadowing)	$>88\,\mathrm{m}^2$
R2	Camera FoV	$>7^\circ$
R3	Mirror focal length (F)	$>1.3D$ (realised with $F = 16\,\mathrm{m}$)
R4	Mirror shape	spherical, hexagonal facets, 1.2 m flat-to-flat
R5	Average specular reflectivity of the reflector at all wavelengths from 300 to 550 nm	>85%
R6	Optical PSF for 80% light containment over 80% of the camera FoV	$<0.18^\circ$
R7	Dish radius of curvature	$1.2F$ (realised with 19.2 m)
R8	Angular pixel size	$<0.18^\circ$
R9	Slewing speed to any point on the sky $>30^\circ$ in elevation	90 s
R10	Positioning range in elevation	-20 to 90°
R11	Tracking range in elevation	$<89.2^\circ$
R12	Tracking precision	$<0.1^\circ$ in each axis
R13	RMS post-calibration pointing precision in space	$<7''$

Table 5.1.: Main requirements and specifications of the MST[164].

5.3. The monitoring system of the MST structure

The design and implementation of the telescope structure monitoring system at the MST prototype was my main contribution to the project.

I started with a theoretical and practical course on the measurement of structural parameters as the modal frequency, the Eigenmodes, and damping ratio using the Operational Modal Analysis (OMA). In the course, I used the software ARTEMIS Modal[165]. I transferred the methodology and analysis into my code. I adapted it to the project and made it independent from external software licenses. Description of the method can be found in Sec. 5.3.3.

Accelerometers were used to measure the vibration of the telescope structure. I have defined the required sensitivity range, conducted a market survey and tested several sensors. Results of my investigation lead to the selection of three very high sensitive tri-axial acceleration sensors,

Figure 5.5.: One of the three GeoSIG[166] sensors attached to the MST prototype (Berlin, 2019).

which were mounted on selected locations at the CSS. These sensors can measure vibrations while the telescope is excited by external forces, mainly the wind. Details about the sensors are described in Sec. 5.3.1.

This section is largely based on the results I presented at two conferences and published in the corresponding proceedings Barbosa Martins et al. (2019)[28] and Barbosa Martins & Garczarczyk (2020)[29].

5.3.1. Hardware

Besides the telescope structure itself, a weather station mounted at the prototype site, three accelerometers, and the data acquisition system are part of the monitoring system hardware. The weather station measures, among other variables, the wind direction and wind speed. The wind is the telescope's primary excitation source, apart from the telescope movements themselves. The proprieties of the chosen three force-balance accelerometers[166] are detailed in Tab. 5.2 and one of the sensors is shown in Fig. 5.5 attached to the backside of the dish structure.

The sensor working principle is based on a test mass, which is moved by an external force, sensed by a very-high-resolution displacement sensor, and counterbalanced by an equal and opposite force that stabilizes the object. The GeoSIG AC-73 was first developed for earthquake detection; though its large dynamic range and good sensitivity to faint excitation forces, they perfectly match the needs of our application. The larger the dynamic range, the larger is the acceleration range the sensor can detect. For the use in the telescope structure monitoring system, the acceleration range is defined between 0 and 2g, where g is the gravitational acceleration.

According to the sensitivity curve of the sensor[166], the minimum amplitude it can detect at 1 Hz is $\approx 3 \times 10^{-4}\,\mathrm{m/s^2}$.

Vendor	**Geosig**[166]
Model	AC-73
Technology	Force balance
Measurement directions	3 axis
Frequency range	Digital Count (DC) to 200 Hz
Dynamic range	<165 dB
Acceleration range	$0 \pm 2g$
Output signal	20 Volt from peak to peak (Vpp)
Operating temperature	$-20°C$ to $70°C$

Table 5.2.: Main proprieties of the Geosig AC-73 sensor[166].

The data acquisition of the accelerometer signal is performed by a commercial self-sustained operating controller (*Q.station*) from Gantner Instruments[167]. Attached to the *Q.station* are the *Q.bloxx* modules, responsible for the anti-alias filtering and AD-conversion of the sensor signal. Two kinds of modules were used: the *Q.bloxxA*111, which supports up to 100 kHz sampling rate per channel, suitable for the drive sensors and the *Q.bloxxA*108, which offers a lower sampling rate of up to 10 kHz but better sensitivity, suitable for the selected sensors. The station was responsible for controlling the data acquisition, and it was connected to the local computer through an ethernet cable. An FTP protocol transferred the data to a dedicated server, which forwarded them further to a NoSQL database server running MongoDB.

The data acquisition system was located inside the telescope tower, as shown in Fig. 5.6. Figure 5.7 shows a picture of the MST prototype with marked positions of the three accelerometers mounted on the CSS. The locations were selected focused on the CSS, to cover the entire structure and maximize the distances between the sensors.

5.3.2. Operational Modal Analysis (OMA)

The Operational Modal Analysis (OMA) is a method to estimate the modal parameters of large structures based on vibration measurements. Every rigid body has its modal frequencies and modal shapes, depending on its stiffness and shape. When a structure, for instance, a bridge, a building, or a telescope, is excited, it vibrates in a superposition of its Eigenstates. The OMA is capable of decomposing the vibration into these Eigenstates, deriving the Eigenfrequencies and damping ratio. The goal of the monitoring system is to track these modal parameters

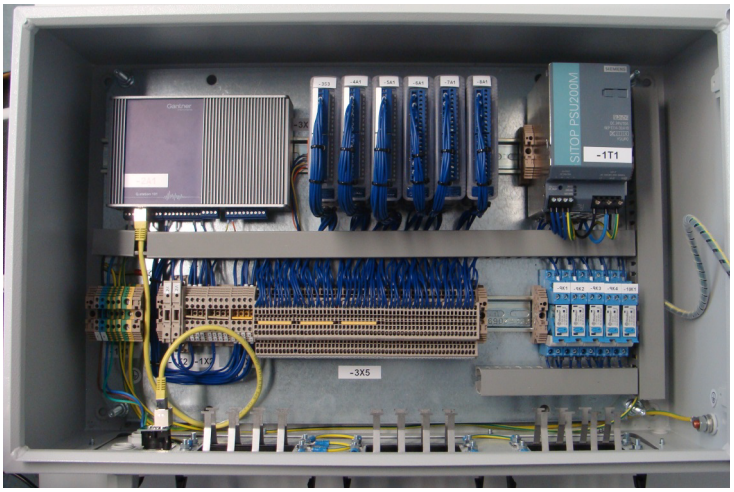

Figure 5.6.: The data acquisition system from Gantner Instruments[167] of the condition monitoring system, located inside the telescope tower. The six modules were located in the upper center and the *Q.station* in the upper left part of the image. The system also controlled the drive monitoring system.

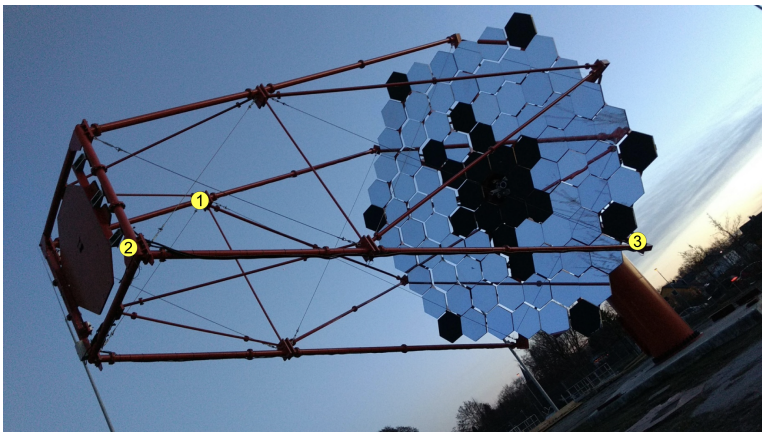

Figure 5.7.: A picture of the MST prototype in 2019 in Berlin with a dummy load in the place of the Cherenkov camera. The numbers indicate the position where the triaxial accelerometers AC-73 from GeoSIG[166] were fixated: 1) at the upper beam on the left side of the CSS as seen from the front of the telescope, 2) at the camera frame lower right beam and 3) at the lower right beam on the dish. The CSS steel ropes are identified as the thinner lines connecting the CSS.

throughout time. A change in those parameters would point to a change in the structure itself, which could be caused, for instance, by material fatigue, settlement, bending, loosening of screws, and relaxation of the CSS ropes. The early automated identification of such changes and the alert transmitted to the responsible personnel are crucial to avoiding major failures and

downtime of the telescopes. Alternatively, the Finite Element Method (FEM) can provide the modal parameters through simulation. However, it does not model the experimental conditions such as inhomogeneities in the material, welds, and unexpected misalignment of components. The comparison of both results assures the correct understanding of the structure and the experimental conditions.

The OMA is a robust method as long as the following requisites are fulfilled:

- Broadband and homogeneous excitation force: it must be approximately a white noise, i.e., to excite the structure in a large range of frequencies;
- The sensors must cover the entire structure: to avoid only detecting the modal parameters of substructures, the whole structure must be excited;
- The sensors must be sensitive enough to detect movements caused by the exciting force: if the sensor is not sensitive enough, the acceleration is not detected; hence the method cannot be applied. It is especially important when the excitation force is the wind, which is rather small.

The wind can be considered a broadband excitation force due to its varying speed and direction. The entire telescope structure is subject to the wind since no dome is built around it. The larger the number of sensors attached to the structure, the larger the number of Eigenmodes detected. For a high number of sensors (>5), more complex modes are detected, and changes in the structure could be, therefore, more precisely localized. However, given the high price of such sensitive sensors, a cost-effective solution with three sensors was chosen. Given that each sensor has 3 degrees of freedom (triaxial), a maximum of 9 Eigenmodes can be significantly distinguished from one another.

A telescope is a movable structure that can track objects in the sky. The telescope behaves as a different rigid body for each orientation, with different modal parameters. Therefore, the monitoring of the modal parameters shall always be conducted at the same pointing position, which for simplicity, was defined as azimuth and elevation angles equal to 0°, i.e., the telescope optical axis pointing towards the horizon, in the direction of the geographic North. Other environmental conditions such as temperature and humidity should slightly influence the modal parameters, though on a very small scale compared to structural changes.

According to the good practices of OMA[165,168], the sampling rate of the sensors should be at least 2.5 times the maximum frequency of interest. The total acquisition time should be at least $1000/\nu_{\min}$ s, where $\nu_{\min}$ is the minimum frequency of interest. From the FEM simulations of the MST, the first Eigenfrequencies are in the range from 0 to 10 Hz, which results in a sampling rate of at least 25 Hz. Nevertheless, an oversampling factor of 2 to 5 is suggested for a good noise

reduction. Hence, a factor of 4 was adopted and the final sampling rate fixed at 100 Hz. Tests with a sampling rate of 200 Hz were also conducted but with no further improvements in the results. Different acquisition times were tested, and the final choice was a run duration of one hour (due to technical reasons 3750 s), which allows detecting frequencies as small as ≈ 0.3 Hz.

5.3.3. The pipeline

Figure 5.8 illustrates the pipeline of the structure monitoring system implemented at the MST prototype. The pipeline was executed fully automatically using a *cronjob* script on the computer controlling the telescope. Automatic data acquisition was performed during about four months, in the period between September 5$^{\text{th}}$ and December 26$^{\text{th}}$, 2019. The procedure was scheduled during the morning, starting at 6 *am*. During twilight, remote-controlled dark time tests, especially the tracking of stars for the pointing precision tests, were finalized and the telescope parked in the safe position (at $-20°$ elevation). No technicians worked at the telescope site during early mornings; hence, no conflict with other activities was created.

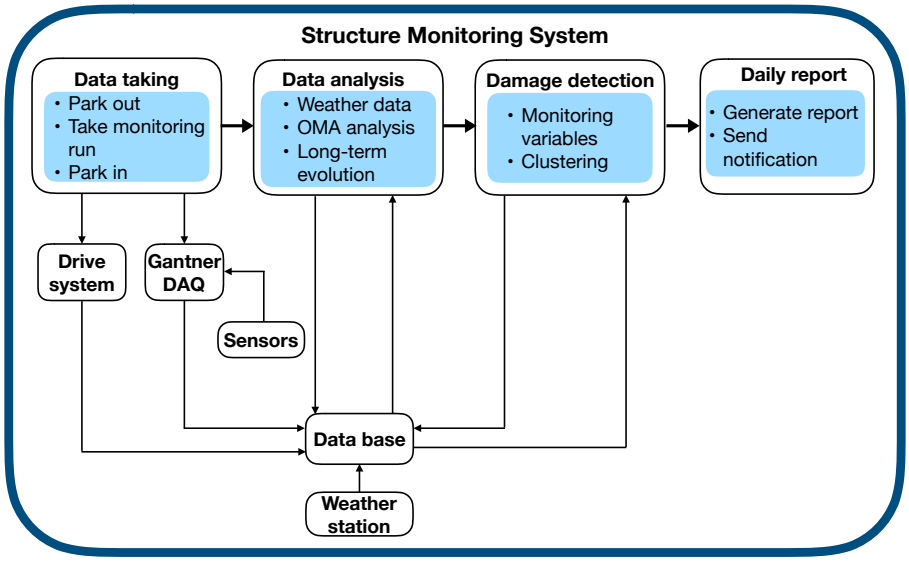

Figure 5.8.: Diagram of the structure monitoring system of the MST. It is divided in data taking, data analysis, damage detection and daily report. The main related systems are also shown.

The procedure starts with parking out of the telescope. The telescope is moved to the direction of 0° in azimuth and 0° in elevation, pointing North toward the horizon. Once the position was reached data acquisition run was started. In the consecutive 3750 s, the Gantner station

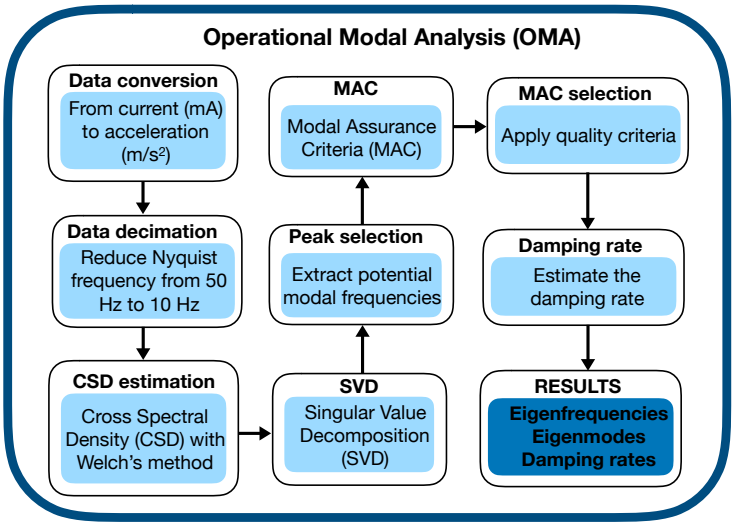

Figure 5.9.: Diagram of the OMA algorithm implemented for the MST.

digitized and recorded the signal from all connected sensors locally in its memory. At the end of the acquisition run, the data was transferred via FTP protocol to the MongoDB database. Finally, the telescope was moved back into the safe parking position.

The next step in the pipeline is data analysis. Self-written scripts access the sensor data from the database, including the weather station data, wind direction, and wind speed. The structural parameters are calculated for the data run and stored back into the MongoDB database. A trend analysis is performed by comparing the new results with previous measurements.

The damage detection analysis compares pre-defined variables, which indicated a change in the structure performance from experiments and tests. Complementary, a clustering method is used to detect different structure states.

At the end of the pipeline, an automatic report containing the main results from the analysis is generated. This report was sent via email to interested users.

I developed a Python script performing the OMA analysis. I compared the results of my analysis with the results obtained with commercial Artemis Modal software[165]. For the data runs taken at the telescope, the results were identical, proving the reliability of my analysis and scripts. The OMA algorithm is subdivided into several steps, from the data acquisition to the final modal parameters, as shown in the diagram in Fig. 5.9. An application of the algorithm is shown in Sec. 5.4.

5.4. Application of the OMA algorithm for the MST

The data taken on August 25$^{\text{th}}$, one of the first days after the installation of the sensors, are used in this section to exemplify the procedure shown in Fig. 5.9.

5.4.1. Data conversion and decimation

The first step of the data conversion is to subtract the mean from the data in each channel since the orientation of the sensors is not important for the method. The units, given in mA, are converted to m/s^2 (and cm/s^2 for convenience) using the response function given in the manufactures data-sheet. Figure 5.10 shows the acceleration detected by the sensor located at the CSS camera frame (Sensor 2 in Fig. 5.7) on August 25$^{\text{th}}$. The direction of the axes is shown in the sketch on the lower panel. The acceleration in the Z-axis, parallel to the telescope optical axis, is smaller than in the X and Y directions. The three channels show some correlation due to the common excitation force. The wind blows at different speeds, and directions and the sensors could detect it, as shown by the spikes above the noise level.

After the data conversion, the data decimation is applied. It uses the *signal.decimate* function from SciPy[130] to reduce the Nyquist frequency, given by one-half of the sampling rate, from 50 Hz to the selected maximum frequency of interest (10 Hz). The function uses a Chebyshev[169] type I low-pass filter of 5$^{\text{th}}$-order. The combination of oversampling and decimating helps reduce the noise and improve the resolution of the spectrum for the upcoming steps of the analysis.

5.4.2. The Cross Spectral Density (CSD) and the Singular Value Decomposition (SVD)

Considering that each of the nine channels (3 sensors $\times$ 3 axes) has recorded N data-points during the acquisition time, the vector $\overrightarrow{Y^i} = \begin{bmatrix} Y_1^i & Y_2^i & ... & Y_N^i \end{bmatrix}$ describes the acceleration detected by the i^{th}-channel. A Discrete Fourier Transform (DFFT) is applied to each channel, which yields the vector in the frequency domain: $\overrightarrow{\Phi^i} = \begin{bmatrix} \Phi_1^i & \Phi_2^i & ... & \Phi_N^i \end{bmatrix}$. The correlation between the individual the channel i and j in frequency space is given by the Cross Spectral Density (CSD) $\overrightarrow{G^{i,j}}$, calculated by the element-wise product:

$$\overrightarrow{G^{i,j}} = \overrightarrow{\Phi^i} \odot \overrightarrow{\Phi^j} = \begin{bmatrix} G_1^{i,j} & G_2^{i,j} & ... & G_N^{i,j} \end{bmatrix}, \tag{5.1}$$

where i and j varies from 1 to 9 and represent the available channels, and the symbol '$\odot$' represents the element-wise product of matrices. The CSD is calculated for each channel with all channels, including with itself. For a total of nine channels, 81 CSD vectors are produced. For

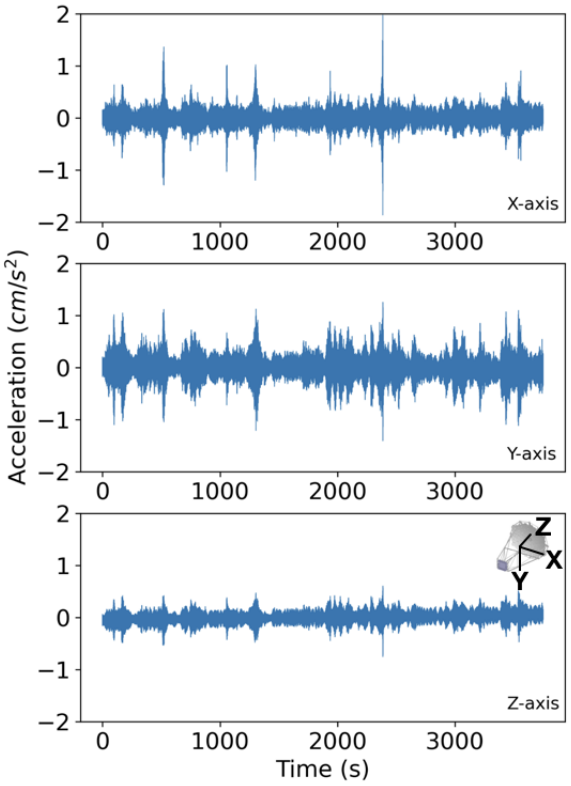

Figure 5.10.: Sample data from August 25th, 2019 for the sensor fixed at the camera frame (Fig. 5.7). The excitation of the structure detected by the sensor in its three axis are shown.

each frequency bin ν, the correlation among all the channels is expressed as the 9×9 correlation matrix $\overrightarrow{M^{\nu}}$:

$$\overrightarrow{M^{\nu}} = \begin{bmatrix} G_{\nu}^{1,1} & G_{\nu}^{1,2} & \dots & G_{\nu}^{1,9} \\ G_{\nu}^{2,1} & G_{\nu}^{2,2} & \dots & G_{\nu}^{2,9} \\ \vdots & \vdots & \ddots & \vdots \\ G_{\nu}^{9,1} & G_{\nu}^{9,2} & \dots & G_{\nu}^{9,9} \end{bmatrix}_{9\times 9} . \tag{5.2}$$

The next and most important step of the OMA algorithm is the Singular Value Decomposition (SVD), or more broadly Frequency Domain Decomposition (FDD)[168]. SVD decomposes the $\overrightarrow{M^{\nu}}$ matrix from Eq. 5.2 into three matrices, according to:

$$\overrightarrow{M^{\nu}} = \overrightarrow{U^{\nu}} \cdot \overrightarrow{S^{\nu}} \cdot \overrightarrow{V^{\nu}}, \tag{5.3}$$

where the matrices are given by Eq. 5.4: $\overrightarrow{S^{\nu}}$ is a 9 x 9 diagonal matrix, which contains the singular values s_i^{ν} of $\overrightarrow{M^{\nu}}$ in decreasing order (s_1^{ν}>s_2^{ν}>...>s_9^{ν}), $\overrightarrow{U^{\nu}}$ is the shape parameter, a 9 x 9 matrix, which carries information about the mode shapes in its columns, and $\overrightarrow{V^{\nu}}$ is usually the transposed $\overrightarrow{U^{\nu}}$.

$$\overrightarrow{U^{\nu}} = \begin{bmatrix} U_{1,1}^{\nu} & U_{1,2}^{\nu} & ... & U_{1,9}^{\nu} \\ U_{2,1}^{\nu} & U_{2,2}^{\nu} & ... & U_{2,9}^{\nu} \\ \vdots & \vdots & \ddots & \vdots \\ U_{9,1}^{\nu} & U_{9,2}^{\nu} & ... & U_{9,9}^{\nu} \end{bmatrix}_{9\times 9}, \quad \overrightarrow{S^{\nu}} = \begin{bmatrix} s_1^{\nu} & 0 & ... & 0 \\ 0 & s_2^{\nu} & ... & 0 \\ \vdots & \vdots & \ddots & \vdots \\ 0 & 0 & ... & s_9^{\nu} \end{bmatrix}_{9\times 9}, \quad \overrightarrow{V^{\nu}} = \overrightarrow{U^{\nu}}^{T}. \tag{5.4}$$

The method to derive the matrices from Eq. 5.3 is used from NumPy[129] *linalg* package. If a considered frequency bin ν corresponds to a modal frequency, then its first singular value s_1^{ν} in the $\overrightarrow{S^{\nu}}$ matrix will be much larger than the second and the subsequent values ($s_1^{\nu} \gg s_2^{\nu}$). A peak in the second singular value indicates a change in the dominant modal shape. Peaks in the higher-order singular values are linked to the multi-dimensionality of the first-order peak, i.e., the higher the singular value, the more mode shapes are linked to that specific frequency. Figure 5.11 shows the result of the SVD for the selected data-set. Given the complexity of the telescope structure, a large number of peaks are identified in the spectrum. The first singular values are shown in blue, and the peaks indicate potential modal frequencies of the structure.

The intensity of the power spectrum is given in dB by:

$$dB = 10log_{10}\left(\frac{I}{I_{\text{ref.}}}\right), \tag{5.5}$$

where I is the power spectrum, $I_{\text{ref}} = 10^{(1/10)}$ is the reference power for 1 dB. A simple algorithm based on the *SciPy*[130] $signal.find\_peaks$ function is used to extract the frequency of the peaks in the first singular value curve. The function must be able to identify all the peaks even at the cost of identifying a certain amount of extra fake peaks, for instance, the first potential modal frequency indicated in Fig 5.11.

5.4.3. Modal Assurance Criteria (MAC)

The Modal Assurance Criteria (MAC) is the criteria defined to remove all the linearly dependent frequencies from the selected peaks, keeping only the independent frequencies, which are finally classified as modal frequencies of the structure. The MAC number p_{ν_1,ν_2} is estimated based

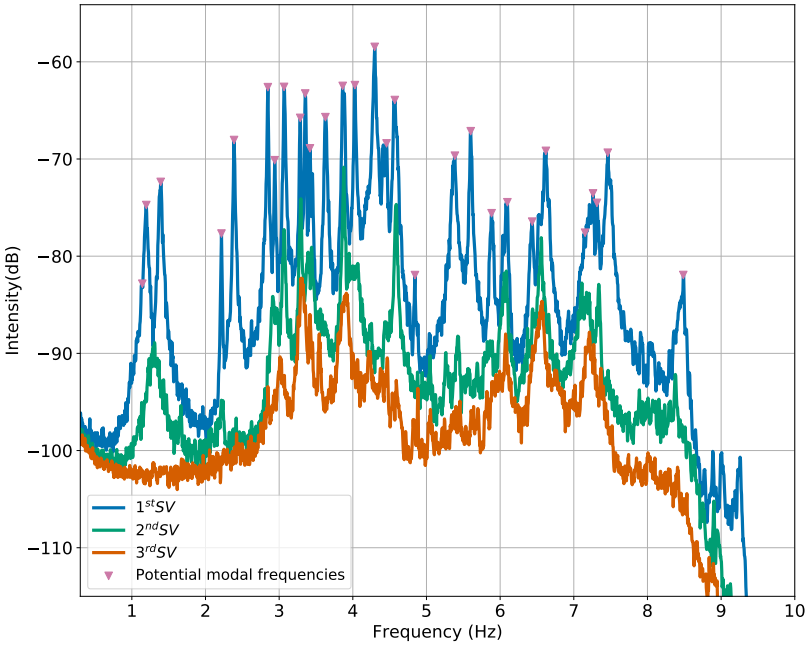

Figure 5.11.: SVD result for data acquired on August 25$^{\text{th}}$, 2019. The blue, green and orange are respectively the first, second and third singular values. The markers show the peaks of the first singular values.

on the shape parameters $\overrightarrow{U^{\nu}}$. It measures how two mode shapes ($\overrightarrow{U^{\nu_1}}$ and $\overrightarrow{U^{\nu_2}}$) are linearly correlated. It yields 0 if they are not correlated and 1 if they are highly linearly correlated:

$$p_{\nu_1,\nu_2} = \frac{\overrightarrow{U^{\nu_1}} \cdot \overrightarrow{U^{\nu_2}}}{\sum_{i=1}^{9} \overrightarrow{U^{\nu_1}} \cdot \overrightarrow{U^{\nu_2}}}. \tag{5.6}$$

The MAC value is calculated for every pair of potential modal frequencies, obtained by the peak selection (pink triangles in Fig 5.11). The resulted MAC matrix is shown in Fig. 5.12, where the correlation between all frequencies is shown. Naturally, the correlation of one peak with itself is 1, and the diagonal of the matrix is 1. The first two frequencies, for instance, are correlated, i.e., they correspond to the same mode shape.

A criterion, usually defined as p_{ν_1,ν_2}<0.3, shall be adopted to cut off the linearly dependent frequencies. Because of the complexity of the telescope structure, there is a large number of very similar modes, for instance, identified by the number of peaks from 2.6 to 5 Hz in Fig 5.11. Furthermore, with the limited number of accelerometer channels (9), it is not easy to

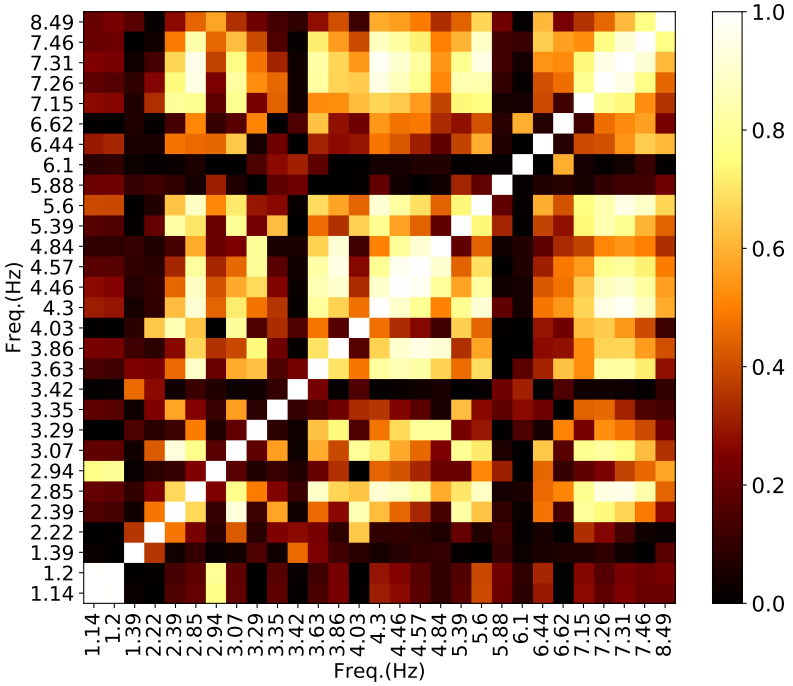

Figure 5.12.: MAC matrix with the correlation of the potential modal frequencies with one another for data acquired on August 25$^{\text{th}}$, 2019. A MAC value of 1 indicates a perfect correlation and the value of 0 indicates no correlation.

disentangle those modes as linearly independent even if they are modal frequencies. Therefore, a more relaxed criterion of p_{ν_1,ν_2}<0.6 was adapted to recognize a frequency as a modal frequency. The advantage of this approach is to monitor a larger number of frequencies even though some of them might show a certain level of correlation. The one with the highest intensity is kept whenever two potential frequencies are correlated. Figure 5.13 shows the final MAC matrix after the applied criterion.

5.4.4. The damping rate

The modal frequencies obtained with the MAC approach are associated with the modal shape given by the $\overrightarrow{U^{\nu}}$ matrix from Eq. 5.3. Although the mode shape visualization is difficult with only three sensors, one can still derive the damping rate parameter. The damping rate describes how fast the vibration at the mode shape is damped with time. First, to extract the frequency range in which the mode shape is dominant, a second MAC value is calculated between the $\overrightarrow{U^{\nu}}$ matrices of the peak frequency and its nearby frequency bins. Whenever the MAC value is

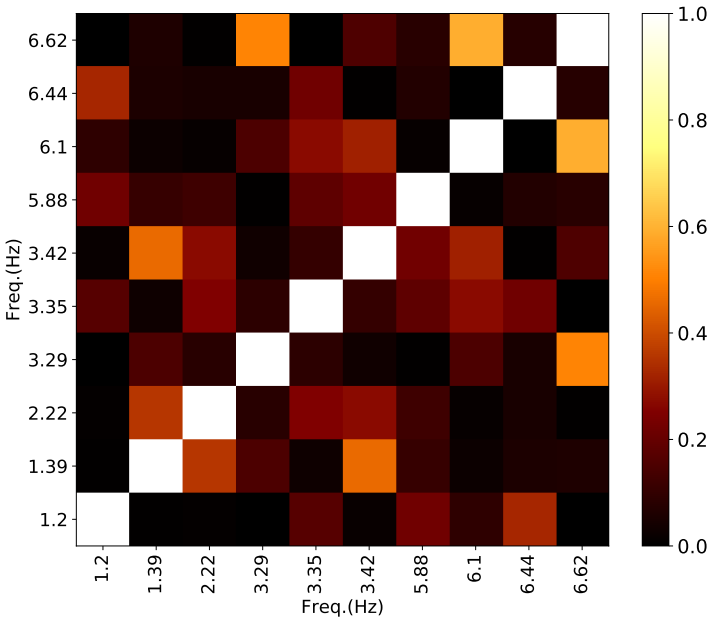

Figure 5.13.: MAC matrix with the correlation of the modal frequencies with each other after the cut of η<0.6 for data acquired on August 25$^{\text{th}}$, 2019.

larger than 0.95 the mode shape is considered dominant in the region and its intensity is given by the intensity (in dB) of the first singular value. The region where the MAC value is smaller than 0.95 is set to zero. The result is similar to a Bell shape curve as shown in Fig. 5.14 for the modal frequency at 2.22 Hz, the first stable mode of the structure as it will be demonstrated in Sec. 5.5.

In order to retrieve the decay curve of the mode shape, an Inverse Fourier Transform (IFFT) is applied to the Bell-curve, which is then normalized to maximum intensity 1 and mean 0. The result is the auto-correlation function. The method has limitations since the Bell-curve does not represent one mode shape alone, especially further away from the peak. The high number of modal frequencies in a narrow range also makes reconstructing a pure decay curve difficult. The range of the auto-correlation function, where its estimate is reliable, is between 0.3 and 0.7, far from the start and end of the decay curve. Figure 5.15 shows the auto-correlation function of the modal frequency at 2.22 Hz.

The auto-correlation function is used to obtain the logarithm decimation (*logdec*) function, which is then used to estimate the damping factor. The *logdec* function is defined as the logarithm of the rate between the intensity of the first peak and the n-peak in the auto-correlation

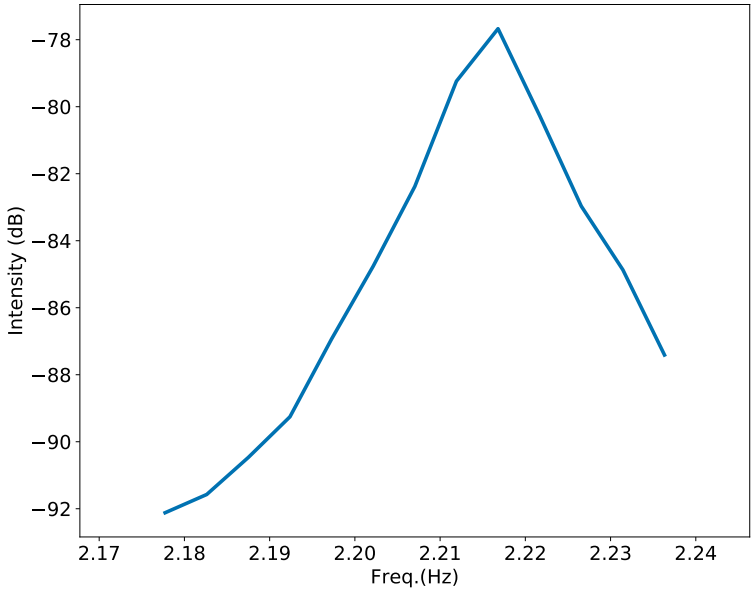

Figure 5.14.: Bell-shape curve for the mode shape at the frequency of 2.22 Hz.

curve. The slope of the logarithm decimation function in the region of interest gives the *logdec* factor ξ. The region of interest comprises the same time interval used in the auto-correlation function (green curve in Fig. 5.15), and the goal is to avoid regions close to the start and end of the excitation. Figure 5.16 shows the logarithm decimation function of the the 2.22 Hz modal frequency. An alternative definition uses both the peaks and valleys as extremes, which would imply an additional factor 2 in the ξ definition, though the final *logdec* factor would not change significantly.

Finally, the damping rate δ is defined based on the *logdec* factor ξ:

$$\delta = \frac{1}{\sqrt{1 + \left(\frac{2\pi}{\xi}\right)^2}}. \tag{5.7}$$

The uncertainty of the damping rate estimation is considerable since it contains various assumptions, including the definition of the MAC value cutoff at 0.95, which ignores contribution from other modes at the vicinity of the modal frequency, and the definition of the region of interest for the auto-correlation function. Nevertheless, it is an essential modal parameter to be monitored. In theory, the stiffer the structure, the larger the damping rate of a mode shape. Based on the damping rate, a correction factor is applied to the modal frequencies according to

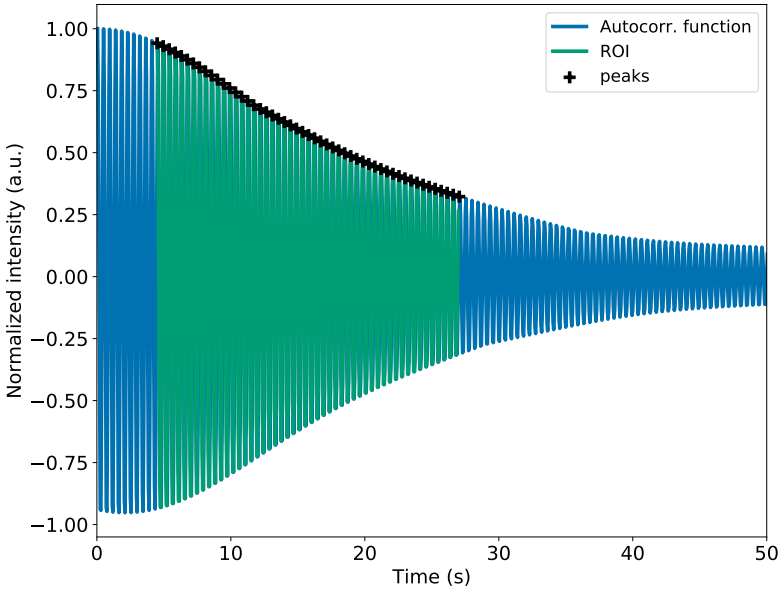

Figure 5.15.: The auto-correlation function (decay curve) of the mode shape at 2.22 Hz. The function is given by the blue line and the region of interest (ROI) given by the green curve. Peaks (and valleys) are given by the black crosses.

yield the weighted modal frequencies:

$$\nu_\omega = \frac{\nu}{\sqrt{1-\delta^2}}. \tag{5.8}$$

For the exemplary data-set from August 25$^{\text{th}}$, the corrected modal frequencies show no differences in comparison to the frequencies before the correction due to the low damping rates. An improvement in the mode shape can also be achieved by weighting the U_i^ν matrix by its singular values S_i^ν and adding the contribution of the underlying shape parameters through the dot product:

$$\overrightarrow{U_\omega^\nu} = \overrightarrow{U^\nu} \cdot \overrightarrow{S^\nu} \tag{5.9}$$

where $\overrightarrow{U_\omega^\nu}$ is the weighted mode shape, $\overrightarrow{U^\nu}$ and $\overrightarrow{S^\nu}$ are defined by Eq. 5.3.

I applied the steps of the analysis described in this subsection to the modal frequencies of Fig 5.13 and the results are shown in Tab. 5.3. I cross-checked the analysis with the commercial software Artemis Modal[165]. The results were similar and can be seen in App. D along with

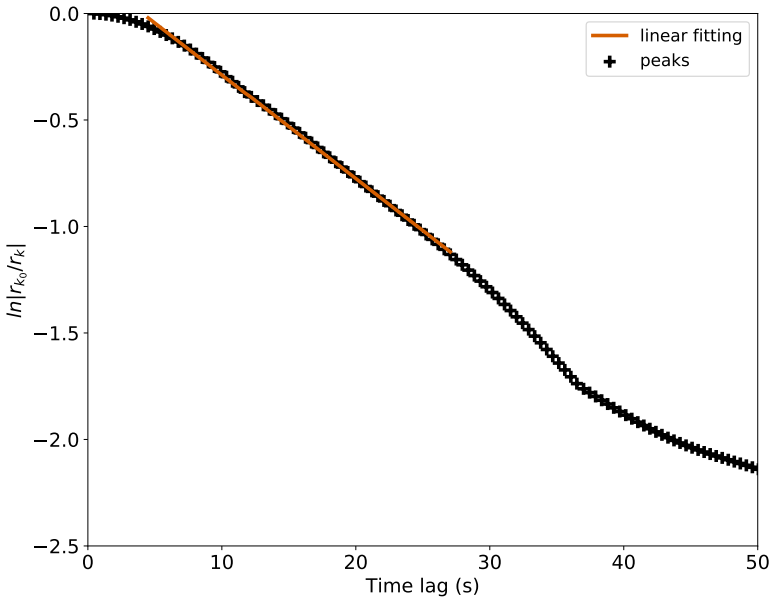

Figure 5.16.: The logarithm decimation function for the modal frequency at 2.22 Hz. The function is calculated as the logarithm of the n-peak to the first peak in the autocorrelation curve.

the visualization of the mode shapes. The first two modes, at 1.20 Hz and 1.40 Hz are rather unstable as realized by analyzing data-sets from other days. They are highly dependent on the wind speed and are likely related or contaminated by a slight translation movement of the structure provoked by high wind speeds; therefore, they shall not be considered mode shapes of the structure.

A Finite Element Method (FEM) simulation was conducted by the engineering team of the MST project and delivered the expected modal frequencies of the MST structure. It identified even the most complex mode of vibration. According to the simulation, the first mode is at 0.75 Hz and relates to the horizontal vibration of the CSS (parallel to the ground). In comparison, the second mode is at 1.20 Hz and relates mainly to the vertical movement of the CSS (gravity direction). The third mode from the FEM simulations is originated from the lateral vibration of the counter-weight structure and the back structure of the telescope dish, at a frequency of 2.24 Hz. At 3.61 Hz, the fourth mode indicates a vibration in the direction along the main telescope axes.

A relative difference between the modal frequencies derived by the FEM simulation and by the OMA analysis is expected since the FEM does not comply with the actual field conditions

Modal freq. (Hz)	**Damping rate (%)**
1.20	1.92
1.40	1.40
2.22	0.35
3.29	0.22
3.35	0.22
3.42	0.22
5.88	0.23
6.1	0.18
6.44	0.25
6.62	0.27

Table 5.3.: Summary of the modal parameters resulted from the OMA algorithm applied to the data from August 25$^{\text{th}}$, 2019.

of the MST such as the rope's tension. The frequencies are strongly dependent on the tension of the CSS ropes as it will be investigated in Sec. 5.5. The frequency at $\approx 2.2\,\text{Hz}$ encountered by both the FEM simulation and the OMA analysis is likely due to the same Eigenmode, i.e., due to the horizontal vibration of the counterweight and back structure of the telescope dish. However, the visualization of the mode shapes derived by the OMA analysis is rather complex due to the small number of sensors distributed over the structure. Although not necessary for the mode detection, an extra sensor on the counter-weight structure would enable us to confirm if the Eigenfrequency at 2.2 Hz is indeed due to the counter-weight structure vibration.

5.5. Proof-of-concept of the monitoring system

The MST team, including me, conducted a proof of concept at the MST prototype on November 26$^{\text{th}}$ and 27$^{\text{th}}$, 2019, to investigate the response of the monitoring system to changes in the pre-tensioning of the CSS ropes. The pre-tension of the eight steel ropes was adjusted with the telescope pointing towards Zenith. At this orientation, the gravity load of the Cherenkov camera and the CSS is homogeneously distributed over the structure. The tension in the ropes was monitored using digital tensiometers. Two different pre-tension loads were applied and tested. After each procedure, instead of one hour of data taking, a 15 minutes-long monitoring run was taken. During the runs, the telescope pointed towards 0° elevation and 0° azimuth. Reducing the acquisition time from the typical one hour to 15 minutes enabled us to conduct more tests on the same day at the expense of a good resolution of the frequency peaks. Finally,

I investigated the influence of tightening and releasing of the ropes, the time for relaxation, and the effects of the telescope operation. The test procedure is described with the following steps:

- Initial state: A dedicated 15 minutes run was taken to extract the initial modal parameters;
- Tighten: The CSS ropes were tightened with 7.5 kN each, with the telescopes pointing to 90° in elevation angle;
- Current state: A dedicated 15 minutes run was taken;
- Relaxation: The telescope stood still for about 1 hour;
- Current state: A dedicated 15 minutes run was taken;
- Operation: The telescope was moved in a random direction during about 10 minutes;
- Current state: A dedicated 15 minutes run was taken;
- Release: The tension of two of the CSS ropes was released to 3 kN;
- Current state: A dedicated 15 minutes run was taken;
- Tighten: The nominal tension of 10 kN was applied to every rope with the telescope pointing to 90° in elevation;
- Current state: A dedicated 15 minutes run was taken;
- Relaxation: The telescope stood still for about 12 hours until the next morning;
- Current state: The last dedicated 15 minutes run was taken.

In each step of tightening or releasing, the ropes' tension was measured by the engineers of the MST project at the 90° elevation and in steps of 10° down to 0° elevation, where the dedicated 15 minutes runs were acquired. The tension is applied homogeneously to the ropes (Tighten) with the telescope pointing towards 90°; however, the tensions are redistributed between the ropes when the telescope moves to lower elevations. Half of the CSS ropes are tightened, while the other half is compressed. Figure 5.17 indicates the position of the ropes with their identification from 1 to 8 and Tab. 5.4 shows the tension measured at 0° elevation between some of the procedure steps according to the definition given by the figure. In the initial state, the *compression ropes* (ropes 1, 2, 5, and 7) had no tension applied, which indicates that the pre-tensioning of the *tension ropes* (ropes 3, 4, 6, 8) was not sufficiently high. The process of applying the tension is mechanical and, therefore, not very accurate as of the spread in the tension between the

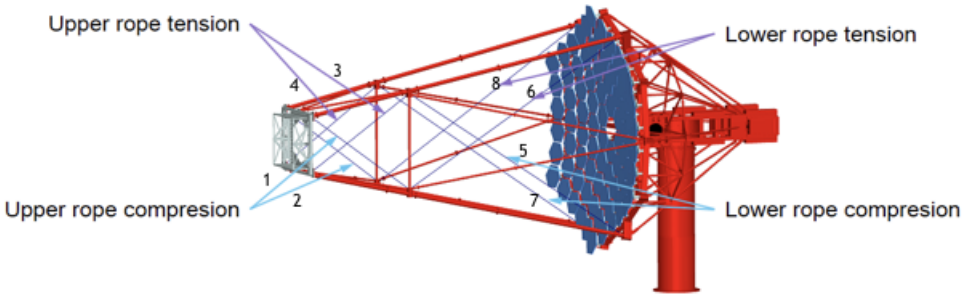

Figure 5.17.: The identification of the eight steel ropes of the CSS. Four ropes are tightened and four ropes are compressed when the telescopes moves from zenith to the horizon defining the tension and compression ropes.

Rope	**Initial state**	**Tighten (7.5 kN)**	**After operation**	**Release (Ropes 4 and 8)**	**Tighten (10 kN)**
1	0.00	2.16	2.19	2.01	4.18
2	0.00	3.45	3.20	0.00	5.09
3	10.80	14.00	14.00	14.50	18.00
4	10.4	16.90	16.50	13.00	19.6
5	0.00	2.86	2.54	2.38	4.49
6	7.53	12.60	12.50	12.70	15.10
7	0.00	2.78	2.34	0.00	4.19
8	8.36	12.90	12.60	8.09	14.90

Table 5.4.: Tension of the CSS steel ropes during the proof-of-concept. The tension was adjusted with the telescope pointing towards zenith and measured with the telescope pointing towards the horizon. The rope numbers are identified in Fig. 5.17.

tension ropes shown after the tightening procedures. The operation of the telescope in random directions for 10 minutes caused a slight decrease in the overall tension of the cables, though not significantly. The release of the *tension ropes* 4 and 8 to 3 kN at 90° elevation lead to a distortion of the CSS shape and resulted in a loss of pre-tension in ropes 2 and 7.

The data acquired during the proof-of-concept was analyzed with the OMA as it was described in Sec. 5.4. Figure 5.18 shows the first singular values of the FDD for each of the runs. A shift of 15 dB on the baseline was artificially introduced from the second run onward to improve the visualization of the spectrum in the same window. The first two peaks are very sensitive to the wind speed and, therefore, are noisy for the data-set acquired during strong winds. The wind speed throughout the proof-of-concept is shown in Fig. 5.19. The strongest winds happened during and after the data acquisition of the first relaxation (7.5 kN), which led to the higher

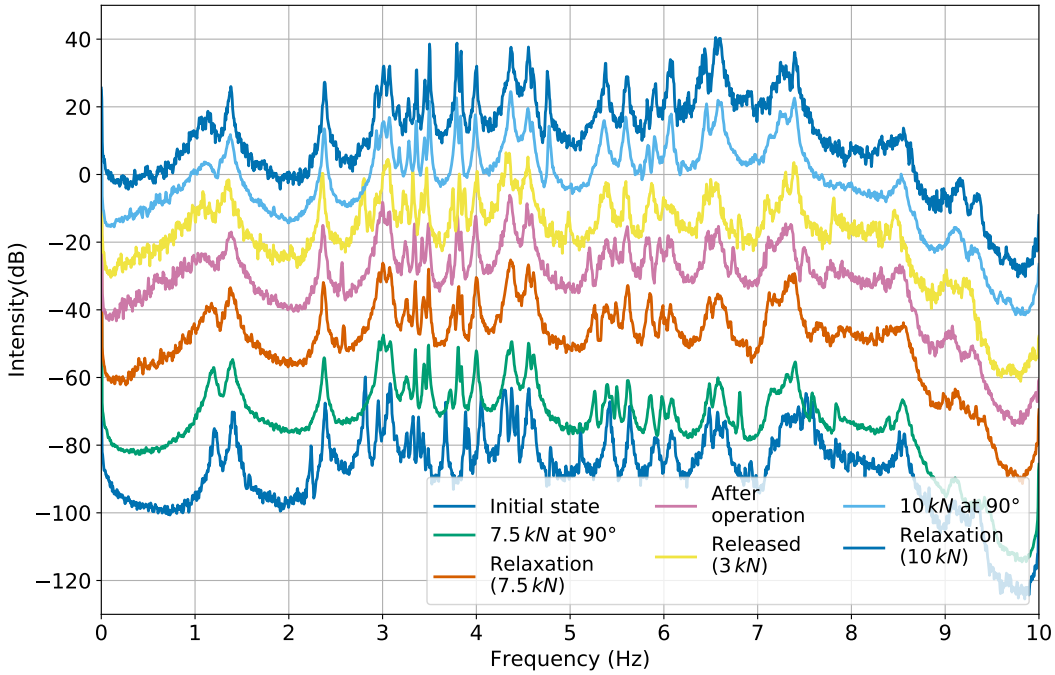

Figure 5.18.: The first singular values of each of the 15 minutes dedicated runs according to the test described in the text. The spectrum is artificially shifted by 15 dB at each step to facilitate visualisation.

noise detected in the first two peaks of the OMA first singular values in Fig. 5.18.

It is noticeable from Fig. 5.18 that the peaks change throughout the different steps of the test. The peak at 2.2 Hz, 3.7 Hz and 5.1 Hz in the initial state disappeared after the tightening of the ropes. It indicates that asymmetries in the structure are corrected through the homogeneous tightening of the cables. The peak at 2.8 Hz shifted to a higher frequency (3 Hz), while the peaks at 3.9 Hz and 4.1 Hz slightly shifted to lower frequencies, indicating that parts of the structure became softer and parts of it became stiffer, respectively. The three peaks around 4.4 Hz merged after the tightening, which is interpreted as correcting asymmetries in the structure. After the relaxation, a small peak appeared at 2.6 Hz and slightly increased after the operation of the telescope, which indicates a softening of the rope's tension after the relaxation as also confirmed by Tab. 5.4. By releasing the tension to 3 kN in ropes 4 and 8 (Fig. 5.17), the three peaks around 3 Hz split once more, and one of the modes reached down to 2.8 Hz. The splitting of peaks is interpreted as new Eigenmodes resulting from asymmetries created in the structure.

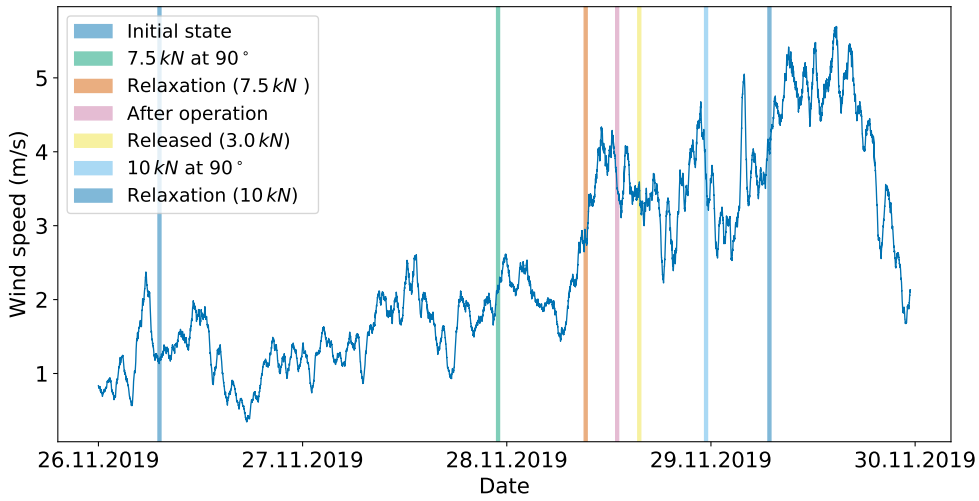

Figure 5.19.: Wind speed measured by the weather station at the MST prototype site during the proof-of-concept with the time windows indicating the 15 minutes during which the accelerometers acquired data.

Furthermore, after the release of the ropes, three peaks shifted to the right and two to the left within 3 and 4 Hz, showing different effects on the stiffness of different parts of the structure, and one peak appeared at 5 Hz, likely the return of the mode at 5.1 Hz from the initial state. The tightening of the ropes to 10 kN merged the peaks around $3\,Hz$ again, eliminating the asymmetries. Furthermore, it shifted the peaks between 3 and 4 Hz in the opposite direction compared to the step of releasing the tension. The peaks around 5 and 6 Hz became better defined, and two new peaks appeared, one at 3.2 Hz and the other at 4.8 Hz. The new peaks at a higher tension are interpreted as new Eigenmodes, which become accessible in a stiffer structure, likely related to the consequent tightening of the CSS main beams.

The eventual connection between the features in the OMA spectrum and their localization on the structure can only be achieved by a dedicated study and a higher number of sensors spread throughout the structure, which was not the scope of this work.

The test conducted at the prototype telescope structure showed that the implemented monitoring system is capable of detecting changes in the structure, at least regarding the tension of the CSS ropes. Long-term monitoring would indicate whenever the tension reaches critical levels and consequently when a maintenance service should be scheduled. Although not tested at the prototype, the system is also expected to detect other sources of changes, such as material degradation, cracks on the structure, loosening of screws, and any change in the structure

weight and stiffness. The study is just a beginning of a project planned to be continued once the first telescope is installed at the observatory site. Equipping all MSTs with such a structure monitoring system will allow us to study long-term evolution, as well as an alert in case a single or group of telescopes starts to behave differently.

5.6. The long-term monitoring of the structure parameters

A fully automatic operation of the structure monitoring system was executed in the period between September 5^{th}, 2019 and February 10^{th}, 2020. Every day at 6 *am* the telescope parked out, moved to the 0° elevation position, and took monitoring data for about one hour. The OMA analysis and a report followed automatically after the data acquisition. The automatic test continued almost until the end of the project. In January 2020, a problem in the local configuration prevented taking data until the end of the month, and in February, the telescope prototype structure was finally dismantled. Since only a single data-set taken in 2020 was available after the quality criteria, I decided to keep the long-term analysis in the time window between September 5^{th} and December 27^{th}, 2019.

During the mentioned period, the weather conditions varied under different aspects: humidity, rain, temperature, wind, and pressure. By strong winds, more complex modes are excited, and the FDD spectrum has more peaks. However, they cannot be properly monitored if they do not appear constantly. On the contrary, few modes are excited on weak wind days, and monitoring is also not possible. A definition of threshold and quality criteria was necessary to increase the method's reliability. Two of the weather variables monitored by the weather station were chosen due to their main role as the excitation force: the average wind speed and standard deviation of its direction during the period of data acquisition. Table 5.5 shows the definition of the adopted criteria. The average wind speed should not be too low; otherwise, fewer modes will be excited. On the other hand, powerful winds might excite more complex modes, not accessible in previous days. The wind direction shall vary during the data acquisition to assure that the structure is excited as a whole. Hence, a minimum value for the standard deviation of the wind direction is considered.

The other weather variables, such as temperature, humidity, and pressure, have a smaller influence on the modal parameters of the structure, at least in the period when the tests were performed. Strong seasonal variations between summer and winter time might influence the position of the Eigenfrequencies. Therefore, they were not included yet in the quality criteria. Diagrams were developed to facilitate the visualization of both the wind speed, direction, and time evolution, as shown in Fig. 5.20 for three different days. The length of the lines gives the wind speed, the Cartesian coordinates give the wind direction, and the color bar gives the time

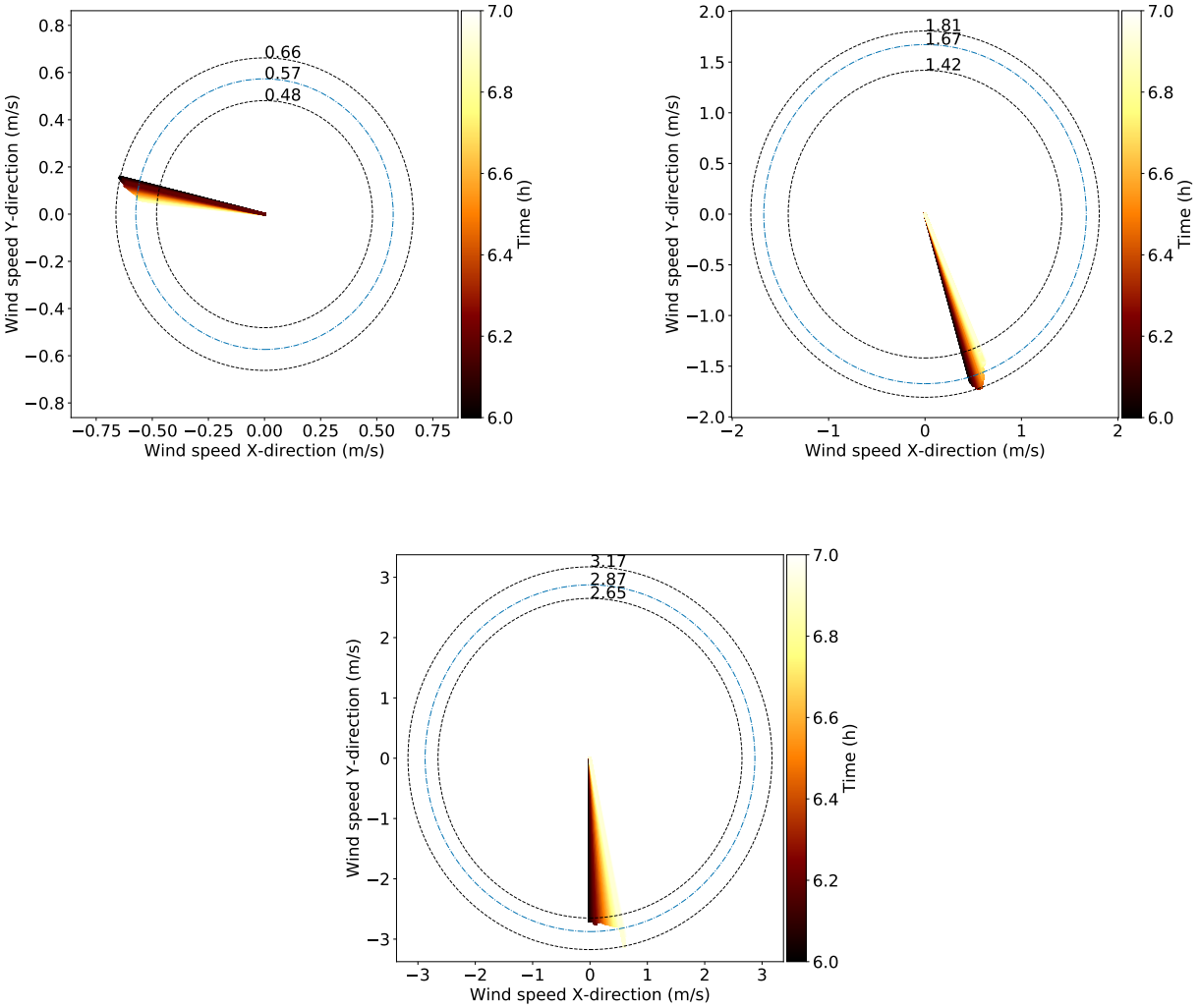

Figure 5.20.: Wind diagrams for: November 7$^{\text{th}}$ (upper left), December 25$^{\text{th}}$ (upper right) and December 10$^{\text{th}}$ (bottom), 2019. While the first and last diagrams have not passed the quality criteria due to very weak (0.57 m/s) and very strong (3.17 m/s) wind average, respectively, the second diagram (1.67 m/s) is qualified for further data analysis. The colors show the time of the measurement, the length of the lines represents the wind speed and its direction is given by the Cartesian plan with the North pointing upwards.

Parameter	Min.	Max.
Average wind speed (ms^{-1})	1	2.5
Standard deviation of the wind direction (°)	180	-

Table 5.5.: Quality criteria defined based on the wind strength and direction.

evolution during data acquisition.

After applying the quality criteria, the long-term tracking of the modal parameters becomes possible. For each modal frequency of a specific day, a MAC value was calculated between its mode shape and all the mode shapes of the next day. When the modes of subsequent days are correlated, their MAC value should be higher than 0.95. Figure 5.21 shows the tracking of related modal frequencies throughout the days. Black lines connect correlated modes. The same is shown for the damping ratio in Fig. 5.22. Many modal frequencies can be properly tracked, although some do not make it through the quality cut in days of weaker winds. More tracked modes would be achieved with a less strict MAC value, though at the same time, the system would be more susceptible to false alarms. The damping rate varies considerably throughout the days due to the uncertainties in its estimation, especially the two modes with frequencies close to 1 Hz, which appear to be very sensitive to wind speed. A break after November 26^{th} is seen in both figures, where only one correlation is found with the next day. It is the effect of the tests and adjustments of the CSS ropes tension (see Sec. 5.5), which resulted in a change of the structure and its modal parameters.

5.6.1. The monitoring of change indicators

The last step of the long-term analysis is defining the change indicators to be monitored. Since the system runs automatically, it shall decide whether there was an indication of a physical change in the structure. The positions of the correlated peaks are a good indicator, though the noisy modes might bias the result. For instance, a more effective indicator is based on the frequency variation of stable peaks, as present in the interval from 2 to 4.2 Hz in Fig. 5.21. Another difficulty in finding the right indicator to monitor is that an abrupt change in the structure also changes the mode shape itself; therefore, the modes of subsequent days might not be correlated up to the defined MAC value of 0.95.

Since the monitoring system is expected to detect both gradual and abrupt changes, I followed two different approaches: monitoring the change indicators and identifying groups by a machine

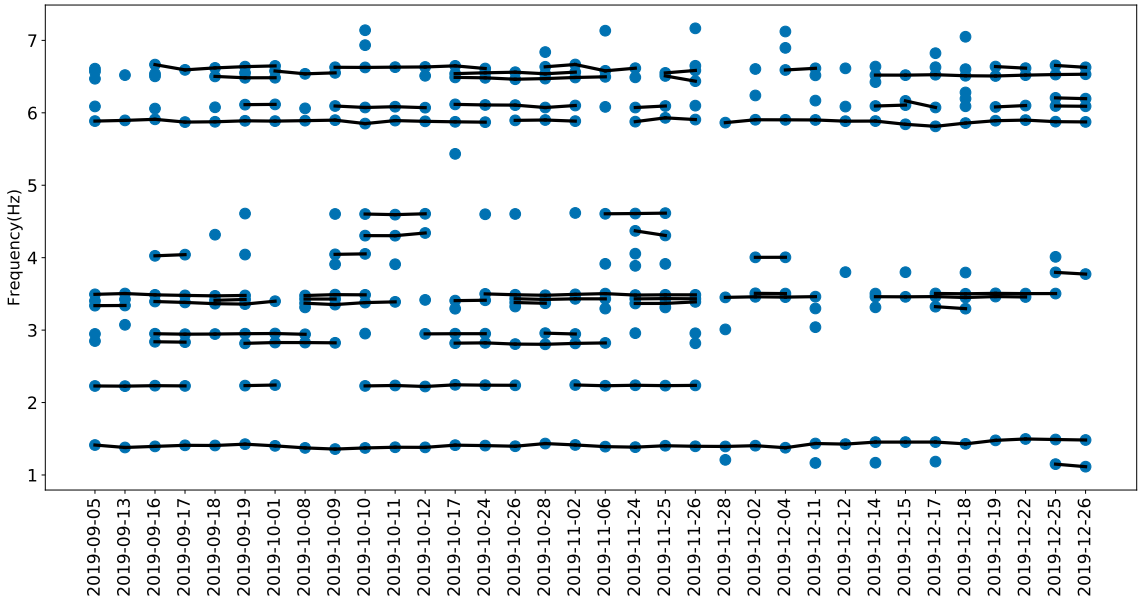

Figure 5.21.: Tracking of the modal frequencies in the long-term monitoring. The dots represent the modal frequencies of the day and the black lines connects whenever the modes of subsequent days are correlated.

learning algorithm. In the first case, the modal frequencies ν and damping rate δ in the defined safe region (2 to 4.2 Hz) are monitored by the change indicators α and β:

$$\begin{aligned} \alpha_i &= \Sigma_j^N (\nu_{i,j} - \nu_{0,j})^2 / N, \\ \beta_i &= \Sigma_j^N (\delta_{i,j} - \delta_{0,j})^2 / N, \end{aligned} \tag{5.10}$$

where the sum is calculated for the N correlations in the i-day, in comparison to the day 0, where the initial healthy state of the telescope is defined. The first day with good winds, September 5^{th}, was defined as the initial healthy state. Figure 5.23 and 5.24 show in blue the results for α and β. Both indicators vary randomly up to the day after the test, on November 28^{th}, where they became zero since no correlated mode shape was found with the healthy state. This change persists throughout the next days, indicating something happened to the structure. A new healthy state can be defined at November 28^{th} and the indicators calculated again as shown in the same figures by the green lines. No more changes were detected on the structure for the period, which is a good sign that the CSS ropes can keep the 10 kN pre-tension during at least one month. For gradual changes in the structure, the α and β indicators are expected to have a positive derivative and show a consistent rise with time. Nevertheless, during the short time

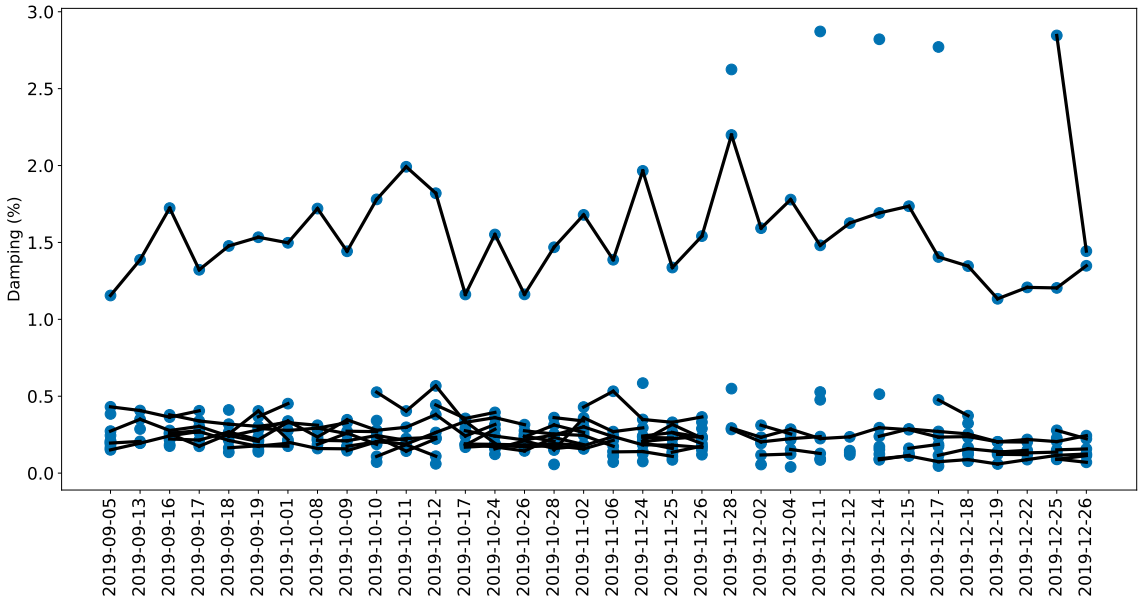

Figure 5.22.: Tracking of the damping ratio of the mode shapes in the long-term monitoring. The dots represent the damping ratio of the day, and the black lines connect whenever the modes of subsequent days are correlated. The big change in the highest damping rate from December 25$^{\text{th}}$ to December 26$^{\text{th}}$ corresponds to the unstable mode at 1.2 Hz and shall not be interpreted as caused by a change in the structure.

when the MST prototype was monitored, this behavior was not observed.

5.6.2. Monitoring of structural changes using Machine learning

The second approach for identifying a change in the structure is to apply a machine learning algorithm for unsupervised clustering. The algorithm is based on the Hierarchical Density-Based Spatial Clustering of Applications with Noise (HDBSCAN)[170,171]. It identifies different clusters in the ensemble of first singular value spectra (blue curve in Fig. 5.11). The advantage of this method is defining a 2D parameter space. The ensemble can be clustered in different groups; however, the defined parameters are not directly related to any physical quantity. The clustering algorithm was applied to the OMA spectrum (first singular values) from August 30$^{\text{th}}$ to February 10$^{\text{th}}$, although few data-sets were available in January and February. Figure 5.25 shows the clustering results. Four clusters were found, and some of the spectra remained unclustered (value = -1).

Spectra from the same cluster tend to be similar and reproduce the same features. Figures 5.26 to 5.30 show a sample of 4 spectra for each cluster, artificially shifted for better visualisation.

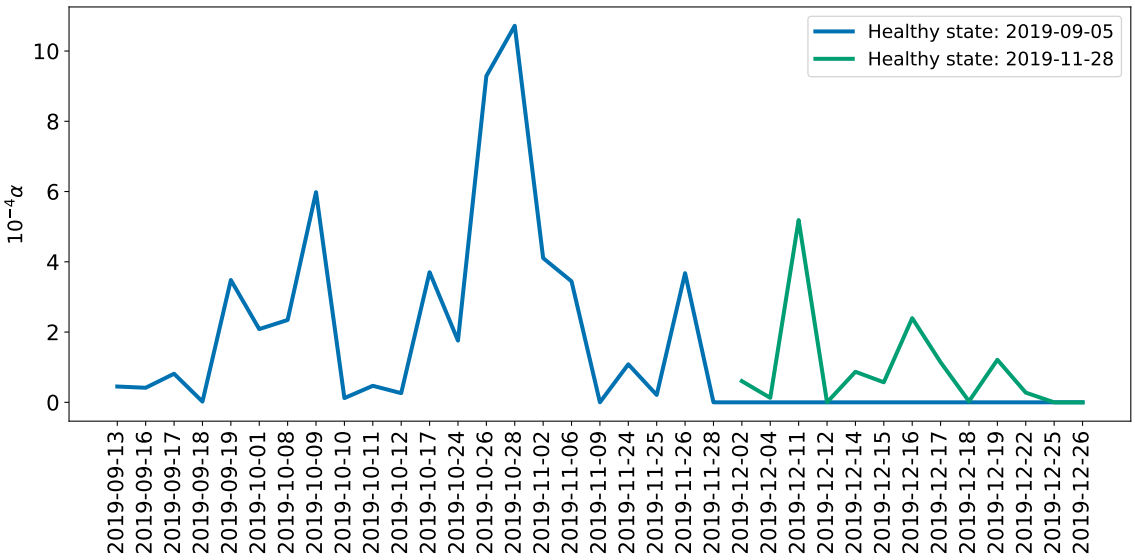

Figure 5.23.: α indicator (Eq. 5.10) throughout the days. The initial healthy state is defined as September 5^{th} and the second healthy state is defined as November 28^{th}. After November 28^{th} no correlation is found anymore with the initial state with the first healthy state.

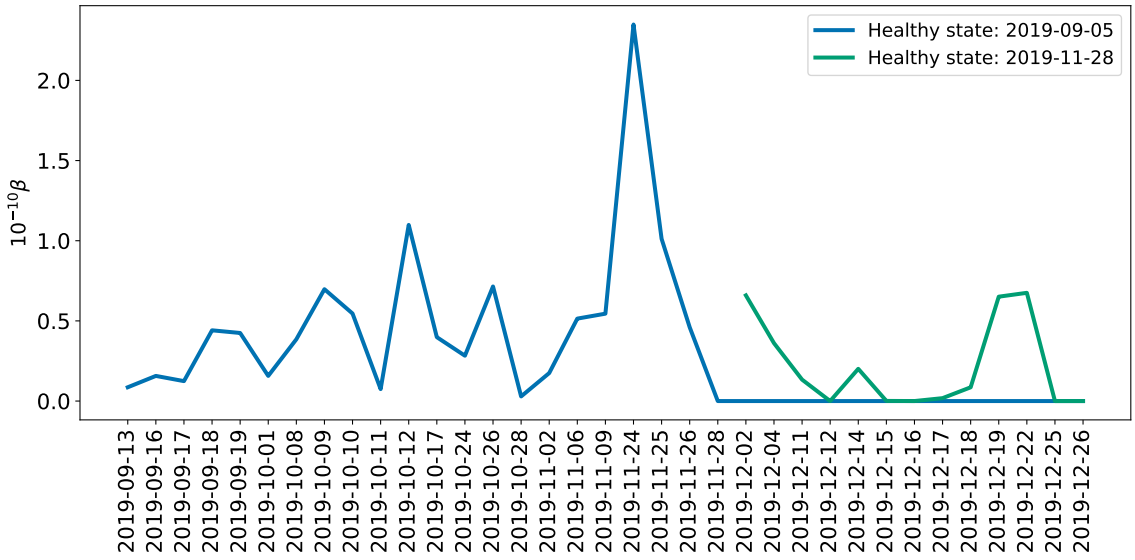

Figure 5.24.: β indicator (Eq. 5.10) throughout the days. The initial healthy state is defined as September 5^{th} and the second healthy state is defined as November 28^{th}. After November 28^{th} no correlation is found anymore with the initial state with the first healthy state.

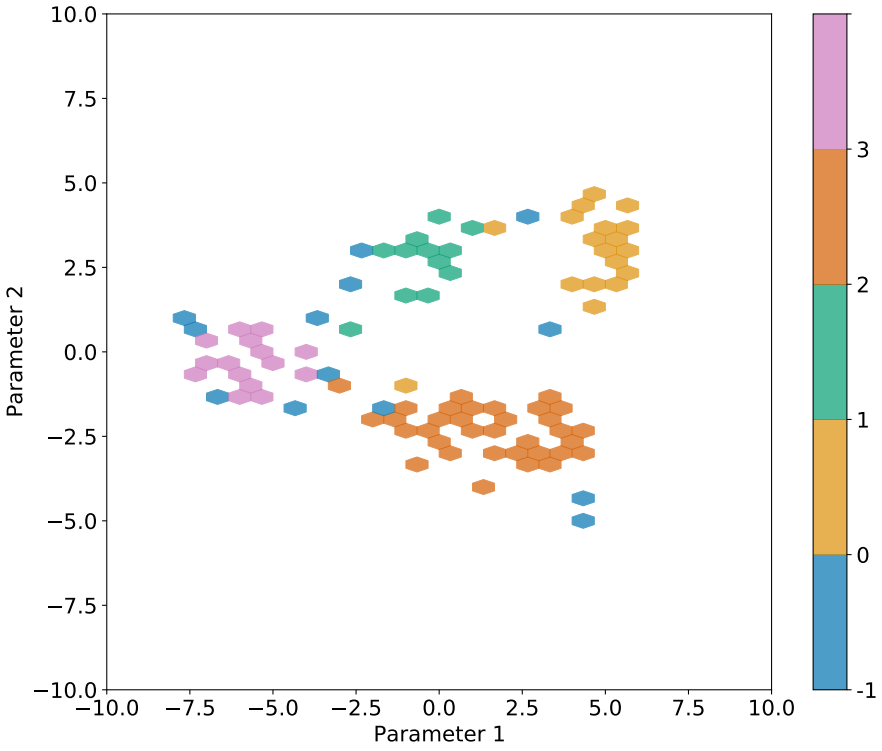

Figure 5.25.: The clustering of the OMA spectra from August 30$^{\text{th}}$, 2019 to December 26$^{\text{th}}$ based on the HDBSCAN algorithm. Each pixel is one OMA spectrum from one day. The parameters 1 and 2 in the X and Y axis are non-physical quantities derived from the machine learning algorithm. Four cluster (0 - 3) and a group of non-clustered (-1) spectra are derived.

Based on the previous knowledge of the spectrum shape, it is possible to distinguish these clusters into:

- **Cluster -1: Unclustered.** Various spectrum shapes, which does not fit any other cluster;
- **Cluster 0: Weak winds.** Weak wind days, identified by the low amplitude of the peaks, especially the first two ones;
- **Cluster 1: After the proof-of-concept.** After the proof-of-concept, where the ropes were tightened (Sec. 5.5), the 3 peaks around 3 Hz narrowed each other;
- **Cluster 2: Before the proof-of-concept.** Before the proof-of-concept, the 3 peaks around 3 Hz were more separated from each other in comparison to Cluster 1;

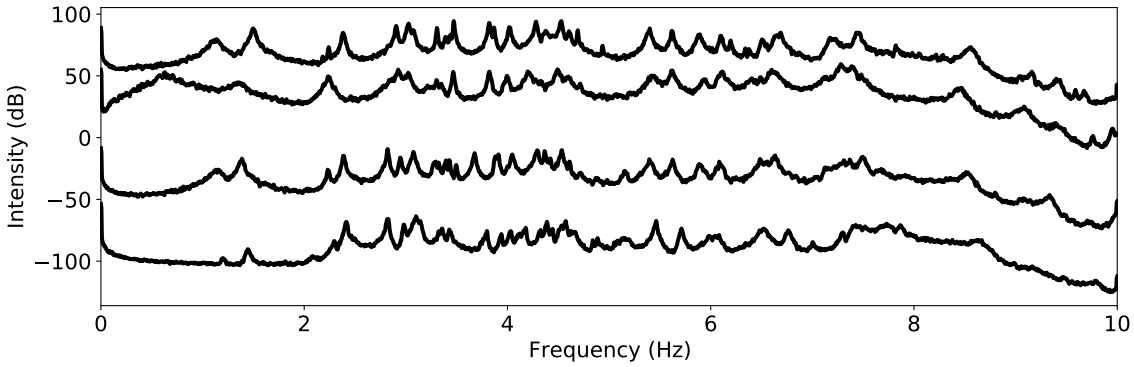

Figure 5.26.: Unclustered sample of OMA spectra.

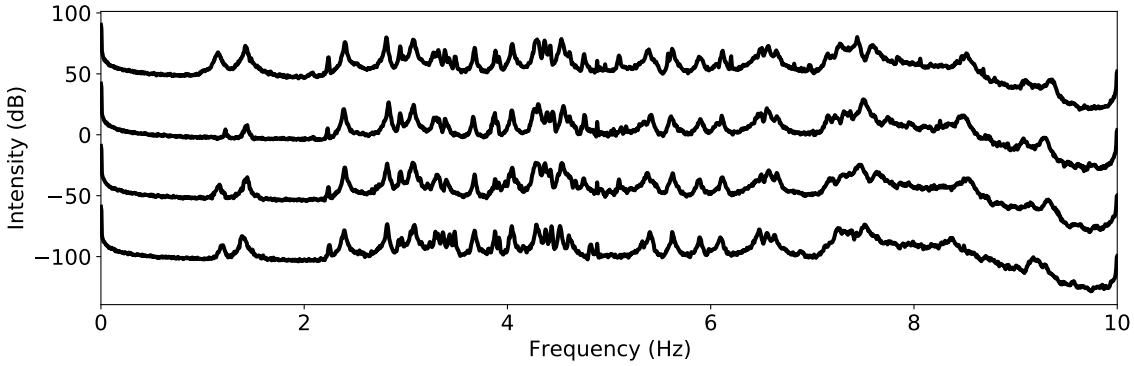

Figure 5.27.: Cluster 0 sample of OMA spectra.

- **Cluster 3: Strong winds.** Strong wind days, identified by the higher amplitude of the peaks and the noisy broad first two peaks.

A closer inspection of the average wind speed throughout the days confirms the interpretation of clusters 0 and 3. For clusters 1 and 2, it suffices to look at the dates and compare them to the date of the proof-of-concept (November 28$^{\text{th}}$, 2019), when the CSS ropes were tightened to 10 kN. Figure 5.31 shows the clustering versus the date. Stronger winds happened more frequently in December 2020, and the cluster changed from Cluster 2 to Cluster 1 exactly after the date of the tightening of the CSS ropes, confirming the interpretation of the results.

The structure monitoring system for the MSTs, as part of the larger set of monitoring parameters, has proven to be able to spot changes in the telescope structure. At the prototype, an automatic daily report from the OMA analysis was sent via email. The parameters will be added to a broader monitoring application in future operations. With the monitoring of all planned MSTs, a more extensive set of spectra will become available. The structure monitoring

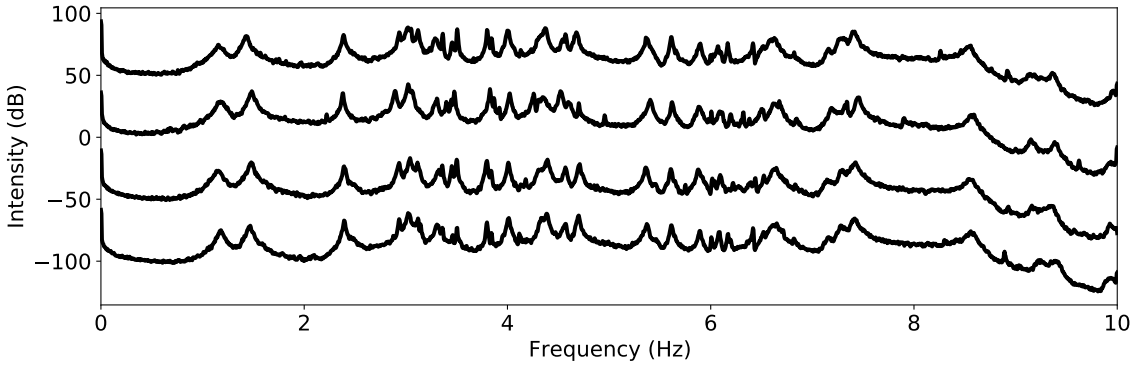

Figure 5.28.: Cluster 1 sample of OMA spectra.

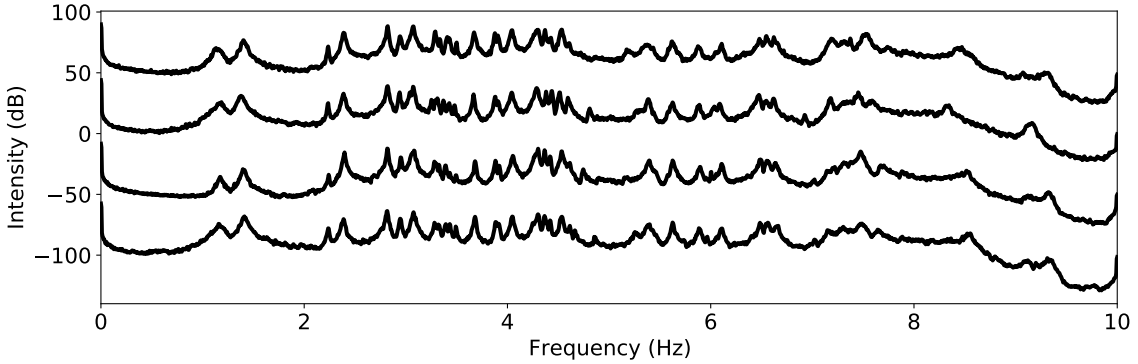

Figure 5.29.: Cluster 2 sample of OMA spectra.

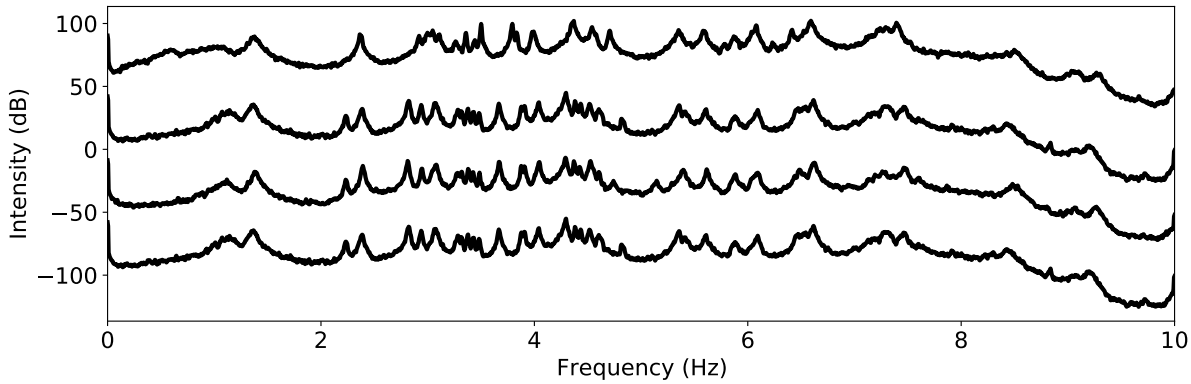

Figure 5.30.: Cluster 3 sample of OMA spectra.

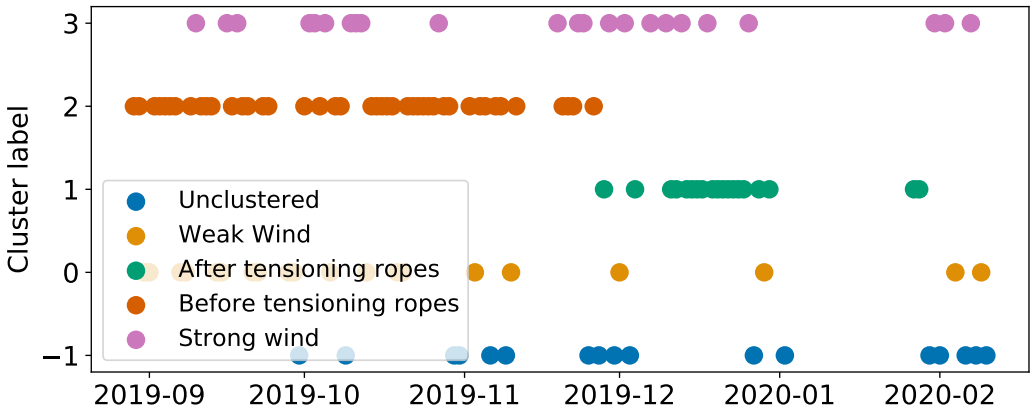

Figure 5.31.: Clusters throughout the time. The machine learning algorithm identified 4 different clusters: spectra from days with weak winds, spectra from days with strong winds, spectra from before the experiment of tightening the CSS ropes, and after the experiment. Unclustered spectra refer to spectra that are either unique or could fit more than one cluster simultaneously.

system I have designed will allow us to identify physical changes to the telescope's mechanical properties. Long-term monitoring and trend analysis of the natural frequencies, indicators, and clusters allows now to warn the maintenance team and schedule preventive maintenance activities before critical changes or damages occur. The dedicated test runs performed during the proof-of-concept allowed me to identify the corresponding frequencies and how their behavior was affected by the ropes tightening. More dedicated tests with other impacts, such as losing screwed connections, shall be carried out in the future to allow identifying other correlations. The implementation of the system at all MSTs will make it relatively easy to identify local changes from a single telescope when a group of telescopes will be available for comparisons. Finally, the monitoring system becomes a vital element of the telescope, which allows the observatory to reduce the maintenance efforts and keep the mechanical performance of the telescope stable over time.

Despite not being covered in this study, the accelerometers may also work as inclinometers, measuring the angle to the gravity direction at any moment. The potential of this application covers the estimation of the pointing accuracy, sagging, and the shift between the camera and dish structure during the tracking of sky coordinates. The combination of this application with the studies from the pointing accuracy extracted from the pointing model[53] and the telescope pointing position from the motor encoders will help further decrease the systematic uncertainties of the MSTs. Furthermore, with a long-term high telescope availability, assured by the correct

application of the structure monitoring system, and well understood systematic uncertainties, the CTAO will deliver its full potential regarding the key science projects[26].

As one of the most exciting sources, M87 will be observed by CTAO. Its gamma-ray morphology will be probed with a much better energy and angular resolution than the current IACTs. The potential to unravel the predicted hadronic emission (Sec. 4.5) and distinguish it from the core and the jet emission will help us understand the problem of cool core clusters (Sec. 3.3) and the role of cosmic rays in the dynamics of the galaxy and galaxy clusters. In the next section, I investigate the prospects of CTA observations of M87 using a similar approach as in Sec. 4.6, where I investigated the potential of further H.E.S.S. observation detecting the gamma-ray extension.

5.7. Prospects of M87's observations with CTA

According to the results shown in Sec. 4.6, the H.E.S.S. experiment will not be able to detect the gamma-ray extension of M87 given the steady-state model as described in Sec. 4.5. Nevertheless, CTAO will be able to deeper probe the extended gamma-ray emission due to its better angular resolution and sensitivity.

The CTA performance, i.e. the sensitivity, PSF, effective area and background are publicly available in CTAO (2021)[172]. The data-set consists of results of MC simulations for the Alpha Configuration of the Northern Array (Sec. 5.1), conducted for different zenith angles and time of observations. I used the data-set for 50 h of observations at a zenith angle of 40°, which is a relatively high zenith angle for M87, considering the location of the CTAO Northern Array. The 68.7% c.r. of the CTA PSF for this configuration reaches a level of $\approx 0.050°$, a factor 1.4 better than the H.E.S.S. PSF ($\approx 0.070°$). The pointing uncertainties of the CTA MSTs will be also improved in comparison to the H.E.S.S. telescopes and should reach the level of $7''$.

The tools developed for Sec. 4.6 helped generating two-dimensional sky maps for the background, PSF and effective area, with bin size of 0.01°, as in the H.E.S.S. analysis. Similarly to the study of further H.E.S.S. observations of M87 (Sec. 4.6), I created a CTA template for the diffuse (steady-state) emission of M87's low state (Sec. 4.5.1 and App. A.1). A template for the hybrid emission was also created with 10% of the emission due to the diffuse component, according to the H.E.S.S. low state emission ($1.4 \times 10^{-12}\,\mathrm{cm^{-2}\,s^{-1}}$ as shown in Tab. 4.3).

Figure 5.32 shows the excess counts, on the left, for the steady-state diffuse template and, on the right side, for the hybrid template, both convolved with the CTA PSF. The maximum intensity of the color map is fixed, for both sky maps, to the maximum value of the hybrid model, which corresponds mainly to the emission from the core.

Based on the template created for the hybrid emission, the On map, represented by the matrix

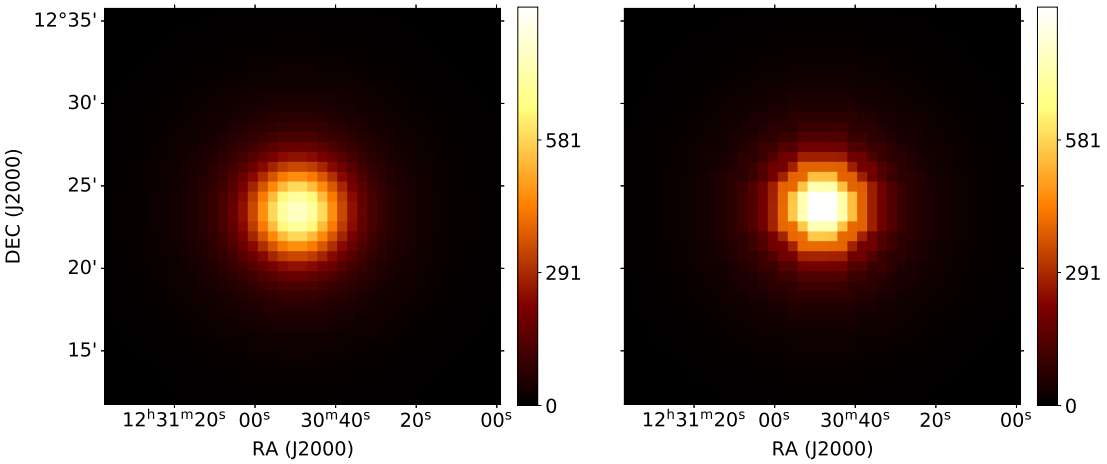

Figure 5.32.: Excess counts of the CTA template for the (left) steady state model and (right) hybrid model with 10% of the emission due to the diffuse component and 90% due to the core.

O, is defined as:

$$O = B + L \times T \odot E \tag{5.11}$$

where B is the background, T is the template for the hybrid emission, already convolved with the PSF, L is the live-time of observation, and E is the effective area. A set of live times ranging from 10 to 260 h were defined in steps of 50 h. At each live-time, a hundred sky maps were simulated for the On counts based on Eq. 5.11. The morphology of the simulated maps was fitted with a point-like and a Symmetrical Gaussian model, as in Ch. 4. The significance of the Symmetrical Gaussian model in comparison to the point-like model is given in Fig. 5.33 as a function of the live-time. The error bars indicate the $1\,\sigma$ standard deviation between the hundred simulated matrices at each live-time. The figure shows that CTA Northern Array will be able to significantly detect the gamma-ray extension from the M87's low state with about 210 hours of observation.

If the cosmic-rays pressure in the inner cluster turns out to be smaller than the prediction from the hadronic model, the diffuse gamma-ray emission would be fainter and even less extended. To investigate how small can the CTA Northern Array constrain the size of the extended gamma-ray emission, I conducted another set of simulations, as before, though for a pure point-like

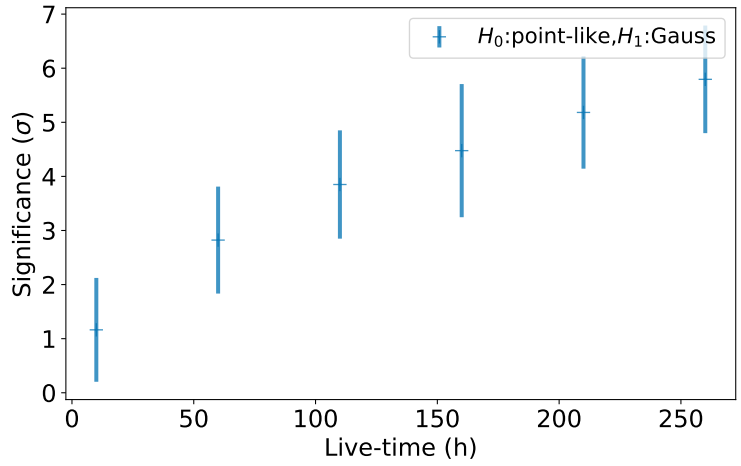

Figure 5.33.: Significance of the Symmetrical Gaussian model in comparison to the point-like model of the simulated maps with 10% contribution of the diffuse template. Each step in live-time corresponds to 100 simulated sky maps and the error bars give the 1 σ standard deviation among them.

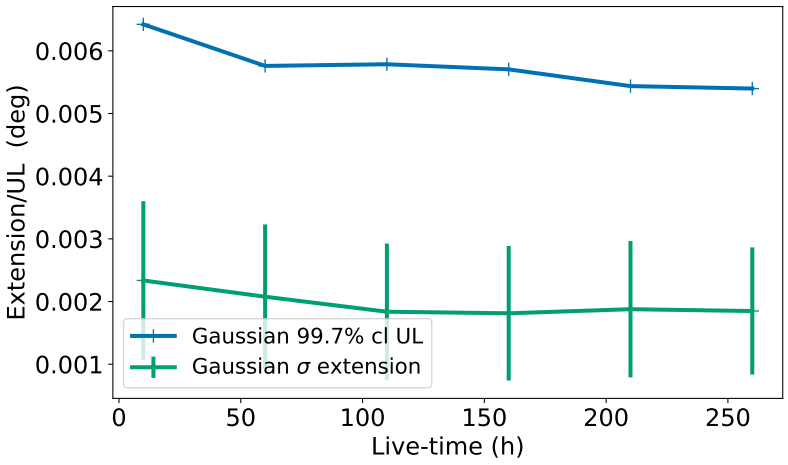

Figure 5.34.: The best fit Gaussian σ parameter and the 99.7% c.l. of the extension UL as function of the live-time for the simulations of a pure point-like emission as detected by CTA. Each step in live-time corresponds to 100 simulated sky maps.

template. Figure 5.34 shows the dependence of the 99.7% c.l. of the extension UL as function of the live-time. The extension UL of M87's gamma-ray low state is smaller than the bin size of the simulated sky maps (0.01°), which indicates a limitation of the morphology fit algorithm rather than a limitation in the CTAO angular resolution.

To illustrate the localizing power of CTAO for the simulated maps of a point-like emission region, Fig. 5.35 shows the average fit statistics of the simulations conducted for 210 h of observations. The results for the fit of a Gaussian model is depicted: the 1σ systematic ($7''$) and 1σ statistical uncertainties ($\approx 9''$) of the best fit position centered at M87's core and the 99.7% c.r. of the extension UL. The Chandra X-ray map of M87's jet[173] is shown for comparison in

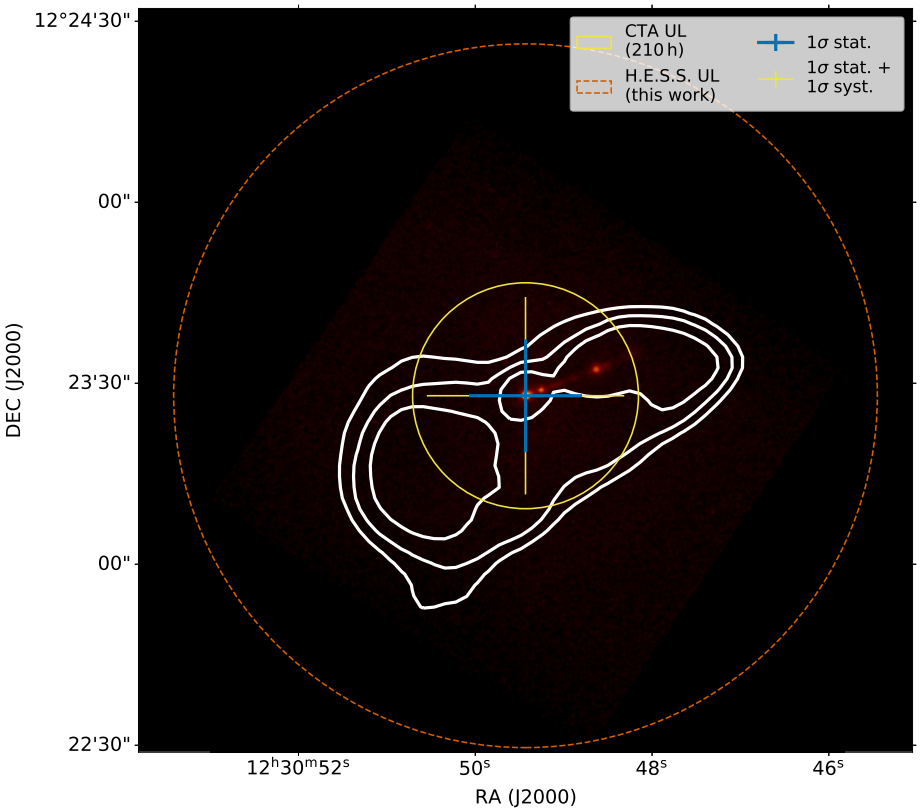

Figure 5.35.: The localizing power of CTAO 210 h of observations of M87. The square root of the Chandra X-ray map[173] is shown by the color intensity (a.u.) and the VLA radio 21.4 cm is shown by the white contours. The average 1σ uncertainty of the fitted Gaussian position of the 100 simulated maps at 210 h live-time is shown centered at M87's core with and without the systematic uncertainty. The extension UL of the predicted CTA observations and the H.E.S.S. results of Tab. 4.8 are shown for comparison.

colors and the VLA[151] radio 21.4 cm in contours. The figure shows that CTA will be able to probe the region inside the inner radio cocoon (white contours), though it will not be able to resolve the inner jet and distinguish a point-like emission within it. Nevertheless, this limitation might arise due to the bin size of the sky maps used in the simulations, which was kept at 0.01° as in the morphology fit of the H.E.S.S. sky maps. A new set of simulations with a smaller bin size could help improve the statistical uncertainties of the best-fit position and the extension UL. Furthermore, it would allow us to explore further the actual potential of CTAO resolving M87's jet structure.

Further studies of the CTAO sensitivity towards an extended emission in M87 would have to rely on simulated sky maps with smaller bin sizes. With better-resolved sky maps, the simulations would probe the size of the emission from the jet, for instance, through a morphology fit of a template based on the Chandra observations. Therefore, the perspectives of detecting an extended gamma-ray emission in M87 with CTAO are clear, and I am planning to continue the studies with more simulations, aiming at a later publication.

6. Conclusions

The main goal of the thesis was to search for extended VHE-gamma-ray emission from M87 and probe the propagation of relativistic protons from the base of the jet towards the ICM. The gamma-ray emission from the flares is believed to originate from very compact regions, likely from the VHE core[119]. On the other hand, the origin of the low state emission is not yet well established. No single-zone model for the SED emission of the VHE core manages to explain its emission including the gamma-ray data[114]. Different sub-structures are visible in high-resolution X-ray images, for instance, the prominent relativistic jet and the knots, which could also be the origin of the VHE low state emission. Relativistic electrons, accelerated in the core region, can explain the non-thermal emission up to the X-ray regime. The inner region of the Virgo Cluster is populated with a plasma of density $\approx 0.1\,\mathrm{cm}^{-3}$, which could act as target material for the inelastic scattering with relativistic protons, resulting in the production of charged and neutral pions. The neutral pions rapidly decay to gamma rays, which could be detected by H.E.S.S.[21,110].

The goal of the analysis was to separate the gamma-ray emission stemming from the jet and the gamma-ray resulting from relativistic protons interactions with the ICM by considering the VHE gamma-ray emission from M87's low-state. The first strategy adopted was to study the VHE gamma-ray light curve of M87 and compare it with the X-ray emission. The angular resolution of X-ray satellites, for instance, Chandra, is much better than the angular resolution of IACTs, which allows them to search for flux variations in the different sub-structures of the jet and compare with the core flux. A correlation between the X-ray emission of a specific sub-structure of the jet (core or HST -1) with the gamma-ray flux would indicate a common origin and facilitate the classification of the gamma-ray source states (Sec. 4.1). However, no correlation has been found, which motivated a Bayesian block analysis to derive the source states solely based on the VHE gamma-ray data (Sec. 4.2). The morphology fit of the gamma-ray source states showed no sign of an extension (Sec. 4.3). An extension UL of 16 mdeg ($\approx 5.4\,\mathrm{kpc}$) on the gamma-ray emission above 300 GeV of M87's low state was derived, improving the current best extension limit by a factor of 2 (Sec. 4.3.2). The best-fit position of M87's gamma-ray low state is $31''$ ($\approx 2.4\,\mathrm{kpc}$) away from the SMBH, though consistent with it and with several prominent X-ray features, such as the jet and the knots. On the other hand, the large-scale ($\approx 80\,\mathrm{kpc}$)

radio lobes[96] can be excluded as the main site of gamma-ray emission (Fig. 4.6). The best fit positions of the source states are compatible with each other and with the SMBH. The H.E.S.S. observations probe already the inner-most part of the Virgo Cluster, on the level of the optical half-light radius of the stars (7.2 kpc)[152].

I considered the scenario of diffuse emission from the Virgo Cluster and derived a gamma-ray template for its emission (Sec. 4.5.1). The morphology fit of the hybrid model, composed by the emission from the core and the template for the diffuse emission, provided an UL of 55% on the contribution of the diffuse component to the total gamma-ray low state emission. Furthermore, the H.E.S.S. UL on the diffuse component was used to constrain the ratio of the cosmic-ray to thermal pressure down to $X_{CR,\mathrm{max}} = X_{CR}(3.3\,\mathrm{kpc}) = 0.52$ at the position of its maximum (Sec. 4.5.4). This limit does not constrain the model from Jacob & Pfrommer (2017)[21], since the ratio of cosmic-ray pressure to thermal pressure predicted by the model is already lower ($X_{CR,\mathrm{max}} \approx 0.1$, see Fig. 4.13) than the H.E.S.S. flux UL. Further studies of the cosmic-ray pressure in the Virgo Cluster with H.E.S.S. could consider the estimation of the gamma-ray flux UL at larger distances from the cluster center, where no AGN related activity is expected to contribute to the measurement. In this case, a broader profile for the cosmic-ray distribution would have to be considered, as in Ackermann et al. (2015)[24], and the average of the ratio of cosmic-ray to thermal pressure $\langle X_{CR} \rangle$ could be estimated up to the virial radius of the cluster.

As an alternative to the hadronic scenario, I fitted a single zone leptonic model of the SED to describe the X-ray and gamma-ray emission from M87's low state. The results showed that the emissions are compatible with a single region, as long as there is particle dominance of $\sim 10^5$. Such high particle dominance indicates an emission region far from the vicinity of the SMBH, where a mildly magnetic dominance is observed[114].

The derived UL on the extension does not reach the level necessary to probe the jet and knot regions as the origin of the gamma-ray emission. Furthermore, it also does not exclude the diffuse emission as predicted by the steady-state model[21,110]. Therefore, I investigated the potential of H.E.S.S. towards deeper observations (Sec. 4.6). I developed an algorithm to simulate sky maps from the hybrid model, composed of the steady-state hadronic model and the core emission, and fitted their morphology. I could show that even with a very deep exposure of up to 800 h of observations, H.E.S.S. will not be able to resolve the cluster emission as predicted by the hadronic steady-state model[21,110]. Since the history of the particle injection and the consequent radiative processes along the jet are unknown, the steady-state model does not consider them. Furthermore, the gravitational potential used in Jacob & Pfrommer (2017)[21] is governed by assumptions of the underlying dark matter distribution to satisfy the standard cosmological model of the universe. Given that the assumptions of the steady-state model are not necessarily true, H.E.S.S. could still manage to constrain more generalized models, which take

into consideration different radial distributions of the relativistic protons. A more generalized model could be generated based on the radio observations, which trace the location of relativistic electrons. The Low-Frequency Array (LOFAR)[174], a new generation of radio telescopes, has measured M87's radio lobes with high quality and has shown that the morphology does not change with the energy for frequencies of the order of GHz[96]. This result indicates that the cooled electrons are in a steady-state trapped within the halos by the local magnetic field and by the pressure exerted by the ICM. The distribution of relativistic protons could also follow the halo's shape and be trapped by it. To extend the studies of this thesis, I would like to investigate the cluster emission based on the LOFAR template, which will provide a more generalized limit on the hadronic component of the gamma-ray emission.

To improve further the results of the M87's morphology in gamma rays with H.E.S.S. the Precision Pointing (Sec. 2.3.5) could be applied to the H.E.S.S. observations. The method uses CCD images of known stars taken during observations to correct the pointing accuracy of the telescopes. It can improve the systematic uncertainties of the pointing from $20''$ down to $6''$, which would result in smaller statistical uncertainties of the best-fit position of the morphology fits. Therefore, the source could be better localized with the method. Nevertheless, the PSF would remain the same, and the sensitivity of the H.E.S.S. telescopes towards an extended emission would also remain unchanged.

The second part of my thesis deals with the next generation of IACTs, the CTAO. Chapter 5 describes my contribution to it, through the development of the MST structure monitoring system (Sec. 5.3). The system is based on vibration measurements and the OMA method. The monitoring system tracks the telescope Eigenfrequencies and the respective damping rate throughout time. Based on the changes in these parameters, changes in the MSTs structures can be identified, and alerts can be issued. The goal of the system is to avoid major failures by acting upon the warnings of structural changes (predictive maintenance), for instance, the tension of the CSS ropes, which proved to largely influence the Eigenfrequencies (Sec. 5.5). The changes in the structure could be identified according to two different methods. The first method is based on the definition of the α and β parameters, which account for changes in the Eigenfrequencies and damping rate, respectively, according to a past known healthy state (Sec. 5.6). Secondly, I adapted a machine learning algorithm based on clustering to identify different states (Sec. 5.6.2). The algorithm proved to be sensitive to the pre-tensioning of the cables and even to different states caused by very strong and very weak winds. The system was successfully tested on the MST prototype in 2019 and 2020 in Berlin and will be installed on all future MSTs.

Despite not being investigated with the MST prototype, seasonal changes such as the temperature and the long-term operation of the telescopes might affect the stability of the telescopes

and the quality of the acquired gamma-ray data. Therefore, the MST structure monitoring system will help CTAO to keep the telescopes in a healthy state and available for observations. The full potential of CTAO for delivering its key science results[26] will only be explored with the long-term availability of the telescopes and the high-quality acquired data. Keeping the systematic uncertainties such as the pointing accuracy under control will improve the precision of the localization of gamma-ray emission regions and the capabilities of morphology studies in the various sources. CTAO Northern Array (Alpha configuration) is expected to achieve a PSF 1.4 times better than H.E.S.S. (Sec. 5.7), which will ultimately allow CTAO to probe a possible extension of M87 and the Virgo Cluster. Contemporaneous MWL observations and the combination of data sets across IACTs will help better to determine the low-state emission association to the jet and knot structures (Fig. 4.1).

Based on the released CTAO performance of the Alpha configuration, I simulated sky maps and fitted their morphology. The results showed that 210 h of M87's observations would be sufficient to significantly unravel an extended gamma-ray emission assuming that the system is in a steady-state (Sec. 5.7). I would like in the future to improve the simulations and investigate the sensitivity of CTAO towards an emission from the inner jet and the X-ray knots by using a smaller bin size for the simulated sky maps. CTAO offers good perspectives on unraveling an extended gamma-ray emission from M87's low state either due to π^0 decay or due to jet emission. The detection of jet emission would support the interpretation from Abdalla et al. (2020)[74] that large-scale jets of radio-loud AGN are commonplace for the acceleration of relativistic electrons. On the other hand, the detection of diffuse emission from the Virgo Cluster would offer a solution for the CF problem. Furthermore, it would allow the estimation of the contribution of radio-galaxies to the total flux of VHE cosmic rays detected at Earth, helping unravel the hundred years mystery of their origin.

Bibliography

[1] N. Copernicus, *On the revolutions of heavenly spheres*, Prometheus Books, **2010**.

[2] A. V. Helden, "The Invention of the Telescope", *Transactions of the American Philosophical Society* **1977**, *67*, 1–67, http://www.jstor.org/stable/1006276.

[3] G. Galilei, *Sidereus Nuncius, or the sidereal messenger*, University of Chicago Press, **2016**.

[4] S Abdollahi et al., "Fermi Large Area Telescope Fourth Source Catalog", *The Astrophysical Journal Supplement Series* **2020**, *247*, 33, DOI 10.3847/1538-4365/ab6bcb.

[5] P. Morrison, "On gamma-ray astronomy", *Il Nuovo Cimento* **1958**, *7*, 858–865, DOI 10.1007/BF02745590.

[6] V. Hess, "Über Beobachtungen der durchdringenden Strahlung bei sieben Freiballonfahrten", *Physicalische Zeitschrift*, *13*, 1084 –1091, https://inspirehep.net/literature/1623161.

[7] W. Kraushaar et al., "Explorer XI Experiment on Cosmic Gamma Rays.", *Astrophysical Journal* **1965**, *141*, 845, DOI 10.1086/148179.

[8] National Aeronautics and Space Administration Goddard Space Flight Center, NASA's HEASARC: Observatories, https://heasarc.gsfc.nasa.gov/docs/heasarc/missions/oso3.html, (Accessed: 22 November 2021).

[9] Kraushaar et al., "High-energy cosmic gamma-ray observations from the OSO-3 satellite", *The Astrophysical Journal* **1972**, *171*, 341–363, DOI 10.1086/151713.

[10] L. Evans, P. Bryant, "LHC Machine", *Journal of Instrumentation* **2008**, *3*, DOI 10.1088/1748-0221/3/08/S08001.

[11] G. Giavitto et al., "The upgrade of the H.E.S.S. cameras", *Nuclear Instruments and Methods in Physics Research Section A: Accelerators Spectrometers Detectors and Associated Equipment* **2017**, *876*, 35–38, DOI 10.1016/j.nima.2016.12.057.

[12] J. Aleksić et al., "The major upgrade of the MAGIC telescopes, Part II: A performance study using observations of the Crab Nebula", *Astroparticle Physics* **2016**, *72*, 76–94, DOI 10.1016/j.astropartphys.2015.02.005.

[13] D. B. Kieda, "The gamma ray detection sensitivity of the upgraded VERITAS observatory", *Proceedings of the 33rd International Cosmic Rays Conference ICRC 2013* **2013**, *2013-October*, https://inspirehep.net/literature/1250279.

[14] G. Di Sciascio, "The LHAASO experiment: From Gamma-Ray Astronomy to Cosmic Rays", *Nuclear and Particle Physics Proceedings* **2016**, *279-281*, 166–173, DOI 10.1016/j.nuclphysbps.2016.10.024.

[15] J. P. Blakeslee et al., "The ACS Fornax cluster survey. V. Measurement and recalibration of surface brightness fluctuations and a precise value of the Fornax-Virgo relative distance", *Astrophysical Journal* **2009**, *694*, 556–572, DOI 10.1088/0004-637X/694/1/556.

[16] S. Bird et al., "The inner halo of M 87: A first direct view of the red-giant population", *Astronomy and Astrophysics* **2010**, *524*, 1–9, DOI 10.1051/0004-6361/201014876.

[17] K. Akiyama et al., "First M87 Event Horizon Telescope Results. VI. The Shadow and Mass of the Central Black Hole", *The Astrophysical Journal Letters* **2019**, *875*, 44, DOI 10.3847/2041-8213/ab1141.

[18] S. Kim et al., "The extended Virgo Cluster catalog", *Astrophysical Journal Supplement Series* **2015**, *215*, DOI 10.1088/0067-0049/215/2/22.

[19] D. S. Hudson et al., "What is a cool-core cluster? a detailed analysis of the cores of the X-ray flux-limited HIFLUGCS cluster sample", *Astronomy and Astrophysics* **2010**, *513*, 1–40, DOI 10.1051/0004-6361/200912377.

[20] J. R. Peterson, A. C. Fabian, "X-ray spectroscopy of cooling clusters", *Physics Reports* **2006**, *427*, 1–39, DOI 10.1016/j.physrep.2005.12.007.

[21] S. Jacob, C. Pfrommer, "Cosmic ray heating in cool core clusters - I. Diversity of steady state solutions", *Monthly Notices of the Royal Astronomical Society* **2017**, *467*, 1449–1477, DOI 10.1093/mnras/stx131.

[22] A. Pinzke, C. Pfrommer, L. Bergström, "Prospects of detecting gamma-ray emission from galaxy clusters: Cosmic rays and dark matter annihilations", *Physical Review D - Particles Fields Gravitation and Cosmology* **2011**, *84*, 1–43, DOI 10.1103/PhysRevD.84.123509.

[23] M. Ackermann et al., "Search for cosmic-ray-induced gamma-ray emission in galaxy clusters", *Astrophysical Journal* **2014**, *787*, DOI 10.1088/0004-637X/787/1/18.

[24] M. Ackermann et al., "Search for extended gamm-ray emission from the Virgo galaxy cluster with Fermi-LAT", *Astrophysical Journal* **2015**, *812*, DOI 10.1088/0004-637X/812/2/159.

[25] J. H. Matthews et al., "Fornax A, Centaurus A, and other radio galaxies as sources of ultrahigh energy cosmic rays", *Monthly Notices of the Royal Astronomical Society: Letters* **2018**, *479*, L76–L80, DOI 10.1093/mnrasl/sly099.

[26] The Cherenkov Telescope Array Consortium, *Science with the Cherenkov Telescope Array*, World Scientific, **2019**, DOI 10.1142/10986.

[27] CTAO Astrodiversity Project, Best practices for colour blind friendly publications & descriptions, https://www.cta-observatory.org/wp-content/uploads/2021/02/CTA_ColourBlindnessBestPractices.pdf, (Accessed: 24 November 2021).

[28] V. Martins et al., "A condition monitoring concept studied at the MST prototype for the Cherenkov Telescope array", *36th International Cosmic Ray Conference -ICRC2019* **2019**, *358*, https://arxiv.org/abs/1908.02180.

[29] Barbosa Martins, Victor and Garczarczyk, Markus, "The structure monitoring of the Medium-sized Telescope (MST) prototype of Cherenkov Telescope Array (CTA)", *Ground-based and Airborne Telescopes VIII* **2020**, (Eds.: H. K. Marshall, J. Spyromilio, T. Usuda), DOI 10.1117/12.2560930, http://dx.doi.org/10.1117/12.2560930.

[30] MPI, Arrangement of the telescopes, https://www.mpi-hd.mpg.de/hfm/HESS/pages/about/telescopes/, (Accessed: 17 May 2021).

[31] MPI, H.E.S.S. Experiment, https://www.mpi-hd.mpg.de/hfm/HESS/, (Accessed: 17 May 2021).

[32] R. Chalmé-Calvet et al., "Exploiting the time of arrival of Cherenkov photons at the 28 m H.E.S.S. telescope for background rejection: Methods and performance", *Proceedings of Science* **2015**, *30-July-2015*, DOI 10.22323/1.236.0842.

[33] MPI, Characteristics of the H.E.S.S. telescopes, https://www.mpi-hd.mpg.de/hfm/HESS/pages/about/HESS_I_II/, (Accessed: 17 May 2021).

[34] J. Matthews, "A Heitler model of extensive air showers", *Astroparticle Physics* **2005**, *22*, 387–397, DOI 10.1016/j.astropartphys.2004.09.003.

[35] J. K. Fabian Schmidt, Imaging Atmospheric Cherenkov Technique, https://www-zeuthen.desy.de/~jknapp/fs/showerimages.html, (Accessed: 12 September 2021).

[36] P. A. Ćerenkov, "Radiation of particles moving at a velocity exceeding that of light, and some of the possibilities for their use in experimental physics", *Nobel Lecture* **1958**, https://www.nobelprize.org/uploads/2018/06/cerenkov-lecture.pdf.

[37] I. Frank, I. TAMM, "Coherent visible radiation of fast electrons passing through matter", *Comptes Rendus (Doklady) de l' Aeademie des Sciences .de l'URSS* **1937**, *14*, 109–114, DOI 10.1007/978-3-642-74626-0_2.

[38] T. C. Weekes et al., "Observation of TeV gamma rays from the Crab nebula using the atmospheric Cerenkov imaging technique", *The Astrophysical Journal* **1989**, *342*, 379, DOI 10.1086/167599.

[39] D. I. Meyer et al., "Detection of TeV photons from the active galaxy Markarian 421", *Letters to Nature* **1992**, *358*, 477–478, DOI 10.1038/358477a0.

[40] A. Barrau et al., "The CAT imaging telescope for very-high-energy gamma-ray astronomy", *Nuclear Instruments and Methods in Physics Research Section A: Accelerators Spectrometers Detectors and Associated Equipment* **1998**, *416*, 278–292, DOI 10.1016/S0168-9002(98)00749-9.

[41] F. Aharonian et al., "Measurement of the flux, spectrum, and variability of TeV γ-rays from Mkn 501 during a state of high activity", *Astronomy and Astrophysics* **1997**, *327*, 7–10, https://arxiv.org/abs/astro-ph/9706019.

[42] R Enomoto et al., "Design study of CANGAROO-III, stereoscopic imaging atmospheric Cherenkov telescopes for sub-TeV γ-ray detection", *Astroparticle Physics* **2002**, *16*, 235–244, DOI https://doi.org/10.1016/S0927-6505(01)00112-8.

[43] L. A. Antonelli, "The Next Generation of Cherenkov Telescopes", *Memorie della Societa Astronomica Italiana - Journal of the Italian Astronomical Society* **2009**, *14*, 250–253, https://arxiv.org/pdf/0906.4114.pdf.

[44] J. M. Davies, E. S. Cotton, "Design of the quartermaster solar furnace", *Solar Energy* **1957**, *1*, 16–22, DOI https://doi.org/10.1016/0038-092X(57)90116-0.

[45] S. Gillessen, PhD thesis, Ruperto-Carola University of Heidelberg, **2004**, http://archiv.ub.uni-heidelberg.de/volltextserver/4754/.

[46] K. Bernlöhr, "Simulation of imaging atmospheric Cherenkov telescopes with CORSIKA and sim$_t$*elarray*", *Astroparticle Physics* **2008**, *30*, 149–158, DOI https://doi.org/10.1016/j.astropartphys.2008.07.009.

[47] R Cornils et al., "The optical system of the H.E.S.S. imaging atmospheric Cherenkov telescopes. Part II: mirror alignment and point spread function", *Astroparticle Physics* **2003**, *20*, 129–143, DOI https://doi.org/10.1016/S0927-6505(03)00172-5.

[48] S Funk et al., "The trigger system of the H.E.S.S. telescope array", *Astroparticle Physics* **2004**, *22*, 285–296, DOI https://doi.org/10.1016/j.astropartphys.2004.08.001.

[49] B. Bi et al., "Performance of the new FlashCam-based camera in the 28m telescope of H.E.S.S.", *Proceedings of 37th International Cosmic Ray Conference — PoS(ICRC2021)* **2021**, DOI 10.22323/1.395.0743, http://dx.doi.org/10.22323/1.395.0743.

[50] T. Ashton et al., "A NECTAr-based upgrade for the Cherenkov cameras of the H.E.S.S. 12-meter telescopes", *Astroparticle Physics* **2020**, *118*, DOI 10.1016/j.astropartphys.2019.102425.

[51] Aharonian, F. et al., "Very high energy gamma rays from the direction of Sagittarius A*", *A&A* **2004**, *425*, L13–L17, DOI 10.1051/0004-6361:200400055.

[52] F. Aharonian et al., "Observations of the Crab nebula with HESS", *Astronomy and Astrophysics* **2006**, *457*, 899–915, DOI 10.1051/0004-6361:20065351.

[53] G. Spengler, U. Schwanke, D. Zhurov, "CTbend: A Bayesian open-source framework to model pointing corrections of Cherenkov telescopes", *ICRC* **2021**, *37*, 699, DOI 10.22323/1.395.0699.

[54] I. Braun, PhD thesis, Ruperto-Carola University of Heidelberg, **2007**, p. 135, https://archiv.ub.uni-heidelberg.de/volltextserver/7354/.

[55] F. Acero et al., "Localizing the VHE γ-ray source at the galactic centre", *Monthly Notices of the Royal Astronomical Society* **2010**, *402*, 1877–1882, DOI 10.1111/j.1365-2966.2009.16014.x.

[56] M. Haupt, PhD thesis, Potsdam University, **2020**, https://publishup.uni-potsdam.de/opus4-ubp/frontdoor/deliver/index/docId/47460/file/haupt_diss.pdf.

[57] M. K. Daniel, "The Atmospheric Monitoring Strategy for the Cherenkov Telescope Array", *Journal of Physics: Conference Series* **2015**, *595*, 12009, DOI 10.1088/1742-6596/595/1/012009.

[58] J Hahn et al., "Impact of aerosols and adverse atmospheric conditions on the data quality for spectral analysis of the H.E.S.S. telescopes", *Astroparticle Physics* **2014**, *54*, 25–32, DOI https://doi.org/10.1016/j.astropartphys.2013.10.003.

[59] T. L. Holch, PhD thesis, Humboldt Universität zu Berlin, **2020**, https://edoc.hu-berlin.de/handle/18452/23124.

[60] A. Hillas, "Cherenkov light images of EAS produced by primary gamma-rays and by nuclei", *International Cosmic Ray Conference (ICRC 1985)* **1985**, https://ui.adsabs.harvard.edu/abs/1985ICRC....3..445H.

[61] M. de Naurois, "Analysis methods for Atmospheric Cerenkov Telescopes", *7th Workshop on Towards a Network of Atmospheric Cherenkov Detectors 2005* **2006**, 149–161, https://inspirehep.net/literature/721331.

[62] F. A. Aharonian et al., "The potential of ground based arrays of imaging atmospheric Cherenkov telescopes. I. Determination of shower parameters", *Astroparticle Physics* **1997**, *6*, 343–368, DOI 10.1016/S0927-6505(96)00069-2.

[63] S. Le Bohec et al., "A new analysis method for very high definition Imaging Atmospheric Cherenkov Telescopes as applied to the CAT telescope", *Nuclear Instruments and Methods in Physics Research Section A: Accelerators Spectrometers Detectors and Associated Equipment* **1998**, *416*, 425–437, DOI 10.1016/S0168-9002(98)00750-5.

[64] M. de Naurois, L. Rolland, "A high performance likelihood reconstruction of γ-rays for imaging atmospheric Cherenkov telescopes", *Astroparticle Physics* **2009**, *32*, 231–252, DOI 10.1016/j.astropartphys.2009.09.001.

[65] R. D. Parsons, J. A. Hinton, "A Monte Carlo template based analysis for air-Cherenkov arrays", *Astroparticle Physics* **2014**, *56*, 26–34, DOI 10.1016/j.astropartphys.2014.03.002.

[66] S. Ohm, C. van Eldik, K. Egberts, "γ/Hadron Separation in Very-High-Energy γ-Ray Astronomy Using a Multivariate Analysis Method", *Astroparticle Physics* **2009**, *31*, 383–391, DOI 10.1016/j.astropartphys.2009.04.001.

[67] D. Berge, S. Funk, J. Hinton, "Background modelling in very-high-energy γ-ray astronomy", *Astronomy and Astrophysics* **2007**, *466*, 1219–1229, DOI 10.1051/0004-6361:20066674.

[68] T. P. Li, Y. Q. Ma, "Analysis methods for results in gamma-ray astronomy.", **1983**, *272*, 317–324, DOI 10.1086/161295.

[69] T. G. developers, IRF Theory, https://docs.gammapy.org/dev/irf/theory.html#irf-theory, (Accessed: 12 November 2021).

[70] H.E.S.S. Collaboration, "The H.E.S.S. Experiment: Current Status and Future Prospects", *International Cosmic Ray Conference (ICRC 2019)* **2019**, 0–8, https://pos.sissa.it/358/656/.

[71] H. Abdalla et al., "A very-high-energy component deep in the γ-ray burst afterglow", *Nature* **2019**, *575*, DOI 10.1038/s41586-019-1743-9.

[72] M Holler et al., "A run-wise simulation and analysis framework for Imaging Atmospheric Cherenkov Telescope arrays", *Astroparticle Physics* **2020**, *123*, 102491, DOI https://doi.org/10.1016/j.astropartphys.2020.102491.

[73] H. Abdalla et al., "Resolving the Crab pulsar wind nebula at teraelectronvolt energies", *Nature Astronomy* **2020**, *4*, 167–173, DOI 10.1038/s41550-019-0910-0.

[74] H. Abdalla et al., "Resolving acceleration to very high energies along the jet of Centaurus A", *Nature* **2020**, *582*, 356–359, DOI 10.1038/s41586-020-2354-1.

[75] G Bicknell, M Begelmann, "Understanding the kpc-scale structure of M87", *Astrophysical Journal* **1996**, *467*, 597–621, https://ui.adsabs.harvard.edu/abs/1996ApJ...467..597B.

[76] C. Messier, Catalog of Nebulae and Star Clusters, http://www.messier.seds.org/xtra/history/m-cat71.html, (Accessed: 15 April 2021).

[77] F. Macchetto et al., "The Supermassive Black Hole of M87 and the Kinematics of Its Associated Gaseous Disk", *The Astrophysical Journal* **1997**, *489*, 579–600, DOI 10.1086/304823.

[78] K. Gebhardt, J. Thomas, "The black hole mass, stellar mass-to-light ratio, and Dark Halo in m87", *Astrophysical Journal* **2009**, *700*, 1690–1701, DOI 10.1088/0004-637X/700/2/1690.

[79] K. Gebhardt et al., "The black hole mass in M87 from Gemini/NIFS adaptive optics observations", *Astrophysical Journal* **2011**, *729*, 1–12, DOI 10.1088/0004-637X/729/2/119.

[80] J. L. Walsh et al., "The M87 black hole mass from gas-dynamical models of space telescope imaging spectrograph observations", *Astrophysical Journal* **2013**, *770*, DOI 10.1088/0004-637X/770/2/86.

[81] H. D. Curtis, "Descriptions of 762 Nebulae and clusters photographed with the Crossley reflector", *Publications of the Lick Observatory* **1912**, *XIII*, http://articles.adsabs.harvard.edu/pdf/1918PLicO..13....9C.

[82] K.-W. Wong et al., "Hard X-Ray Emission from the M87 AGN Detected with NuSTAR", *The Astrophysical Journal* **2017**, *849*, L17, DOI 10.3847/2041-8213/aa92c2.

[83] R. Blandford, D. Meier, A. Readhead, "Relativistic Jets from Active Galactic Nuclei", *Annual Review of Astronomy and Astrophysics* **2019**, *57*, 467–509, DOI 10.1146/annurev-astro-081817-051948.

[84] B. Fanaroff, J. Riley, "The morphology of extragalactic radio sources of high and low luminosity", *Monthly Notices of the Royal Astronomical Society* **1974**, *167*, 31–36, DOI 10.1093/mnras/167.1.31P.

[85] Y. Y. Kovalev et al., "The Inner Jet of the Radio Galaxy M87", *The Astrophysical Journal* **2007**, *668*, L27–L30, DOI 10.1086/522603.

[86] A. Jordan et al., "The ACS Virgo Cluster Survey. III.ChandraandHubble Space TelescopeObservations of Low-Mass X-Ray Binaries and Globular Clusters in M87", *The Astrophysical Journal* **2004**, *613*, 279–301, DOI 10.1086/422545.

[87] F. A. Aharonian, *Very High Energy Cosmic Gamma Radiation - A Crucial Window on the Extreme Universe*, World Scientific, **2010**, DOI 10.1142/9789812561732.

[88] Fermi Gamma-ray Space Telescope, Exploring Active Galactic Nuclei, https://fermi.gsfc.nasa.gov/science/eteu/agn/, (Accessed: 28 September 2021).

[89] C. S. Volker Beckmann, *Active Galactic Nuclei*, Wiley Online Library, **2012**, Chapter 3, DOI https://doi.org/10.1002/9783527666829.ch3.

[90] E. Fermi, "On the Origin of the Cosmic Radiation", *Phys. Rev.* **1949**, *75*, 1169–1174, DOI 10.1103/PhysRev.75.1169.

[91] M. S. Longair, *High Energy Astrophysics*, University Press, Cambridge, **2011**.

[92] S. Funk, PhD thesis, Ruprecht-Karls-Universität Heidelberg, **2005**, https://archiv.ub.uni-heidelberg.de/volltextserver/5542/.

[93] F. A. Aharonian, A. M. Atoyan, T. Kifune, "Inverse Compton gamma radiation of faint synchrotron X-ray nebulae around pulsars", *Monthly Notices of the Royal Astronomical Society* **1997**, *291*, 162–176, DOI 10.1093/mnras/291.1.162.

[94] G. B. Rybicki, A. P. Lightman, *Radiative Processes In Astrophysics*.

[95] S. Funk, "Ground- and Space-Based Gamma-Ray Astronomy", *Annual Review of Nuclear and Particle Science* **2015**, *65*, 245–277, DOI 10.1146/annurev-nucl-102014-022036.

[96] F. De Gasperin et al., "M87 at metre wavelengths: The LOFAR picture", *Astronomy and Astrophysics* **2012**, *547*, DOI 10.1051/0004-6361/201220209.

[97] G. R. Blumenthal, R. J. Gould, "Bremsstrahlung, Synchrotron Radiation, and Compton Scattering of High-Energy Electrons Traversing Dilute Gases", *Review of Modern Physics* **1970**, *42*, https://journals.aps.org/rmp/pdf/10.1103/RevModPhys.42.237.

[98] Max Planck Insitute for Nuclear Physics in Heidelberg (MPIK), GAMERA, A C++/python library for source modeling in gamma astronomy, http://libgamera.github.io/GAMERA/docs/main_page.html, (Accessed: 13 September 2021).

[99] J. A. Hinton, W. Hofmann, "Teraelectronvolt astronomy", *Annual Review of Astronomy and Astrophysics* **2009**, *47*, 523–565, DOI 10.1146/annurev-astro-082708-101816.

[100] A. Franceschini, G. Rodighiero, M. Vaccari, "Extragalactic optical-infrared background radiation, its time evolution and the cosmic photon-photon opacity", *Astronomy and Astrophysics* **2008**, *487*, 837–852, DOI 10.1051/0004-6361:200809691.

[101] A. Neronov, F. A. Aharonian, "Production of TeV Gamma Radiation in the Vicinity of the Supermassive Black Hole in the Giant Radio Galaxy M87", *The Astrophysical Journal* **2007**, *671*, 85–96, DOI 10.1086/522199.

[102] F. Aharonian et al., "Fast variability of tera-electron volt γ rays from the radio galaxy M87", *Science* **2006**, *314*, 1424–1427, DOI 10.1126/science.1134408.

[103] ESO, Virgo Supercluster, https://supernova.eso.org/exhibition/images/0106F_Virgu_Superlcuster/, (Accessed: 16 April 2021).

[104] M. Arnaud et al., "The universal galaxy cluster pressure profile from a representative sample of nearby systems (REXCESS) and the y SZ - M 500 relation", *Astronomy and Astrophysics* **2010**, *517*, DOI 10.1051/0004-6361/200913416.

[105] E. D. Feigelson et al., "X-rays from the radio halo of M87", *The Astrophysical Journal* **1987**, *312*, 101, DOI 10.1086/164852.

[106] O. Urban et al., "X-ray spectroscopy of the Virgo Cluster out to the virial radius", *Monthly Notices of the Royal Astronomical Society* **2011**, *414*, 2101–2111, DOI 10.1111/j.1365-2966.2011.18526.x.

[107] MPI, Virgo Cluster, ROSAT PSPC, https://www.mpe.mpg.de/990081/VirgoCluster, (Accessed: 20 April 2021).

[108] S. W. Allen, R. W. Schmidt, A. C. Fabian, "The X-ray virial relations for relaxed lensing clusters observed with Chandra", *Monthly Notices of the Royal Astronomical Society* **2001**, *328*, 0–4, DOI 10.1046/j.1365-8711.2001.05079.x.

[109] S. Ettori et al., "Mass profiles of galaxy clusters from X-ray analysis", *Space Science Reviews* **2013**, *177*, 119–154, DOI 10.1007/s11214-013-9976-7.

[110] S. Jacob, C. Pfrommer, "Cosmic ray heating in cool core clusters - II. Self-regulation cycle and non-thermal emission", *Monthly Notices of the Royal Astronomical Society* **2017**, *467*, 1478–1495, DOI 10.1093/mnras/stx132.

[111] K. W. Cavagnolo et al., "Intracluster medium entropy profiles for a Chandra archival sample of galaxy clusters", *Astrophysical Journal Supplement Series* **2009**, *182*, 12–32, DOI 10.1088/0067-0049/182/1/12.

[112] J. G. Bolton, G. J. Stanley, O. B. Slee, "Positions of Three Discrete Sources of Galactic Radio-Frequency Radiation", *Nature* **1949**, *164*, 101–102, DOI 10.1038/164101b0.

[113] F. N. Owen, J. A. Eilek, N. E. Kassim, "M87 at 90 Centimeters: A Different Picture", *The Astrophysical Journal* **2000**, *543*, 611–619, DOI 10.1086/317151.

[114] J. C. Algaba et al., "Broadband Multi-wavelength Properties of M87 during the 2017 Event Horizon Telescope Campaign", *The Astrophysical Journal Letters* **2021**, *11*, DOI 10.3847/2041-8213/abef71.

[115] S. Yang et al., "Statistical analysis on X-ray flares from the nucleus and HST-1 knot in the M87 jet", *Monthly Notices of the Royal Astronomical Society* **2019**, *489*, 2685–2693, DOI 10.1093/mnras/stz2302.

[116] A Felix et al., "Detection of TeV gamma-rays from the BL Lac 1ES1959+650 in its low states and during a major outburst in 2002", *A&A* **2003**, *406*, L9 –L13, DOI 10.1051/0004-6361:20030838.

[117] S. De Jong et al., "High-energy emission processes in M87", *Monthly Notices of the Royal Astronomical Society* **2015**, *450*, 4333–4341, DOI 10.1093/mnras/stv927.

[118] V. A. Acciari et al., "Radio imaging of the very-high-energy γ-ray emission region in the central engine of a radio galaxy", *Science* **2009**, *325*, 444–468, DOI 10.1126/science.1175406.

[119] A. Abramowski et al., "The 2010 very high energy γ-ray flare and 10 years of multi-wavelength observations of M 87", *Astrophysical Journal* **2012**, *746*, DOI 10.1088/0004-637X/746/2/151.

[120] V. A. Acciari et al., "Monitoring of the radio galaxy M87 during a low-emission state from 2012 to 2015 with MAGIC", *Monthly Notices of the Royal Astronomical Society* **2020**, *492*, 5354–5365, DOI 10.1093/mnras/staa014.

[121] E. A. Baltz et al., "Detection of neutralino annihilation photons from external galaxies", *Physical Review D* **1999**, *61*, DOI 10.1103/physrevd.61.023514, http://dx.doi.org/10.1103/PhysRevD.61.023514.

[122] W. Bednarek, "Morphology of TeV Gamma-Ray Emission from the Kiloparsec-scale Jets in Radio Galaxies", *The Astrophysical Journal* **2020**, *891*, 145, DOI 10.3847/1538-4357/ab774b.

[123] V. A. Acciari et al., "Observation of Gamma-Ray Emission from the Galaxy M87 above 250 GeV with VERITAS", *The Astrophysical Journal* **2008**, *679*, 397–403, DOI 10.1086/587458.

[124] J. Albert et al., "VHE -Ray Observation of the Crab Nebula and its Pulsar with the MAGIC Telescope", *The Astrophysical Journal* **2008**, *674*, 1037–1055, DOI 10.1086/525270.

[125] F. A. Harrison et al., "The Nuclear Spectroscopic Telescope Array (NuSTAR) high-energy X-ray mission", *Astrophysical Journal* **2013**, *770*, DOI 10.1088/0004-637X/770/2/103.

[126] M. C. Weisskopf et al., " An Overview of the Performance and Scientific Results from the Chandra X-Ray Observatory ", *Publications of the Astronomical Society of the Pacific* **2002**, *114*, 1–24, DOI 10.1086/338108.

[127] R. D. Parsons, M. Gajdus, T. Murach, "HESS II data analysis with ImPACT", *Proceedings of Science* **2015**, *30-July-2015*, DOI 10.22323/1.236.0826.

[128] G. Van Rossum, F. L. Drake Jr, *Python reference manual*, Centrum voor Wiskunde en Informatica Amsterdam, **1995**, https://ir.cwi.nl/pub/5008.

[129] C. R. Harris et al., "Array programming with NumPy", *Nature* **2020**, *585*, 357–362, DOI 10.1038/s41586-020-2649-2.

[130] P. Virtanen et al., "SciPy 1.0: fundamental algorithms for scientific computing in Python", *Nature Methods* **2020**, *17*, 261–272, DOI 10.1038/s41592-019-0686-2.

[131] T. P. Robitaille et al., "Astropy: A community Python package for astronomy", *Astronomy Astrophysics* **2013**, *558*, A33, DOI 10.1051/0004-6361/201322068.

[132] A. M. Price-Whelan et al., "The Astropy Project: Building an Open-science Project and Status of the v2.0 Core Package", *The Astronomical Journal* **2018**, *156*, 123, DOI 10.3847/1538-3881/aabc4f.

[133] C. Deil et al. in 35th International Cosmic Ray Conference (ICRC2017), **2017**, 766, p. 766, https://ui.adsabs.harvard.edu/abs/2017ICRC...35..766D.

[134] Nigro, C. et al., "Towards open and reproducible multi-instrument analysis in gamma-ray astronomy", *A&A* **2019**, *625*, A10, DOI 10.1051/0004-6361/201834938.

[135] P. Freeman, S. Doe, A. Siemiginowska in Astronomical Data Analysis, *Vol. 4477*, (Eds.: J.-L. Starck, F. D. Murtagh), International Society for Optics and Photonics, SPIE, **2001**, pp. 76–87, DOI 10.1117/12.447161.

[136] B. L. Refsdal et al. in Proceedings of the 8th Python in Science Conference, (Eds.: G. Varoquaux, S. van der Walt, J. Millman), Pasadena, CA USA, **2009**, pp. 51–57, http://conference.scipy.org/proceedings/scipy2009/paper_8/full_text.pdf.

[137] M. C. Weisskopf, "The Chandra X-Ray Observatory: An overview", *Advances in Space Research* **2003**, *32*, 2005–2011, DOI 10.1016/S0273-1177(03)90639-9.

[138] The SciPy community, Calculate a Spearman correlation coefficient with associated p-value, https://docs.scipy.org/doc/scipy/reference/generated/scipy.stats.spearmanr.html, (Accessed: 21 Januar 2021).

[139] C. P. Enßlin, T. A., "Probing the cosmic ray population of the giant elliptical galaxy M 87 with observed TeV gamma-rays", *Astronomy and Astrophysics* **2003**, *407*, L73–L77, DOI 10.1051/0004-6361:20031088.

[140] C. Pfrommer, "Toward a comprehensive model for feedback by active galactic nuclei: New insights from M87 observations by LOFAR, FERMI, and H.E.S.S.", *Astrophysical Journal* **2018**, *779*, DOI 10.1088/0004-637X/779/1/10.

[141] J. D. Scargle et al., "Studies in astronomical time series analysis. VI. Bayesian block representations", *Astrophysical Journal* **2013**, *764*, 1–82, DOI 10.1088/0004-637X/764/2/167.

[142] M. L. Ahnen et al., "Long-term multi-wavelength variability and correlation study of Markarian 421 from 2007 to 2009", *Astronomy and Astrophysics* **2016**, *593*, DOI 10.1051/0004-6361/201628447.

[143] E. Resconi et al., "The classification of flaring states of blazars", *Astronomy and Astrophysics* **2009**, *502*, 499–504, DOI 10.1051/0004-6361/200911770.

[144] S. J. Wolk et al., "Stellar Activity on the Young Suns of Orion: COUP Observations of K5-7 Pre–Main-Sequence Stars", *The Astrophysical Journal Supplement Series* **2005**, *160*, 423–449, DOI 10.1086/432099.

[145] W. Cash, "Parameter estimation in astronomy through application of the likelihood ratio", *The Astrophysical Journal* **1979**, *228*, 939–947, DOI 10.1086/156922.

[146] J. S. Kaastra, "On the use of C-stat in testing models for X-ray spectra", *Astronomy and Astrophysics* **2017**, *605*, 2–5, DOI 10.1051/0004-6361/201629319.

[147] J. C. Lagarias et al., "Convergence properties of the Nelder-Mead simplex method in low dimensions", *SIAM Journal on Optimization* **1998**, *9*, 112–147, DOI 10.1137/S1052623496303470.

[148] S. S. Wilks, "The Large-Sample Distribution of the Likelihood Ratio for Testing Composite Hypotheses", *The Annals of Mathematical Statistics* **1938**, *9*, 60–62, DOI 10.1214/aoms/1177732360.

[149] S. B. Lambert, A. M. Gontier, "On radio source selection to define a stable celestial frame", *Astronomy and Astrophysics* **2009**, *493*, 317–323, DOI 10.1051/0004-6361:200810582.

[150] A. Abramowski et al., "Search for extended γ-ray emission around AGN with H.E.S.S. and Fermi -LAT", *Astronomy and Astrophysics* **2014**, *562*, DOI 10.1051/0004-6361/201322510.

[151] The FIRST project team: R.J. Becker, D.H. Helfand, R.L. White M.D. Gregg. S.A. Laurent-Muehleisen., VLA FIRST (1.4 GHz): FIRST, https://skyview.gsfc.nasa.gov/, (Accessed: 29 October 2021).

[152] M. L. Weil, J. Bland-Hawthorn, D. F. Malin, "Diffuse Stellar Light at 100 Kiloparsec Scales in M87", *The Astrophysical Journal* **1997**, *490*, 664–681, DOI 10.1086/304886.

[153] V. A. Acciari et al., "Teraelectronvolt emission from the γ-ray burst GRB 190114C", *Nature* **2019**, *575*, 455–458, DOI 10.1038/s41586-019-1750-x.

[154] A. M. Taylor et al., "Revealing x-ray and gamma ray temporal and spectral similarities in the GRB 190829A afterglow", *Science* **2021**, *372*, 1081–1085, DOI 10.1126/science.abe8560.

[155] Stefan J. Wagner for the H. E.S. S. collaboration, ATel #14857: H.E.S.S. observations of soft spectrum VHE gamma-ray emission from the recurrent nova RS Ophiuchi, **2020**, https://automeris.io/WebPlotDigitizer.

[156] CTA, Cherenkov Telescope Array Observatory, https://www.cta-observatory.org, (Accessed: 17 August 2021).

[157] H. Abdalla et al., "Evidence of 100 TeV γ-ray emission from HESS J1702-420: A new PeVatron candidate", *Astronomy and Astrophysics* **2021**, *653*, DOI 10.1051/0004-6361/202140962.

[158] T. Deyoung, "The HAWC observatory", *Nuclear Instruments and Methods in Physics Research Section A: Accelerators Spectrometers Detectors and Associated Equipment* **2012**, *692*, 72–76, DOI 10.1016/j.nima.2012.01.026.

[159] P. Abreu et al., "The Southern Wide-Field Gamma-Ray Observatory (SWGO): A Next-Generation Ground-Based Survey Instrument for VHE Gamma-Ray Astronomy", **2019**, http://arxiv.org/abs/1907.07737.

[160] E. Liang et al., "Low-Luminosity Gamma-Ray Bursts as a Unique Population: Luminosity Function, Local Rate, and Beaming Factor", *The Astrophysical Journal* **2007**, *662*, 1111–1118, DOI 10.1086/517959.

[161] Garczarczyk et al., "Status of the Medium-Sized Telescope for the Cherenkov Telescope Array", *The 34th International Cosmic Ray Conference* **2015**, https://arxiv.org/abs/1509.01361.

[162] G. Pühlhofer et al., "FlashCam: A fully-digital camera for the medium-sized telescopes of the cherenkov telescope array", *Proceedings of Science* **2015**, *30-July-2015*, DOI 10.22323/1.236.1039.

[163] J. F. Glicenstein, M. Shayduk, "NectarCAM, a camera for the medium sized telescopes of the Cherenkov telescope array", *AIP Conference Proceedings* **2017**, *1792*, DOI 10.1063/1.4969030.

[164] Medium-Sized Telescope Technical Design Report, (CTAO internal document), **2016**.

[165] Svibs, Download Papers on Operational Modal Analysis, https://svibs.com/literature/, (Accessed: 20 August 2021).

[166] GeoSIG, Swiss to measure., GeoSIG, https://www.geosig.com, (Accessed: 19 August 2021).

[167] Gantner Instruments., Gantner, https://www.gantner-instruments.com, (Accessed: 19 August 2021).

[168] R. Brincker, L. Zhang, P. Andersen in *Vol. 18*, **2000**, pp. 625–630, https://ui.adsabs.harvard.edu/abs/2000SPIE.4062..625B/abstract.

[169] ScienceDirect, Chebyshev Type, https://www.sciencedirect.com/topics/engineering/chebyshev-type, (Accessed: 15 November 2021).

[170] The hdbscan Clustering Library, https://hdbscan.readthedocs.io/en/latest/, (Accessed: 08 September 2021).

[171] R. J. Campello, D. Moulavi, J. Sander, "Density-based clustering based on hierarchical density estimates", *Lecture Notes in Computer Science (including subseries Lecture Notes in Artificial Intelligence and Lecture Notes in Bioinformatics)* **2013**, *7819 LNAI*, 160–172, DOI 10.1007/978-3-642-37456-2_14.

[172] Cherenkov Telescope Array Observatory and Cherenkov Telescope Array Consortium, CTAO Instrument Response Functions - prod5 version v0.1, version v0.1, **2021**, DOI 10.5281/zenodo.5499840.

[173] D. G. York et al., "The Sloan Digital Sky Survey: Technical Summary", *The Astronomical Journal* **2000**, *120*, 1579–1587, DOI 10.1086/301513.

[174] M. P. Van Haarlem et al., "LOFAR: The low-frequency array", *Astronomy and Astrophysics* **2013**, *556*, 1–56, DOI 10.1051/0004-6361/201220873.

[175] A. Rohatgi, Webplotdigitizer: Version 4.4, **2020**, https://automeris.io/WebPlotDigitizer.

Appendices

Appendix A.

Gamma-ray template for a hadronic scenario in the M87 low state

This appendix aims at deriving a gamma-ray template for M87's low state based on the steady-state model from Jacob & Pfrommer (2017)[21,110], which is introduced in Sec. 4.5.

The base for the development of the gamma-ray template is the radial profile of the cosmic-ray pressure resulting from the steady-state model, as shown in Fig. 4.13 and reconstructed in Fig. A.1. Sec. A.1 describes the assumptions of the model to derive the gamma-ray source function at the source location. Afterward, I considered the geometry of the system to integrate the emission along the line of sight as shown in Sec. A.2. The final product is a 2D template for the gamma-ray emission.

A.1. The differential gamma-ray flux estimation

The authors in Jacob & Pfrommer (2017)[21,110] derive the cosmic-ray pressure profile as a function of the radius from the cluster core but do not derive the gamma-ray emission profile. Hence, this section is dedicated to estimating the radial profile of the gamma-ray emission, considering the steady-state model.

An online tool[175] was used to extract the data points (X_{CR}) from Fig. A.1 and derive the cosmic-ray to thermal pressure ratio as a function of the distance from the cluster core. The thermal pressure can be obtained from the ICM density and temperature distributions using the ideal gas law[21]:

$$P_{\mathrm{th.}} = \frac{\rho k T}{\mu m_{\mathrm{p}}} = \frac{\mu_{\mathrm{e}}}{\mu} n_{\mathrm{e}} k T, \tag{A.1}$$

where k is the Boltzmann factor; μ and μ_e are the mean molecular weight per particle and per electron, respectively. As discussed in Sec. 3.3, the ICM profile and temperature are obtained and fitted in Jacob & Pfrommer (2017)[21] based on ACCEPT[111] X-ray data, assuming

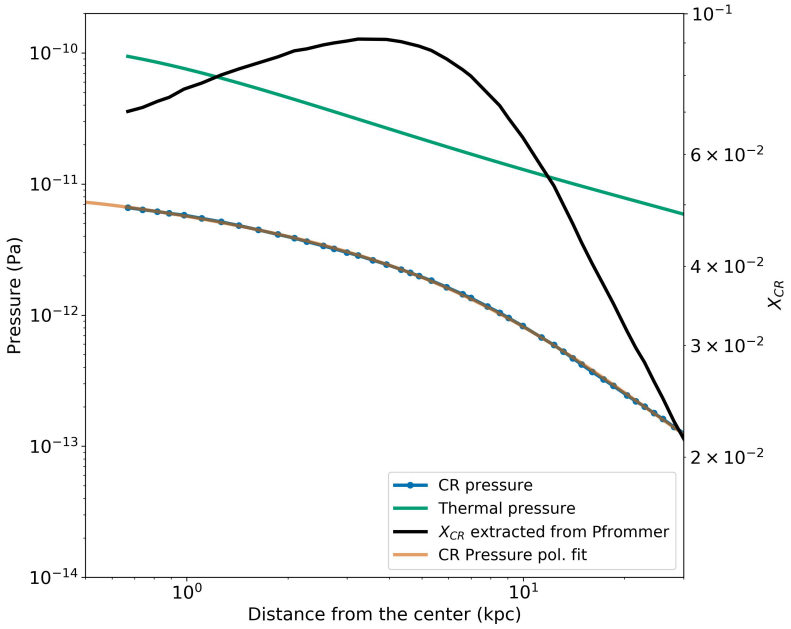

Figure A.1.: The thermal and cosmic-ray pressures in Pa according to the model in Jacob & Pfrommer (2017)[21] for the M87's low state. The $X_{\rm CR}$ on the right axis shows the curve extracted from the same publication.

an hydrogen mass fraction $X = 0.7$ and helium mass fraction of $Y = 0.28$[110]. With this composition, the ICM density is given by $n_{\rm ICM} = n_{\rm H} + 4n_{\rm He} = \mu_e n_e$, where $\mu_{\rm e} = 1.18$ is the mean molecular weight per electron. Finally, combining the estimated $P_{\rm th.}$ with the extracted $X_{\rm CR}$, it is possible to estimate the radial distribution of the cosmic-ray pressure $P_{\rm CR}$:

$$P_{\rm CR} = X_{\rm CR} \times P_{\rm th.} \tag{A.2}$$

A polynomial function of fifth-order was fitted to extracted points in a logarithm scale to yield a finely-binned curve. With the best-fit parameters, the function is compared to the original extracted points as shown in Fig. A.1. The cosmic-ray and thermal pressures are shown on the left axis, while the original cosmic-ray pressure ratio to thermal pressure is shown in black on the right axis.

Before estimating the gamma-ray production, some assumptions have to be considered for the CR proton distribution. The analytical calculations presented below are extracted from App. B of Jacob & Pfrommer (2017)[110], where the author assumes the CR proton distribution to be a power law in momentum:

$$f_p(p_p) = \frac{dN}{dp_p dV} = C_p p_p^{-\alpha_p} \theta(p_p - q_p), \tag{A.3}$$

where $C_p = C_p(r)$ is the normalization, $p_p = P_p/(m_p c)$ is the dimensionless proton momentum, $\alpha = 2.4$ is the assumed proton spectral index, θ denotes the Heaviside function and $q_p = 0.5$ is the momentum threshold. The normalization C_p depends on the distance from the core and gives the proton spatial distribution. It can be directly estimated from the cosmic-ray pressure[110]:

$$C_p(r) = \frac{6 P_{\rm CR}(r)}{m_{\rm p} c^2} \left[B_{\frac{1}{1+q_p^2}} \left(\frac{\alpha_p - 2}{2}, \frac{3 - \alpha_p}{2} \right) \right]^{-1}, \tag{A.4}$$

where $P_{\rm CR}(r)$ is the cosmic-ray pressure exerted into the ICM at radius r from the center and $B_{\rm x}(a, b)$ is the incomplete beta function.

The gamma-ray source function $s_\gamma(E_\gamma)$ is a combination of the p-p interaction cross section and the decay function to gamma rays. The differential gamma-ray flux is given by the energy integration of the source function[110]:

$$\lambda_\gamma = \int_{E_1}^{E_2} dE_\gamma s_\gamma(E_\gamma) = \frac{4 C_{\rm p}}{3 \alpha_p \delta_\gamma} \frac{m_{\pi^0} c \sigma_{\rm pp} n_N}{m_p} \left(\frac{m_{\rm p}}{2 m_{\pi^0}} \right)^{\alpha_{\rm p}} \left[B_{\rm x} \left(\frac{\alpha_{\rm p} + 1}{2\delta_\gamma}, \frac{\alpha_{\rm p} - 1}{2\delta_\gamma} \right) \right]_{x_1}^{x_2}, \tag{A.5}$$

where $E_1 = 0.3\,\mathrm{TeV}$ and $E_2 = \infty$ are the limits of the integration, $\delta_\gamma \approx 0.14 \alpha_p^{-1.6} + 0.44$ is the shape factor, $\sigma_{\rm pp} = 32 \left(0.96 + e^{4.4 - 2.4(\alpha_e - 1)} \right)$ is the proton-proton cross-section, m_{π^0} is the π^0 mass, $m_{\rm p}$ is the proton mass, $n_{\rm N}$ is the ICM density and X is a factor given by:

$$x_i = \left[1 + \left(\frac{m_{\pi^0} c^2}{2 E_i} \right)^{2\delta_\gamma} \right]^{-1}. \tag{A.6}$$

With the polynomial function describing $P_{\rm CR}$, Eq. A.2, Eq. A.4) and Eq. A.5 can be used to derive the differential gamma-ray flux within the first 30 kpc from the source. Fig. A.2 shows the estimated distribution of the locally produced gamma-ray. Since the region from which the data were extracted lies between 0.5 and 30 kpc, the polynomial function was also kept within this same range to avoid creating artifacts in the graphs.

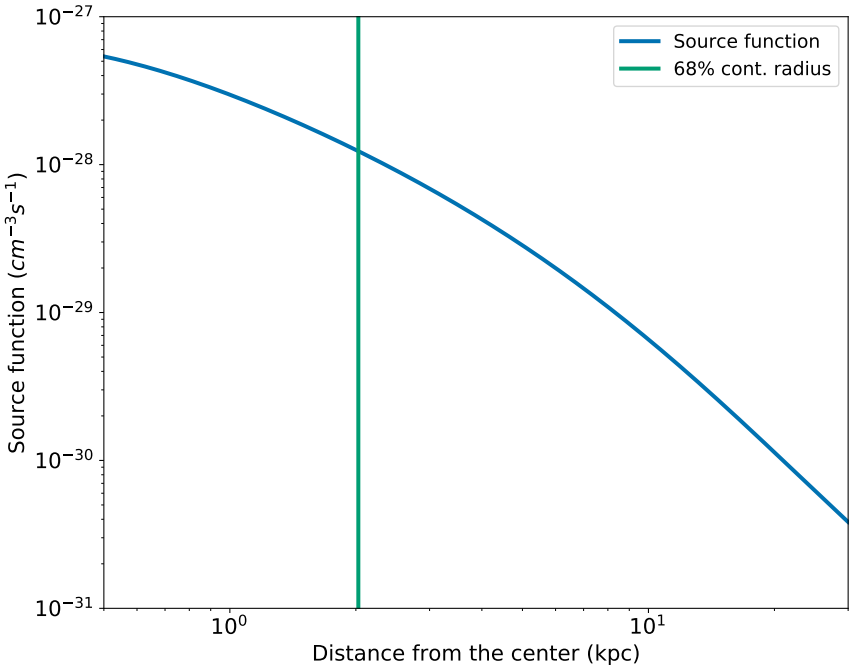

Figure A.2.: The gamma-rays source function, i.e. the gamma rays produced at the source per volume and time as function of the distance from the cluster core (M87). The vertical line indicates the 68% c.r. at $\approx 2\,\mathrm{kpc}$.

A.2. The gamma-ray template for the H.E.S.S. telescopes

The integration of the radial profile of the gamma-ray emission along the line of sight yields the 2D gamma-ray template. Since the emission is isotropic in each direction[21,110], a spherical coordinate system is defined with its center at the cluster core as shown in Fig. A.3.

Since the emission should be isotropic, and centered at the cluster core, the integration is conducted in the sphere, from $y = -30\,\mathrm{kpc}$ to $y = 30\,\mathrm{kpc}$:

$$\Phi_{\mathrm{2D}}(x, y, z) = \int_{-30kpc}^{30kpc} \frac{dN}{dxdydz} dy \tag{A.7}$$

The spherical coordinates is well known defined by the equations:

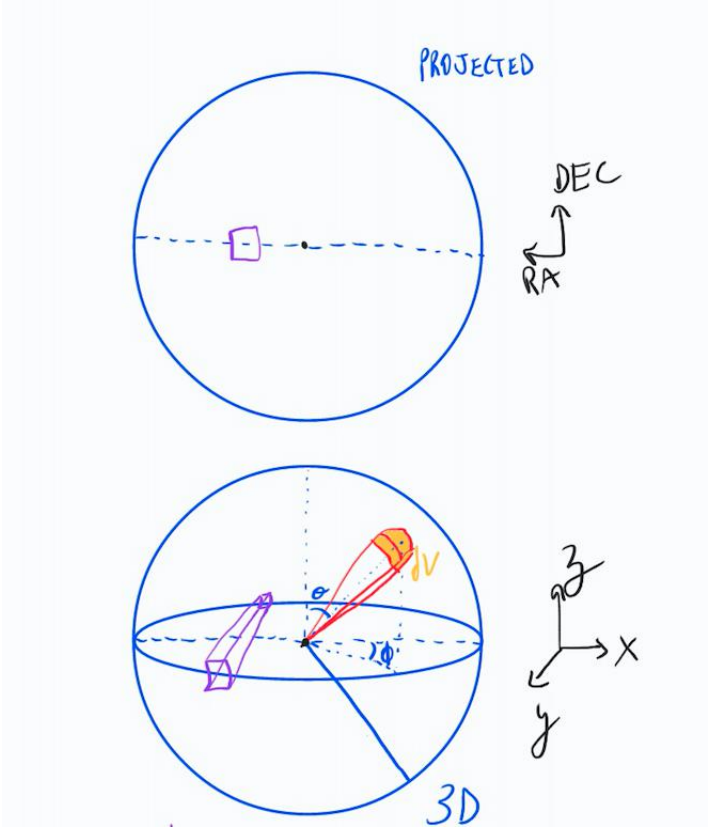

Figure A.3.: The defined coordinate system for the 3D gamma-ray distribution. In the upper panel, a projected view along the line of sight is shown. The blue sphere represents the 30 kpc radius delimiting the region of interest and the purple square indicates the size of one bin. The coordinate system is given in RA and DEC. In the lower panel, a 3D projection is shown in spherical coordinates to indicate the integration along the line of sight (Y direction).

$$x = r cos\phi sin\theta, \tag{A.8}$$

$$y = r sin\phi sin\theta, \tag{A.9}$$

$$z = r cos\theta. \tag{A.10}$$

Since the integration in Eq. A.7 is conducted along the Y axis, the differential in Y can be written as:

$$dy = d(rsin\phi sin\theta) = rsin\phi cos\theta d\theta + rsin\theta cos\phi + sin\phi sin\theta dr. \tag{A.11}$$

Substituting Eq. A.11 into Eq. A.7 and using the best polynomial fit for the source function (Fig A.2), the integral is analytically calculated. First, a very fine bin of size 0.05 kpc is chosen to allow a good visualization of the emission and its extent (Fig. 4.14). Secondly, the same emission is converted to the H.E.S.S. angular resolution (0.01°/bin), considering that $1'' \approx 78$ pc (Fig. 4.15 (a)). Afterward, the emission is convolved with the H.E.S.S. PSF and result is the 2D template of the gamma-ray emission for the hadronic model (Fig. 4.15 (b)).

The total flux at Earth is obtained by integrating the radial distribution from Fig. A.2 within the volume up to 30 kpc from the cluster core and dividing through the area covered by the distance to Earth (16.5 Mpc[15,16]):

$$N = \int_V \frac{dN}{dr d\phi d\theta} dV, \tag{A.12}$$

$$\Phi_{\text{Earth}} = \frac{N}{4\pi D_{\text{M87}}^2}, \tag{A.13}$$

which yields $\approx 1.76 \times 10^{-13}\,\text{cm}^{-2}\,\text{s}^{-1}$, which is approximately 10% of the low state flux detected by H.E.S.S. (Tab. 4.7). As a sanity check for the integration algorithm, the map displayed in the H.E.S.S. resolution (Fig. 4.15 (b)) was also integrated considering the flux at each bin as constant to yield a flux at Earth of $6.2 \times 10^{-14}\,\text{cm}^{-2}\,\text{s}^{-1}$, therefore, slightly smaller but in agreement with the more precise integration of the radial distribution.

Appendix B.

Systematic uncertainties of the morphology analysis

The fit morphology algorithm and the results are presented in Sec. 4.3 for the main analysis. However, several aspects of the morphology algorithm could directly influence the morphology fit results. Therefore, I analyzed different configurations to explore their influence on the final result.

First, I present the residuals of the main analysis in App. B.1. In the main analysis, the PSF is convolved with the pointing uncertainties. To evaluate the influence of the convolution in the final morphology result, I also fitted the data when the pointing uncertainties are not previously convolved with the PSF, as shown in App. B.2. Another aspect of the main analysis is the center of the geometrical models used. They are kept free for the fit in the main analysis, and the fit algorithm yields the best position. In App. B.3 I fixed the center of the models to the M87's core, motivated by the VHE emission from the vicinities of the SMBH. To increase the reliability of the morphology algorithm, I reanalyzed the Crab Nebula data-set from Abdalla et al. (2020)[73] in App. B.4 and the gamma-ray extension detected. Regarding the point-like model, I tested different functions to evaluate the fit conversion and reported the results in App. B.6. Finally, I tested a series of different configurations for the H.E.S.S. analysis in App. B.5, individually: the cut-off on the zenith angle of the observations is tightened from 50° to 45°, the energy threshold is increased from 0.3 to 0.7 TeV, the bin size of the H.E.S.S. maps is changed from 0.01° to 0.005° and a shift of 0.005° is introduced in the test position (center of the H.E.S.S. sky maps).

All the systematic checks in this appendix point towards the reliability and stability of the final results. Therefore, the extension UL derived in Sec. 4.3 is not an effect of the analysis configuration but rather a physical result.

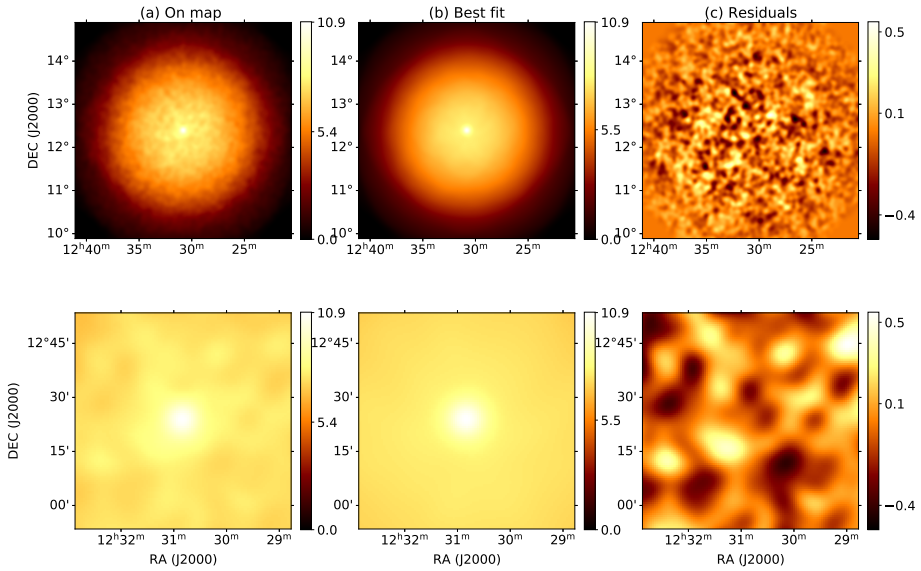

Figure B.1.: Morphology fit results of the point-like model for the low state (Blocks 0, 4, 6): (a) The On counts, (b) the best model and (c) the residuals are shown. The lower panel shows a zoom-in in the center of the maps. All maps are convolved with the 68% c.r. of the PSF for better visualization.

B.1. Residuals of the morphology fit

I present the residuals of the morphology fit from Sec. 4.3 in this section for the low state. The point-like model results is shown in Fig. B.1 and the Gaussian model results in Fig. B.2. The maps show the On counts (detected signal) in the first column, the best model in the second column, and the residuals in the third one. The lower panel shows a zoom-in in the center of the maps. The sky maps are convolved with the 68% c.r. of the PSF for better visualization. The 1D histograms of the residuals with a Gaussian fit are given in Fig. B.3 and Fig. B.4 for the point-like and Gaussian model, respectively. Lastly, the parameter space for the width FWHM is shown in Fig. B.5 for the Gaussian model.

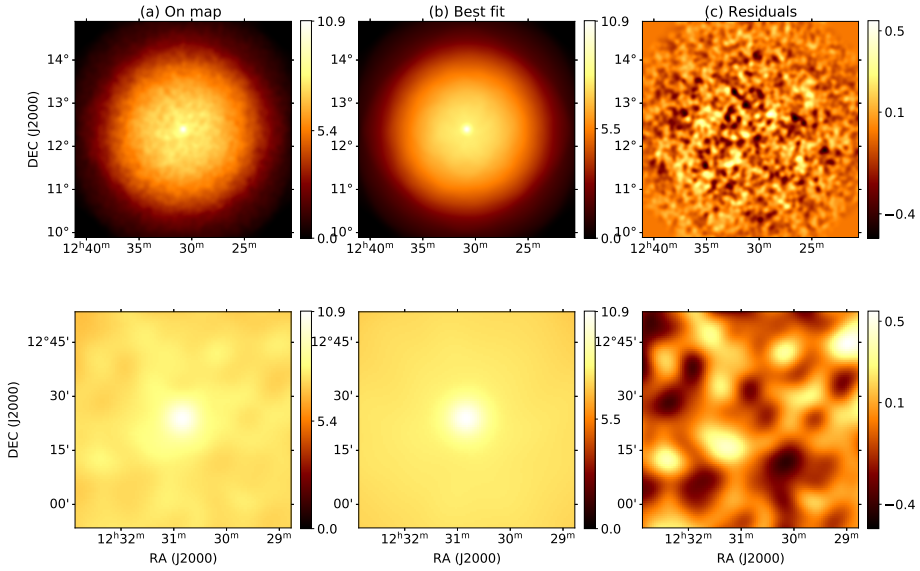

Figure B.2.: Morphology fit results of the Gaussian model for the low state (Blocks 0,4,6): (a) The On counts, (b) the best model and (c) the residuals are shown. The lower panel shows a zoom-in in the center of the maps. All maps are convolved with the 68% c.r. of the PSF for better visualization.

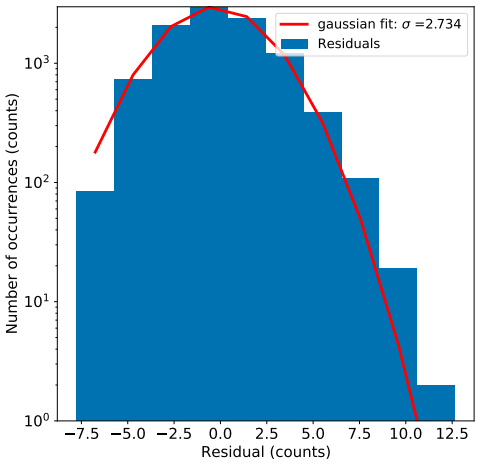

Figure B.3.: Low state: histogram of the residuals from Fig. B.1 right panel

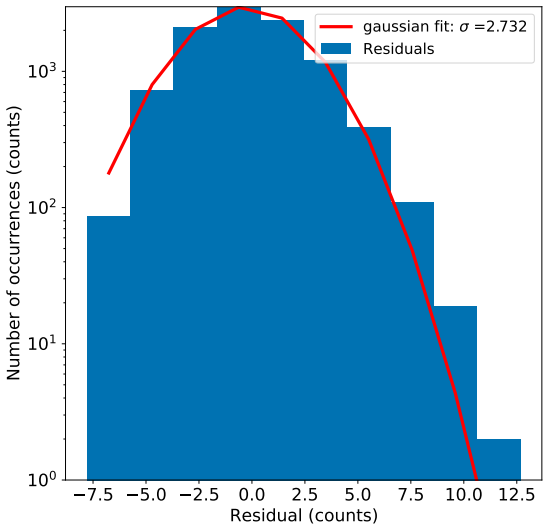

Figure B.4.: Low state: histogram of the residuals from Fig. B.2 right panel

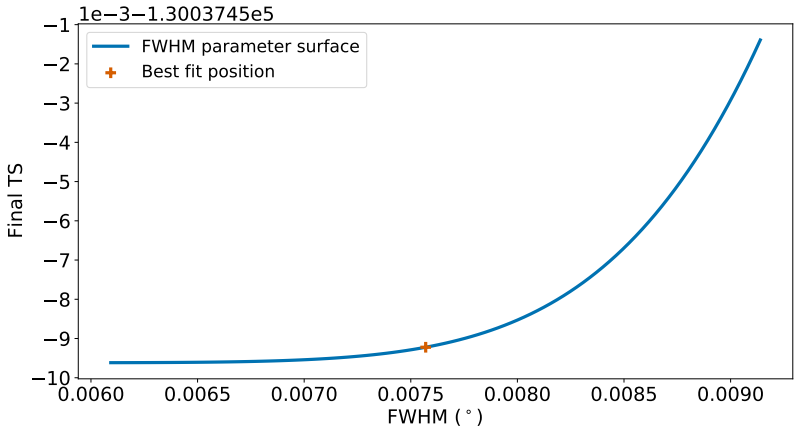

Figure B.5.: Low state: parameter space of the FWHM estimate for the Gaussian model.

B.2. Pointing uncertainties

The convolution of the systematic (pointing) uncertainties with the PSF might influence the result of the extension UL. To investigate this effect, I analyzed the same data as in Sec. 4.3, though without the convolution. As in the main analysis, the zenith angle cut is 50° and the energy threshold 0.3 TeV. The statistic of the available data and the PSF parameters are the same as in Tab. 4.3 and Tab. 4.4. Tables B.1, B.2, B.3 and B.4 show the fit statistics, the best parameters for the extension and the extension UL estimation for the source states, respectively.

	Point-like		**Symmetrical Gaussian**		**Comparison**	
	Final stat.	**d.o.f.**	**Final stat.**	**d.o.f.**	**ΔTS**	**Signif.(σ)**
Low state	-130038.8	7842	-130038.2	7841	-0.6	-
Intermediate state	10774.9	7842	10771.4	7841	3.5	1.8
High state	10147.6	7842	10146.7	7841	0.9	1.0

Table B.1.: Fit statistics for the source states for the point-like and Gaussian models. Results of the main analysis are in Tab. 4.7 for comparison. The PSF is not convolved with the systematic uncertainties.

Point-like model			
State	**RA(°)**	**DEC(°)**	**Ampl.(a.u.)**
Low	187.711±0.003	12.398±0.003	3.5±0.2
Intermediate	187.707±0.005	12.395±0.005	3.9±0.4
High	187.705±0.002	12.397±0.002	9.7±0.6

Table B.2.: The best-fit parameters for the source states for the point-like model. 1σ statistical errors are given. Results of the main analysis in Tab. 4.5 for comparison. The PSF is not convolved with the systematic uncertainties.

Symmetrical Gaussian model				
State	**RA(°)**	**DEC(°)**	**Ampl.(a.u.)**	**FWHM (°)**
Low	$187.711^{+0.005}_{-0.002}$	$12.397^{+0.003}_{-0.002}$	10^{+20}_{-9}	$0.007^{+0.011}_{-0.002}$
Intermediate	187.706±0.006	12.395±0.005	$0.21^{+0.28}_{-0.08}$	0.04±0.01
High	187.705±0.003	12.397±0.002	$1.9^{+124.5}_{-1.0}$	$0.02^{+0.01}_{-0.02}$

Table B.3.: The best-fit parameters for the symmetrical Gaussian. 1σ statistical errors are given. Results of the main analysis are in Tab. 4.6 for comparison. The PSF is not convolved with the systematic uncertainties.

State	$3\,\sigma$ UL (mdeg)	$3\,\sigma$ UL (kpc)
Low	16.9	4.8
Intermediate	36.2	10.4
High	22.1	6.4

Table B.4.: Results of the estimated extension UL with 99.7% c.l. of the σ extension for the source states. The UL is given both in units of mdeg and in kpc. Results of the main analysis are in Tab. 4.8 for comparison. The PSF is not convolved with the systematic uncertainties.

The best fit position for the point-like and Gaussian models in Tab. B.3 are within $1\,\sigma$ consistent with the values in Tab. 4.6. The best Gaussian extension and UL slightly increased but the effect is negligible as the comparison of Tab. B.4 with Tab. 4.8 indicates. Therefore, the convolution of the PSF with the pointing uncertainties does not bias the final results.

B.3. Fit with the center fixed

The emission center was kept free during the fit in the main analysis. The assumption that the center of the emission coincides with the M87's core is justified for the case of perfect pointing precision and a core emission model. I conducted an analysis analogous to Sec. 4.3, though this time, the center of the morphology models are kept fixed for the fit. As in the main analysis, the zenith angle cut is 50° and the energy threshold 0.3 TeV. The PSF is convolved with the pointing uncertainties before the fit, and the same data-set as in the main analysis is used. Therefore, the statistic of the available data and the PSF parameters are the same as in Tab. 4.3 and Tab. 4.4. The morphology fit results are shown in Tabs. B.5, B.6 and B.7, while the derived extension UL is shown in Tab. B.8 for the source states.

	Point-like		**Symmetrical Gaussian**		**Comparison**	
	Final stat.	**d.o.f.**	**Final stat.**	**d.o.f.**	**ΔTS**	**Signif.(σ)**
Low state	-130028.9	7844	-130028.9	7843	0	0
Intermediate state	10775.0	7844	10772.1	7843	2.9	1.7
High state	10152.6	7844	10152.1	7843	0.5	0.7

Table B.5.: Center fixed to the core position. Fit statistics for the source states for the two emission models: point-like and symmetrical Gaussian model. Results of the main analysis are in Tab. 4.7 for comparison.

The ΔTS is 0 for the low state as shown in Tab. B.5, which indicates that the shift of the

State	Point-like model Ampl.(a.u.)
Low	3.5±0.2
Intermediate	4.0±0.4
High	9.8±0.6

Table B.6.: The best-fit parameters for the source states for the point-like model. 1σ statistical errors are given. Results of the main analysis in Tab. 4.5 for comparison. Center fixed to the core position.

State	Symmetrical Gaussian model	
	Ampl.(a.u.)	FWHM (°)
Low	$3.5^{0.3}_{-2.0}$	$0.003^{+0.012}_{-}$
Intermediate	$0.22^{+0.36}_{-0.09}$	$0.04^{0.01}_{-0.02}$
High	2^{+8}_{-1}	$0.02^{+0.1}_{-}$

Table B.7.: The best-fit parameters for the symmetrical Gaussian. 1σ statistical errors are given. Results of the main analysis are in Tab. 4.6 for comparison. Center fixed to the core position. Whenever the '-' sign appears alone in the uncertainties, it indicates that the algorithm did not reach one standard deviation away from the best fit in the direction considered.

Block	$1\,\sigma$ UL (mdeg)	$1\,\sigma$ UL (kpc)
Low	17.1	4.9
Intermediate	36.1	10.3
High	22.3	6.4

Table B.8.: Results of the estimated $1\,\sigma$ UL for the source states. Results of the main analysis are in Tab. 4.8 for comparison. Center fixed to the core position.

best-fit position from the core in the main analysis (Tab. 4.5) is not significant. The morphology fit of the intermediate state slightly prefers a Gaussian model though not significantly. The fit of a point-like model with the center free to vary (main analysis) is preferred compared to the fit with a fixed center by 2.6σ, 0.4σ, and 1.8σ in the low, intermediate, and high state, respectively.

B.4. Cross-check analysis on the Crab nebula

To validate the analysis procedure developed in this work (Sec. 4.3.1), I analyzed, with the fit algorithm from Sec. 4.3.1, the same Crab Nebula data-set used in the discovery of the

Crab extension in gamma rays from the H.E.S.S. publication Abdalla et al. (2020)[73]. The morphology fit for the full energy range (0.7 - 200 TeV) was presented in the publication, though the energy bin morphology was obtained in private communication with the authors. The results of the H.E.S.S. analysis of the Crab Nebula are showed in Tab. B.9. The PSF parameters are derived and shown in Tab. B.10. The morphology fit results are shown in Tab. B.9, and Tab. B.12 and Tab. B.13. The investigation of the parameter space of the Gaussian extension (FWHM) is shown in Fig. B.6. A comparison of the extension derived by H.E.S.S for different sources is shown in the main text in Fig. 4.7. While the result of my analysis yielded a Gaussian σ extension of 17.8 ± 0.4 mdeg, the published results yielded $14.5 \pm 0.8_{\mathrm{stat}} \pm 1.8_{\mathrm{sys}}$ mdeg. Both results are consistent within 2 standard deviations[73].

Energy range (TeV)	**Excess (counts)**	**Signal-to-noise ratio**	**Sign.(σ)**	**Live-time (h)**
0.7 - 1.0	617.12	34.8	50.6	13.9
1.0 - 2.5	1939.45	63.6	98.5	19.8
2.5 - 5	453.6	61.5	47.2	15.2
5.0 - 200.0	331.82	53.4	40.1	19.6
0.7 - 200.0	5752.33	52.2	166.7	23.3

Table B.9.: Results of the H.E.S.S. analysis for the Crab energy bins and the full energy range.

Energy range (TeV)	**68% c.r.** (°)	**99% c.r.** (°)	**A (counts)**	σ_1 (°)	A_2 (**counts**)	σ_2 (°)	$\mathbf{A_3}$ **(counts)**	σ_3 (°)
0.7 - 1.0	0.050	0.261	4.1	0.135	69.6	0.030	10.9	0.060
1.0 - 2.5	0.046	0.264	4.2	0.136	96.4	0.026	10.3	0.057
2.5 - 5	0.041	0.223	14.5	0.103	[0]	0.1	36.7	0.024
5.0 - 200.0	0.040	0.220	16.2	0.100	[0]	0.1	41.5	0.021
0.7 - 200.0	0.048	0.267	4.4	0.137	92.4	0.024	12.8	0.055

Table B.10.: PSF parameters resulted from the H.E.S.S. analysis for the energy bins and full energy range of the Crab data. The brackets indicate fixed parameters.

Energy range (TeV)	Point-like		Symmetrical Gaussian		Comparison	
	Final stat.	d.o.f.	Final stat.	d.o.f.	ΔTS	Signif.(σ)
0.7 - 1.0	4565.0	7842	4527.8	7841	-37.2	6.1
1.0 - 2.5	1288.1	7842	1206.2	7841	-81.9	9.0
2.5 - 5	2724.4	7842	2691.4	7841	-32.9	5.7
5.0 - 200.0	2676.5	7842	2656.1	7841	-20.4	4.5
0.7 - 200.0	-23387.2	7842	-23685.9	7841	-298.7	17.1

Table B.11.: Fit statistics of the Crab data for the energy bins and full energy range for the point-like and symmetrical Gaussian models.

Energy range (TeV)	Point-like model		
	RA(°)	DEC(°)	Ampl. (a.u.)
0.7 - 1.0	83.6280±0.0020	22.0250±0.0010	253±8
1.0 - 2.5	83.6298±0.0008	22.0218±0.0008	280±5
2.5 - 5.0	83.6270±0.0010	22.0220±0.0010	25^{+11}_{-10}
5.0 - 200.0	83.6350±0.0010	22.0230±0.0010	215^{+11}_{-10}
0.7 - 200.0	83.6302±0.0005	22.0214±0.0005	331±4

Table B.12.: The best-fit parameters of the Crab data for the point-like model. $1\,\sigma$ statistical errors are given.

Energy range (TeV)	Symmetrical Gaussian model			
	RA(°)	DEC(°)	Ampl. (a.u.)	FWHM (°)
0.7 - 1.0	83.6280±0.0020	22.0250±0.0020	8^{+2}_{-1}	0.053±0.005
1.0 - 2.5	83.6296±0.0009	22.0219±0.0009	15±2	$0.040^{+0.002}_{-0.003}$
2.5 - 5.0	83.6280±0.0020	22.0210±0.0020	14^{+3}_{-2}	0.040±0.004
5.0 - 200.0	83.6350±0.0020	22.0220±0.0020	16^{+6}_{-4}	0.034±0.004
0.7 - 200.0	83.6300±0.0005	22.0216±0.0005	16±1	0.042±0.001

Table B.13.: The best-fit parameters of the Crab data for the symmetrical Gaussian. $1\,\sigma$ statistical errors are given.

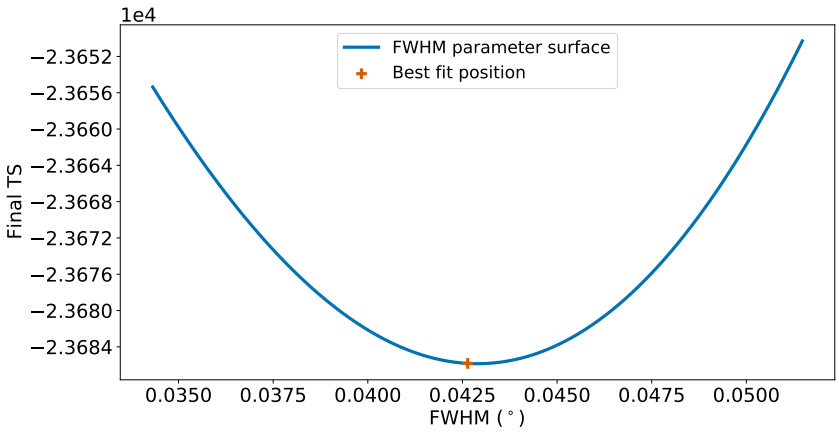

Figure B.6.: Crab morphology (0.7 - 200 TeV): parameter space of the FWHM estimate for the Gaussian model.

B.5. H.E.S.S. analysis configuration

Several aspects of the H.E.S.S. analysis configuration, defined in the introduction of Ch. 4, can directly influence the morphology fit. The energy threshold at 0.3 TeV, and the maximum zenith angle of observation at 50° were applied in the main analysis to improve the PSF. The bin size was set at 0.01° and the test position at RA = 187.7059°, and DEC = 12.3911°.

The perspective of obtaining a better extension UL motivated two new analyses, one for an energy threshold at 0.7 TeV, and a second analysis with the zenith angle cut of 45°. The stability of the main H.E.S.S. analysis motivated another two new analyses, one analysis where the bin size is set to 0.005° and a second analysis where the test position is shifted by $\approx 0.005°$. Hence, I conducted a total of four new analyses as part of the system checks for the gamma-ray low state, each with a different update to the main analysis configuration. I used the same morphology algorithm from Sec. 4.3.1 to derive the H.E.S.S. results and the best-fit parameters for the point-like and Gaussian models. The best fit position of the point-like model with $3\,\sigma$ uncertainty contours is shown in Fig. B.7 (left) and the 99.7% c.l. extension UL is shown in Fig. B.7 (right). The results agree very well with each other and with the main analysis (Sec. 4.3), therefore, confirming their robustness.

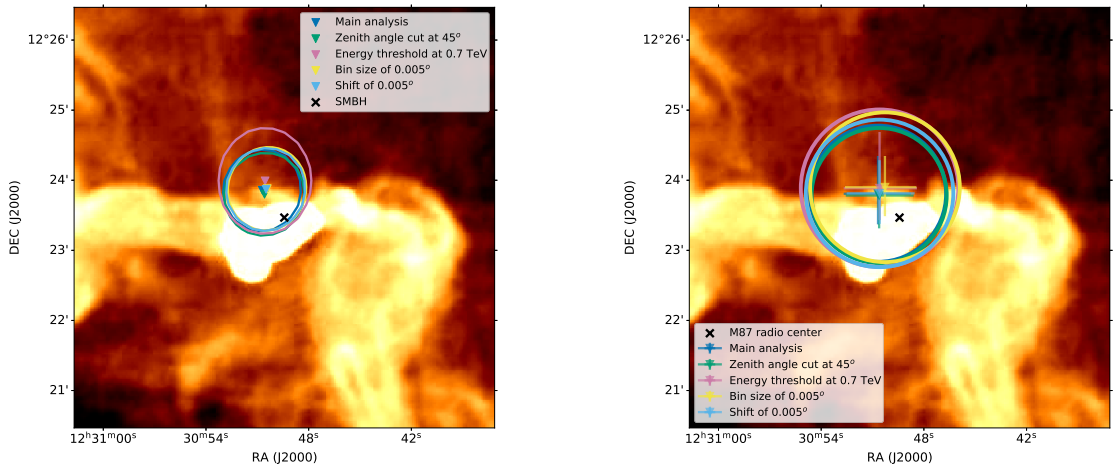

Figure B.7.: Results of the systematic check analyses showing (left) the Best point-like model fit position of the M87's gamma-ray low state with $3\,\sigma$ statistic uncertainties contours and (right) the extension UL of M87's gamma-ray low state with 99.7 % c.l. with the VLA 90 cm radio emission[113]. The best fit position of the Gaussian model is given with $1\,\sigma_{\mathrm{stat}} + 1\,\sigma_{\mathrm{syst}}$ uncertainties.

B.6. Point-like functions

The definition of the point-like function in the fit algorithm is not straightforward. Numerical likelihood estimation takes place in discrete space, and the algorithm has limitations when dealing with noncontinuous functions such as a 2D delta function.

The first attempt to fit a point-like model was defined according to:

$$M_D = B + PSF \circledast \mathrm{Delta2D} \times E, \tag{B.1}$$

where M_D is the model for the detected signal, B the H.E.S.S. background, Delta2D is the Sherpa function, and E is the H.E.S.S. exposure. The seed for the fit position (RA, DEC) was varied up to 5 pixels (0.05°) in each direction. The fit algorithm always yielded the best position in a radius less than a pixel (0.01°) from the initial seed; therefore, the Delta2D function is not appropriate to be used as the point-like model.

A second and more common approach is to use a 2D Symmetrical Gaussian with a fixed and very small width convolved with the PSF. The FWHM was fixed at 0.1 pixels (0.001°). During the fit, the seed for the fit was varied in 5 pixels in each direction. The results are very similar to the test with the delta function, i.e., the fit algorithm remains within 1 pixel from the given

seed position. Therefore, the Sherpa Gaussian function with a fixed width is not a good option for the point-like model.

Finally, the point-like function was defined based on the PSF function as shown in the main text by Eq. 4.3: a sum of three 2D Symmetrical Gaussians. While the center of the first Gaussian is free, the center of the second and third Gaussian functions are linked to it. The other parameters are fixed to the values derived from the H.E.S.S. analysis (Tab. 4.4), based on simulation. The seed position was varied within 5 pixels, and the fit algorithm managed to converge to the same best-fit position, regardless of the seed. Therefore, the PSF function using three Sherpa 2D Gaussian functions was chosen as the point-like model.

Appendix C.

The best fit position of individual flares

Gamma-ray flares from M87 are known to be very fast bursts[102,118,119], therefore, the emission region must come from a very small region close to the SMBH. Due to the IACTs low angular resolution ($\approx 0.05°$) and the very compact regions responsible for the flares emission, it is not expected that IACTs can detect an extended emission in a flare state in M87. Nevertheless, the results from the morphology fit of Tab. 4.7 show a preference of 1.6σ for the Gaussian model in comparison to the point-like model in the intermediate state, which is not significant but motivated further investigation of the best-fit position of the individual flares. Bayesian Blocks (Fig. 4.4) with different emission regions, when stacked together, could lead to an indication of an extension in the source state. I conducted a H.E.S.S. analysis for each block in the intermediate and the high states: Blocks 1-2 corresponds to the 2005 flare, Block 3 is the intermediate state of the 2008 flare, Block 5 is the flare from 2010, Block 7 is the high state in 2018 and Block 8 is the intermediate state after it. The results of the H.E.S.S. analysis statistics are shown in Tab. C.1, while the PSF information is shown in Tab. C.2 and the morphology fit results are shown in Tabs. C.3, C.4 and C.5.

Figure C.1 summarizes the results of the individual flares, showing the 1σ statistical uncertainties contours. Considering the 3σ statistical and the systematic uncertainty on the position the emission origin of the Blocks are consistent with each and with the core. The spectral diagram in Fig. C.2 demonstrates how large the 1σ statistical uncertainties of the spectral index are, specially for low statistic blocks. Blocks 1-2 and 7 have very similar flux levels and spectral index, which could be evidence of the same emission region. Block 5 is a high state, though with a lower flux and steeper spectral index as Blocks 1-2 and 7. The largest uncertainties due to limited statistics are found in Block 3 and the lowest flux and steepest index are found in Block 8. Considering the necessary level of 3 standard deviations to claim a significant difference in the spectral indexes, none of the intermediate/high state blocks can be significantly distinguished in terms of the spectral index.

	Block 1-2	Block 3	Block 5	Block 7	Block 8
Excess counts	261	52.2	161.9	240.0	146.5
Significance (σ)	16.7	6.1	11.2	15.9	8.7
Livetime (h)	14.5	6.4	16.5	12.5	22.1
Flux at 1 TeV 10^{-13}cm^{-2}s^{-1}	12.0±0.9	6±1	7.8±0.9	11±1	3.7±0.4
Spectral index	2.20±0.07	2.30±0.20	2.50±0.10	2.14±0.07	2.4±0.10

Table C.1.: Statistical results of the H.E.S.S. analysis for the flares. Blocks 1-2 corresponds to the 2005 flare, Block 3 is the intermediate state of the 2008 flare, Block 5 is the 2010 flare, Block 7 the high state in 2018 and Block 8 the intermediate state after it (Fig. 4.4).

State	**68% c.r.** (°)	**99% c.r.** (°)	**A (counts)**	σ_1 (°)	A_2 **(counts)**	σ_2 (°)	A_3 **(counts)**	σ_3 (°)
Block 1-2	0.049	0.254	4.6	0.129	77.0	0.024	17.9	0.051
Block 3	0.048	0.248	4.4	0.128	79.8	0.024	19.2	0.051
Block 5	0.048	0.245	4.0	0.127	82.0	0.025	21.2	0.052
Block 7	0.050	0.258	4.4	0.132	79.5	0.024	17.9	0.052
Block 8	0.049	0.244	4.3	0.126	70.7	0.025	19.8	0.052

Table C.2.: PSF parameters resulted from the H.E.S.S. analysis for the flares. Blocks 1-2 corresponds to the 2005 flare, Block 3 is the intermediate state of the 2008 flare, Block 5 is the 2010 flare, Block 7 the high state in 2018 and Block 8 the intermediate state after it (Fig. 4.4). Equation 4.7 defines the model used by H.E.S.S. tools to fit the PSF. Results of the main analysis are in Tab. 4.4 for comparison.

	Point-like		**Symmetrical Gaussian**		**Comparison**	
	Final stat.	**dof**	**Final stat.**	**dof**	**ΔTS**	**Signif.(σ)**
Block 1-2	15279.5	7842	15277.5	7841	-2	1.4
Block 3	11663.6	7842	11663.7	7841	0.1	-
Block 5	15523.0	7842	15523.1	7841	0.1	-
Block 7	15395.7	7842	15394.2	7841	-1.5	1.2
Block 8	13915.0	7842	13911.9	7841	-3.1	1.8

Table C.3.: Fit statistics for the intermediate and high states for the point-like and symmetrical Gaussian models. Blocks 1-2 corresponds to the 2005 flare, Block 3 is the intermediate state of the 2008 flare, Block 5 is the 2010 flare, Block 7 the high state in 2018 and Block 8 the intermediate state after it (Fig. 4.4). Results of the main analysis are in Tab. 4.7 for comparison.

Blocks	Point-like model		
	RA(°)	**DEC(°)**	**Ampl.(a.u.)**
Block 1-2	187.703±0.003	12.394±0.003	11.7±0.9
Block 3	187.707±0.007	12.388±0.006	6±1
Block 5	187.704±0.004	12.401±0.004	7.3±0.8
Block 7	187.709±0.003	12.387±0.003	10.6±0.9
Block 8	187.705±0.007	$12.400^{+0.006}_{-0.007}$	3.4±0.4

Table C.4.: The best fit parameters for the source states for the point-like model. Blocks 1-2 corresponds to the 2005 flare, Block 3 is the intermediate state of the 2008 flare, Block 5 is the 2010 flare, Block 7 the high state in 2018 and Block 8 the intermediate state after it (Fig. 4.4). Results of the main analysis are in Tab. 4.5 for comparison.

Blocks	Symmetrical Gaussian model			
	RA(°)	**DEC(°)**	**Ampl.(a.u.)**	**FWHM (°)**
Block 1-2	187.703±0.003	12.394±0.003	$1.2^{+5.1}_{-0.3}$	0.03±0.01
Block 3	$187.709^{+0.009}_{-0.005}$	$12.387^{+0.008}_{-0.005}$	$12.5^{-}_{-11.9}$	$0.008^{+0.023}_{-0.007}$
Block 5	$187.701^{+0.001}_{-0.008}$	12.401±0.002	25^{+34}_{-22}	$0.005^{+0.012}_{-0.001}$
Block 7	187.709±0.004	12.387±0.003	$1.1^{+5.7}_{-0.5}$	0.03±0.01
Block 8	187.705±0.007	12.398±0.007	$0.13^{+0.20}_{-0.05}$	0.05±0.02

Table C.5.: The best fit parameters for the source states for the symmetrical Gaussian model. Blocks 1-2 corresponds to the 2005 flare, Block 3 is the intermediate state of the 2008 flare, Block 5 is the 2010 flare, Block 7 the high state in 2018 and Block 8 the intermediate state after it (Fig. 4.4). Results of the main analysis are in Tab. 4.6 for comparison.

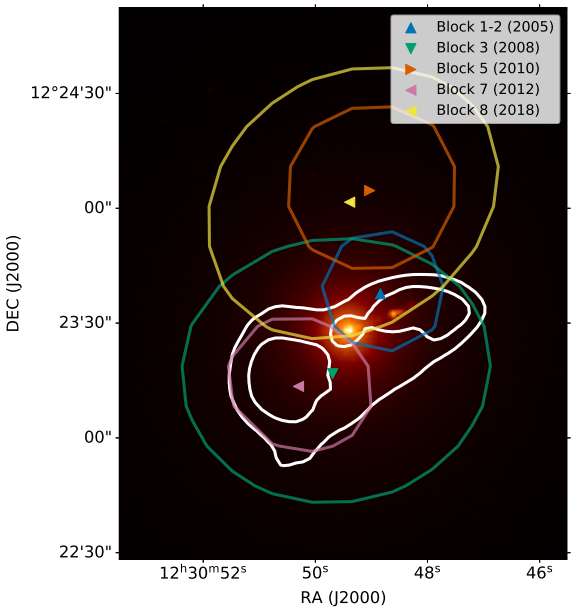

Figure C.1.: Optical sky map of M87 from SDSSg (646 THz)[173] displayed in square root of the intensity. The radio 21.4 cm VLA[151] contours overlaid in white are also shown. The best-fit position for the VHE gamma-ray flares with 1σ statistical uncertainties are shown as seen by H.E.S.S., based on the Bayesian Blocks (Fig. 4.4 and Tab. 4.2). Analogous to Fig. 4.10.

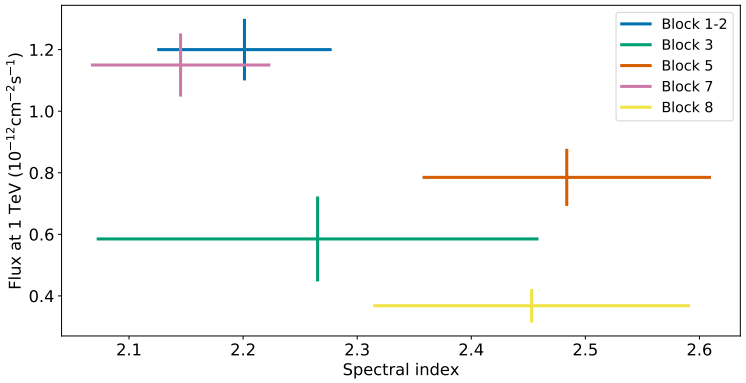

Figure C.2.: Spectral diagram for the intermediate and high states. Blocks 1-2 corresponds to the 2005 flare, Block 3 is the intermediate state of the 2008 flare, Block 5 is the 2010 flare, Block 7 the high state in 2018 and Block 8 the intermediate state after it (Fig. 4.4).

Appendix D.

Artemis Modal® analysis of the MST prototype structure

Artemis Modal Pro® is commercial software from Svibs[165]. It provides a set of tools for analyzing accelerometer data with the application at structural vibrations.

I conducted a cross-check analysis using the software to validate the results of Ch. 5 using the same method, the FDD. First, I defined the geometry of the structure according to the CSS of the prototype, as shown in Fig. D.1. The three sensors are located in the lower beams: at the camera frame, CSS flange, and dish flange (see also Fig. 5.7).

Afterwards, I selected the data from August, 25$^{\text{th}}$, 2019. The Enhanced FDD option was chosen since it allows the estimation of the damping rate. Fig. D.2 shows the resulted FDD spectrum, Fig. D.3 shows the MAC matrix and Tab. D.1 summarizes the modal parameters. A MAC value limit of 0.7 was used as the maximum allowed correlation between modes. In comparison to Tab. 5.3, the commercial software delivered very similar results, with the largest differences encountered in the damping rate of some modes.

One of the advantages of the software is a good visualization of the mode shapes. Fig. D.2 to D.6 show the exaggerated deformation of the mode shapes. The first frequency at 1.19 Hz shows the larger displacement in the direction of the gravity by the sensors in the CSS and camera frame, out-of-phase with one another. The second frequency at 1.39 Hz shows a lateral movement with all the 3 sensors in phase. The mode at 2.39 Hz is dominated by the CSS movement in the direction of gravity, out-of-phase with the two other sensors. All the 3 sensors in-phase move in the direction of gravity at the modal frequency of 3.28 Hz. Therefore, higher modes show more complicated behavior and are not described here.

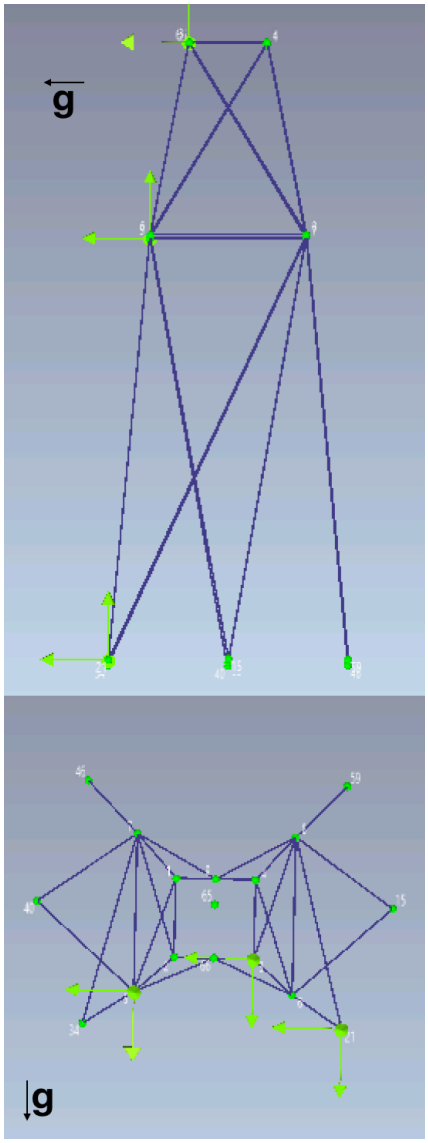

Figure D.1.: CSS simplified CAD model as input in the Artemis software for vibration studies. The direction of the acceleration of gravity is show as well as the position of the three sensors on the structure.

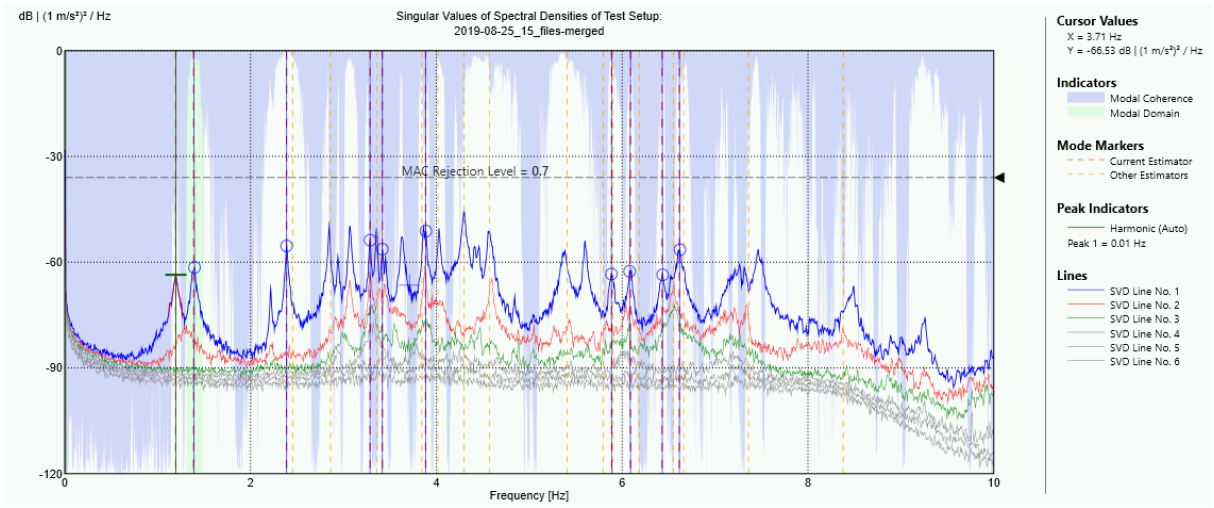

Figure D.2.: The FDD analysis with Artemis Modal® software. First, second and third singular values are shown. The peaks, which passed the criteria are shown by the blue circles.

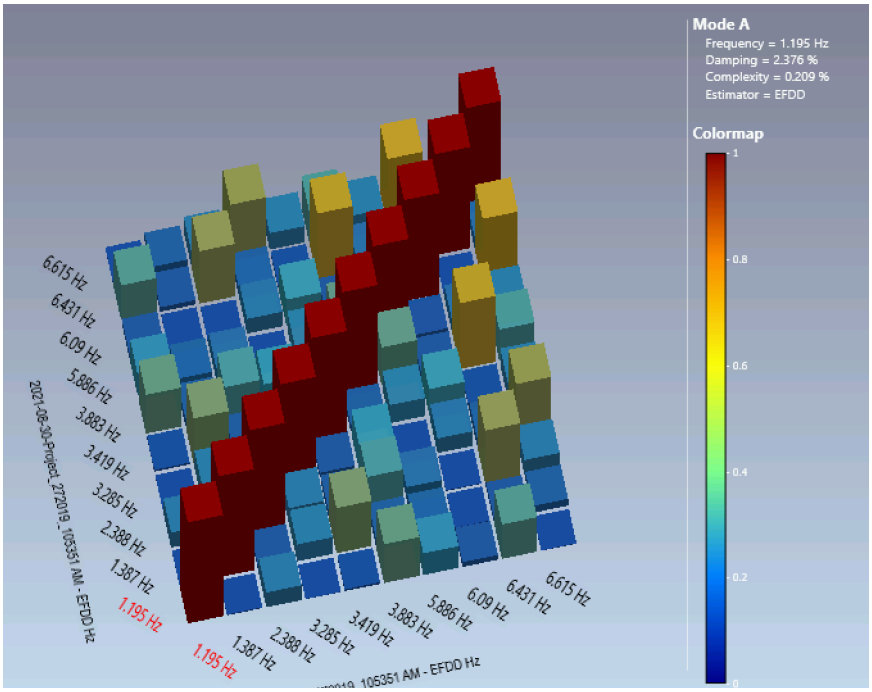

Figure D.3.: The MAC matrix for the modal frequencies after the cut at MAC value of 0.7 as seen by the commercial software.

Modal freq. (Hz)	**Damping rate (%)**
1.19	2.38
1.39	1.47
2.39	0.40
3.29	0.16
3.42	0.26
3.88	0.10
5.89	0.10
6.09	0.20
6.43	0.27
6.62	0.36

Table D.1.: Summary of the modal parameters resulted from the Artemis software applied to the data from August 25$^{\text{th}}$, 2019. Table analogous to Tab. 5.3 from the main text.

The commercial software has more sophisticated tools and more methods of analysis[165]. However, for the use within CTAO, it is necessary that the system is specifically adapted for the case of the MSTs, and eventually for the other telescopes. Long-term analysis with more telescopes, cross-calibration, and the automatic pipeline is the key to assuring the MSTs availability and reliability throughout the years of operation. As opposed to my main analysis pipeline (Sec. 5.4 and 5.6), the Artemis software is not able to provide all those requirements and, therefore, is not included as part of the structure monitoring system.

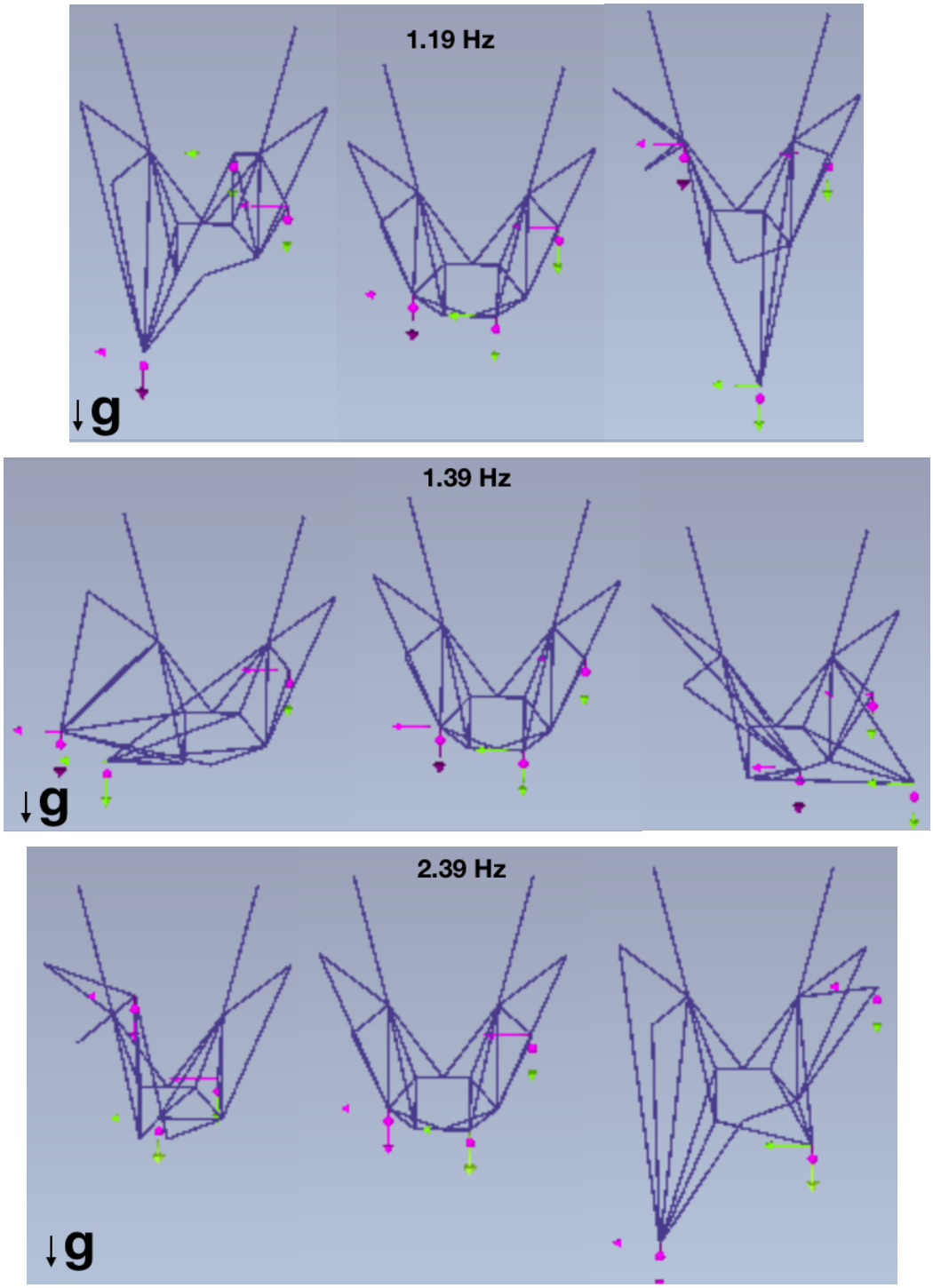

Figure D.4.: Mode shapes at 1.19 Hz, 1.39 Hz and 2.39 Hz.

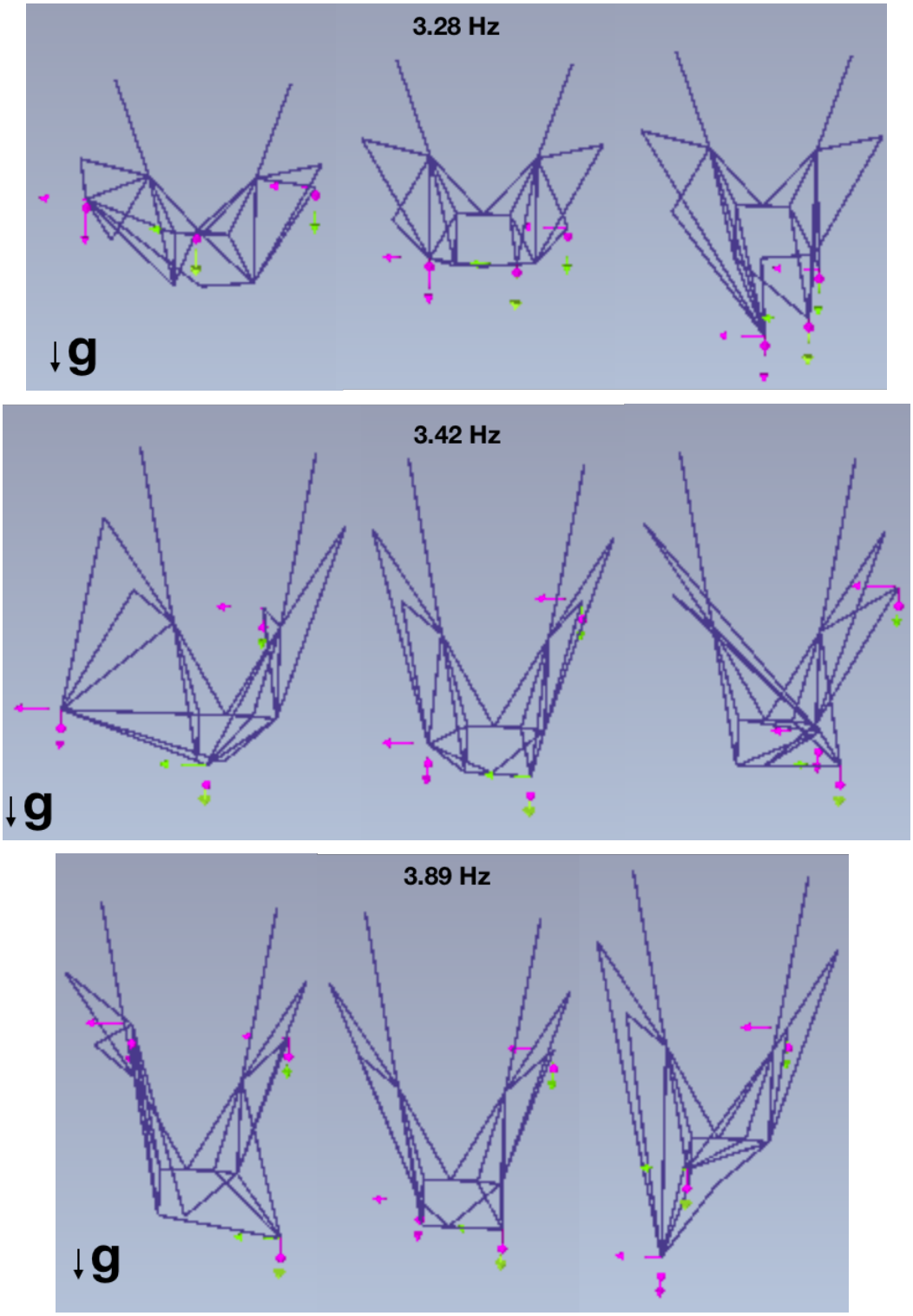

Figure D.5.: Mode shapes at 3.28 Hz, 3.42 Hz and 3.8 Hz.

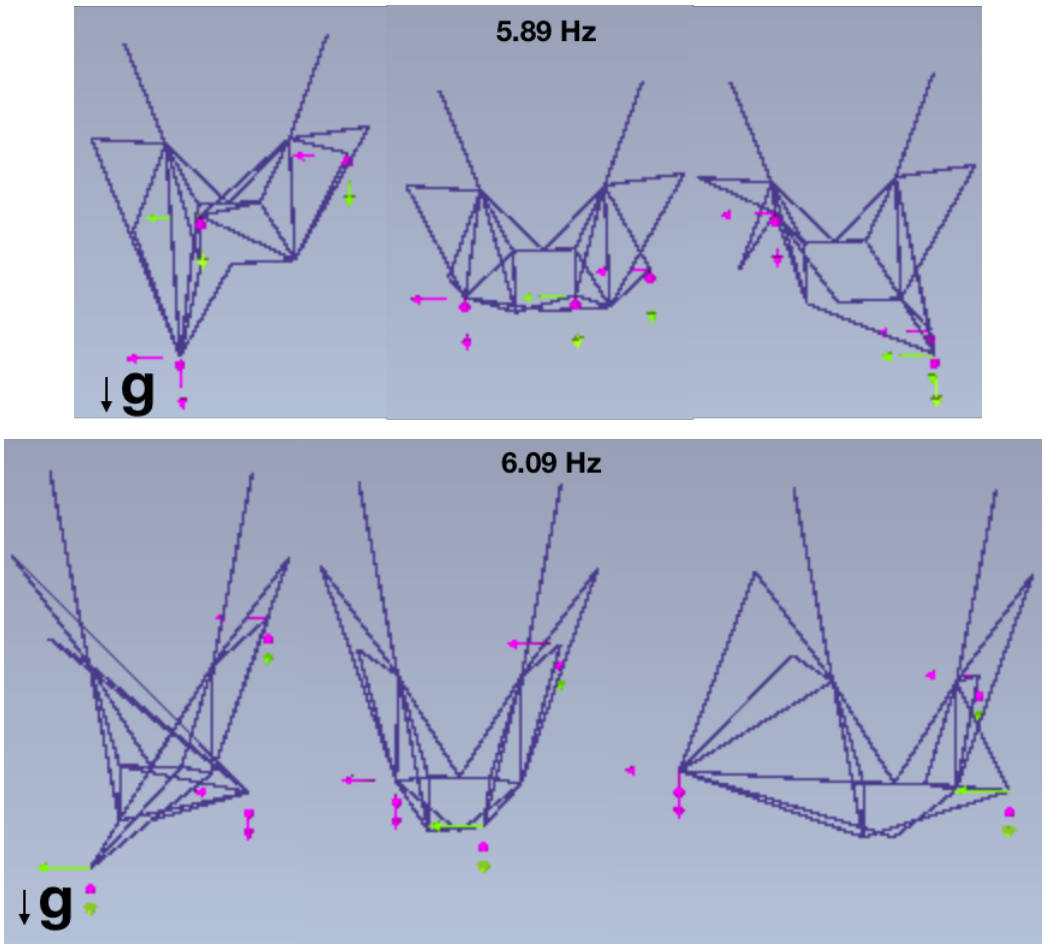

Figure D.6.: Mode shapes at 5.89 Hz and 6.09 Hz.

Acknowledgements

First, I would like to thank my family, Elias, Sinara, and Arthur, for the undying support at every decision and for holding things together across the ocean. Second, I thank my partner Jacobina for standing by me, understanding, and supporting me through the difficulties of the long path to the PhD. I thank my former supervisor Vitor de Souza who officially introduced me to astrophysics back in 2009. I am grateful for the first interview for the PhD position with Stefan Schlenstedt, Ulrich, and Markus back in 2017. They agreed to have me as a PhD student at DESY. I thank David for taking the responsibility of being my official supervisor through the Humboldt University. The daily supervision was conducted by Markus with the focus on the MST work, where I was delighted by freedom and the motivation constantly received. Stefan Ohm was untiring in guiding me through the project within the H.E.S.S. collaboration since picking up a project up to the long process of reviewing the manuscript.

I would like to thank my friends in Berlin who showed me that I was not alone in this PhD enterprise, including Konstantin, Marianna, Pedro, Maria, and Kaori. I thank Orel for all the conversations about career, life and everything. All the Brazilian meet-ups, celebrations, and evenings together kept my heart warm for the European winter; hence, a special thanks to Gabriel, Aline, and Rafael. I was glad to have the soccer team Sparta Lichtenberg III throughout these years. I often played amateur soccer, keeping my body moving and my mind healthy. Finally, I thank my flatmate Jonas for the inspiring conversations about physics, philosophy, and the future.

I thank Gerrit for being my first contact and guide to the MST structure monitoring project, and Maria Haupt for introducing me to the H.E.S.S. analysis software and guiding me through the first steps in the collaboration. I thank Constantin and Simon for the lovely month in Namibia in 2020, when we worked as shifters at the H.E.S.S. site. I was happily surprised by how gentle the Namibian people were, primarily due to the local crew Volker, Toni, and the calm Albert, who very sadly passed away later that same year. I thank Maria and Ruslan for attending my calls and providing the data sets I needed for my analysis. I also thank Heike for the latex template for the thesis and Tim for helping out with the bureaucracy of the thesis submission.

I thank Christoph Pfrommer for explaining me his model of the M87 gamma-ray emission,

with which I interpreted the results of my analysis. I thank Andrew for showing me his way of understanding physics from the basic principles. I also thank my fellow Marc for patiently guiding me through the theory of gamma-ray emission.

I thank individually the ones that helped me review the thesis. Raul, Dima, Constantin, Maria, Stefan, Markus, Uli, Dan, and David had eyes at least at some parts of the thesis and helped improve the text and the clarity of my goals.

I thank both DESY CTA and H.E.S.S. groups for a friendly work environment. The social events such as the group outings, group retreat, astrophysics school, and collaboration meetings contributed with a load of motivation for further work.

I will never forget the peaceful workplace by the beautiful Zeuthener See. Despite the many difficulties imposed by the covid pandemic, I felt mostly supported by the flexibility and guidance offered by the institute. Thank you!